Development and study of microdischarge arrays on silicon

Mukesh Kumar Kulsreshath

▶ **To cite this version:**

Mukesh Kumar Kulsreshath. Development and study of microdischarge arrays on silicon. Other [cond-mat.other]. Université d'Orléans, 2013. English. NNT : 2013ORLE2002 . tel-00843656

HAL Id: tel-00843656

https://theses.hal.science/tel-00843656

Submitted on 11 Jul 2013

HAL is a multi-disciplinary open access archive for the deposit and dissemination of scientific research documents, whether they are published or not. The documents may come from teaching and research institutions in France or abroad, or from public or private research centers.

L'archive ouverte pluridisciplinaire **HAL**, est destinée au dépôt et à la diffusion de documents scientifiques de niveau recherche, publiés ou non, émanant des établissements d'enseignement et de recherche français ou étrangers, des laboratoires publics ou privés.

UNIVERSITÉ D'ORLÉANS

ÉCOLE DOCTORALE Energie - Matériaux - Sciences de la Terre et de l'Univers (EMSTU)

LABORATOIRE GREMI

THÈSE présentée par :

Mukesh Kumar KULSRESHATH

soutenue le : **21 Janvier 2013**

pour obtenir le grade de : **Docteur de l'université d'Orléans**

Discipline : **Physique, Physique des Plasmas**

Development and study of microdischarge arrays on silicon

THÈSE dirigée par :

M. Rémi DUSSART	Maître de conférences, GREMI, Université d'Orléans, France

RAPPORTEURS :

M. Jörg WINTER	Professeur, Ruhr-Universität Bochum, Allemagne
M. Mark BOWDEN	Senior Lecturer, The Open University, Angleterre

---

JURY:

M. Jean-Michel POUVESLE	**(Président du jury)-** Directeur de Recherche, C.N.R.S., France
M. Volker SCHULZ-von der GATHEN	Principal Investigator, Ruhr-Universität Bochum, Allemagne
M. Lawrence John OVERZET	Professeur, University of Texas at Dallas, USA

Acknowledgements

I express my sincere gratitude to Rémi DUSSART for allowing me to conduct this research under his auspices. I am especially grateful for his confidence and the freedom he gave me for this PhD. I would like to thank him for his contribution in major scientific discussions and his very good suggestions related to the PhD work. It is his full support and guidance that allowed me to complete my PhD project on time and with European label. With his support, I was able to work in other European labs, mainly in the microplasma lab of Ruhr-Universität Bochum, Germany.

I would like to thank the current director of the lab Chantal LEBORGNE and the previous director of the lab Jean-Michel POUVESLE for welcoming me at GREMI (Groupe de Recherches sur l'Energetique des Milieux Ionises) and providing their full support during my PhD.

I would like to thank all the jury members, Jean-Michel POUVESLE (president of the jury), Jörg WINTER (rapporteur of the PhD thesis), Mark BOWDEN (rapporteur of the PhD thesis), Volker SCHULZ-von der GATHEN (jury member), and Lawrence John OVERZET (jury member, for their participation and interest in my PhD work.

I would like to acknowledge Nader SADEGHI from LiPhy lab. Grenoble (France), for providing his equipments and his full support to carry out spectroscopy based experiments. I would like to thank Marion WOYTASIK, Guillaume SCHELCHER, David BOUVILLE and other IEF-CTU colleagues at Orsay (France) for providing their full support for the fabrication of microdischarge devices. I would like to thank Jörg WINTER, and Volker SCHULZ-von der GATHEN for welcoming me in their lab. at Ruhr-Universität Bochum (Germany). Specially, I would like to thank Volker SCHULZ-von der GATHEN for assisting and supporting me for the experimental work. I would also like to thank Henrik BÖTTNER and Judith GOLDA for their support in the experimental work. Big thanks also goes to Verena M. SCHARF, she provided her full support in the organisation of my stay.

I would like to thank my research group “Equipe Gravure” for supporting me for my PhD. A special thanks to Philippe LEFAUCHEUX. Philippe supported me a lot with his engineering skills, for maintaining the experimental setup up-to-date. Without his support, it was impossible to complete all the experimental work related to the cleanroom. Other special thanks go to Thomas TILLOCHER and Julien LADROUE for supporting me in my PhD work with their highly skilled etching techniques….. like STiGer process……..!!! I would like to thank Laurent SCHWAEDERLE and Olivier AUBRY for working with me on the microdischarge project and providing us many new innovative ideas for this project. I also thank Valentin FELIX for his support in the last few months of my thesis.

Without the support of all members of my family, I would never finish this thesis and I would never find the courage to overcome all the difficulties during this work. My thanks go to my parents and all the family members, for their confidence and their love during all these years.

I would like to thank my office colleague Mireille GAILLARD, for keeping the working environment very nice and friendly. I would like to thank specially Hagop TAWIDIAN for his full support during my stay at Orleans. I would also like to thank all the colleagues of GREMI for supporting me during my stay at GREMI. Thanks to all of GREMIst! This thesis would not have happened without your help.

Mukesh Kumar KULSRESHATH

Orleans (France), January 2013

Table of contents

ACKNOWLEDGEMENTS **1**

TABLE OF CONTENTS **3**

GENERAL INTRODUCTION **7**

1 INTRODUCTION **11**

1.1 INTRODUCTION TO MICRODISCHARGES 11

1.1.1 Introduction to atmospheric plasmas and micro plasmas *11*

1.1.2 Breakdown Process *12*

1.1.2.1 Explanation of the mechanisms from dark to glow regime 15

1.2 OVERVIEW ON THE DEVICES AND THE METHODS TO GENERATE MICRO DISCHARGES 16

1.2.1 Metal plate discharge *17*

1.2.2 Micro-Torch discharge *17*

1.2.3 Dielectric Barrier Discharge (DBD) *19*

1.2.4 Cathode boundary layer (CBL) discharge *21*

1.2.5 Micro hollow cathode discharges (MHCD) *22*

1.2.5.1 Alumina based MHCD 22

1.2.5.2 Diamond based MHCD 23

1.2.5.3 Si based MHCD 24

1.2.5.4 Microhollow cathode sustained discharges (MCSD) 26

1.3 POTENTIAL APPLICATIONS OF MICRO PLASMAS 27

1.3.1 Source of Excimer radiations *27*

1.3.2 Medicine and biology *28*

1.3.3 Sensors and detectors *28*

1.3.4 Gas treatment and pollution control *29*

1.3.5 On chip analysis and micro-fluidic application *29*

2 DEVICE FABRICATION PROCESS AND EXPERIMENTAL TECHNIQUES **31**

2.1 MICRO-STRUCTURED ATMOSPHERIC PLASMA DEVICES 31

2.2 MICRODISCHARGE REACTORS IN ALUMINA 31

2.3 MICRODISCHARGE REACTORS (MDRS) IN SILICON 32

2.3.1 General arrangement of the structure *32*

2.3.2 General designs *32*

2.3.3 Single hole MDR *34*

2.3.4 Multiple hole array *35*

2.3.5 MDRs with special designs *36*

2.3.5.1 Mixed hole array 37

2.3.5.2 Mixed trench array 37

2.3.5.3 Mixed hole arrays with acronyms 37

2.3.5.4 Concentric rings MDR 38

2.3.5.5 MDR with a long trench 39

2.4 FABRICATION PROCESS FOR SILICON BASED MDRS 40

2.4.1 Presentation of the process flow *41*

2.4.1.1 Si wafer cleaning 41

Cleaning process 41

2.4.1.2 Dielectric layer deposition 41

2.4.1.3 Sputtering and photolithography 42

2.4.1.4 Top Ni - electrode patterning 43

2.4.1.5 Backside contact formation and topside protection 44

2.4.1.6 Cavity etching 46

2.4.1.7 Modification of the process flow for MDRs operating in AC regime 48

2.5 CHALLENGES IN FABRICATION PROCESS AND SOLUTIONS 49

2.5.1 Top Ni electrode adhesion problem ... *49*
2.5.2 Cavities under etching ... *50*
2.5.3 Backside gold layer detachment ... *50*
2.5.4 Deposition of Si_3N_4 layer ... *51*
2.6 EXPERIMENTAL SETUP FOR DC MICRODISCHARGE EXPERIMENTS ... 52
2.7 DIAGNOSTIC SYSTEMS FOR DC MDRS ... 54
2.7.1 Optical Emission Spectrometry (OES) ... *54*
2.7.1.1 Spectrometer ... 54
2.7.2 Microscopy ... *55*
2.7.2.1 Optical microscopy ... 55
2.7.2.2 Scanning Electron Microscopy (SEM) ... 55
2.7.3 Tunable Diode Laser Absorption Spectroscopy (TDLAS) ... *56*
2.8 EXPERIMENTAL SETUP FOR AC ... 57
2.9 DIAGNOSTIC SYSTEMS FOR MDRS OPERATING IN AC ... 58
2.9.1 ICCD camera and spectroscopy setup ... *58*
2.9.2 Phase resolved optical emission spectroscopy ... *59*

3 IGNITION AND EXTINCTION IN ALUMINA BASED MHCD ... 61

3.1 INTRODUCTION ... 61
3.2 STUDY OF IGNITION AND EXTINCTION WITH ELECTRICAL CHARACTERISATION ... 61
3.2.1.1 Ignition ... 62
3.2.1.2 Self pulsing regime ... 63
3.2.1.3 Extinction phase ... 64
3.3 EQUIVALENT ELECTRICAL CIRCUIT ... 65
3.3.1 Ignition ... *65*
3.3.2 Extinction ... *67*
3.4 MEASUREMENTS USING TDLAS ... 67
3.4.1 Metastable density measurements for Al_2O_3 based MHCD in steady state regime ... *67*
3.4.2 Gas temperature measurements ... *70*
3.4.3 TDLAS characterisation for ignition and extinction ... *72*
3.5 CONCLUSIONS ... 75

4 STUDY OF MICRODISCHARGES ON SILICON IN DC ... 77

4.1 INTRODUCTION ... 77
4.2 SINGLE HOLE MICRO DISCHARGE ... 77
4.2.1 V-I characteristics for Standard Polarity (SP) and Reverse Polarity (RP) ... *77*
4.2.1.1 Anisotropic cavity ... 77
4.2.1.2 Isotropic cavity ... 78
4.2.1.3 Through hole cavity ... 81
4.2.1.4 Discussion for single hole devices ... 82
4.2.2 Breakdown (V_{br}) ... *83*
4.2.2.1 Effect of polarity and gas type ... 83
4.2.2.2 Effect of pressure ... 84
4.2.3 Hysteresis ... *86*
4.2.4 Simulations ... *87*
4.2.4.1 Description ... 87
4.2.4.2 Plasma chemistry ... 90
4.2.4.3 Results and discussions ... 90
4.2.5 Neutral temperature measurements ... *94*
4.3 ARRAY OF MICRO DISCHARGES ... 96
4.3.1 Array of 16 holes ... *96*
4.3.1.1 4 x 4 hole array with short interhole distance ... 96
4.3.1.2 4 x 4 hole array with long inter-hole distance ... 98
4.3.1.3 Discussion ... 98
4.3.2 Self pulsing mode in array of 16 x 16 holes ... *99*
4.3.2.1 4 sub-arrays of 256 holes on a chip ... 101
4.3.3 Array of 1024 holes ... *104*

4.3.3.1 V-I characteristics ... 104
4.3.3.2 Breakdown ... 105
4.3.3.3 Ignition dynamics ... 113
4.4 EXOTIC GEOMETRIES ... 116
4.4.1 TRENCH shape microdischarges ... 116
4.4.2 Mixed Concentric Rings (MCR) arrays ... 118
4.5 FAILURE AND LIFE TIME OF THE SILICON MICRO-DISCHARGE REACTORS ... 120
4.5.1 Suggestions for the longer life time of MDRs ... 125
4.6 CONCLUSIONS ... 128

5 CHARACTERISATION OF SI BASED MICROPLASMA REACTORS IN AC ... 131

5.1 INTRODUCTION ... 131
5.2 DISCHARGE CHARACTERISTICS ... 131
5.2.1 Electrical and optical time resolved characterisation of an array ... 131
5.2.1.1 Current, voltage and emission time evolution ... 131
5.2.1.2 Optical space resolved characterisation of the array ... 134
5.2.2 Single hole MDR ... 135
5.2.2.1 Effect of frequency ... 135
5.2.2.2 Ignition dynamics ... 137
5.2.2.3 Effect of pressure ... 139
5.2.2.4 Self-pulsing ... 141
5.2.3 MDR array ... 142
5.2.3.1 Effect of variation in frequency and voltage ... 142
5.2.3.2 Dynamics of the array ... 143
5.2.3.3 Ionisation wave ... 145
5.2.4 Mixed trench Array ... 146
5.2.4.1 Edge ignition phenomena ... 146
5.2.4.2 Ignition wave ... 147
5.2.4.3 Trends of ignition ... 148
5.3 CONCLUSIONS ... 149

CONCLUSIONS ... 151

LIST OF FIGURES ... 155

LIST OF TABLES ... 165

BIBLIOGRAPHY ... 167

APPENDIX — PUBLICATIONS ... 175

General Introduction

Microplasmas are becoming a major topic within the plasma community. Microplasmas comprise Micro Hollow Cathode Discharges (MHCD), Microjets, and Dielectric Barrier Discharges (DBD). They can all work at atmospheric pressure and are non-equilibrium plasmas. Among these different types of microdischarges, MHCDs appear as a very promising device configuration to drive DC or AC current through different gases. In this particular microdevice, a stable microplasma is confined inside a cavity.

Although many configurations of MHCD arrangements have been proposed, integrated systems involving MHCDs and microelectronics have not yet been presented.

Microfabrication techniques, which have been intensively used for semiconductor processing, can be applied to elaborate microdischarge devices. In such microdevices, the plasma volume can be reduced to as low as the nano-litre scale, which can lead to not yet observed physical phenomena, and bring new and various device applications. An American team led by G. Eden from the University of Illinois (Urbana) proposed a novel and original approach to form microplasma arrays of silicon (pyramidal geometry) using a wet etching process ***[Ede-03]***. Even if they have tried different methods and have proposed several configurations in different materials, their system is not really integrated on a device.

The objectives of this Ph.D. work is to propose different types of silicon micro-reactors made by microfabrication techniques, characterise them by electrical and optical diagnostics and test them in parallel for gas processing. Thus, to provide a better understanding of the physical phenomena related to microdischarge arrays made in silicon.

These types of microdischarges have a huge potential for various future applications like display or photonics technology, embedded sensors, sources of UV light and surface treatments. These devices usually run in inert gases. However, despite of their many potential applications in many different technological domains, the understandings of various physical phenomena, like their non-equilibrium behaviour at high pressure, effect of pressure on breakdown in different configurations, gas temperature inside the micrometric configurations are still questions of interest.

The present work is related to the study of microdischarge devices based on alumina and silicon. In this study, both Direct Current (DC) and Alternating Current (AC) regimes are explored using different device configurations. The behaviour of microdischarges are studied for single hole and multiple hole arrays. Only if such plasma characteristics are known for micrometric dimensions, the specific tailoring and modification of new devices according to the required applications is possible. The characteristics of microdischarges are investigated using electrical characterisation, optical emission spectroscopy (OES), absorption spectroscopy, scanning electron microscope (SEM) and using camera images. The experimental results are compared to the numeric simulations.

This PhD work was carried out within the ANR JCJC SIMPAS (Systems of Integrated Micro Plasma Arrays in Silicon) project. This project provided an opportunity to work with a post-doc fellow (Laurent Schwaederlé) during the 2 first years of the PhD.

The studies presented in this PhD work, are carried out in collaborations with many national and international research labs. Since 2005, GREMI is collaborating on microdischarges with L. J. Overzet's team from the University of Texas at Dallas, Richardson, USA. Alumina samples were fabricated there and the very first silicon devices were also built in the clean room facility of UTDallas. Silicon devices were then carried out in collaboration with the clean rooms of IEF-CTU (MINERVE), Orsay, France and CERTeM (Centre d'Etude et de Recherche Technologiques en Microélectronique) in Tours, France. A part of the studies related to the characterisation of the devices, is carried out in the collaboration of J. Winter, V. Schulz-von der Gathen and his team at Ruhr-Universität Bochum (RUB), Bochum, Germany. This collaboration allowed to perform the phase resolved optical emission spectroscopy (PROES) measurements of the mircodischarges running in AC. A part of the PhD work related to the spectroscopy is carried out in collaboration with N. Sadeghi from LiPhy (Laboratoire interdisciplinaire de Physique) at Grenoble, France. These experiments allowed us to measure the gas temperature of the microdischarges and their electron density by using optical emission spectrometry (OES) and diode laser absorption spectroscopy (DLAS). Finally, in collaboration with L. Pitchford Laplace Laboratory (Laboratoire Plasma et Conversion d'Energie) at Toulouse, France, we simulated several experiments of micro-discharges through GDSim software, which allowed us to have knowledge of key physical parameters (spatial distribution of electric field, electron temperature, density of charged species, ...).

Outline of thesis

In the **first chapter**, introduction to atmospheric plasmas, difference between Local thermodynamic equilibrium (LTE) plasmas and Non-local thermodynamic equilibrium (non-LTE) plasmas and their main fields of applications are briefly introduced. Breakdown phenomenon related to pressure is described. A brief outlook is provided for different types of existing atmospheric pressure microplasma technologies including an extended discussion on the working principles of integrated micro hollow cathode discharges (MHCDs) on silicon (Si) platform. Main potential industrial applications of these integrated plasmas are presented in brief.

In the **second chapter**, advances and challenges of the micro-structured atmospheric pressure plasma devices are presented in relation with state-of-art knowledge. An outlook to the designs of integrated Si based microdischarge reactors (MDRs) having different configurations and arrangements is given. An introduction to the fabrication technologies for silicon (Si) based MDRs is presented. Experimental setup and different characterisation methods used for the study are discussed.

Studies of the ignition and extinction phenomenon for alumina (Al_2O_3) based samples are presented in **chapter three**. Here, main emphasis is given to characterise the behaviour of

microdischarges for the starting and ending of the plasma. Spectroscopic measurements using Tunable Diode Laser Absorption Spectroscopy (TDLAS) are presented, for deeper analysis of these phenomena along with gas temperature measurements.

Chapter four presents the results obtained for silicon based MDRs in DC regime. Characteristics of single hole and multiple microdischarge arrays are presented. Simulation results of a single microdischarge are presented to explain the behaviour of plasma species and thickness of sheath for different conditions. Phenomena like edge ignition, life time of the devices are presented.

In **chapter five**, studies of silicon microdischarges in AC regime are presented. Microplasma device characteristics are presented using Phase Resolved Optical Emission Spectroscopy (PROES) and intensified charge-coupled device camera fitted with a long distance microscope. Here, the phenomena like effect of frequency on the ignition, existence of ignition wave and edge ignition are discussed for integrated Si MDRs.

In the end, the main results obtained for the microdischarges in different regimes are summarised.

Chapter 1

Introduction

1.1 Introduction to microdischarges

1.1.1 Introduction to atmospheric plasmas and micro plasmas

Plasmas are more and more used for industrial applications. One of the main fields of applications is dedicated to micro-nano technologies. Plasmas offer many advantages that cannot be achieved by other means (for example: chemical reactions in liquid phase, …). Although, most of plasmas used by semiconductor industry are working at low pressure, near atmospheric pressure plasmas (10 mbar < P < 10 bars) can also be produced for some other applications. Near atmospheric pressure plasmas, if they are well controlled, can provide many benefits in terms of radical density, electron density …

In fact, depending on the amounts of energy density transferred to the plasma, its properties change in terms of electron density and electron temperature. On the basis of these properties, cold plasmas can be divided into two categories: Local thermodynamic equilibrium plasmas (LTE) and Non-local thermodynamic equilibrium plasmas (non-LTE). In thermal plasma or LTE plasmas, transitions and chemical reactions are controlled by collisions with electrons and neutrals, and not by radiative processes. However, here the collisions between the different species should be micro-reversible for various reactions viz. excitation/de-excitation, ionisation/recombination, kinetic balance etc ***[Moi-96]***.

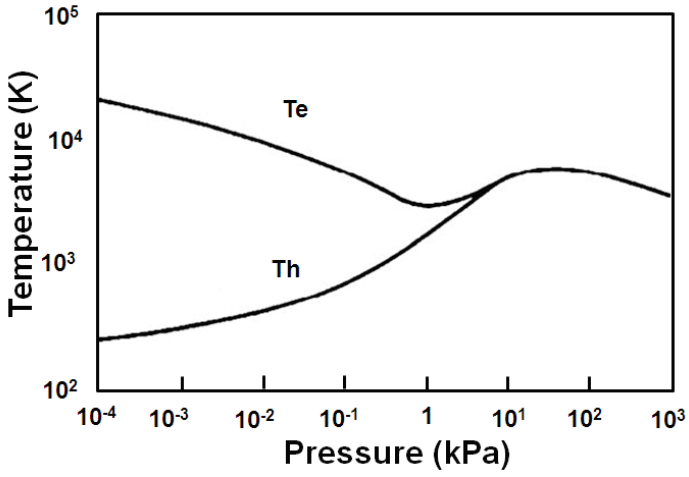

Figure 1.1: Effect of pressure on gas (heavy particle) temperature (T_h) and electron temperature (T_e), in mercury (Hg) plasma. [Bou-94]

Therefore, in thermal plasma, the electron temperature is equal to the gas and ion (heavy particles) temperature ***[Bou-94]***. On the other hand, non-thermal equilibrium plasma presents two distinct temperatures: electron temperature (T_e) and heavy particle temperature (T_h). For low-lying levels, the electron-induced de-excitation rate of the atom is generally lower than the corresponding electron induced excitation rate because of a significant radiative de-

excitation rate ***[Moi-96]***. This leads to the deviation from the Boltzmann distribution behaviour for the density of excited atoms. In this case, electrons move very fast and likely to govern collisions and transition phenomena as compared to the heavy particles. As a consequence, the plasma temperature or gas temperature is determined by the heavy particles (T_h). Figure 1.1 shows an effect of pressure on gas and electron temperature, in mercury (Hg) plasma, from ref. ***[Bou-94]***. From this figure, it is clear that at lower pressure ($10^{-4} \sim 10^{-2}$ kPa), electron temperature is much higher than gas temperature. Thus low pressure plasmas are non-LTE plasmas.

At low pressure, heavy particles are excited or ionised through inelastic collisions with electrons. These inelastic collisions do not raise the temperature of these heavy particles. At higher pressure, collisions between electrons and heavy particles in plasma are intensified. They lead to both plasma chemistry (by inelastic collisions) and heavy particle heating (by elastic collisions). Then, the difference between T_e and T_h decreases and the plasma state is closer to the thermal equilibrium state. Thus, arcs at atmospheric pressure come under LTE category.

But high pressure leads to small mean free paths for the different particles. This leads to high collision rate and atmospheric pressure plasmas are more exposed to instabilities. Apart from surface impact of heavy particles, effective stepwise ionisation, and Penning ionisation involving metastables can lead to avalanche like secondary electron generation. This can lead the discharge from stable glow mode to a thermal arc. Thus an arc can be also characterised by thermal emission of electrons from the cathode. Also atmospheric pressure leads to the demand of higher applied electric field as compared to the low pressure plasmas. This demand of higher applied electric field can be fulfilled by two ways, either by applying higher applied voltage or by reducing the gap between the electrodes. In 1889, Friedrich Paschen was the first, who explained the relationship of breakdown phenomenon with applied voltage, pressure and dimension. His famous law is known as 'Paschen law' in literature ***[Pas-89]***.

A promising idea to avoid instabilities or thermal arc mode and to generate stable glow discharge at atmospheric pressure is to design plasma reactors with small confining configurations down to micrometric dimensions by following the Paschen law. Due to their small dimensions this type of discharges is known as 'microdischarge' or 'microplasma' ***[Foe-06, Iza-08, Bec-06]***. Because of their smaller size and working capabilities at atmospheric pressure, the domain of microplasmas has developed many applications over the last decade ***[Iza-08]***. Mainly, microplasmas could be of interest in display technology (Plasma TV, photonics light sources etc) ***[Kul-12, Iza-08]***, and in bio-medical field ***[Van-12]***.

The basic concepts of discharge breakdown related to Paschen law are described in the next section.

1.1.2 Breakdown Process

With the supply of sufficient energy to a volume of gas, ionisation can be produced. This phenomenon of gas ionisation is known as breakdown of the gas. Breakdown voltage for a wide range of gas pressures (p) can be related to the electrode gap (d), as mentioned by the Paschen law. The Paschen law ***[Pas-89]*** states that the breakdown voltage depends on *pd*

product instead of depending individually on *p* and *d*. Figure 1.2 shows Paschen's curve for different gases, for the breakdown voltage in relation to the product of pressure p and electrode distance d ***[Pap-63]***.

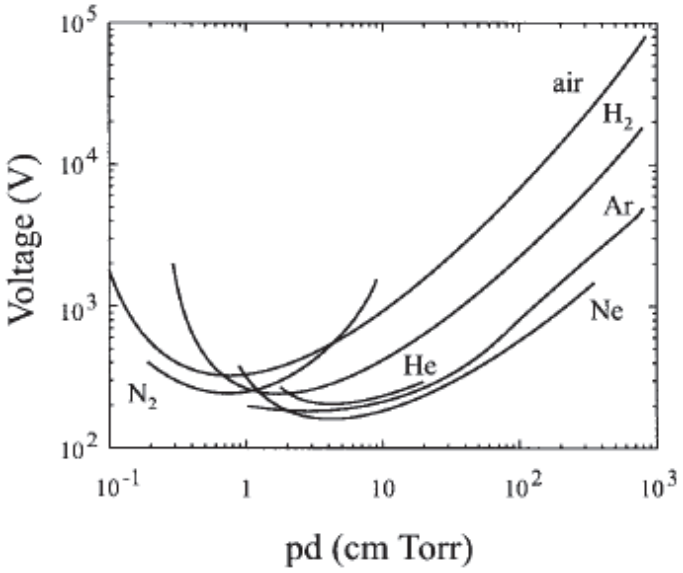

Figure 1.2 : Paschen curves for different gases. [Pap-63]

In the right side of the curve of figure 1.2, breakdown voltage increases with pd product. This indicates that breakdown can develop only if electrons can accelerate sufficiently before colliding with neutrals to efficiently ionise the medium. A higher applied voltage is then needed. On the contrary, in the left side of the curve, breakdown voltage decreases with pd product. Here, electrons do not collide sufficiently to efficiently ionise the medium between the two electrodes. Before going to further details, we will first discuss the V-I characteristic of a DC plasma.

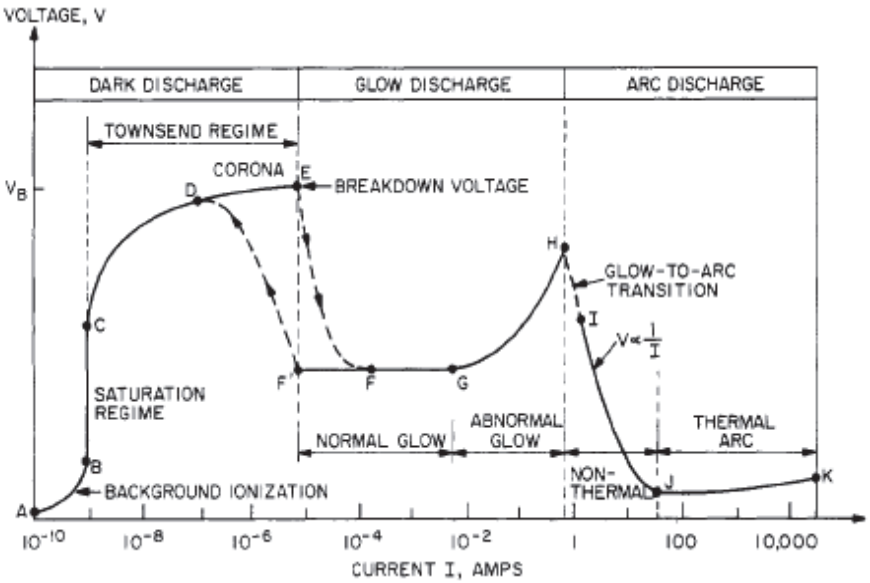

Figure 1.3: Standard V-I characteristics of a low pressure discharge tube in DC. [Rot-95]

The different regimes of DC plasma in a discharge tube at low pressure are shown in figure 1.3, where a V-I characteristics of a low pressure DC discharge is presented (graph is taken from ***[Rot-95]***). The graph has non-linear V-I curve trends.

The regime between points A and B is related to the background ionisation. This is the region where with the increase of applied voltage, ions and electrons are created by background ionising factors sweep out (shown by the region A to B in the plot) ***[Rot-95]***. A sudden change in current can be seen in the region of point B. The next part of the curve from point B to point C shows that ions and electrons are swept out by the electrodes. At this point, electrons do not have enough energy to produce further ionisation. Thus the current remains saturated and this part of the graph is known as saturation regime. The part between point C and E shows the so-called Townsend regime of the V-I curve. In this regime, the applied electric field is able to provide sufficient energy to the electrons to produce further ionisation and an avalanche process. This can lead to an exponential increase in the current as a function to the voltage. But in this regime, the discharge is not self-sustained. Secondary electrons from the cathode are not produced in a sufficient amount to produce a self-sustained discharge. Indeed, in this zone, current and charge density are too weak to induce space charge electric field. The electric field remains homogeneous in the cell. As a consequence, without reaching the breakdown voltage, the discharge is not self-sustained and needs external ionisation source.

In the region between D and E, due to the local electric field concentration on the edge surfaces of the electrodes, unipolar corona discharges can occur, which could exceed the breakdown strength of the surrounding neutral gas. The region from point A to point E is usually known as “Dark Discharge Regime”. In this regime, generally, the discharge remains invisible to human eye except for the corona regime.

By increasing the applied electric field further, Breakdown Voltage (V_B) can be obtained as shown at point E. From this point, onwards electrical breakdown takes place. The discharge makes a transition from the “Dark Discharge Regime” to the “Glow Discharge Regime” which takes place between points E and F. In this regime, the discharge is visible to the human eyes. The discharge voltage remains constant and independent to the increase of the discharge current. Only the area involved at the cathode surface increases with current, maintaining the current density constant. In this regime, secondary electrons are produced in sufficient amount to make the discharge self-sustained.

On further increase in discharge current up to point G, plasma covers the entire cathode area. After this point, discharge enters into the so-called “Abnormal Regime”. This is the regime where voltage increases as a function of current. This region is shown between the points G and H on the plot of figure 1.3. But, due to very high current density at point H, the cathode gets heated and the plasma enters into a discontinuous phase known as “Glow to Arc Transition”. After this point, the plasma becomes a thermal plasma where species are locally in equilibrium in a thermodynamic point of view.

If one goes in backward direction from the normal glow regime (point G), one normally will see a form of hysteresis in the voltage-current characteristic. The discharge will maintain

itself in the normal glow regime to the point F', at considerably lower currents and current densities, and only then make a transition back to the Townsend regime.

1.1.2.1 Explanation of the mechanisms from dark to glow regime

In fact, with the increase of the applied electrode voltage, electric field reaches a breakdown value between the electrodes. At this point, a prebreakdown can be observed, as a very weak current starts flowing between the electrode gap. By increasing the voltage further, breakdown is obtained and characterised by an abrupt increase of the current, itself accompanied by a significant increase of the glow intensity. This is the point of the self-sustained discharge between electrodes. At breakdown, the electrode voltage decreases and the conductivity continues to increase, which helps to maintain the steady state of the plasma. The process of breakdown mainly depends upon two factors, the ionisation coefficient α related to the volume changes of electrons and the secondary electron coefficient γ related to the surface changes of the cathode. Here, α is also called first Townsend coefficient and is related to the electronic avalanche phenomenon, i.e. number of ionisation caused by an electron per unit length in the inverse direction of the applied electric field. The generation phenomenon of secondary electrons at the cathode is related to γ known as second Townsend coefficient. This can be defined as the number of secondary electrons produced per ion impinging the cathode. This effect can also include photoemission effect and bombardment of the cathode by fast atoms or metastables. This secondary electron emission coefficient depends upon the cathodic material, the gas and the reduced field.

With the assumptions that the current is weak at prebreakdown and that the electric field between the electrode gap is not distorted by the access electrons and ions, we can relate the main cause of charge particles disappearance with their drift velocities towards the electrodes. Then, the discharge current density (j) is given by the following relation (1.1).

$$j = j_{em}\,\frac{e^{\alpha d}}{1-\gamma(e^{\alpha d}-1)} \qquad (1.1)$$

Here, j_{em} is the weak photoemission current of cathode, irradiated with ultraviolet radiations. The impact ionisation coefficient depends on the applied voltage and the equation (1.1) can provide the information about the prebreakdown current ***[Kor – 98]***. For low electric field, the term $\gamma(e^{\alpha d}-1) << 1$ and the plot of the equation (1.1) will be a straight line. The technique for measuring the impact ionisation coefficient by the slope of this straight line was first applied by the Townsend for the determination of α. For higher electric fields, the secondary cathode processes are more relevant. At this point, condition for a static breakdown voltage or self-sustaining discharges can be obtained when the denominator of the equation (1.1) tends to zero, which, in other terms, leads to the relation (1.2) ***[Lie-05]***.

$$\alpha d = \ln\left(1+\frac{1}{\gamma}\right) \qquad (1.2)$$

But the breakdown potential also depends on different other parameters like the cathode material, the distance between the electrodes, the gas type and gas pressure. By considering all these factors we can obtain the expression of breakdown given by relation (1.3) ***[Kor – 98, Lie-05]***.

$$V_{br} = \frac{B.p.d}{\ln(A.p.d) - \ln\left[\ln\left(\frac{1+\gamma}{\gamma}\right)\right]} \quad (1.3)$$

Where p is the gas pressure and d is the inter electrode distance. The constants A and B can be generally calculated from experimental measurements. If we introduce a dimensionless constant $\delta = pd/(pd)_{min}$, where $(pd)_{min}$ is related to the minimum breakdown voltage, then the above relation (1.3) can be written as:

$$V_{br} = V_{min} \frac{\delta}{1 + \ln \delta} \quad (1.4)$$

The relation (1.4) is the simplest analytic expression for the Paschen's law. This relationship allows tracing Paschen curve to find out the dependence of the breakdown potential to the scaling law "pressure x distance (p x d)". At low pressure and for a moderate current value, a glow discharge is obtained. At high pressure and for macroscopic dimensions, an arc can be created.

At low pressure, stable operation of glow discharges is possible for *pd* in the range of about 1–10 Torr cm where the breakdown voltage is minimum. In this way, for stable operation at high pressure, one only needs to decrease the discharge gap while keeping the *pd* value in the same range to allow ignition at low voltages. Indeed, discharge operation is unstable at high pressure while keeping the same *d* as in the low-pressure case, which corresponds to *pd* values higher than 10 Torr cm. It is due to the high current density, particularly in the cathode sheath, which is a source of instability and may lead to the glow-to-arc transition (GAT). The dominance of boundary phenomena in microplasmas, with small volume-to-surface ratio compared with low-pressure plasmas plays a stabilising role by evacuating calories. However, in spite of *pd* similarity of the microplasma and its low-pressure counterpart, the current densities in the former one are much higher, making microplasmas simply a scaled down version of a low-pressure plasma. Maintaining stable diffuse glow discharge plasma at high pressure is challenging due to their susceptibility to transition to an arc ***[Rai-91]***. The confinement provided by microplasmas and their high A/V ratio can help maintaining the glow regime and avoid the transition to arc.

The present studied devices are of 'MHCD' (micro hollow cathode discharge) type. That acronym historically refers to a specific mode of discharge operation, the 'hollow cathode' mode in which the discharge has a negative differential resistance. An overview for many different microdischarges will be given and discussed in the next section.

1.2 Overview on the devices and the methods to generate micro discharges

Discovery of microplasmas can be dated back to the late 1950s ***[Whi-59]***. But researchers got more interest in this field from 1990s. With the new technological developments in scale-up technology, a variety of microplasma sources have been introduced in past decades. Recent advances in diagnostics, modelling and manufacturing technology have been driven by industrial requirements and, even more, by large- scale applications like flat plasma display panels (PDPs) ***[Kog-99]***. In this section, we provide an overview of different types of microplasma existing sources.

1.2.1 Metal plate discharge

Discharges in glow regime at atmospheric pressure in air using metal electrodes are hardly attainable due to instabilities which tend to turn into arc discharges. This requires a lower burning voltage of a more efficient process for electron release at the cathode (thermoionic emission) and in the volume (thermoionisation) ***[Kun-00]***. This is an example of the transition from a non-thermal to a thermal discharge. There are generally two steps resulting in arc transition: (a) contraction and thermalisation of the discharge resulting from heating of the neutrals (thermal or ionisation over heating instability) and (b) heating of the cathode resulting in transition from secondary electron emission to thermionic emission of electrons at the cathode. Generally, the thermal instability is suppressed in low pressure discharges by cooling of the walls ***[Sta-05]***.

Staack and his team ***[Sta-05]***, have shown stable glow discharges in air with a varying inter-electrode disctance down to few millimeters. According to them, if the spatial dimension of the discharge is kept small enough, transition to an arc discharge can be avoided. Figure 1.4 shows the images of glow discharge in air with different electrode spacing of 0.1, 0.5, 1 and 3 mm respectively (this figure is taken from ref. ***[Sta-05]***).

Here, the thickness of the cathode fall region, not resolved in the pictures, is on the order of 10 µm. The bright region is a normal glow discharge, thermally stabilised by its size with a typical diameter of the order of 100 µm. The measured rotational temperature was about 1550 K ***[Sta-05]***. Current density and reduced electric field roughly correspond to values derived from similarity laws for glow discharges starting from low pressure air data (j/p^2 = 300 µA.cm^{-2} .Torr^{-2} and E/p = 10 - 30 V.cm^{-1}.Torr^{-1}), provided that a correction is made for the high gas temperature.

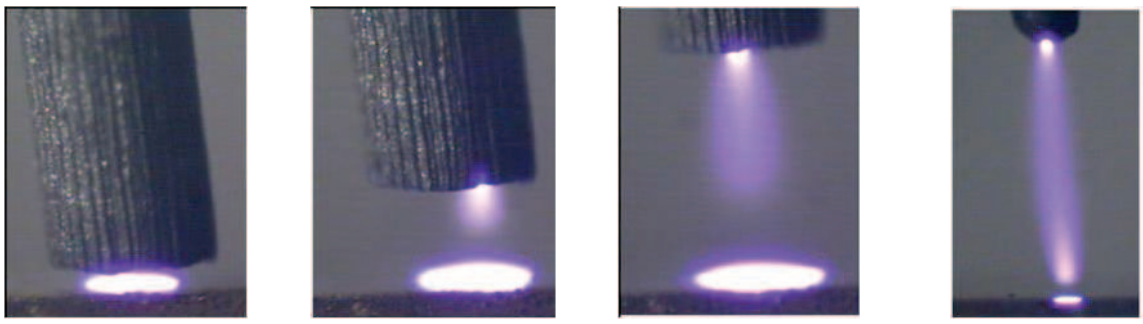

(0.1 mm) (0.5 mm) (1 mm) (3 mm)

Figure 1.4: Images of glow discharge in atmospheric pressure air at different electrode spacing. [Sta-05]

1.2.2 Micro-Torch discharge

Since the 1990s, numerous micro-torch discharges with different features have been developed. They are also known as micro-jets or Atmospheric Pressure Plasma Jets (APPJ). They all differ in design and size, working gas, frequency of applied voltage, but the working

principle is the same for all. The plasma is produced inside a nozzle equipped with one or two electrodes and expanded outside the nozzle via a gas flow. Figure 1.5 shows few examples of APPJs. Part (a) of the figure show stainless steel capillary tubes ranging from 178 µm to 508 µm inner diameter as cathodes and a metal mesh or a temperature controlled molybdenum (Mo) substrate as anode (example is taken from ref. ***[San-02]***). The electrode distance could be varied from a fraction of 1 mm to several mm. By extending the principle of operation of hollow cathode microdischarges to tube geometry, the formation of stable, high-pressure plasma microjets under DC regime in a variety of gases including Ar, He, and H_2 was shown. Microjets parallel operation was demonstrated with ballast resistors. Figure 1.5 (b) shows APPJs examples taken from the references ***[Wel-08] [Foe-05]*** and are used for biomedical applications. They are driven by means of RF-voltage (13 or 27 MHz) in Ar as working gas. The power used was below 50W. Micro-Torch discharges (MTD) or Atmospheric-pressure plasma jets (APPJs) use rare gases for their operation and have non-equilibrium plasma states.

An experimental study of atmospheric-pressure rare gas plasma propagation in a high-aspect-ratio capillary was reported by one of the research groups at GREMI working for biomedical applications. This work reported on the new performance and characterisation of a plasma gun device named as pulsed atmospheric-pressure plasma streams (PAPS) as shown in the figure 1.5 (c), in the framework of non-thermal plasma source studies and assessment for biomedical applications ***[Rob-12]***.

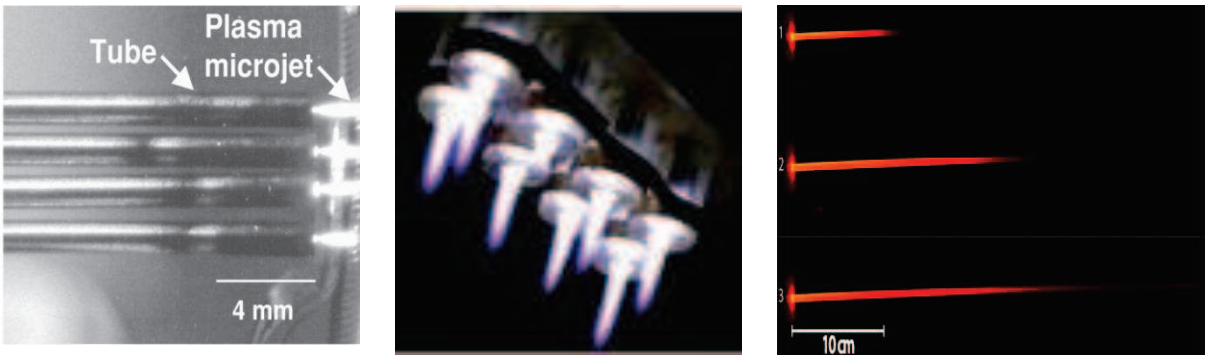

(a) (b) (c)

Figure 1.5: Examples of Atmospheric Pressure Plasma Jets (APPJs (a) A photo of four Ar plasma microjets operating in parallel [San-02], (b) a module consisting of six APPJs, and [Wel-08] (c) Digital camera pictures of neon PAPS propagation in a 45 cm long borosilicate capillary for the three voltage waveforms. [Rob-12]

The plasma was generated with a plasma gun device based on a dielectric barrier discharge (DBD) reactor powered by either nanosecond or microsecond rise-time high-voltage pulses at single-shot to multi-kHz frequencies. The unique properties of such non-thermal plasma launching in capillaries, far from the primary DBD plasma, were associated with a fast ionisation wave travelling with velocity in the 10^7–10^8 cm s^{-1} range. This type of plasma was propagating in capillaries and expanding in ambient air .

1.2.3 Dielectric Barrier Discharge (DBD)

Dielectric barrier discharges (DBD) have been known for more than one century. Nowadays, DBDs are widely used to generate atmospheric pressure, non-equilibrium plasmas in a controllable way. Figure 1.6 shows examples of some generally used DBD configurations. A DBD consists of two electrodes separated by a dielectric layer ***[Hip-07, Bec-04]***. Usually DBDs operate in AC with a frequency range of kHz, as DC cannot flow through the dielectric layer. The presence of one or more dielectric layers across the discharge gap between the electrodes is important for this kind of discharges. This dielectric layer is useful to avoid transition to arc regime as they limit the discharge current. Microdischarges form due to the electron accumulation on the dielectric layer. The dielecric layer helps distributing microdischarges randomly on the electrode surface. This role of the surface charges typically leads to the filamentation of the discharge, and is characterised by current spikes of much shorter duration than the AC excitation period. Typical materials for dielectric barriers are glass, quartz and ceramics. Plastic foils, teflon plates, silicone tube and other insulating materials can also be used ***[Wag-03]***.

There are two different modes of DBD viz. filamentary mode and diffuse mode. DBDs generally operate in the filamentary mode. If the local electric field in the gas spacing gap reaches the ignition level, the breakdown occurs at many points followed by the development of filaments ***[Gui-00, Don-05, Kog-03]***. Second type of mode, diffuse (glow-like) discharges have also been observed in DBD ***[Kle-01, Ner-04]***. Diffuse mode of discharges are preferred in the application point of view. In diffuse mode, discharges are more predictable and provide a more uniform treatment. However, diffuse mode leads to low-density discharges. A diffuse discharge mode can be achieved through seed electrons, photoemission, and photoionisation ***[Gol-05]***.

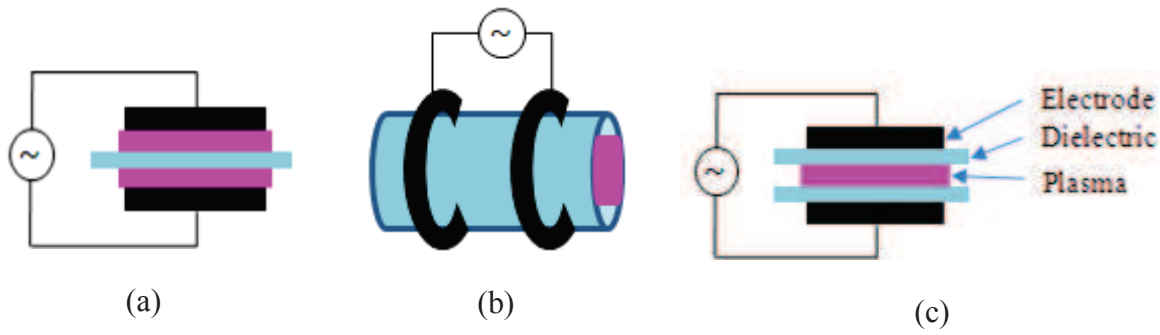

Figure 1.6: Examples of generally used DBD configurations.

Here, the ignition process of microdischarges can be explained with the concept of streamers. In fact, with the increase of voltage at the breakdown point, a primary quasineutral plasma or streamer is formed. A streamer is a weakly ionised plasma formed from the primary avalanche in a sufficient strong electric field. Streamers play an important role for the breakdown conditions and have a certain conductivity. They can modify the field upon reaching the electrodes that the degree of ionisation and the current may be greatly increased; ultimately, this will lead to a spark discharge in the gap. Here, the ionisation process by

electron-ion collisions and a photoionisation process play an important role for the generation of secondary avalanches. The streamers can be of two types: cathode-directed or positive or anode-directed or negative streamers.

Positive streamer

The generation of a positive streamer is shown in figure 1.7 ***[Rai-91]***. With the primary avalanche, excited atoms produce photons in the direction of the primary avalanche, towards the cathode. The electrons produced by the photons initiate secondary avalanche process in the same direction. This secondary avalanche electron mix with the ions generated during the first avalanche and form a quasi-neutral plasma. Thus, secondary ion avalanche enchances the effect of the positive charge near the cathode and expands the plasma channel, which results in to the formation of a streamer.

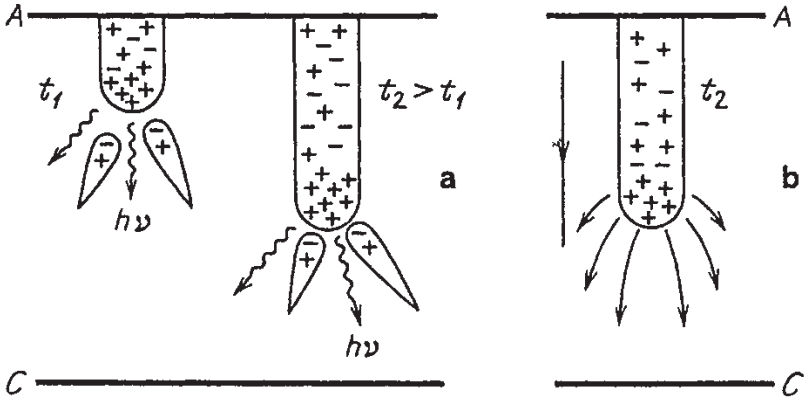

Figure 1.7: Positive or cathode-directed streamer, (a) Streamer at two consecutive moments of time, with secondary avalanches moving towards the positive head of the streamer, wavy arrows are photons that generate seed electrons for avalanches, (b) Lines of force of the field near the streamer head. Taken from ref. [Rai-91]

Negative streamer

The streamer is called negative if the beginning of the avalanche process is close to the primary cathode, and the streamer moves mainly in the direction of the anode as shown in figure 1.8 ***[Rai-91]***. Propagation characteristics are different from those presented in the case of positive streamer, because in this case the electrons drift in the same direction as the front of the plasma streamer, not counter to it as in the case of cathode-directed growth. As a result of radiation causing photoionisation, secondary avalanches are produced in front of the negatively charged streamer head facing the anode.

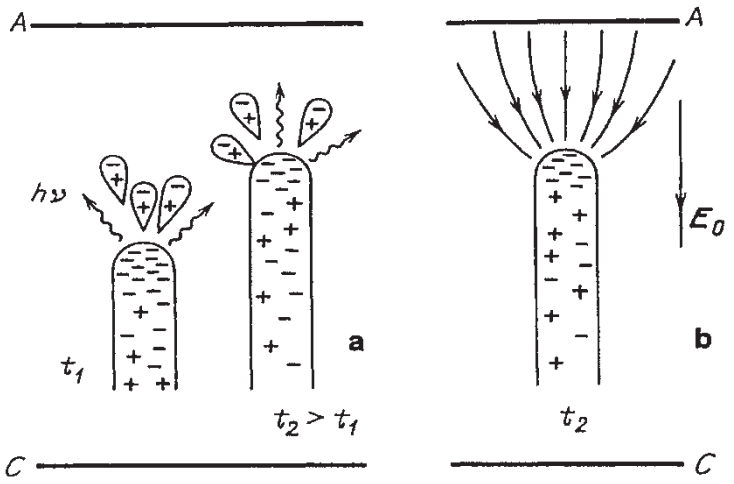

Figure 1.8: Negative or anode-directed streamer, (a) Photons and secondary avalanches in front of the streamer head at two consecutive moments of time, (b) Field in the vicinity of the head. Taken from ref. [Rai-91]

1.2.4 Cathode boundary layer (CBL) discharge

Schoenbach et. al. ***[Sch-04]*** presented an article on cathode boundary layer (CBL) in 2004. Figure 1.9 shows a structure diagram for CBL discharges. CBL discharges can be produced between a planar cathode and a ring shaped anode separated by a dielectric layer having a thickness of the order of 100 μm at high or atmospheric pressure. Diameter of the cylindrical cavity is of the order of few 100s of microns. As the cathode is close and has a planar surface, the discharge is restricted to the cathode fall and negative glow, with the negative glow serving as a virtual anode. The plasma in the negative glow region provides a radial current path to the ring-shaped metal anode.

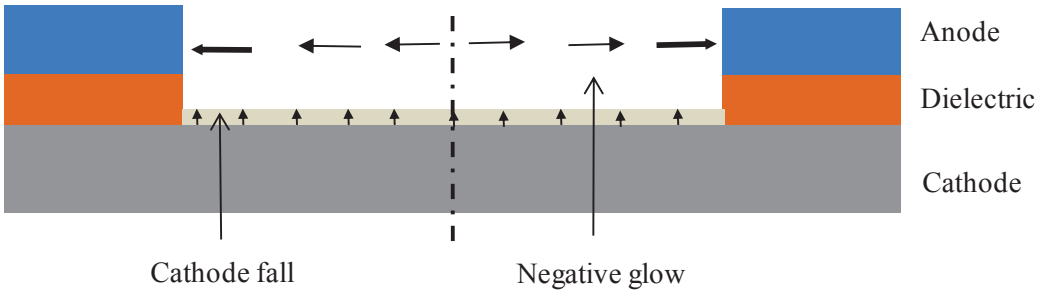

Figure 1.9: Structure of cathode boundary (CBL) layer discharges.

Figure 1.10 shows examples of CBL discharges taken from ***[Sch-04]***. CBL discharges were operating in Xe for different pressures and currents. The diameter of the anode opening was 0.75 mm. The plasma pattern consisted of filamentary structures arranged in concentric circles. The self-organisation structures are most pronounced at pressures below 200 Torr and become less regular when the pressure is increased. An important feature of CBL discharges is the positive slope of the V –I characteristics over most of the current. The parallel operation of these discharges is possible without individual ballast resistors. This has been demonstrated

by Frame and Eden in 1998 ***[Fra-98]*** with arrays of microplasma devices in silicon (Si) having the structure described in next coming sections.

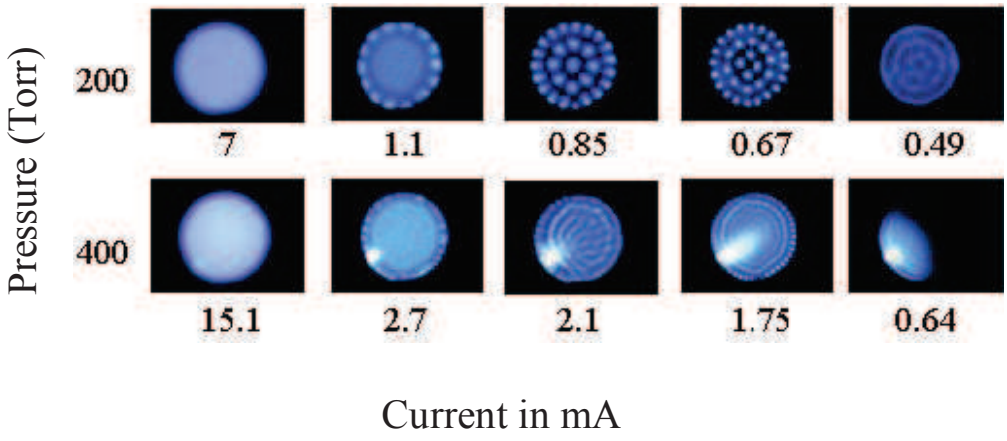

Figure 1.10: CBL discharges images for Xe gas as a function of pressure and current for 200 and 400 torr pressure, with decreasing current for various pressures. The diameter of the anode opening is 0.75 mm. [Sch-04]

1.2.5 Micro hollow cathode discharges (MHCD)

New types of atmospheric non-equilibrium microdischarges were developed in the form of Micro Hollow Cathode Discharges (MHCD) and were first proposed by Schoenbach and co-workers ***[Sch-96]*** in 1996. The MHC (Micro-Hollow Cathode) device arrangement is composed of sandwich layers of metal/dielectric/metal drilled partially or totally. The hole can be made by a mechanical drilling process, or by a laser drilling process or by plasma etching. The MHC concept extends hollow cathode discharge operation, normally restricted to low pressure, to atmospheric pressure by using tiny cylindrical holes of typically 0.1– 0.25 mm diameter (D) in the flat sandwich configuration. By taking advantage from the pd scaling law (p is pressure and d is the inter-electrode distance) given by Paschen ***[Pas-89]*** and concept of generation of microdischarges given by White ***[Whi-59],*** there exists a second scaling law connected to micro hollow cathode discharges (MHCD). This involves the product of pD, where p is pressure and D is the diameter of the cathode aperture. If the pD product is in the range between 0.1 and 10 Torr.cm, discharges can develop and are called MHCD. These types of discharge are non-equilibrium plasmas. Their typical gas temperature is about 2000 K. Their electron density is typically about $10^{15}cm^{-3}$ in DC. Numerical simulations by Kushner ***[Kus-05]*** show that this discharge has many similarities with a glow discharge: a thin localised cathode fall region of high field strength and a moderate gas temperature.

1.2.5.1 Alumina based MHCD

In a previous study ***[Duf-09]***, alumina was used as dielectric layer and sandwiched between two nickel (Ni) metal electrodes having one or several through holes. The dielectric layer Al_2O_3 had a thickness as high as 250 µm whereas the nickel electrode thickness was only

6 µm. Ni was deposited by an electro deposition process. The holes were made by laser drilling. The dielectric area was 1×1 cm^2 and the electrode area was 0.9 × 0.9 cm^2.

This work explained several physical mechanisms and specific operating conditions for DC operated MHCDs. Self-pulsed regime was studied for a limited current value of the power supply and for a linearly increasing voltage ramp. In this case, the dark-to-glow transition showed the existence of a single current peak, having the same characteristics of those obtained in the self-pulsed regime.

Normal glow regime was studied by electrical characterisation, imaging and optical emission spectrometry (OES). The study of V-I curves provided information about the current density of these devices. Plasma spreading on the cathodic surface was found using ICCD camera. Using OES, ro-vibrational spectra of N_2 were analysed. These studies were carried out to evaluate the gas temperature inside the MHCD cavity. For He gas at atmospheric pressure, typical gas temperature was found between 440 K (for 2mA) and 800 K (for 15 mA). Electron density was also measured by considering the Stark broadening of H_β. At atmospheric pressure, this density was found to be varying between 5.5 x 10^{14} cm^{-3} (for 2 mA) and 9 x 10^{14} cm^{-3} (for 15 mA).

The existence of an abnormal glow regime had been reported by reducing the cathodic surface for these types of MHCDs ***[Duf-08]***. This can allow one to initiate the plasma in several micro-reactors simultaneously without individual ballast. Gas temperature, sheath thickness and electron density were also studied experimentally and by simulation. It was found that limiting the cathode surface area had a large influence on the discharge properties – operating voltage, maximum current and hysteresis (in V-I curve). This reduction or limitation on cathode has a strong influence on the cathode sheath thickness and on the gas temperature, which was found to reach up to 600 K at 4 mA ***[Duf-10]***. Experimentally, the existence of a hysteresis phenomenon attributed to the relaxation time of the heat transferred by the sample was demonstrated. Depended on several parameters: time, pressure, thermal conductivity of the gas and the overall size of the sample was studied for this effect for alumina based MHCDs.

1.2.5.2 Diamond based MHCD

One research group of N. Braithwaite and M. Bowden, from The Open University (United Kingdom), demonstrated recently the fabrication and operation of MHCD devices using a microcrystalline diamond substrate. There devices consist of metal electrodes or electrodes composed of p-type microcrystalline diamond (heavily doped with boron), deposited onto the faces of an undoped microcrystalline diamond wafer. A single sub-millimetre hole was machined through the conductor–insulator–conductor structure using a high power laser. The discharges were generated in helium. Breakdown voltages of around 500 V and discharge currents in the range of 0.1–2.5 mA were maintained by a sustaining DC voltage of 300 V. They reported a longer operational life time of more than 5 hours for these MHCD devices ***[Mit-12]***.

1.2.5.3 Si based MHCD

In last decades, using the techniques, intensively used in complementary metal oxide semiconductor (CMOS) and micro electro-mechanical systems (MEMS) technologies, a concept with the idea of scaling-up of microdischarges has been introduced and realised ***[Che-02, Ede-03, Ede-05]***. The idea of achieving high packing densities with a huge coverage area is realised in the form of microplasma arrays having micro-structured electrode (MSE) configuration mainly in Si. The fabrication of these devices is completely compatible with currently existing MEMS/ CMOS technology. Explanation of the fabrication steps for this type of devices is provided in the next chapter.

Gary Eden's group, at the University of Illinois at Urbana-Champaign first showed the operation of Si based microdischarges using p-type Si(100) wafers ***[Che-02, Ede-03, Ede-05]***. In one of their designs, they used inverted pyramidal structure produced by lithographical patterning and anisotropic wet etching with KOH solution. Figure 1.11 shows the cross-sectional diagram of an inverted pyramidal microcavity (a) and a SEM top view image of a single reactor (b). The area of each inverted pyramid is 50 x 50 μm^2 in this case. But this area can be extended up to 100 x 100 μm^2, and more recently down to 10 x 10 μm^2. Typical cavity dimensions were 13 - 400 µm wide and between 0.2 and 2 mm deep.

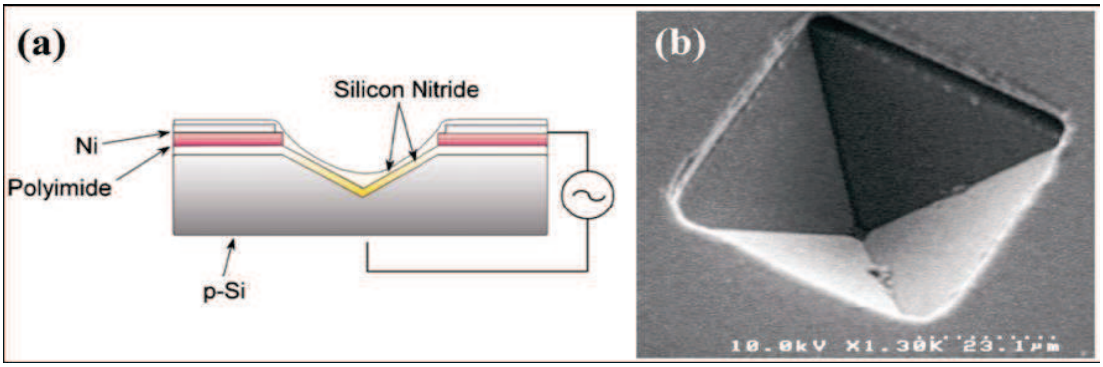

Figure 1.11: Examples of Si based microdischarge reactors fabricated by G. Eden's team, (a) Cross-sectional diagram of an inverted pyramid microcavity and a dielectric structure designed for ac or bipolar operation; (b) SEM top view image of a single micro discharge device. [Bec-06]The silicon nitride covering the whole structure is not present when operating in DC.

In their experiments, it has been shown that the role of dielectric layers is very important in determining the characteristics of the microplasma because of its impact on the spatial variation of the electric field within the cavity. Earlier in this study, it was claimed that microdischarge arrays running in DC without top dielectric layer (figure 1.12), can provide more stable plasma operation with the capability to drive higher currents when the polarity was reversed, i.e. when Si is acting as an anode in DC regime ***[Che-01]***. A common feature of all these DC discharges operating at power densities exceeding 10 $kWcm^{-3}$ is the cathode erosion. These arrays are shown in the figure 1.12. First image is SEM photograph of 10 x 10 MDR array having 50 µm cavity depth and cavities are separated by 50 µm from each other. The second image shows the working of the arrays in DC regime with 200 V and 20 mA

current at 1200 Torr Ne. From the same group, the solution to increase the life time of the arrays running in DC was proposed by using the composite dielectric layer ***[Par-02]***. The composite dielectric layer was consisted of 0.9 µm SiO_2, 0.5 µm of Si_3N_4, and 8 µm of dry-etchable polyimide. This technique resulted to achieve the extended life time of the MDR arrays, up to more than a factor of 50 times larger than those obtainable with a single polyimide dielectric film.

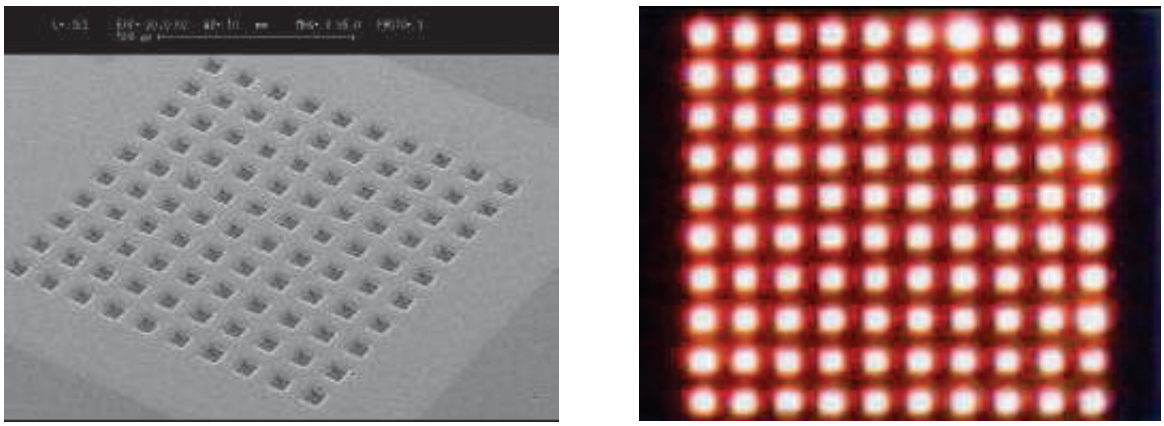

(a) (b)

Figure 1.12: Pyramidal Cavity MDR array fabricated by G. Eden's group (a) SEM image of a 10 x 10 device array of 50 µm cavities with 50 µm spacing and (b) image of the same 10x10 array running in DC at 244 V, 20 mA, 1200 Torr Ne. [Che-01]

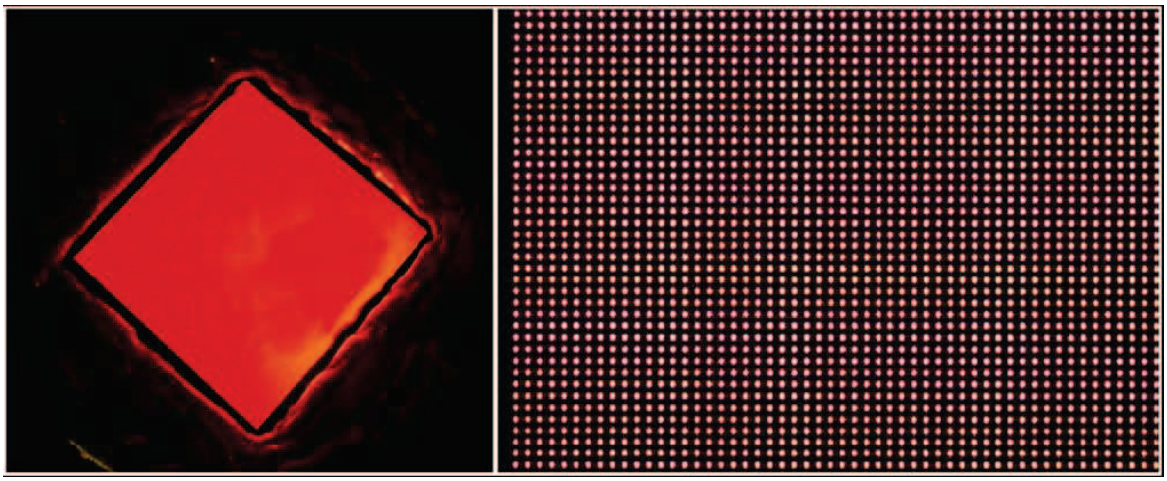

Figure 1.13: Images showing example of Si based arrays produced by the team of G. Eden running in AC at 700 Torr Ne, (a) single pixel and (b) a part of the array of pyramidal microplasma devices [Bec-06]

G. Eden's team showed promising results in terms of lifetime especially by covering both electrodes by a Si_3N_4 dielectric layer deposited on both electrodes and by running the array in AC regime ***[Ede-03]***. Using the same techniques, arrays having thousands of holes were operating having extended lifetime ***[Ede-05]***. Figure 1.13 shows an example of array containing 250 000 cavities running in AC and in Ne at 700 Torr. The pitch for these arrays was 100 µm ***[Bec-06]***. For these devices, an injected power density as high as 250 $kWcm^{-3}$ was reached.

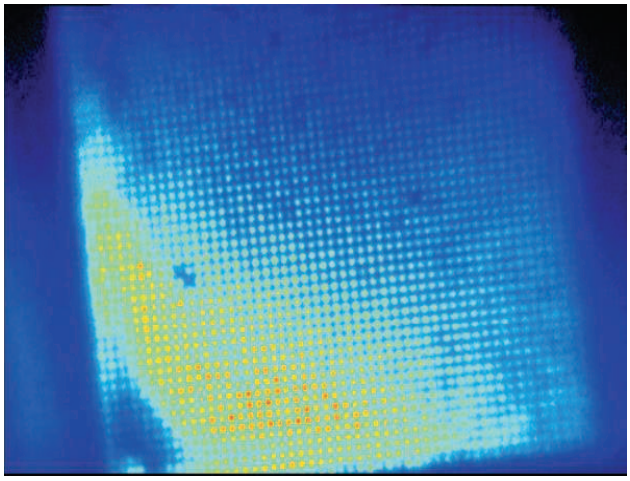

Figure 1.14: Edge ignition phenomena reported by the German research group of RUB using PROES, image is registered with the ICCD camera (false colours) for a gate interval of 200 ns (p = 1000 mbar, f = 10 kHz, Vpp = 780 V). [Boe-10]

The AC operation of these arrays had also been characterised by a German research group of J. Winter and V. S. Gathen, at Ruhr-Universität in Bochum, Germany ***[Boe-10]***. They studied the dynamics of the microdischarges using phase resolved optical emission spectroscopy (PROES) in AC regime. In their studies, they demonstrated the existence of the ionisation wave for these arrays. They showed that the ignition of the array was not continuous, but instead, it was including the successive ignition of the cavities present on an array as shown in the figure 1.14 ***[Boe-10, Was-08]***. Here, the image is taken with an ICCD camera (false colours) for a gate interval of 200 ns at pressure 1000 mbar Ar, Vpp = 780 V and with a frequency of 10 kHz. They calculated the velocity of this ionisation wave on the order of a few km. s^{-1}. They also showed the edge ignition phenomenon for these arrays in the same study.

1.2.5.4 Microhollow cathode sustained discharges (MCSD)

Robert H. Stark and Karl H. Schoenbach in 1999 demonstrated the possibility to extend the plasma generated inside a MHCD device to an external third electrode ***[Sta-99a]***. This type of extended discharge was named "microhollow cathode sustained glow discharge" or MCSD. Figure 1.15 shows an example of MCSD system reported by R. Stark et al, in air (end-on) with the MHCD sustained glow between hollow anode and third electrode (side on) at 10 Torr pressure ***[Sta-99b]***. The sustaining voltage of the microhollow cathode discharge was in the range from 400 to 600 V depending on current, gas pressure, and gap distance. The MHCD current was limited to values of less than 22 mA (DC) to prevent overheating of the sample.

The parallel operation of these discharges indicated the potential of this technique for the generation of large volume plasmas at high gas pressure through superposition of individual glow. MCSD at high-pressure can be generated by using any gas. The working principle of an MCSD is similar to the vacuum triode. Here, electrons are extracted from the MHCD plasma by means of a positively biased external third electrode, placed at a distance of few mm on the anode side of the MHCD device. To switch to the MCSD mode, MHCD geometry requires that the electric field generated by the third electrode is on the same order as the field in the

MHCD. This would require very high voltages applied to the third electrode, which is placed at a larger distance as compared to the electrodes gap of the MHCD.

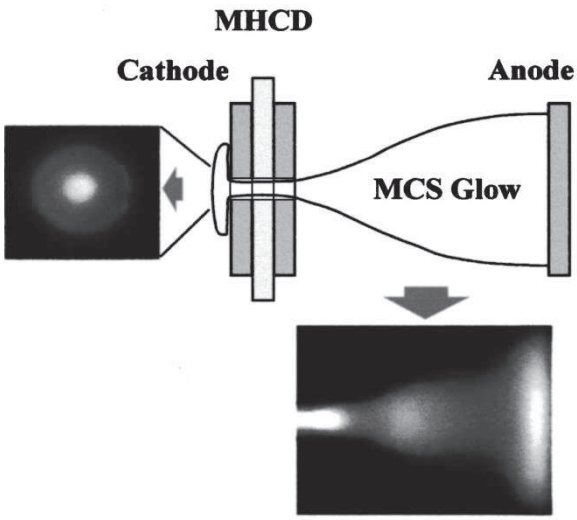

Figure 1.15: MCSD system with the appearance of the discharge plasma, end-on and side-on. [Sta-99b]

For this type of discharge, small changes in the control voltage could lead to large changes in the third electrode. This feature of the MCS glow discharge can be used to generate patterns by individually controlling discharges in discharge arrays. Another feature of the MCSD is the threshold current required for its onset, which opens the possibility to switch a large volume glow discharge with a small voltage swing. Experimental results from W. Shi and K. H. Schoenbach, indicated that parallel operation of MCSD could have current densities on the order of 100 A. cm^{-2} ***[Sta-99a]***.

1.3 Potential Applications of micro plasmas

The technology of microplasma has potential industrial and academic applications. Their capabilities at the micrometric scale make them quite suitable for bio-medical applications, local treatment, embedded devices, light sources…

1.3.1 Source of Excimer radiations

MHCDs can be used as a source of excimer radiations. Frame et al. were able to show the production of ultraviolet light (UV) with Si based MHCDs ***[Fra-97, Fra-98a]***. For these devices, a hollow cathode effect was observed with a high power density of 10 $kWcm^{-3}$ at or above 50 Torr gas pressure. Such an environment is ideally suitable for producing transient molecules such as di-atomic and tri-atomic excimers. In 1998, the continuous-wave (CW) excitation of a rare gas-halide molecule (xenon monoiodide, XeI) was first demonstrated ***[Fra-98a]***. In this study, an intense UV emission was observed from mixtures of Xe gas and I vapour.

In 2011, V. Martin et al. reported a MHCD based vacuum ultraviolet (VUV) light source ***[Mar-11]***. The light source was mainly composed of an alumina based MHCD operating in an Ar/Cl_2 mixture. The diameter of the MHCD hole was lower than 1 mm resulting in a high current density discharge with a high density of excited Cl atoms. With MHCD operating in the normal discharge mode, a reliable, point-like, VUV lamp was developed. This source was well suited for measuring the densities of chlorine atoms in the spin–orbit split $^2P_{3/2,1/2}$ ground state. Determination of Cl density in process reactors is of particular interest for the on-line monitoring of etching reactors used in microelectronic industries.

1.3.2 Medicine and biology

Plasma has been used for medical equipment sterilisation and to implant blood coagulation ***[Dei-08, Far-94]***. With recent developments in the field of microplasmas and due to their capabilities to produce large fluxes of reactive plasma species close to room temperature at atmospheric pressure, they have got attention of medical community. The size of individual microdischarges which approaches cellular dimensions suggests novel applications in medicine and biology. With their highly non-equilibrium character and capability to provide the treatment at tissue level at atmospheric pressure, many different treatment technologies have been generated and open up new horizons ***[Bec-06, Kon-09, Iza-08]***. In a recent article published by M G Kong et al. ***[Kon-09]***, a vast outlook on the applications of microplasmas in bio-medical field has been provided. To name a few applications as explained in this article viz. removal and sterilisation of the bio-films and planktonic bacteria by microwave-induced argon plasma at atmospheric pressure ***[Lee-09]***, and Cell permeabilisation using non-thermal plasma ***[Led-09]***.

The research group led by J.M. Pouvesle and E. Robert at GREMI, Orleans (France) is working on the applications of microplasmas in the field of bio-medicine. As already mentioned in this chapter, they have developed a microplasma source called pulsed atmospheric-pressure plasma streams (PAPS) ***[Rob-12]***. The unique properties of such non-thermal plasma launching in capillaries, far from the primary DBD plasma, are associated with a fast ionisation wave travelling with velocity in the 10^7–10^8 cm s^{-1} range. They reported the use of this source for the treatment of various diseases including cancer, both in vitro and in vivo ***[Van-12]***.

1.3.3 Sensors and detectors

For the detection of trace concentrations of hazardous species at both atomic and molecular level, microplasma based sensors can be used. Their atmospheric pressure operation, less demand of power and the smaller sizes of newly developed microdischarge reactors, made them a good choice for sensing applications.

They can be used as gas chromatographers to detect environmentally hazardous molecules. The team of C M Herring at Caviton Inc. (Champaign, IL, USA) reported the coupling a microplasma device (D = 100 μm) with a commercial gas chromatography column ***[Bec-06]***. They showed the detection of toxic elements like mercury (Hg) using microplasmas. The detection of halogenated hydrocarbons was also presented in another article published by

Miclea et al ***[Mic-02]***. After looking at the results presented by these studies, it could be predicted that multiple holes arrays could be useful in fabricating a very high sensitivity detector with a larger detection surface area.

1.3.4 Gas treatment and pollution control

The development of microhollow cathode sustained discharges (MCSE), made possible to extend the plasma to an external anode (third electrode) ***[Sta-99a, Sta-99b]***. L. Baars-Hibbe et al., using many parallel micro-structured electrode (MSE) plasmas, showed important applications in pollution control, like the abatement of CF_4, NO_x and hydrocarbons ***[Baa-03]***. This configuration could also be used for surface treatment.

Since plasmas can inactivate micro-organisms like cells, bacteria, spores, viruses, microplasma or MSE arrays have been investigated with respect to the decontamination and sterilization of surfaces ***[Baa-04, Bec-05]***. High energy electron beams, corona discharges, DBDs and various surface-type discharges, sometimes in conjunction with a packed bed of ferroelectric pellets, have been the most widely utilised discharge configurations for the generation of non-thermal plasmas for environmental applications ***[Yin-03]***.

1.3.5 On chip analysis and micro-fluidic application

With the integration of multiple technologies on a chip, it is now possible to have analysers and micro-fluidic devices fitted with a microplasma source. Jan C. T. Eijkel, in his publication ***[Eij-00]***, demonstrated a micro machined plasma chip coupled to a conventional gas chromatograph to investigate its performance as an optical emission detector. The device employed a 180 nL plasma chamber in which an atmospheric pressure DC glow discharge was generated in helium. It was demonstrated that the optical emission detector on a chip can also be used for gas chromatography. Molecular emission was used to detect carbon-containing compounds. This, on-chip chromatographer showed a good detestability using microplasma source.

On the other hand, Jon K. Evju by his publication ***[Evj-04]*** showed the integration of a DC microdischarge technique for the chemical modification of microchannel walls using a micro-fluidic device. By using an on-chip microplasma source, he showed that the properties of the micro-fluidic channels can be altered between hydrophilic or hydrophobic with an appropriate gas. This localised tuning of the surface and wetting properties is expected to be useful in the manufacturing of micro-fluidic channels in a variety of substrates.

From the above sections, it is clear that microdischarges have a huge potential for many future applications. Despite of their potential applications, the understandings of related physical phenomena is limited. Latest fabrication technologies can allow the specific tailoring and modification of new microplasma devices according to the measurement requirements. Then, by using specially designed devices, a better understanding of the undiscovered physical phenomena related to microdischarges could be possible. In the next chapter, we present an explanation of state-of-art technology with fabrication process used for the integrated MSE devices.

Chapter 2

Device fabrication process and experimental techniques

2.1 Micro-structured atmospheric plasma devices

Micro-structured electrodes (MSE) microplasma devices are having many potential applications at atmospheric pressure due to their flexible nature in both molding of their design to a specific application requirement as well as purpose of use ***[Baa-04, Ede-05]***. This speciality enhances the technological advances for the development of new microplasma sources. The understanding of basic physical phenomena and discharge dynamics of these devices is a current necessity of time. In particular, phenomena like effect of plasma species on the cavity walls, the coupling of adjacent microdischarges in an array and effect of proximity in ignition have not been studied in detail to date specially for Si based devices. These specific types of measurements need to tailor and optimize the designs of MSE devices according to their requirements. Thanks to the new advances in the manufacturing processes and electrical characterisation as well as integral spectroscopy techniques ***[Ede-05, Kul-12, Par-01]***, studies for MSE devices can be carried out. In next section, we present the different designs of the microdischarge reactors (MDRs) that we have used for this project including single MHCD devices and multiple hole arrays.

2.2 Microdischarge reactors in alumina

Microdischarge reactors using Alumina (Al_2O_3) as dielectric material were used for initial studies. These MHCD reactors were built within a collaboration program between UTDallas (Plasma Science and Application Laboratory, L. J. Overzet) and the GREMI Lab. They consisted of a 250 µm thick layer of alumina dielectric (Al_2O_3) layer sandwiched between two 8 µm thick Ni electrodes made by an electrochemical deposition process (figure 2.1). A through cavity at the center of the chip was formed by laser drilling technique. Drilling was performed by using Nd:YAG laser at the company "Questech Services Corporation", Texas (USA) ***[Que]***. Different diameters of MHCD were available from 250 µm to 400 µm. Note that, due to the laser process, the cavity was not perfectly cylindrical. More details about the fabrication process about these types of MHCD can be found in the PhD thesis of Thierry Dufour ***[Duf-09a]***.

We used these devices for diode laser absorption spectroscopy experiments and to characterise the ignition and extinction of the micoplasma. As it is explained in chapter 3, plasmas obtained with these microdevices were quite stable and the microreactors had a quite long life time (several hours of operation at 10 mA).

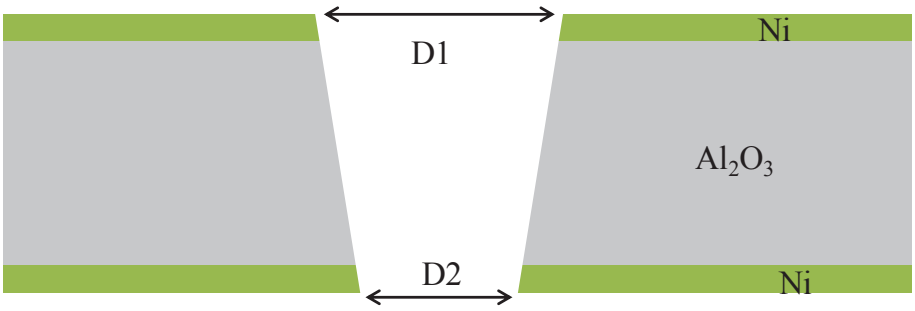

Figure 2.1: Alumina based MHCD reactor with a varying cavity diameter from the top to bottom.

2.3 Microdischarge reactors (MDRs) in silicon

2.3.1 General arrangement of the structure

In this section, different MDR designs using Si platform are presented. For the reactors, silicon dioxide (SiO_2) layer was used as dielectric sandwiched between two electrodes: one made in Si and the other in Nickel. A general structure configuration for Si based MDR is shown in figure 2.2. Fabrication technology used for these devices is explained in detail in the next coming sections.

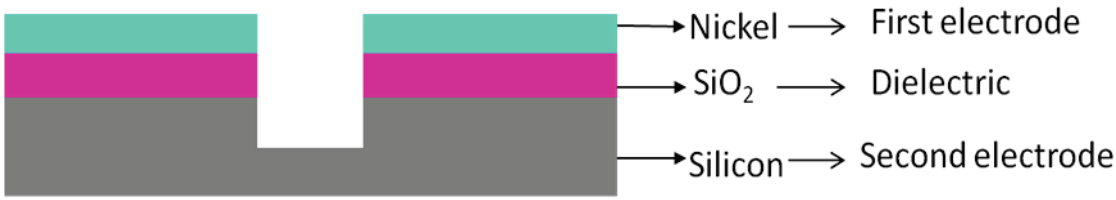

Figure 2.2 : General and simplified MDR structure for Si platform based devices.

2.3.2 General designs

To provide different patterns to the MDR arrays using CMOS compatible technology, the first step is to fabricate the desired MDR patterns on a glass substrate or on a material transparent to UV. This substrate is then used as a stamp to produce many similar patterns using optical lithography technology. The microdischarge reactors used in our studies were patterned using two different principal masks. Figure 2.3(a) and figure 2.4 show the images of these masks. These masks were having dimensions of 5 x 5 inch and can be used for 4 inch wafer. These masks were fabricated using a soda-lime glass having patterns in chrome with anti-reflecting coating. The MDR designs were made using CAD based software. Then the masks were patterned by a German company ML&C at Jena.

The first mask (shown in figure 2.3(a)) was containing 16 microdischarge reactor designs for top square shaped Ni electrode. This mask was containing designs of 4 single hole MDRs with a different cavity diameter: 25, 50, 100 and 150 µm (shown in figure 2.5 (a)); MDR arrays with 1024 holes (32 x 32) with a cavity diameter of 50, 100 and 150 µm each (as shown in figure 2.6 (a)); mixed circles and mixed trenches arrays (shown in figure 2.7); and two arrays containing the acronyms of GREMI, CNRS and ANR (shown in figure 2.8).

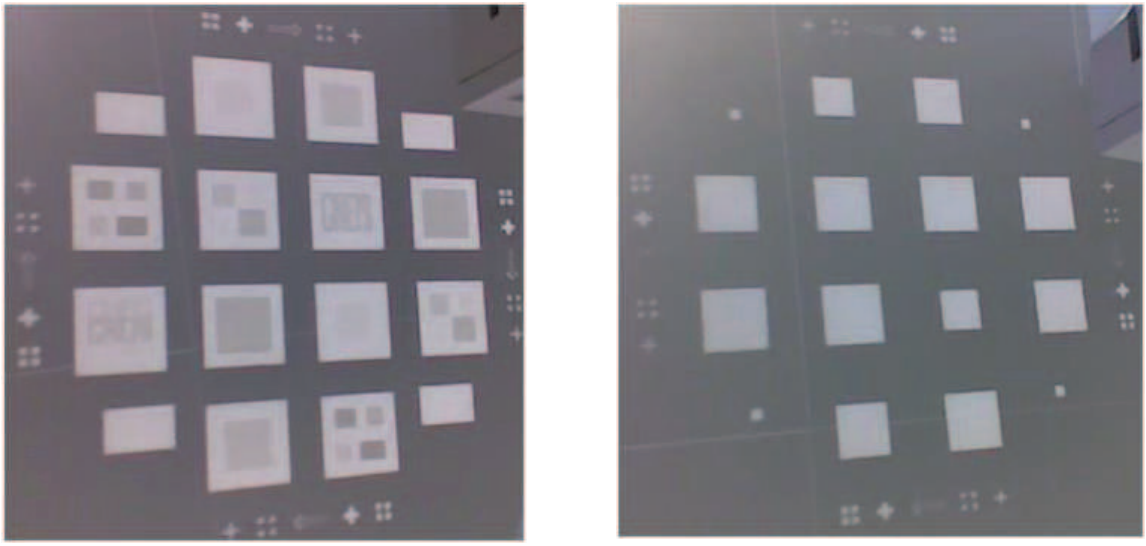

(a) (b)

Figure 2.3: (a) Mask with square type top electrode design used in the first step of optical lithography (b) mask used for second step of optical lithography to facilitate MDR cavities etching by covering the unwanted wafer area by PR.

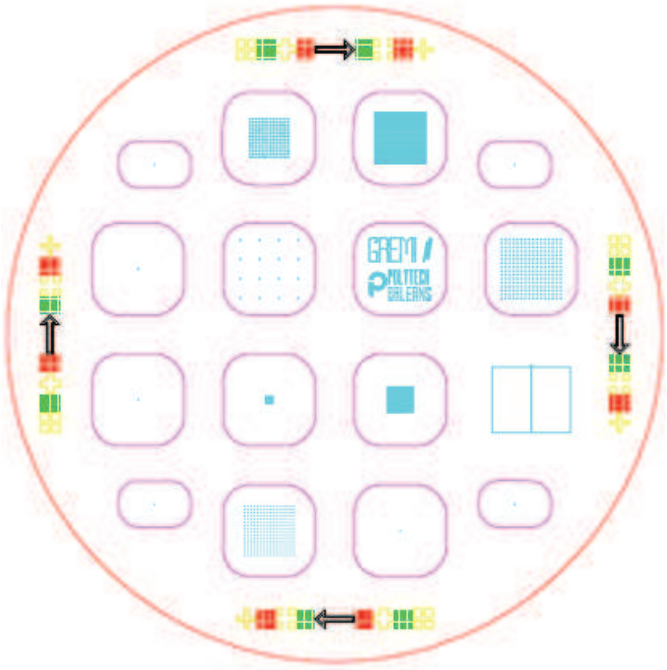

Figure 2.4: Mask layout having oval type top electrode design with 16 MDRs chips.

The second mask containing MDR designs has different configurations with square shaped top Ni electrodes with rounded corners (shown in figure 2.4). This mask also contains 16 designs of microdischarge reactors. It contains single hole MDR designs with 4 cavity diameters: 50, 100, and 150 µm, a 25 µm diameter single hole device; two arrays with 256 holes (16 x 16) with cavity diameters of 25 and 150 µm respectively (as shown in figure 2.6

(b)); two arrays having 16 (4 x 4) holes with cavity diameter 150 µm having different inter hole distance (shown in figure 2.6 (c) and (d)); two array designs with 1600 (40 x 40) holes having hole diameters of 50 and 100 µm (shown in figure 2.6 (e)); and three arrays with special designs: a long trench device (shown in figure 2.10), a mixed Concentriccircle array device (shown in figure 2.9 (a)) and a mixed hole array device with acronyms.

A third mask was made to facilitate the MDR cavities etching (shown in figure 2.3 (b)). This mask was used to protect areas without cavities and without nickel by using thick photoresist (PR) as explained in the next sections. With this mask the chip area (generally 2 cm x 2 cm) for each individual MDR was marked by a line having a trench shaped structure with dimensions of 500 µm x 10 µm. These marks also facilitated the cleaving of the individual chip from the Si wafer after the fabrication. All the masks were designed with many different types of alignment marks having different dimensions to facilitate the multilayer photolithography process.

Thus, single hole microdischarge reactors have chip dimensions of either 1.5 cm x 1.2 cm (rectangular shape) or 2 cm x 2 cm (rounded corner square shape). The dimensions of the nickel electrodes for single hole devices were either 1.1 cm x 0.7 cm or 1.4 cm x 1.4 cm. For MDR arrays, the chip dimensions were kept 2 cm x 2 cm with top Ni electrode dimensions of 1.4 cm x 1.4 cm. Ni electrode can have either square or rounded corner square type structure depending on the design.

These devices were produced with silicon platform using a series of processing steps described in next coming sections. In these devices, silicon was treated as one of the two electrodes. We used n-type silicon wafers with four inch diameter having resistivity of either 5 or 5000 Ω.cm and a thickness of 500 µm.

2.3.3 Single hole MDR

Single hole MDRs were designed with different cavity diameters viz. 25 µm, 50 µm, 100 µm and 150 µm. Drawings of single hole MDRs are shown in figure 2.5. Rectangular (a) and square (b) shapes were designed for the fabrication of the individual chips.

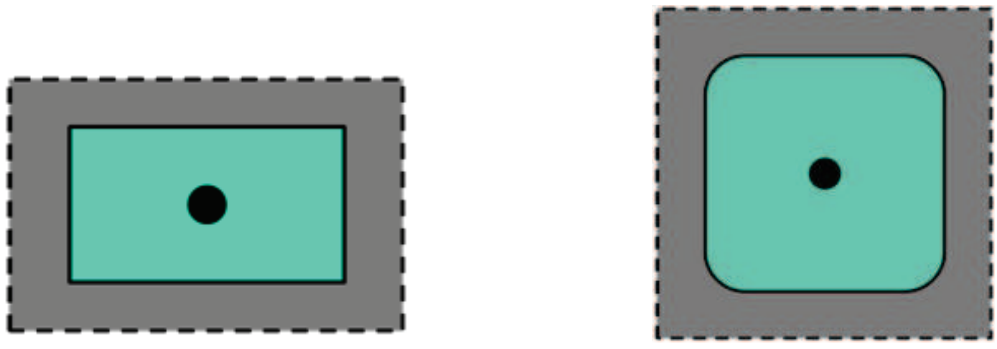

(a) (b)

Figure 2.5 : Single hole MDR having (a) rectangular and (b) square chips.

The upper Ni electrode layer was first designed in a rectangular shape (a). But then we decided to make rounded corners to avoid preferential ignition at those locations. These

devices were designed to study the microdischarges individually, without any effect of neighbouring cavities. Note that figures with MDR reactor configurations are presented in this section without respecting the exact dimensional scale of the real samples.

2.3.4 Multiple hole array

Array arrangements with different hole diameters (D) of 25, 50, 100 and 150 µm were designed. 3 sets of arrays having 1024 holes (32 x 32 matrices) were designed with 50, 100 and 150 µm diameters, separated by a 150 µm edge to edge inter hole distance. Such a structure arrangement is shown in figure 2.6 (a). The distance between the Ni electrode edges and the first line of holes depends on the cavity diameter. It was 3.9 mm for the 50 µm diameter hole arrays, 3.12 mm for the 100 µm hole array and 2.35 mm for the 150 µm hole array. Another set of arrays was designed having hole arrangements in a 16 x16 matrix or 256 holes. The structure of this array is shown in figure 2.6 (b). This array was designed for two cavity hole diameters (D) 25 and 150 µm with rounded corner square shaped Ni electrode. The inter hole distances from edge to edge were 475 and 450 µm for 25 and 150 µm hole arrays respectively. The distances from the Ni electrode edges were around 3.25 mm and 2.40 mm for 25 and 150 µm holes arrays respectively. These arrays were designed to study the effect of the gas pressure on the arrays having different cavity diameters.

Two arrays with 150 µm cavity diameter having 16 holes (4 x 4 matrix) were designed with two very different edge to edge inter hole separations of 2800 µm (shown by figure 2.6 (c), large distance array) and 200 µm (shown by Figure 2.6 (d), short distance array) respectively. These arrays were having 2.5 mm and 6.4 mm distances from the edge of the Ni electrode. These arrays were basically designed to see the effects of one MDR on the nearby MDRs under the plasma operation.

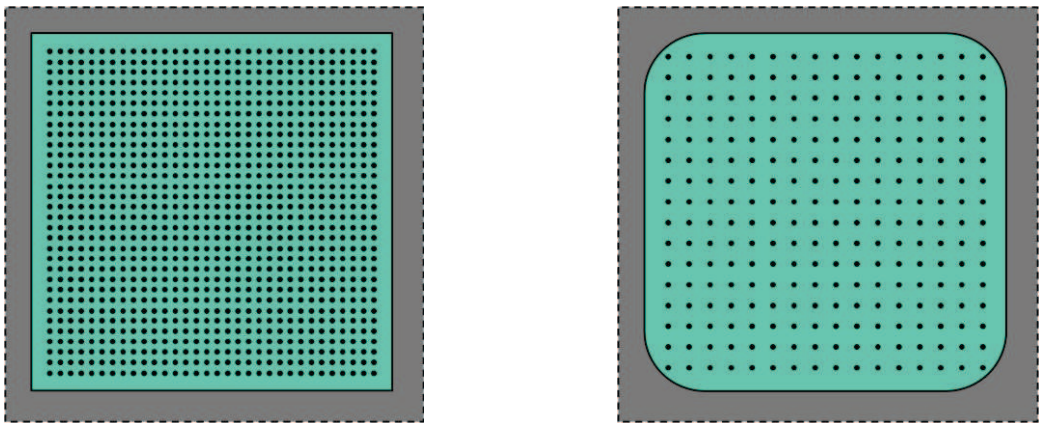

(a) (b)

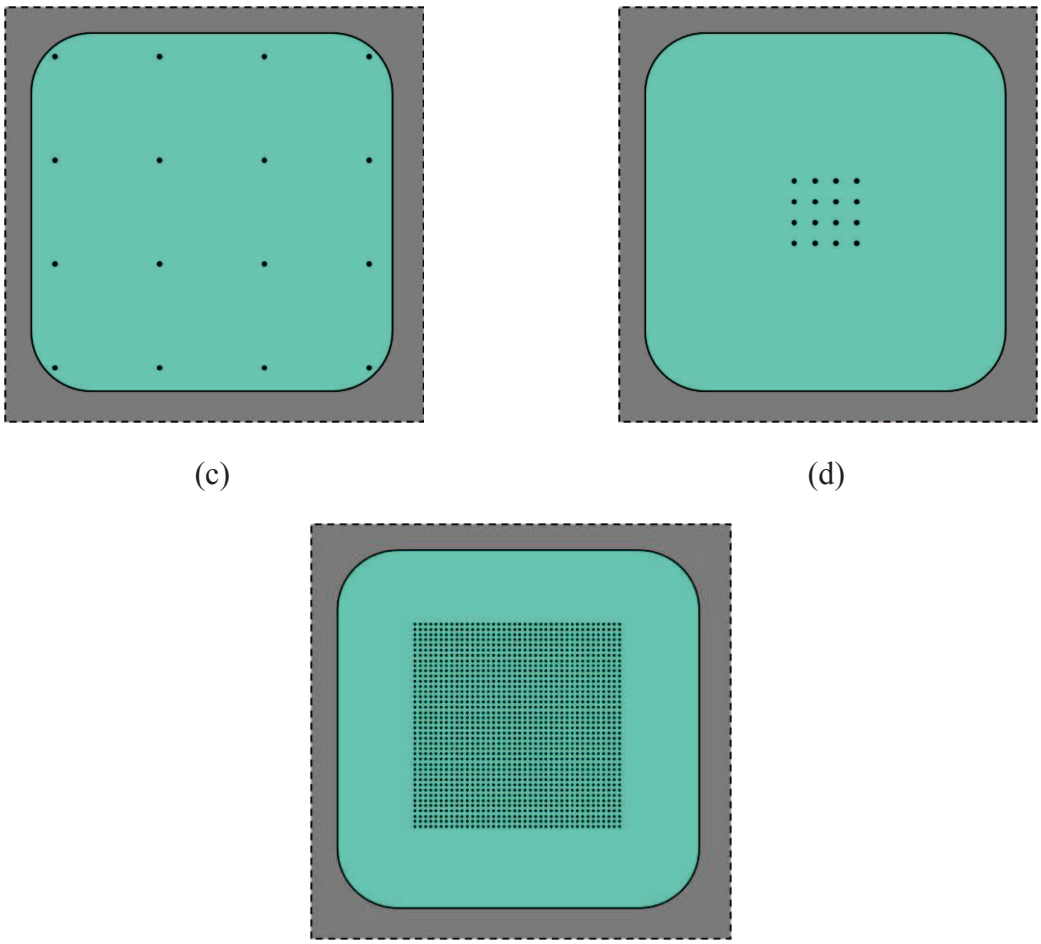

(c) (d)

(e)

Figure 2.6: MDR arrays with different arrangements (a) 1024 (32 x 32) hole array (D between 50 and 150 µm), (b) 256 (16 x 16) hole array (for D = 25 and 150 µm), (c) 16 (4 x 4) hole large distance array for D = 150 µm, (d) 16 (4 x 4) hole short distance array for D = 150 µm and, (e) 1600 (40 x 40) hole array (for D = 50 and 100 µm).

Sets of 40 x 40 matrix or 1600 hole arrays were designed for different cavity diameters of 50 and 100 µm. Cavity arrangements for this type of array is shown in figure 2.6 (e). Side to side cavity inter hole distances for the 50 and 100 µm cavity diameter arrays were 50 and 100 µm respectively.

These arrays were designed to study the effect of neighbouring cavities on the ignition dynamics of the arrays. These types of arrays were specially fabricated for the experiments performed at RUB, Bochum (Germany) in AC regime.

2.3.5 MDRs with special designs

In this part, we present some special designs dedicated to investigate different physical phenomena depending on the MDR design and cavity configuration.

2.3.5.1 Mixed hole array

Four different sub-arrays having 25, 50, 100 and 150 µm diameters were fabricated on a chip. Figure 2.7 (a) shows the electrode structure arrangements for this array. Each of the four sub-arrays has 256 (16 x 16) cavities. Each sub-array was placed at a distance of 2.5 mm from the side edge of the Ni electrode. The side to side inter hole distance for each array was 150 µm. These sub-arrays were created for different reasons. First, the fabrication of our devices is quite complex and needs many different process steps, it is sometimes difficult to exactly reproduce a specific sample. By making this sub-array chip, we make sure that we have the same fabrication steps for all of them and we can really compare their operation versus different parameters. Second, these sub-array chips are quite useful to study discharges versus pressure, discharge current and cavity diameter. We can directly see which sub-array ignites more likely.

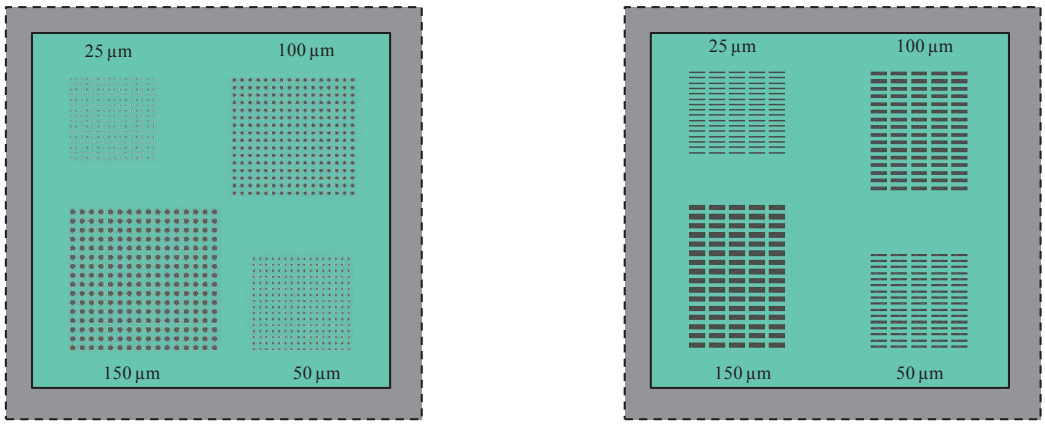

(a) (b)

Figure 2.7 : Electrode structure arrangements for (a) mixed holes and (b) mixed trenches arrays.

2.3.5.2 Mixed trench array

Using the similar concept of the mixed hole sub-arrays, mixed trench sub-arrays were designed. They consist of 80 (16 x 5) trenches with a trench length as high as 500 µm and different trench widths of 25, 50, 100, 150 µm. Figure 2.7 (b) shows the structure arrangement for this type of microdevice. The trenches of each sub-array were placed at a distance of 150 µm edge to edge with the neighbour trench cavities. These arrays were designed to see the effect of wider cavities on the ignition of microdischarges and to study the effect of the variation of different experimental parameters (e.g. pressure), by keeping the sub-arrays under the same physical conditions. They were also used for AC operation as it will be presented in chapter 5.

2.3.5.3 Mixed hole arrays with acronyms

Two arrays with three different mixed hole diameters were designed, representing the acronyms of GREMI (Groupe de Recherches sur l'Energétique des Milieux Ionisés), CNRS (Centre National de la Recherche Scientifique) and ANR (Agence Nationale de la Recherche).

They consist of three separated hole sub-arrays with a diameter of 150, 100 and 50 µm respectively. Figure 2.8 shows the cavity arrangement for these sub arrays on a chip. As shown in figure 2.8 (a), the array was designed by separating the three acronym sub-arrays. The second array (shown in figure 2.8 (b)) was designed by mixing the three sub arrays on top of each other. Note that this overlapping was performed without merging the holes of sub arrays.

The main idea behind these designs, were to see the behaviour of the different sub-arrays with the variation of gas pressure. For a given pressure, if only one type of microdischarges ignited preferentially, we would observe only GREMI for example and switch to CNRS or ANR by changing the pressure. The effect of proximity, due to the neighbouring cavities could be studied with these arrays.

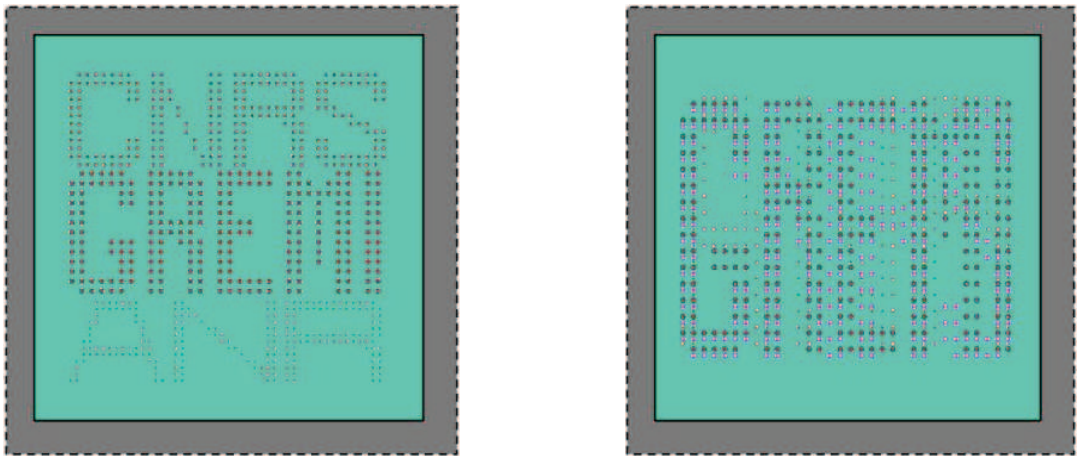

(a) (b)

Figure 2.8: Electrode structure arrangements for mixed hole arrays having acronym for GREMI, CNRS and ANR.

2.3.5.4 Concentric rings MDR

196 (14x14) microdischarges consisting of concentric rings were designed on an array. The structural arrangement for this array is presented in figure 2.9 (a). In this design, each cavity was designed by using three concentric circles having each a diameter of 50, 100 and 150 µm. Each interior circle had 8 µm thick circumference boundaries. Figure 2.9 (b) is a zoom of a MDR cavity of the array.

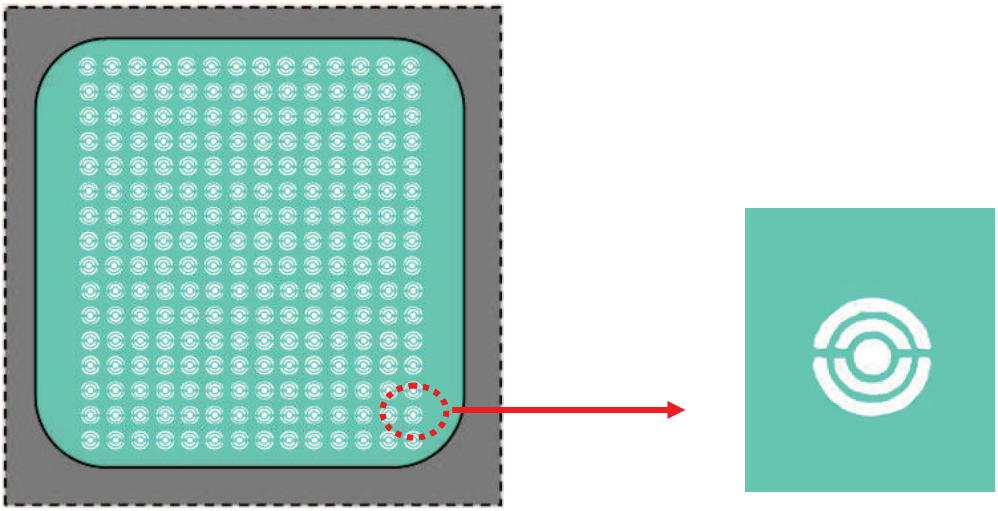

(a) (b)

Figure 2.9: (a) Design for the 196 (14x14) concentric ring array, (b) zoomed in part of the mixed holes MDRs and concentric arrays (marked in red circle).

These arrays were designed to ignite discharges in a wider range of pressures. Since different characteristic dimensions are present in this structure, we could think that some parts of the microstructure should strike at different pressures. The details of the experimental studies are provided in the chapter 4.

2.3.5.5 MDR with a long trench

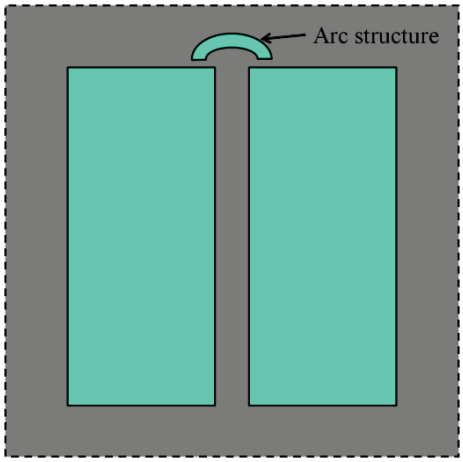

Figure 2.10: Structure configuration of Long trench MDR

A microdischarge device with a long trench was designed as shown in figure 2.10. Two independent Ni rectangles were designed and separated by a 100 µm distance, creating a trench shaped long cavity with dimensions 100 µm x 10 mm. Each rectangle was 6 mm wide. This trench shaped cavity was having open access from one side.

2.4 Fabrication process for Silicon based MDRs

One of the very important issues in this project was relying on the design and fabrication of the microreactors in collaboration with clean room facilities. Using the clean room fabrication technologies, it is possible to create microdischarge reactors in economically feasible quantities. As mentioned in the first chapter, G. Eden's team first showed the possibility to create microdischarges using Si substrates ***[Fra-97, Bec-06, Ede-03]***. Our microdischarge reactors were fabricated with CMOS compatible fabrication technologies using two clean rooms as explained in the next section. More than 20 process steps were necessary for the fabrication of one wafer containing 16 chips of MDRs. The process flow diagram given below shows the sequence of the major processes followed during the MDR fabrication.

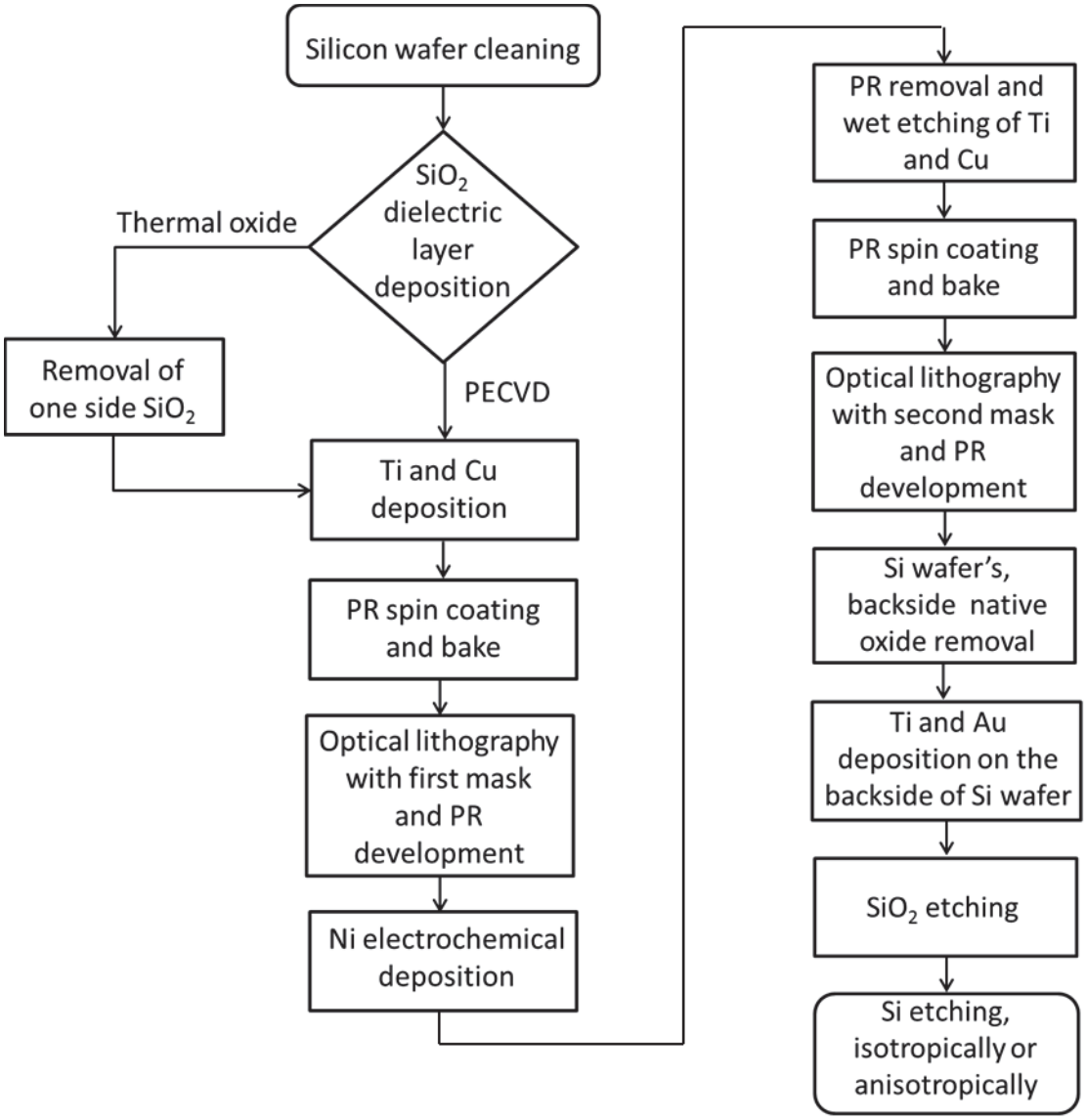

The first part of the fabrication of the microdischarge devices was carried out in the clean rooms of IEF-CTU (MINERVE, Orsay, France) having 10, 000 and 1000 class clean rooms. The other part was made in the clean room of CERTeM (Centre d'Etude et de Recherches Technologiques en Microélectronique) in Tours, France in 1000 class clean room.

2.4.1 Presentation of the process flow

2.4.1.1 Si wafer cleaning

It is one of the first and very important steps for device fabrication technology for micrometric scale devices. Small dust particles, metallic impurities, organic impurities and remaining native oxide on the Si wafer could lead to problems like destruction of micrometric devices or malfunctioning of the devices. To avoid these problems, Si wafers were first cleaned using a standard RCA process ***[Kem-93]***. In between the different fabrication steps, there was a need to clean the wafer from time to time. The so-called Piranha cleaning process was used for those additional cleaning steps.

Cleaning process

The standard cleaning process is composed of the following steps.

The first step is used to remove organic components from the wafer surface. First, the wafer is plunged into a solution of Trichloroethylene at 80 °C for 3 minutes. Then, the wafer is placed inside the beaker containing Acetone with ultrasonic bath. Afterwards, the wafer is immersed in DI (deionised) water for 3 minutes.

The wafer is plunged into a BHF (buffer hydrofluoric) solution for 30 seconds to remove the native oxide of the wafer.

The second step consists of getting rid of the metallic impurities. Metallic particles are first trapped by oxidation: the wafer is put inside a solution containing H_2SO_4 mixed with H_2O_2 (ratio 3/4-1/4) for 3 minutes. This mixture is called Piranha solution and will oxidise the wafer surface. This is an exothermic reaction, which boosts the oxidation mechanism. Then the trapped metallic particles together the oxide layer is removed from the wafer surface by BHF. Then wafer is rinsed with DI water for 3 minutes.

2.4.1.2 Dielectric layer deposition

After the cleaning process, a thin thermal oxide layer (~100 nm) was grown in pure ambient oxygen on both sides of the Si wafer at 1150 °C. The thermal oxide film forms an efficient protection for the Si wafer, which remains impurity free. The total time required by the process was around 3 hours.

Next, a 6 µm thick SiO_2 layer was deposited using Plasma Enhanced Chemical Vapour Deposition (PECVD) process. PECVD deposition process can provide a highly uniform, good quality thick SiO_2 layer in a short duration of time. SiH_4 and N_2O were used as precursor gases in an RF capacity coupled plasma. The chemical, SiH_4, is pyrophoric; the formation of SiO_2 takes place just through its exposure to oxygen. The fundamental reaction is given by:

$$SiH_4 + O_2 \xrightarrow{\overrightarrow{N_2O}} SiO_2 + 2H_2 \uparrow \qquad (2.1)$$

With the wafer at around 300°C, an amorphous film of SiO_2 is formed which is used as the interelectrode dielectric. In these reactions, it is important to minimize the residual H_2 in the

film and to provide a film with suitable electrical properties. A low frequency (380 kHz) PECVD deposition method was used for the deposition of SiO_2 layer (Figure 2.11) using STS PECVD system. Different gases SiH_4, N_2O and N_2 were used with a flow of 12 sccm, 1420 sccm and 392 sccm respectively. A power of 60 W was used with low frequency. Temperature of the showerhead was maintained at 300 °C. 6 µm SiO_2 layer was deposited in 90 minutes. This SiO_2 layer was used as the dielectric layer separating the two electrodes in the production of microdischarges.

Figure 2.11: Cross-sectional view of silicon substrate with 6 µm thick SiO_2 layer.

Variant of the process

Si wafers with 6 µm thick thermal SiO_2 layer on both sides were also used to see if thermal oxide was more efficient dielectric than PECVD SiO_2. These wafers were produced by the company Vegatech based in France. The process of thick thermal SiO_2 layer lasts 72 hours but one can treat 100 wafers at once. Before using these wafers for the further processing steps, one side SiO_2 layer had to be removed. First method was consisting of using HF (with 50 % concentration). A thick photoresist (PR) (AZ4562) was spin coated on one side of the wafer. Then the wafer was plunged inside the HF solution for 5 minutes to remove the 6 µm thick SiO_2 layer. But, the results obtained by this process were not satisfactory. Highly concentrated HF was able to penetrate through the PR coating and to create micrometric holes on SiO_2 of the other side of the wafer. These holes caused some current leak problems in our devices. The second method, suggested by L.J. Overzet, was consisting of spin coating a primer to increase adhesion. Then a thick PR AZ4562 was spin coated and baked on a hot plate for 15 minutes at 90 °C. Then the wafer was immersed in BHF solution for around 75 to 80 minutes. This SiO_2 removal process worked well and provided satisfactory results.

2.4.1.3 Sputtering and photolithography

Sputtering

Thin films of titanium (30 nm) and copper (100 nm) were deposited on the SiO_2 layer using a magnetron sputtering process. The former was used to create a seed layer. The Cu layer was used to make the surface conductive in order to grow the nickel (Ni) electrode by electrodeposition process (Figure 2.12 (a)). A magnetron sputtering system from "Denton Vacuum Sputtering Systems" company was used. Sputtering is a vacuum process which is often used to deposit metal thin films on different substrates. During sputtering, Ar ions strike the negatively biased target plate at high energy. These collisions cause the sputtering of atoms from the target which deposit on the substrate.

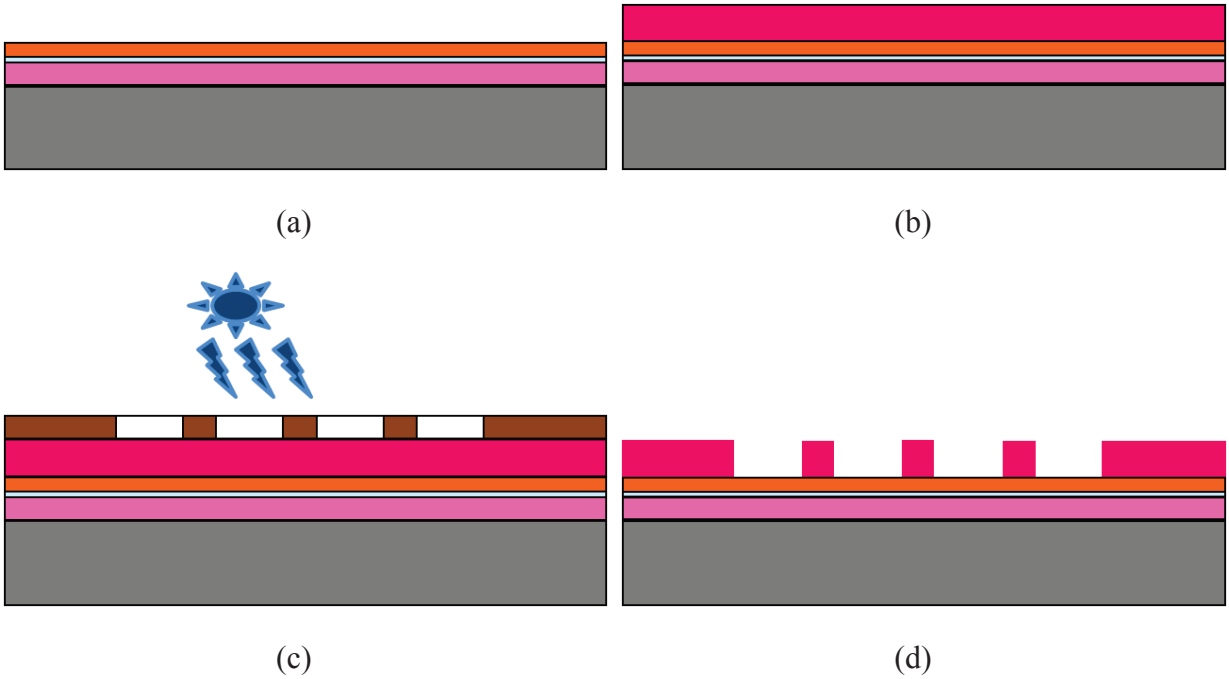

Figure 2.12: MDR fabrication steps for (a) Ti and Cu deposition, (b) PR spin coat, (c) optical lithography and (d) PR development.

1st lithography step

An optical lithography step was then performed to define the microdischarge top electrode patterns. In this step, we used a thick positive photoresist (PR) (AZ4562, Micro Chemicals). This PR was selected because it allowed us to grow a thick nickel layer (typically 8-10 µm thick) to form the top electrodes. This PR was first spin coated at the speed of 2000 rpm (rotation per minutes) for 30 seconds (Figure 2.12 (b)). PR was then baked for one hour on a hotplate at 90 degrees using a ramp from 20 °C to 90 °C in 5 minutes. After baking, the wafer was kept for 3 hours in ambient air environment. This step was used to desorb the organic binder of the PR. This step was necessary to release some humidity and change PR chemically to be ready for optical lithography step. This step was also important to obtain uniform and vertical thick walls of the PR after UV irradiation and development. Using the mask containing the MDR designs on 5 inch glass substrate (Figure 2.12 (c)); optical lithography step was then performed using a double side aligner. The EVG620NT automated mask alignment system was used. This lithography system can handle sizes of substrates starting from less than 5 mm up to 150 mm and can provide alignment accuracies down to 0.1 µm. We used the intense UV line of the Mercury lamp emitting at a wavelength of 365 nm with a dose of 200 mJ/cm^2. With this type of UV lamp, lithographic patterns up to few 100s of nm can be obtained. Then, the wafer was developed using a 1:4 AZ400k developer (Figure 2.12 (d)). This PR can provide straight vertical wall patterns with a thickness of 8 to 10 µm.

2.4.1.4 Top Ni - electrode patterning

An oxygen plasma step was performed after the step of PR development. A capacitive coupled plasma reactor working at RF 13.56 MHz was used. The maximum power was 300 W. This system was capable of working in a range of pressure from 0.2 mbar to 2 mbar. The

Oxygen plasma was generated at 80 W at 600-800 mbar for 30 seconds. This step allowed cleaning and opening the PR under developed structures.

Next step was to deposit Ni for the top electrodes (Figure 2.13). For the MDRs working in DC, the thickness of Ni electrodes was typically 7 µm. For the MDRs working in AC, a nickel thickness of about 1 µm was used.

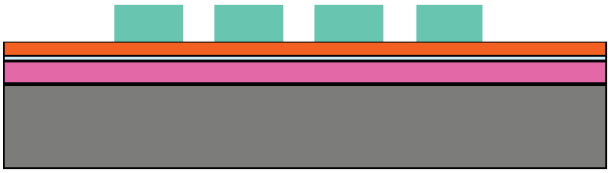

Figure 2.13: Fabrication step with electrochemical deposition of top Ni electrodes.

Due to the large thickness of the Ni layer, electrochemical deposition was preferred over sputtering for this step. For Ni electrochemical deposition process, we used the Ni metal plate as anode and silicon wafer as cathode. They were immersed in a Watts bath containing a solution composed of $NiSO_4$, $6H_2O$: 0.75 mol/l + $NiCl_2$, $6H_2O$: 0.02 mol/l + H_3BO_3: 0.4 mol/l + Saccharin: 0.016 mol/l ***[Sch-00a]***. This Watts solution acted as an electrolyte. This solution contained the salt of the metal to be deposited, as shown in the composition of the solution. After putting the source/anode (Ni plate) and the target/cathode (Si wafer) inside the electrolyte, a DC current of 0.3 A was flowing between the electrodes. Under the applied current, the anodic metal atoms dissolve into the solution. The metallic ions of the solution carry a positive charge and are attracted to the target. When they reach the negatively charged target, electrons are provided to reduce the positively charged ions, such that they "plate out" onto the cathode/target. The rate of Ni deposition was 0.2 µm/min during our process.

2.4.1.5 Backside contact formation and topside protection

Afterwards, the first PR layer was removed. This step was performed by immersing the wafer inside acetone solution for few minutes. Then it was rinsed with isopropanol and DI water. Afterwards wafer was dried with N_2.

The remaining Cu and Ti layers, which were covered by PR during the electrodeposition process were wet etched using copper etch solution (BTP) and Buffered HF (BHF) respectively (Figure 2.14 (a)).

A second optical lithography step using the same type of PR (AZ4562) as used previously was performed with the second mask (Figure 2.14 (b)). This mask was designed in order to protect the SiO_2 region around the periphery of the Ni layer as shown in figure 2.14 (c). This extended SiO_2 is important to reduce the risk to have transient arcs between nickel and silicon at the edge of the nickel electrode during the MDR operation.

Finally, a wet etching step was performed with BHF to remove the 100 nm thick thermal oxide layer deposited on the back side of the wafer. To make an ohmic contact on the

backside of the wafer, Ti (30 nm) and Au (200 nm) were sputter-deposited (Figure 2.14 (d) and Figure 2.15).

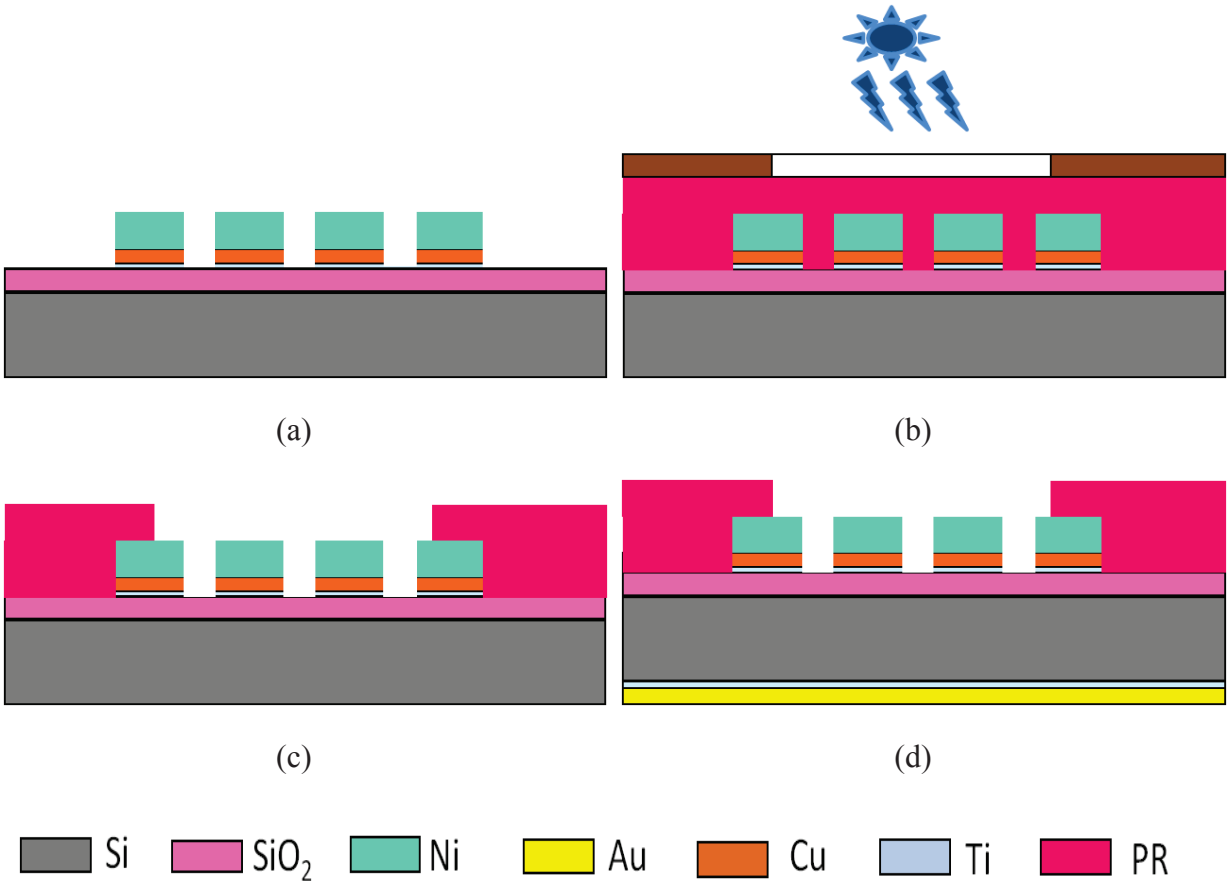

Figure 2.14: Fabrication steps for microdischarge reactors for (a) wet etching of Cu and Ti layer, (b) second mask optical lithography, (c) PR development, and (d) back side ohmic contact with Ti and Au layers.

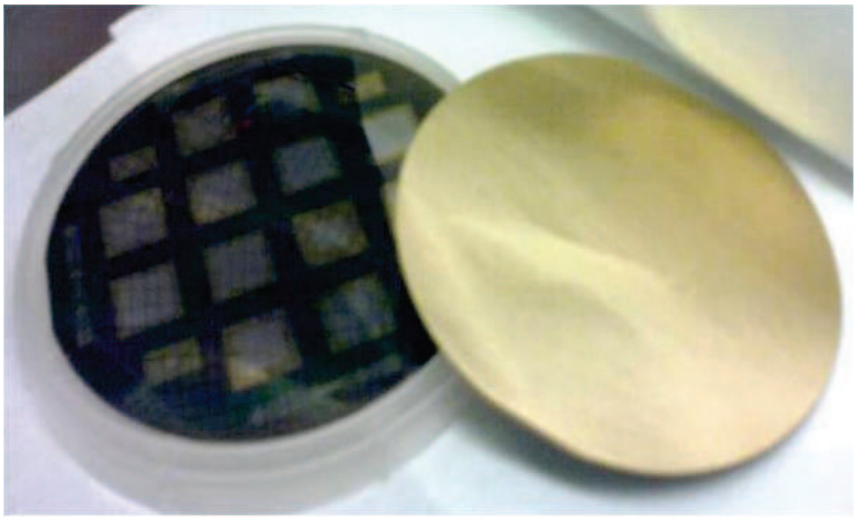

Figure 2.15: Pictures of the wafer after back side Ti and Au layer deposition.

2.4.1.6 Cavity etching

The last step was the etching of SiO_2 and silicon to form the microdischarge cavities. The SiO_2 layer was etched anisotropically by using a "Corial 200 IL" reactor (Figure 2.16).

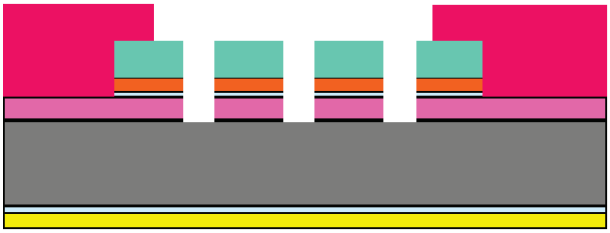

Figure 2.16: Etching step of SiO_2 layer.

This reactor allows to generate large area inductively coupled plasma (ICP) using a 2 MHz RF power supply. The plasma is contained inside a chamber which is surrounded by an inductive coil. An alternating magnetic field is induced by the RF coils located in front of the RF transducer, which produces an azimuthal motion of the electrons and high-density plasma.

Four inch diameter wafers could be mechanically clamped to the chuck and biased independently using a 13.56 MHz power supply. A RF load power of 240 W was used in this process. The chuck was also thermally regulated at 5 °C temperature using a chiller. A "low damage" etching process was designed by our team at GREMI to avoid a lift-off of the Ni layer. CHF_3 and C_2H_4 gases were injected in the chamber with a flow of 30 sccm and 3 sccm respectively. The etch rate was 220 nm/min. This step was carried out in the CERTeM clean room in Tours, France. A SEM image presenting the cavity obtained after this SiO_2 etching is shown in figure 2.17.

Once the oxide is etched, two different silicon cavity geometries can be produced: isotropically etched cavities and anisotropically etched cavities. Si etching was performed at GREMI lab (Orleans, France) using an etching tool Alcatel A601 Etcher. This reactor is dedicated to deep reactive ion etching (DRIE) of silicon.

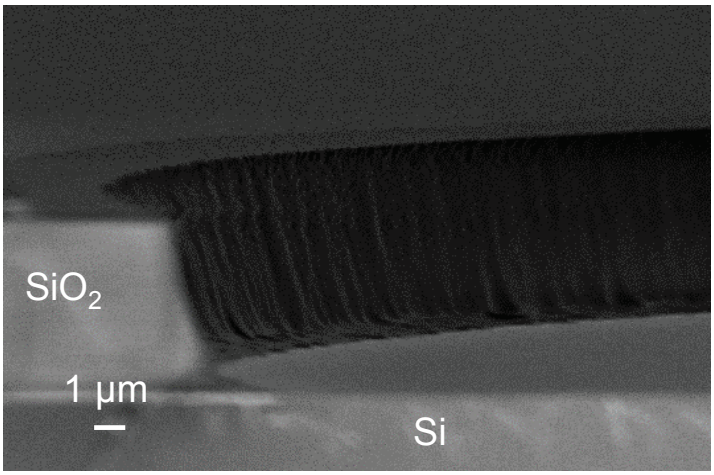

Figure 2.17 : MDR cavity after SiO_2 etching.

The system consists of a wafer vacuum loadlock assembly, connected to the processing chamber. The process chamber is fitted with a high-density ICP type plasma source with a temperature controlled and RF powered substrate holder. Installed gas lines with mass flow controllers allow the supply and regulation of process gases inside the reactor. High performance vacuum pumps are connected to the loadlock as well as to the process module for evacuation and for pumping out reactive gases and by-products. It has the same ICP working principle as explained above except that both RF power supplies are working at 13.56 MHz. Note that Alcatel A601 Etcher system is capable of etching deep anisotropic Si cavities due to the presence of a chuck cooling system, which can provide required etching temperature to the Si wafer down to – 120 °C.

To make isotropically etched cavities, (Figure 2.18 (a) and Figure 2.19 (a)) a SF_6 plasma was used. This etching was performed with 1500 W source power and with 100 V chuck bias in 9 Pascal pressure at 10 °C. Gas flow of 350 sccm was maintained for SF_6.

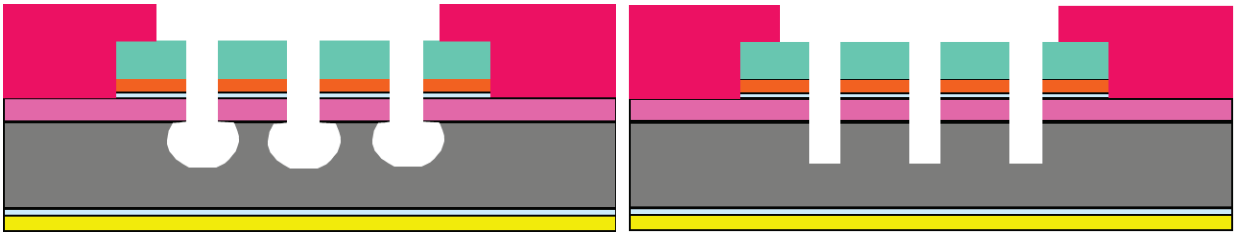

(a) (b)

Figure 2.18: Si cavity etching (a) isotropically and (b) anisotropically.

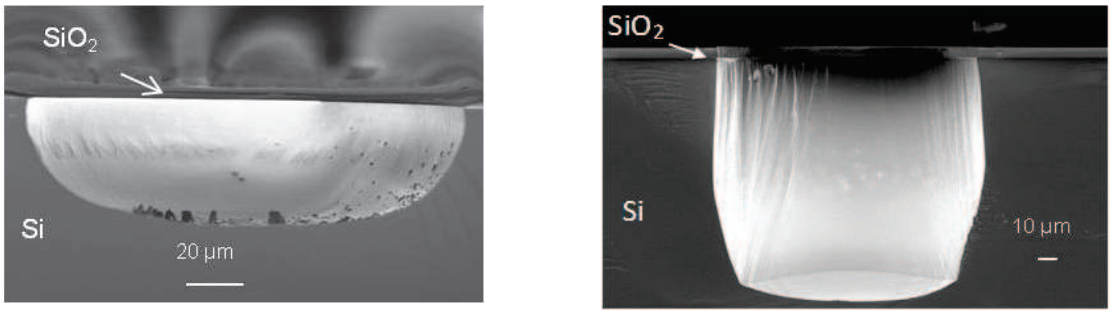

(a) (b)

Figure 2.19: (a) Isotropically and (b) anisotropically etched cavities. The nickel anode film unstuck when the sample was cleaved for anisotropic case.

To form anisotropically etched cavities (Figure 2.18 (b) and Figure 2.19 (b)), we used the so-called STiGer process. The STiGer process was developed by our team at GREMI ***[Til-08]***. It is a cryogenic process that consists in the alternating isotropic etching steps of SF_6 plasmas with deposition steps in SiF_4/O_2 plasmas. In this process, SF_6 plasma is used to etch silicon, for few seconds. Then, SiF_4/O_2 plasma is used for few seconds to create a passivation layer on the side walls of the etched cavities. Due to the low substrate temperature ~ -110 °C, the plasma of SiF_4/O_2 is able to deposit a protective layer (passivation layer) on the side walls of

the cavity. This protective layer allows etching Si in vertical direction and creating a deep anisotropic cavity. For this etching process, it was shown that nearly no passivation layer was remaining on the structure sidewalls after a cryogenic etching process ***[Dus-04]***.

2.4.1.7 Modification of the process flow for MDRs operating in AC regime

The fabrication steps described in the last sub-section were used for microdischarge reactors operating in DC regime. To be able to use reactors in AC regime, some further fabrication steps were performed.

Deposition of Silicon Nitride layer

As explained in the first chapter, electrodes have to be covered by a dielectric layer under AC operation and form a DBD like structure. Si_3N_4 (Silicon Nitride) material seemed to be a good candidate, as shown by G. Eden and his team ***[Ede-05a]***. This is why, we decided to use Si_3N_4 as a dielectric layer to cover the electrodes.

Before depositing Si_3N_4 on the sample, the remaining PR has to be removed. Oxygen plasma produced in the Corial 200 IL reactor is used to etch the remaining PR and clean the top Ni electrodes. For PR etching, a low temperature of around 5 °C is maintained to avoid burning the remaining PR and maintain the nickel layer stuck.

After PR etching, a low frequency PECVD is performed at around 300 °C for the deposition of 2 µm thick Si_3N_4 layer on the top Ni electrode and inside the cavities. The deposition rate is around 30 nm per minute. We also modified the process duration for the top Ni electrode growth, in order to create a 1 µm thick layer.

A low frequency (380 kHz) PECVD deposition method was used for the deposition of the Si_3N_4 dielectric layer. Different gases SiH_4, NH_3 and N_2 were used with a flow of 22.5 sccm, 10 sccm and 1071 sccm respectively. A power of 60 W was used with the low frequency. Temperature of the showerhead was maintained at 300 °C. The deposition rate of Si_3N_4 was 100 nm/min.

A scheme of the MDR arrangement used for AC experiments is shown in figure 2.20 (a). A SEM image of a cleaved MDR is also presented in figure 2.20 (b). The top Ni electrode does not appear on the SEM picture, but we clearly see the vertical Si_3N_4 layer which was deposited on the Ni sidewall and survived to the cleavage.

(a)

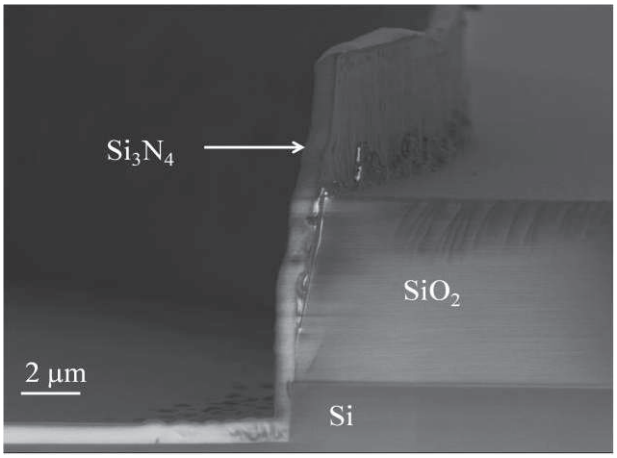

(b)

Figure 2.20: (a) Cavity configuration arrangement of the MDRs for AC regime and (b) SEM image showing different layers of a MDR after cleaving without Ni electrode.

2.5 Challenges in fabrication process and solutions

In this section, some of the main difficulties faced during the fabrication processes are explained. Some solutions to overcome those difficulties are also suggested and described.

2.5.1 Top Ni electrode adhesion problem

During the fabrication of the first wafers, it was sometimes found that the top Ni electrode could unstick during the SiO_2 etching steps. Such an example is shown in figure 2.21.

During wet etching process of Ti and Cu layers, some PR remains (due to underdevelopment) were found to create the lift off of the Ni electrodes. The problem of Ni electrode detachment was also occurred during the dry etching of the Si cavities. In this case, it was concluded that the thickness of adhesive layer of Ti (10 nm) was not sufficient to hold the top Ni electrode during the Si etching.

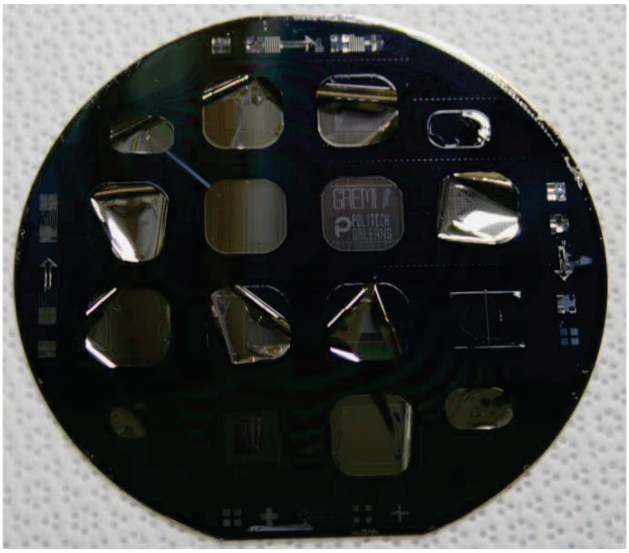

Figure 2.21: Ni electrode adhesion issues.

The solution of the Ni electrode detachment was found by using a longer PR development time and increasing the thickness of Ti adhesive layer to a thickness of 30 nm.

2.5.2 Cavities under etching

A problem for SiO_2 etching layer occurred sometimes. The SiO_2 layer was not always uniformly etched so that some micromasking effect could appear at the surface. Another problem was the deposition of organic thin material on the top of Si surface after SiO_2 etching. Indeed, the SiO_2 etching process is supposed to form a passivation layer made of polymer on vertical sidewalls. But this polymer layer deposits preferentially on silicon rather than SiO_2. This is also why Si is sometimes used as a mask for SiO_2 etching ***[Gab-01]***. As a consequence, when the SiO_2 etching process is too long, such a polymer layer can form on silicon and act as a mask during the silicon etching process. Figure 2.22 is an example of a profile that was obtained after such a problem.

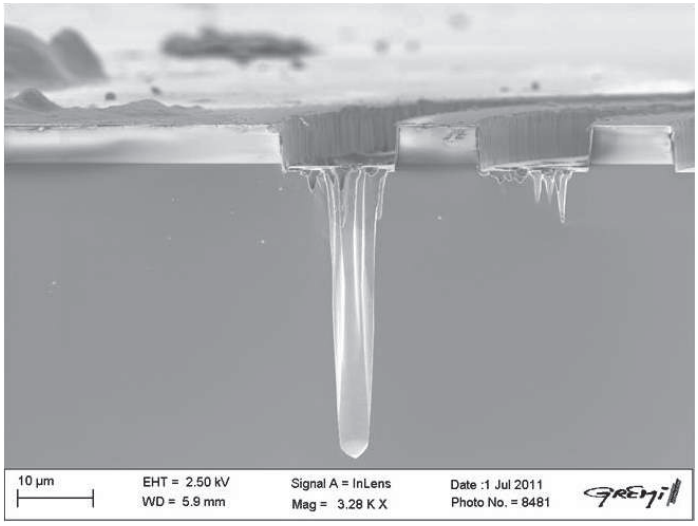

Figure 2.22: Example of the non-uniform etching of Si cavities due to residual micromasking effect.

This problem was solved by cleaning the reactor used for SiO_2 etching with oxygen plasma after the etching of each wafer. Also during the Si etching process, a bias was used on the substrate chuck of the DRIE etcher, to have more energetic plasma species. By this way the few nm thick polymer layer can be etched away and Si cavities can have nice etching.

2.5.3 Backside gold layer detachment

Sometimes, it was found that Au layer deposited on the backside of Si wafer was not sticking well. The problem seems to be related to the thickness of the adhesive Ti layer (~10 nm), which was probably too thin. This problem could also occur if a thin layer of native oxide or thermal oxide was remaining after backside wet etching of the Si wafer. Figure 2.23 shows some examples of this problem.

The solution to this problem was to clearly verify the etching of native or thermal oxide on the backside Si wafer. This verification process included the observation of the Si backside surface behaviour during the DI water rinse. Due to the hydrophobic nature of the Si, it is

easier to verify the etching of the top SiO_2 layer. If DI water does not stay on the backside surface during the rinsing of the Si wafer, it can be assumed that the SiO_2 layer is etched off. Another suggested solution was consisting of increasing the thickness of the adhesive Ti layer. We finally used 30 nm thick Titanium layer to reduce the risk of detaching the Au layer.

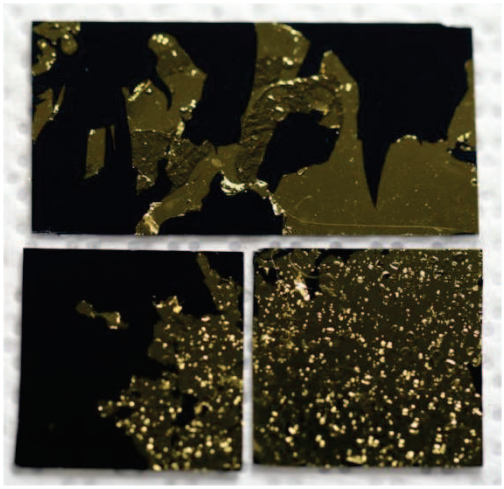

Figure 2.23: Problem of backside gold layer detachment.

2.5.4 Deposition of Si_3N_4 layer

As explained before, a Si_3N_4 dielectric layer was deposited on the top of Ni electrode for the MDRs operated in AC regime. Although the deposition process worked well once, we were not able to reproduce the experiment to obtain a uniform Si_3N_4 layer without defect. It turned out that the deposited Si_3N_4 layer was either easily breakable on touching or porous with micrometric level holes. Figure 2.24 shows some examples of this problem.

The very first experiments of Si_3N_4 PECVD deposition were performed at a quite high temperature (~ 400 °C), but it caused some large stress on the Ni layer, which immediately unstuck when the wafer was cooled down to ambient temperature.

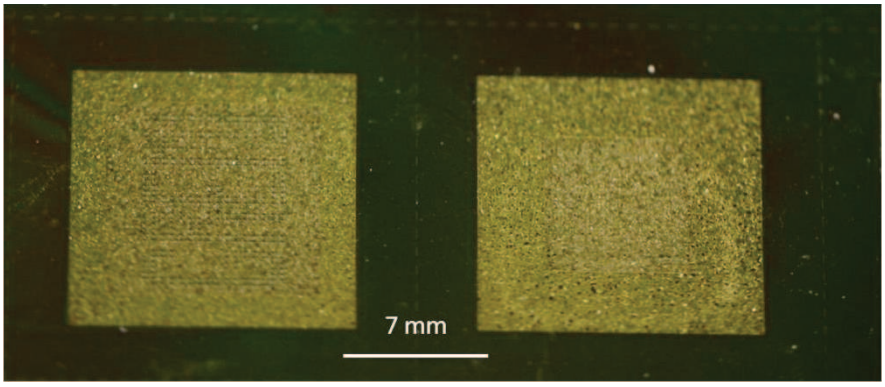

(a)

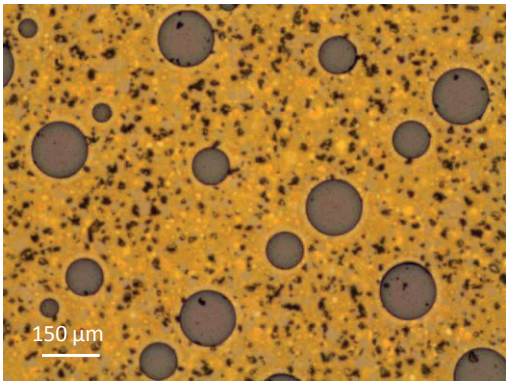

(b)

Figure 2.24: Examples of problems in the deposition of Si_3N_4 layer; (a) images of two MDR arrays of 32 x 32 holes, having holes' diameters 150 µm (left) and 50 µm (right); and (b) image of Mixed holes sub-arrays chip with holes' diameters of 150, 100 and 50 µm .

The occurrence of this type of problem could also be possible by the dirty surfaces of the Ni electrodes, caused by the oxidation plasma PR etching process. Recently, it was found that, the Si_3N_4 layer was depositing well on samples, for which the SiO_2 layer was not etched. Thus, it was concluded that the SiO_2 etching process was somehow modifying the wafer surface, and was further causing the problems for the Si_3N_4 layer deposition.

Thus, most of the problems were overcome. Now, we are able to fabricate quite reproducible samples as far as the process flow is followed carefully and rigorously. The improvement of different fabrication processes was one of the major parts of this PhD study.

2.6 Experimental setup for DC microdischarge experiments

The schematic of the experimental setup is shown in figure 2.25. The experiments were conducted inside a ~2 litre stainless-steel octagonal vacuum chamber in which gas pressure could vary from 10^{-6} to 10^{3} Torr. The diameter and height of this vessel were 14 cm and 11 cm respectively. On each side of the octagonal walls, circular openings were available. Three of these openings were used for gas supply, for electrical connectors and for the sample holder positioning system. We placed glass windows on the other openings for optical measurements and direct observation. The top of the vessel was covered by a stainless-steel plate and separated by a rubber gasket for the tightness. A glass window was also placed in the middle of this plate. The lower portion of the chamber was connected to the pumping system. The microdischarge reactors were installed in the chamber using a home-made sample holder. Within this project, He and Ar gases were mainly used, but different gases like SF_6 and N_2 were also available.

Before an experiment, the chamber was first evacuated to 10^{-5} Torr, with a primary pump and a turbo molecular pump. It was subsequently back filled with the desired gas to a set pressure. A Baratron gauge and a Penning gauge were used to measure the working and base pressures respectively. A digital mass flow controller (0- 100 sccm) was used to inject the gas during the experiments to renew it.

Two DC power supplies were available for the experiments. Most of time, we were using the Heinzinger PNC-/PNChp-Series with output DC 1500 V / 100 mA, which was quite stable even for low current and voltage. A TECHNIX model Sr-2.5-R-300 (0 to 2.5 kV) DC (300 W) was also used for experiments which needed two power supplies like the 3 electrode experiments. But this power supply was not as stable as the other one because it is based on a switched mode power supply system. As a result, some waviness could be observed on the signal especially at low voltage and current. A ballast resistance was placed between the microdischarge device and the power supply to limit the current and avoid arcs. For this, a connector box containing different high power resistances (1.5 kΩ, 39/35 kΩ or 1 MΩ) was used. Generally a ballast resistor (R_b) of 35-39 kΩ was used for the experiments. This box was fitted with BNC connectors to provide power to the microdischarges and to connect the high power probes to the oscilloscope.

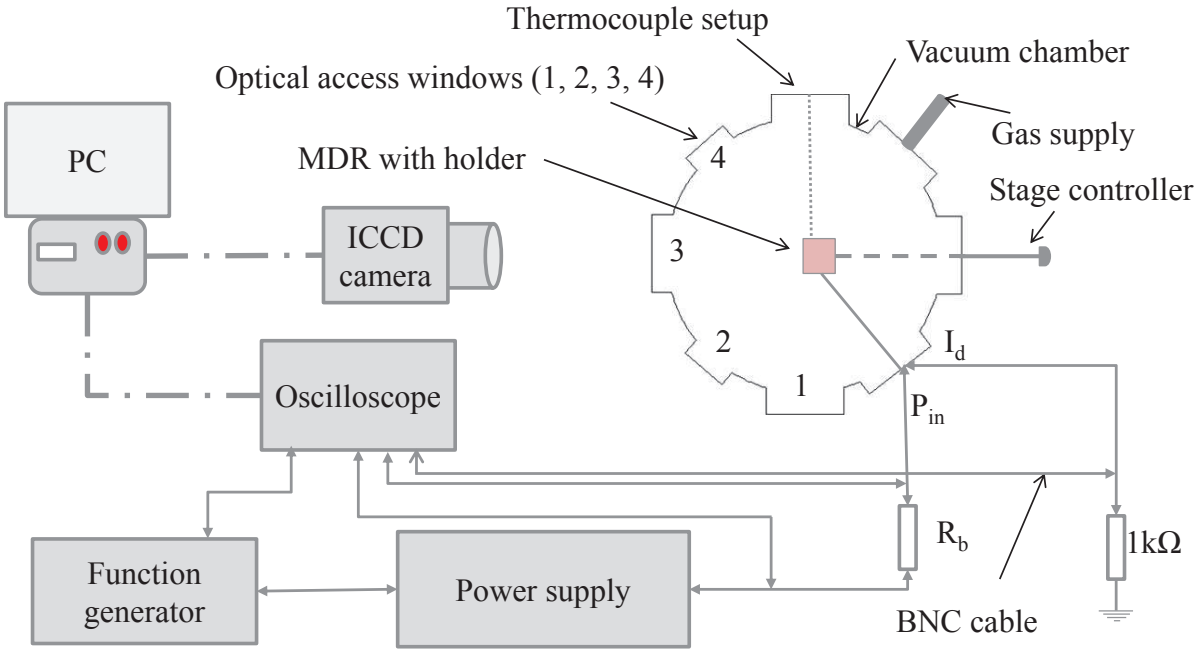

Figure 2.25: Experiment setup for DC operation of MDR.

The power unit can be controlled manually or using an external function generator (Escort brand (CGS 3230)). In general, in order to record a complete cycle in our oscilloscope, we used a 27 mHz frequency for the voltage ramp. The typical voltage ramp was 24 $V.s^{-1}$. The discharge current and voltage were both recorded during the slow ramp using an oscilloscope (Tektronix oscilloscope model T3014B, 200 MHz). The current was measured across a 1000 Ω resistance placed between the discharge and ground. This triangular voltage signal from the power supply allowed us to obtain a full V-I curve. The data was transferred from the oscilloscope to the computer directly using a home-made Visual Basic automated program/software. Two polarities were used for the experiment. We call "Standard Polarity (SP)", the case for which the silicon was biased to be the cathode (negatively with respect to the nickel electrode). The opposite case was named the "Reverse Polarity (RP)". The anode (V_A) and cathode (V_C) voltages were recorded in order to infer the discharge voltage $V_d = V_A - V_C$ and the discharge current $I_d = V_C / 1\ k\Omega$.

Image analyses were made using a digital reflex camera, a video camera and an intensified charge coupled device (ICCD) camera. The digital reflex camera was a Canon EOS 350 D. The video camera was a Panasonic AG-HMC71E with a high definition. The ICCD camera was an i-Star ANDOR 3979 having 1024 x 1024 pixels (13 μm^2 effective pixel size), and a head size of 18 mm. It was controlled by a classic PCI controller card of 1 MHz. We installed a Nikon macro objective with a focal length of 105 mm and maximum aperture of f/2.8. The ICCD system was cooled down to – 20 °C.

2.7 Diagnostic systems for DC MDRs

2.7.1 Optical Emission Spectrometry (OES)

For optical emission spectroscopy (OES), light emitted by the microdischarge was focused by a convex lens with a focal length of 5 cm on the entrance slit of the spectrometer. The calibration of the spectrometer was performed using three intense lines emitted by a mercury vapour lamp at 3650.15 Å, 4046, 56 Å and 5460.74 Å. UV emission characterisation could be carried out using appropriate SiO_2 optical windows achieving a good transmittance in the UV region from 120 nm to 300 nm.

2.7.1.1 Spectrometer

TRIAX 550 (HORIBA) spectrometer was used for OES. The spectrometer (as shown in figure 2.26), TRIAX 550, is equipped with toroidal mirrors and characterised by an asymmetric optical path. It is an imaging spectrograph having a focal length of 550 mm, 2 available entrance slits, and 2 available exit slits. The aperture of the spectrometer is F/6.4. It was equipped with larger focusing mirrors for a maximized non-vignetted and maximum optical throughput. It was having three gratings mounted on a single turret. This allowed tremendous flexibility in the choice of the gratings for optimum resolution and desired spectral range. Three gratings can be used:

- Grating with 150 lines / mm
- Grating with 1200 lines / mm
- Grating with 2400 lines / mm

A high-speed drive and precise motorized slits fully automate the adjustments on the spectrometer. The rays from the entrance slit were directed to the collimating mirrors, which then were reflected by one of the three gratings, fixed on a motorized rotating turret. The optical system of the spectrometer dispersed light according to its wavelength to the focusing mirror. This mirror, like its predecessor, was concave and had an asymmetric surface for correcting geometric aberrations, including astigmatism. The role of the mirror is to reflect and focus the beam to the exit slit. The spectrum was then detected by the ICCD camera. This was the same ANDOR brand ICCD camera as the one described previously.

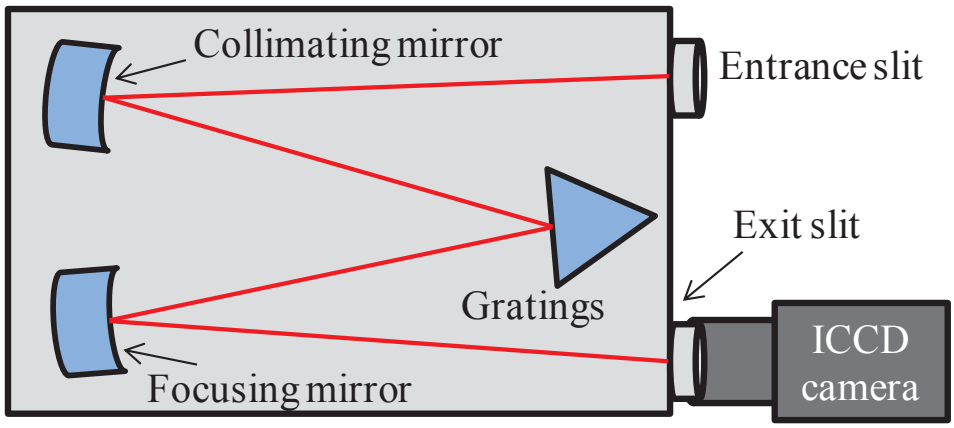

Figure 2.26: Configuration of TRIAX 550 spectrometer used in OES.

2.7.2 Microscopy

2.7.2.1 Optical microscopy

We used an Olympus optical microscope (model B202), overall magnification of 200 X. The magnification of the eyepiece was 10 X and the objective magnification was 10 X. The observed sample was placed on the observation platform with a moving micrometric position driver powered by a DC power supply (Burleigh model 7000). The microscope was used to determine the diameter of the MDR cavities with an accuracy of about 2 microns. It also provided an optical image analysis for the MDR reactor surfaces before and after the plasma operation, and thus to get an idea of the aging effect on the sample.

2.7.2.2 Scanning Electron Microscopy (SEM)

We used a scanning electron microscope (SEM) from Carl Zeiss AG company (model SUPRA™ 40) to observe the microscopic structure profiles of MDRs. It is a general purpose high resolution Field Effect SEM based on the 3rd generation GEMINI® column. It has a large specimen chamber for the integration of optional detectors and accessories. An energy dispersive X-ray spectrometer EDX is integrated to the SEM and fixed inside the specimen chamber with a Bruker's brand detector. The recommended minimum working distance for EDX was 8.5 mm. It can work at different voltage ranges from 0.1 to 30 kV. It has a rather high current probe from 4 pA to 10 nA, with two different detectors: "High efficiency In-lens detector" and "Everhart-Thornley Secondary Electron Detector". It can be operated using a Windows based computer.

In this PhD work, we used SEM to see and analyse the MDR cavities after cleaving them. EDX analyses were performed to discover the effects of the plasma operations on the MDR cavities.

2.7.3 Tunable Diode Laser Absorption Spectroscopy (TDLAS)

As presented in the next chapter, experiments of TDLAS were carried out to determine the gas temperature and evaluate the metastable density of alumina MDR, especially during the ignition and extinction.

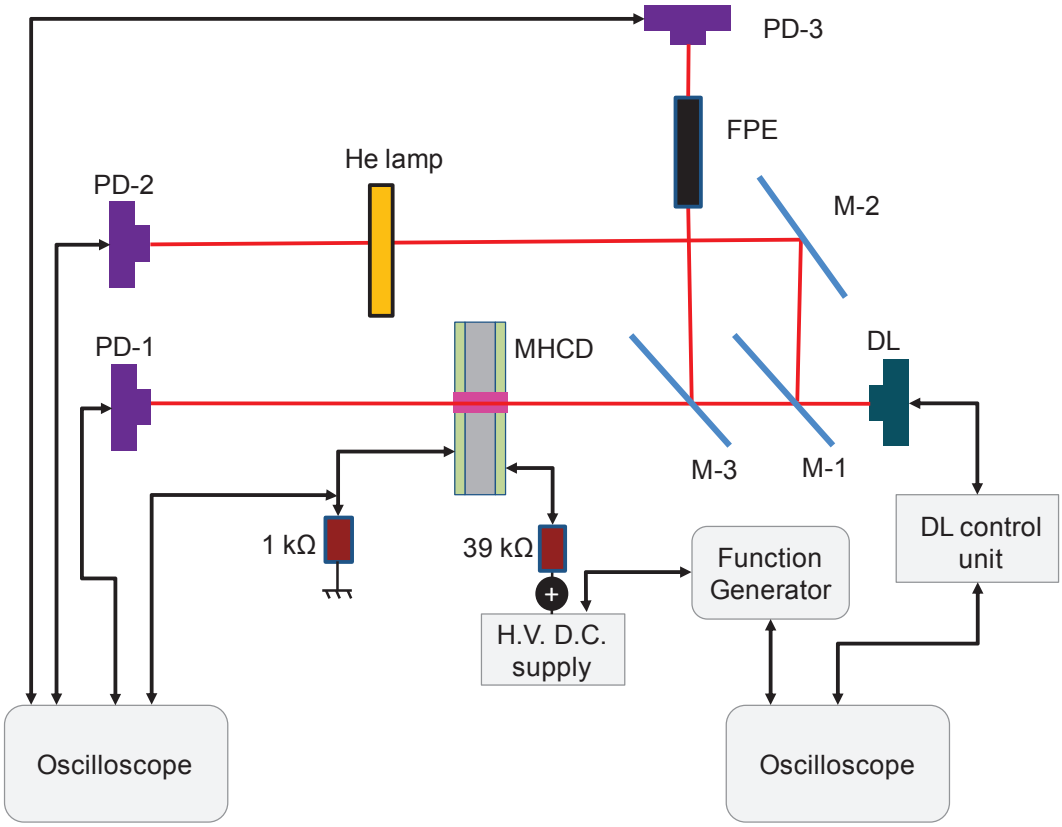

Figure 2.27: TDLAS experimental setup used for MHCD characterisation.

The experimental setup for TDLAS is shown in figure 2.27. We used a tuneable Diode Laser (DL) emitting at 1083 nm. This wavelength corresponds to the transitions between He* $^3S_1$ metastable state and $^3P_{0,1,2}$ excited states. As the two components $^3P_2$ and $^3P_3$ of these lines are not resolved, the recorded profile is the sum of two Voigt profiles, whose relative amplitude is 5 and 3 (for lines to $^3P_2$ and $^3P_1$ levels respectively) and are separated by 2.34 GHz. The DL beam was first split into 3 beams: one of them was directed to a standard He source lamp, which provided a reference for the absorption spectrum profile of He, second one was sent to the 20 cm long Fabry Perot Etalon (FPE) which provided the Free Spectral Range (FSR) of 0.375 GHz, and the third one was directed to the MHCD hole. Each beam was detected by an independent photodiode (PD), whose signal was recorded by an oscilloscope. The experimental setup for TDLAS measurements was provided by Nader Sadeghi from the LiPHY laboratory.

2.8 Experimental setup for AC

Experiments related to the microdischarges operating in AC regime were performed in collaboration with microplasma group of J. Winter at Ruhr Universität Bochum (RUB), Bochum (Germany). For these studies, we worked with the team of Volker Schulz-von der Gathen and his PhD student Henrik Böttner. The results are presented in the chapter 5. The experimental setup used for the experiments in AC regime is shown in figure 2.28.

A stainless steel cylindrical chamber having an inner diameter of 25 cm and a height of around 13 inch was used. The top of the cylinder was covered by a circular heavy stainless steel cover. To make vacuum inside the chamber, the top cover was placed with a re-usable circular rubber gasket. The pumping system was consisting of a diaphragm pump (Pfeiffer MD 4TC) and a turbo molecular drag pump (TMP, Pfeiffer TMU 520 PC). The final vacuum could be made down to a pressure of 10^{-6} mbar. The pumping system was installed at the bottom of the chamber.

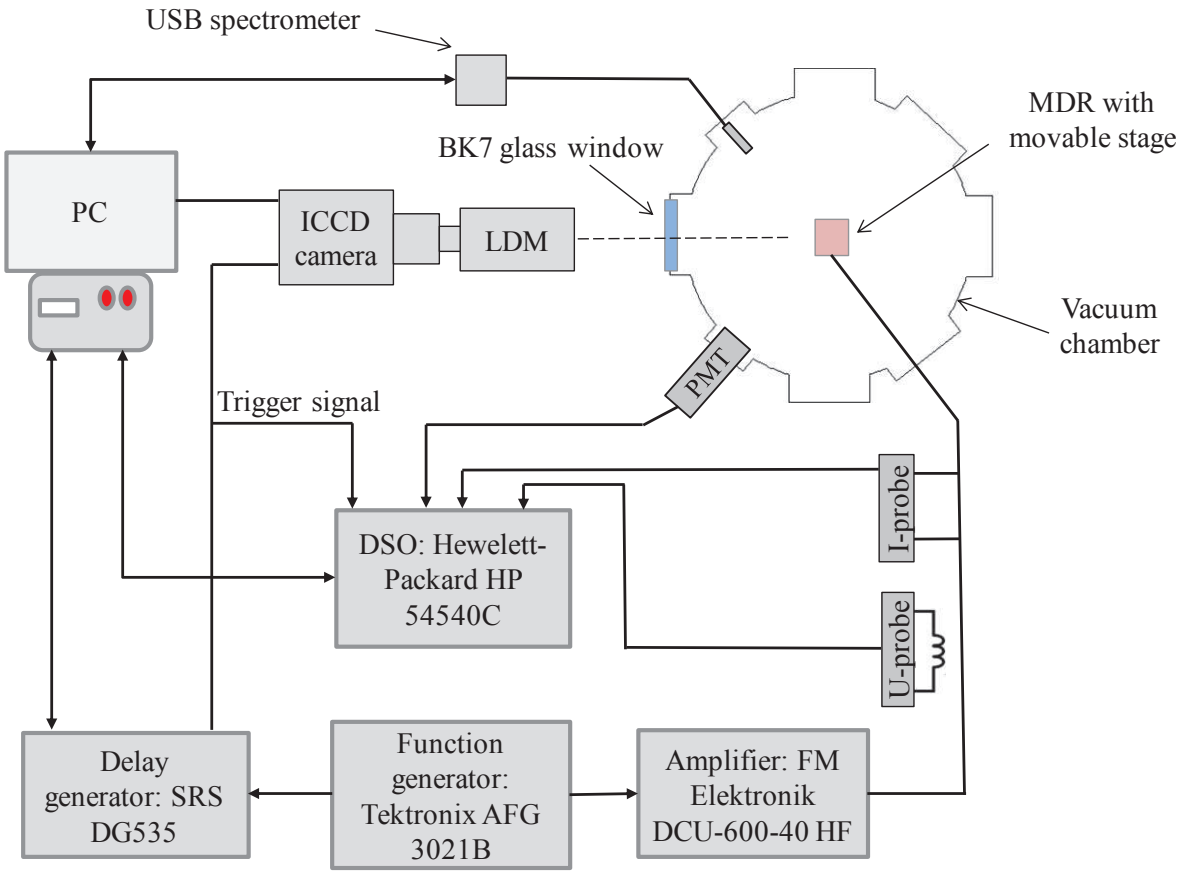

Figure 2.28: Experimental setup used for AC operation of MDRs.

The sample was mounted inside the chamber using a sample holder fitted with a three dimensional, computer controlled moving platform to facilitate the alignment process during optical measurements. The chamber was fitted with a Pirani gauge and an inverted magnetron gauge for low pressure measurements. An additional capacitive gauge was also available for

higher pressure measurements. For in-situ optical measurements, a photomultiplier tube (PMT, Hamamatsu R3896) and an optical fiber with front lens (f/2 fused silica collimated lens, Ocean Optics 74-UV, 200-2000 nm) attached with a USB grating spectrometer (Ocean Optics HR 4000) were fitted inside the chamber. The chamber was having one bigger BK7 glass window for the ICCD camera access (for spectroscopic measurements) and a small normal glass window for visual observations.

A broadband power amplifier (FM Elektronik DCU 600-40 HF) was connected using a 50 Ω BNC cable with an arbitrary function generator (Tektronix AFG 3021B). The amplified signal was directly connected to the high voltage feed through flange. The MDR electrodes were soldered with a varnish coated flexible copper wire having a diameter of 3 mm and then fitted inside the vacuum chamber. The devices were powered using a bi-polar triangular voltage waveform, having a positive half cycle with a peak value of $+V_{max}$ and a negative half cycle with a peak value of $-V_{max}$. The Ni electrode of the MDRs was connected to the power supply and the Si electrode was grounded. Commercial capacitive voltage (Tektronix P6015A) and inductive current (Tektronix P6021) probes were inserted between amplifier and feed through flange. Measured voltage and current signals were monitored and recorded with a digital storage oscilloscope (DSO, Hewlett-Packard HP-54540C).

2.9 Diagnostic systems for MDRs operating in AC

2.9.1 ICCD camera and spectroscopy setup

For the optical and spectroscopy measurements, an intensified charge coupled device (ICCD) camera (LaVision PicoStar HR16) with a high gating rate was used. It was having 512 x 512 pixel ICCD chip. The experiments were performed by using a long distance telescope (LDM, Questar QMI). It was capable to provide an effective spatial resolution of 2 μm per pixel when additional lenses (1.5 x and 2 x of Barlow brand) were inserted in between the microscopic system. ICCD cameras as well as the microscope were mounted on a straight guided rail. The working distance could be varied from 0.56 m to 1.52 m and could provide a numerical aperture from 0.0255 to 0.0580 respectively. The system was capable of providing a magnification up to 12 times of the original image. The microscopic setup was housed inside a light-proof black polyoxymethylene (POM) covering. ICCD camera was fitted with a gateable intensifier and micro-channel plate (MCP). A switchable voltage between the photocathode and MCP made the intensifier gateable.

Gating of the ICCD for spectroscopy measurements was performed with a commercial digital delay generator (Stanford Research Systems DG535). There was also a possibility to use liquid crystal tunable filter (CRi VariSpec NIRR) in between the camera and the microscope for spectral discrimination of the images. The system of ICCD camera, oscilloscope (DSO) and delay generator were remotely controlled via GPIB parallel port using visual basic homemade control software.

2.9.2 Phase resolved optical emission spectroscopy

"Phase Resolved Optical Emission Spectroscopy" stands for PROES. The experiments consisted in analysing emission dynamics of MDRs under AC operation within one excitation period. By synchronising them to the driving frequency, their related periodic behaviour can be studied. To achieve high temporal and spatial resolution, a charges-coupled device chip combined with a fast repetitively gateable intensifier in form of a microchannel plate and an optical telescope system was used.

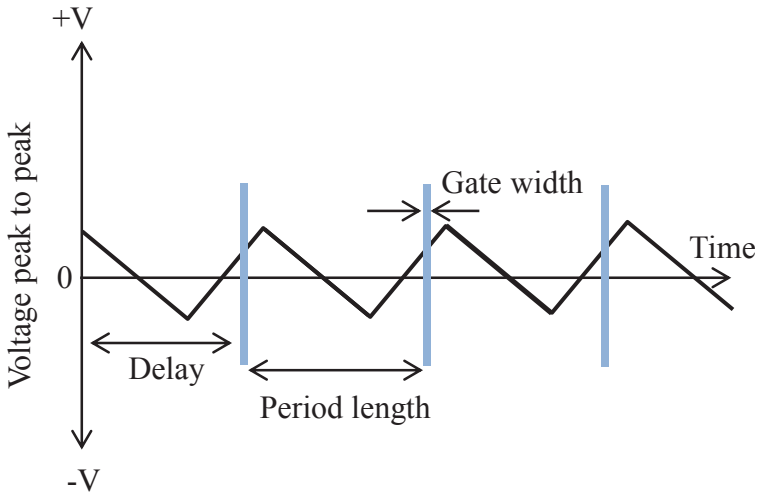

Figure 2.29: PROES gating mechanism.

The fluorescence signal for each phasing was integrated over several excitation periods by gating the fluorescence detector with a fixed gate width and was synchronised to the driving frequency (Figure 2.29). This provided a high temporal resolution of the MDR signals within the excitation period at high photon yields. The obtained signal was then analysed using homemade software, designed by Henrik Böttner (RUB, Bochum) using Visual Basic.

Chapter 3

Ignition and extinction in alumina based MHCD

3.1 Introduction

The aim of this chapter is to present the study of ignition and extinction of microdischarges. For these experiments, the single hole alumina based MHCDs were used. As previously described in chapter 2, these microdevices were drilled and were quite suitable for the tunable diode laser absorption spectroscopy (TDLAS) experiments that are presented in this chapter. We will see it in the next chapters; these devices were also much more robust than the microdischarge reactors (MDRs) made in silicon. This was one of the reasons to use them for such a characterisation.

In this chapter, electrical characterisations for single hole MHCD reactors are first presented with a focus on their ignition and extinction. Then, the study related to the evaluation of metastable density and gas temperature for MHCD using TDLAS experiment is discussed. Transient phenomena at the ignition and extinction are then explored using TDLAS.

3.2 Study of ignition and extinction with Electrical characterisation

For this experiment Helium (He) gas was used. A remote triangular signal with 50 mHz frequency to control the DC voltage ramp was used as mentioned in the second chapter. Figure 3.1 shows the time evolution of voltage and current for a period of the triangular applied voltage. He pressure was 400 torr. A typical electrical behaviour of the MHCD was obtained: before plasma ignition, voltage keeps on rising. At the breakdown (A), the discharge voltage drops and the current reaches a certain value depending on the value of the used ballast resistor. Then, the discharge voltage remains constant as far as the cathode is not limited as reported in ref ***[Duf-08]***. Finally, the discharge current decreases until it reaches zero (B).

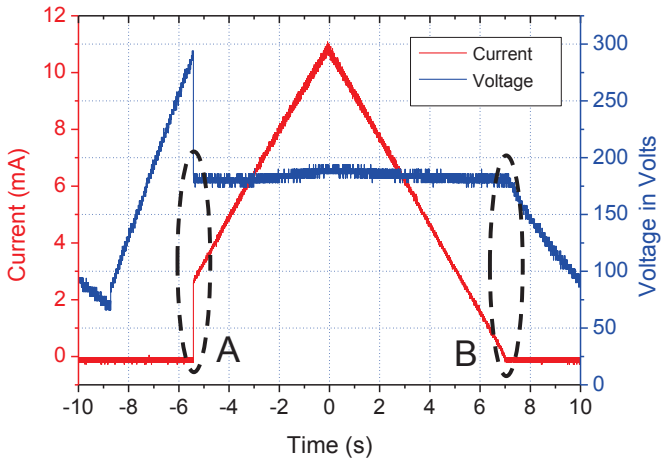

Figure 3.1: Standard voltage and current plots with respect to (w.r.t.) time for a single hole MHCD reactor at 400 Torr He.

With this time scale in seconds, it is of course impossible to detect the transient phenomena involved at the ignition and at the extinction of the microdischarge. To study the ignition and extinction of the microplasma, the time scale of the oscilloscope was reduced to microsecond range. Regions (A) and (B) (figure 3.1) were investigated to analyse the ignition and extinction of the MHCD.

3.2.1.1 Ignition

In figure 3.2, current and MHCD voltage waveforms are shown during the ignition of the plasma at (a) 350 Torr and (b) 750 Torr. The discharge inside the MHCD reactor starts with a large current pulse and reaches a steady state regime after some oscillations. The typical pulse duration is around 2 µs FWHM (full width at half maximum). The same types of oscillations, but out of phase to the current signal, are also observed on the voltage waveform (blue and dashed curve in figure 3.2). In fact, before breakdown, the voltage rises slowly and charges the MHCD reactor. Afterwards, plasma starts to ignite and a sharp voltage drop can be seen. The huge current peak corresponds to the transient regime of the microplasma before reaching the steady state regime ***[Rou-06, Duf-09]***.

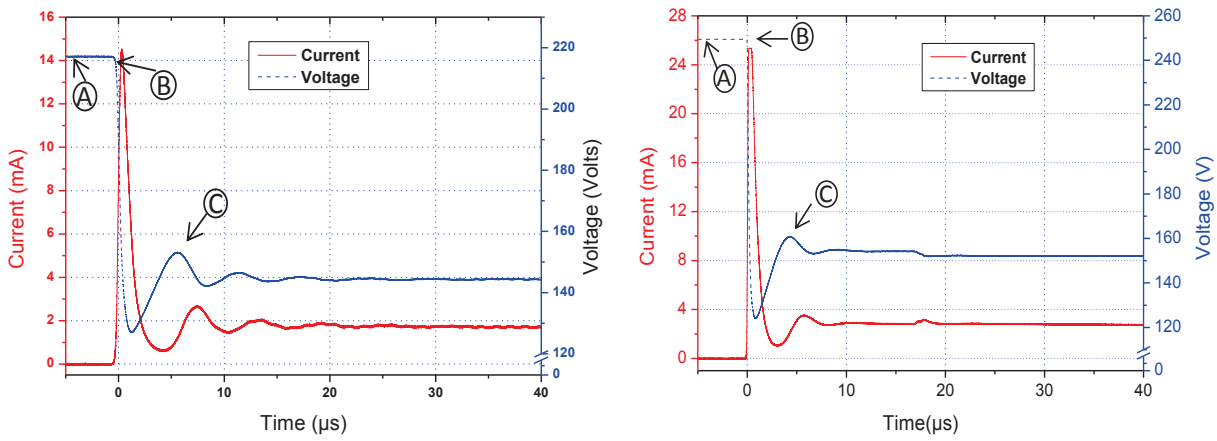

(a) (b)

Figure 3.2: MHCD current and voltage waveforms at the ignition of Helium micro discharges (a) at 350 Torr and (b) at 750 Torr.

It is possible to quantify the stabilisation time required for the microdischarges to reach the normal glow regime. The plots of figure 3.2 can be explained step by step to better visualise the plots immediately after the breakdown phenomenon. We can distinguish three zones: the pre-breakdown zone (between points A and B), the transition zone (between B and C) and the normal glow (after point C onwards). In the pre-breakdown, the current is zero but the voltage increases till breakdown potential is reached. Some research teams ***[Sch-97, Che-02]*** have used the same type of geometry for micro-hollow cathode reactors and measured a very low current before the voltage drop and the normal glow regime, thus justifying the existence of a pre-breakdown regime. Experimentally, we cannot measure the current from our samples because our cathode thickness is about 8 µm, while this regime is observed for cathodes with a thickness of several hundreds of microns.

At the breakdown, the transient phenomenon appears. The current initially reaches a value of approximately 15 mA for 350 Torr and 25 mA for 750 Torr in around 300 ns and then drops and stabilises after a few microseconds to about 5 mA. At the microscopic level, this means that the electric field and cathode sheaths also stabilised after few microseconds. Moreover, this period of stabilisation depends slightly on the pressure.

3.2.1.2 Self pulsing regime

The ignition signal can be compared to the self pulsing regime ***[Aub-07]***. This regime appears when the micro-discharge is fed by a quite low discharge current, typically less than 1 mA. It is quite easy to obtain with our setup: we just need to switch the ballast resistance to 1 MΩ to significantly reduce the current. Then, the current is self-pulsed as reported by several other teams ***[Hsu-05, LAZ-11…]***. Figure 3.3 shows current and voltage waveforms in this particular regime. At point A, the voltage increases until it reaches the breakdown potential (point B). The current appears suddenly (at point B) and reaches a value of 28 mA at point C. The pulse duration is typically 1-2 µs.

By analogy with an RC circuit, the duration between A and B is the time needed to accumulate charges on the cathode of the equivalent capacitor of the MHCD until the voltage reaches the breakdown voltage. Then, the discharge of this capacitor creates a high current peak. Between points B and C, X. Aubert and A. Rousseau showed that the discharge extends on the outer surface of cathode ***[Aub-07]***. Then, after the high pulse, the power supply does not provide a sufficient voltage to maintain the discharge current between the two electrodes. As a consequence, the discharge is not self-sustained and vanishes after 2 µs (between points C and D). Between these two points, if the electrodes are sufficiently thick, it was shown that a weak micro-discharge is confined inside the cavity of the micro-cathode. Images obtained by ICCD camera illustrating this phenomenon are presented in the work of X. Aubert and A. Rousseau ***[Aub-07]***.

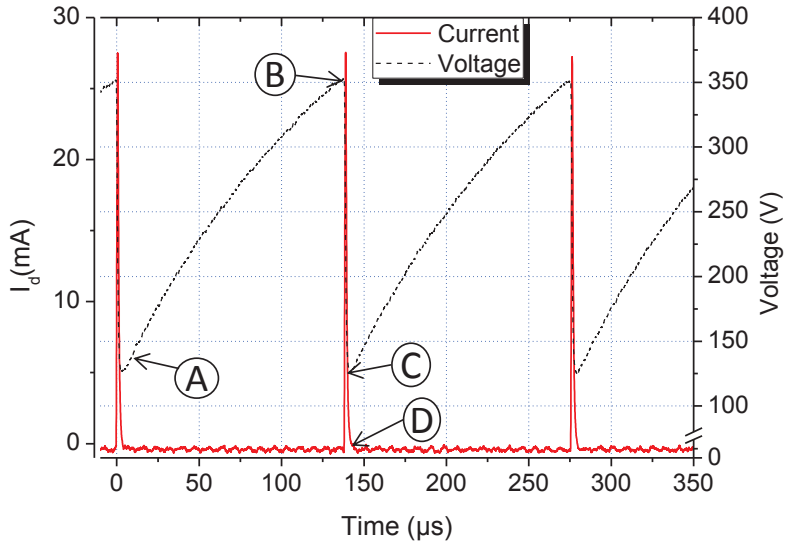

Figure 3.3: Current and voltage plots w.r.t. time for the MHCD operating in self-pulsing regime in 200 Torr helium.

The same ignition phenomenon is followed by MHCD running in steady state regime. For the starting of the discharge, we see a big current peak (figure 3.2). But in this case, the power supply provides a sufficient voltage to maintain a discharge current between the two electrodes, and we see a stable glow discharge in MHCD device.

3.2.1.3 Extinction phase

For the extinction of plasma, a different behaviour was obtained. Figure 3.4 shows the current and voltage waveforms for the ending of the microdischarges at (a) 350 and (b) 750 Torr He (zone B in figure 3.1). These plots show the voltage and current behaviour of MHCD in a window of few tens of micro seconds, just before the extinction of the plasma inside the cavity. From figure 3.4 (a), at 350 Torr, we see that at the end of the normal glow regime, the current starts decreasing slowly from few mA to 100s of µA. At the same time, the voltage tends to increase slowly. Then the current drops to zero in about 20 micro seconds. In this region of low pressure, we just observe a monotonic and smooth curve decreasing without instability during the extinction of plasma.

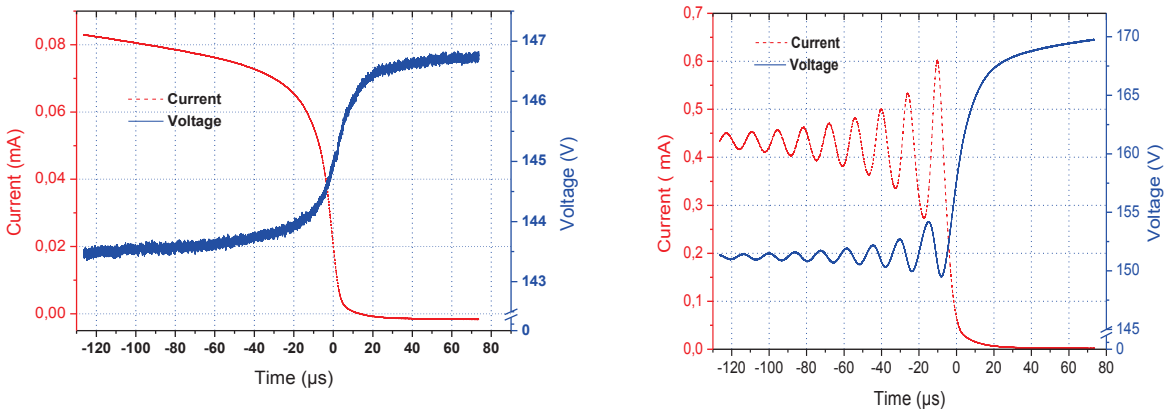

(a) (b)

Figure 3.4: Current and voltage curves w. r. t. time for the ending of the microdischarges at (a) 350 and (b) 750 Torr He.

Figure 3.4 (b) shows the extinction of the MHCD at higher pressure (750 torr). Here, it can be seen that, before the ending of the plasma in the region of few 10's of micro seconds, the current and the voltage follow an oscillating behaviour. This behaviour is completely different from the ending of the microdischarges at lower pressure (< 400 Torr) and from the ignition phenomena. This curve corresponds to a sinusoidal exponential oscillation. The period of oscillation is around 14 µs.

To make sure that these oscillations were not an electrical noise, the Photo Multiplier Tube (PMT) signal was recorded during the ending of the plasma. An example of such a PMT signal is shown in the figure 3.5. From this figure, clear oscillations in the light intensity of the microdischarge can be observed. This indicates that these oscillations are generated by the microdischarge itself. These PMT measurements are confirmed by the Tuneable Diode Laser Spectroscopy (TDLAS) experiments, which are presented in this chapter.

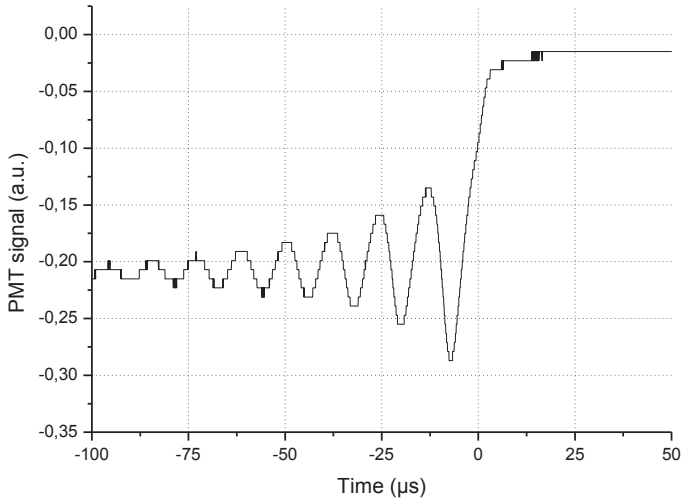

Figure 3.5: PMT signal recorded for the extinction of the microdischarge.

3.3 Equivalent electrical circuit

To reproduce the current behaviour versus time during the ignition and extinction phase of the microplasma by electrical simulation, an equivalent electrical circuit with PSPICE software was simulated. This section presents the results obtained by these simulations.

3.3.1 Ignition

An equivalent electrical circuit, to simulate the ignition of the discharges in MHCD was used, as shown in figure 3.6. PSPICE simulation tool was used to simulate this equivalent electrical circuit. In this circuit the MHCD reactor part is indicated by the rectangle (red dashed lines).

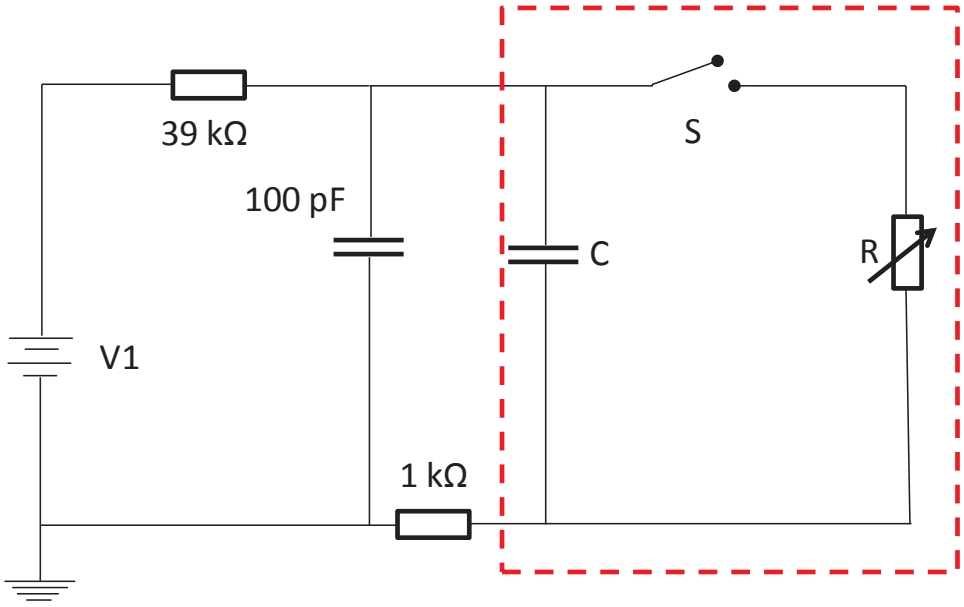

Figure 3.6: Equivalent electrical circuit used in the simulations, to show the ignition of microdischarges inside MHCD reactors. Red dashed lines indicate the equivalent circuit for MHCD

In this circuit, a DC voltage supply (V1) was a voltage source for the circuit with maximum voltage of 240 V. The 39 kΩ ballast resistor was added in series. A 100 pF capacitor was added in order to take into account the equivalent capacitance of the co-axial cables. The input voltage was evaluated by placing a voltage probe after the ballast resistor. In the MHCD part, a 50 pF capacitor (C) was placed for the equivalent capacitance of the MHCD itself. A variable resistance R was put in parallel to C to simulate the microplasma resistance during its ignition. A voltage controlled switch S is placed in the circuit to simulate the breakdown of the discharge. The resistance R was varied from 5 kΩ upto 100 kΩ to simulate the ignition of the microdischarge. For MHCD current measurements, a current probe was placed at the resistance of 1kΩ.

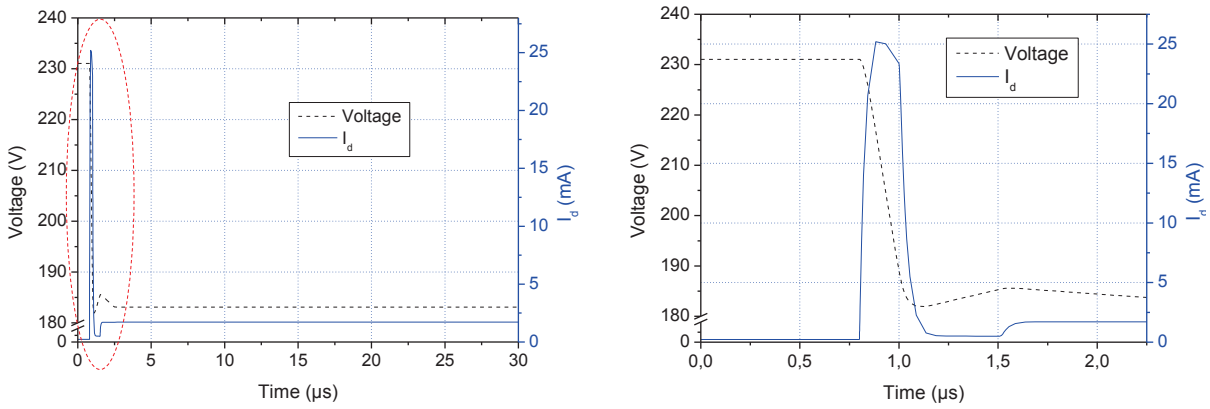

Figure 3.7: (a) Output of the simulated equivalent electrical circuit for the ignition of microdischarge in terms of voltage and current curves vs. time using PSPICE, and (b) is the zoomed part of the graph as indicated by red dashed lines in the part (a).

Figure 3.7 shows the voltage and current curves with respect to the time, taken directly from PSPICE simulations. In this plot, we see that, on the closing of the switch S, voltage drops and a current peak appears. This current peak has maximum current (I_d) amplitude of 25 mA and pulse duration of around 1 µs. This current amplitude and pulse duration are approximately similar to the discharge current peak obtained for 750 Torr case (figure 3.2 (b)). After this peak, the current drops rapidly and reaches a value near to zero mA. At the same time, the voltage increases again. After 2 µs, we see stabilised current and voltage waveforms. This behaviour is also similar to the behaviour of current and voltage plots obtained for 750 Torr (figure 3.2 (b)).

When the switch S is closed, the MHCD capacitor starts to discharge through the resistance. At this point, we see a voltage drop and a high current peak. This peak corresponds to the discharge of the capacitor through the microplasma. During the sheath formation, there is a small fluctuation of the current. Then, secondary electrons are produced to sustain the stable DC microplasma. In the self-pulsing regime, with a higher ballast resistance, the capacitor is emptied due to the large current peak and the charging of the capacitor is not fast enough to supply the necessary electrons and allow the secondary emission process.

3.3.2 Extinction

As already mentioned, if the microdischarge runs at lower pressure (<400 Torr), then a smooth extinction can be obtained. But at higher pressures, some oscillations occur during the extinction phase. For the extinction part, it seems that a simple equivalent electrical circuit is not sufficient to show such instability.

TDLAS experiment was also performed to investigate the role and the dynamics of the metastables during the ignition and the extinction of the MHCD.

3.4 Measurements using TDLAS

This section presents tunable diode laser absorption spectroscopy (TDLAS) measurements performed to study the He metastable density evolution. In this paragraph, the TDALS experiment results are first presented for the steady state glow regime of the microdischarge. Gas temperature measurements are also reported here. Afterwards, the study related to the ignition and the extinction of the MHCD using TDLAS is presented.

3.4.1 Metastable density measurements for Al_2O_3 based MHCD in steady state regime

In this part, the TDLAS measurement to calculate the metastable density and gas temperature of a MHCD are presented.

For these experiments, a single hole alumina MHCD was ignited in normal glow regime at a desired gas pressure. The diode laser beam was passing through the MHCD hole from the anode side to the cathode side and was detected by a photodiode using the experimental setup arrangement presented in chapter 2. These experiments were performed in collaboration with Nader Sadeghi from the *LiPhy* laboratory. The experiments were performed in Helium for 4 values of discharge current (5, 10, 15 and 20 mA) and for 3 different pressures (350, 500, and 750 Torr).

At this point, it would be interesting to see the He structures in terms of energy levels. Figure 3.8 shows the Grotrian energy level diagram for He, taken from ref ***[Fan-06]***. As mentioned by Fantz in his article ***[Fan-06]***, Helium has two electron system and the energy levels are separated in two multiplets systems viz. a singlet and a triplet. Due to Pauli's exclusion principle He can have fine structure for 2^3 P state (figure 3.8). Here, the electronic states which cannot decay via radiative transitions have a long lifetime and are called metastable states (2^3 S and 2^1 S). Transitions which are linked directly to the ground state are called resonant transitions. For our study, the transition between 2^3S metastables state and 2^3P states were used.

For the measurement, the wavelength of the tunable diode laser was tuned to the transitions $2^3S_1 \rightarrow 2^3P_J^0\ (J = 1, 2)$ of He at around 1083 nm. Then the spectral profiles of helium absorption lines were recorded to deduce He* ($^3S_1$) metastable densities for various discharge conditions. Due to their long lifetime, atoms in metastable states are a reservoir of energy in the discharge, and stepwise ionisation through these states is known to be an important

ionisation mechanism in rare gas plasmas, especially when the electron temperature is low. The metastables can be quenched by electron collisions: this one of the main mechanisms for their decay.

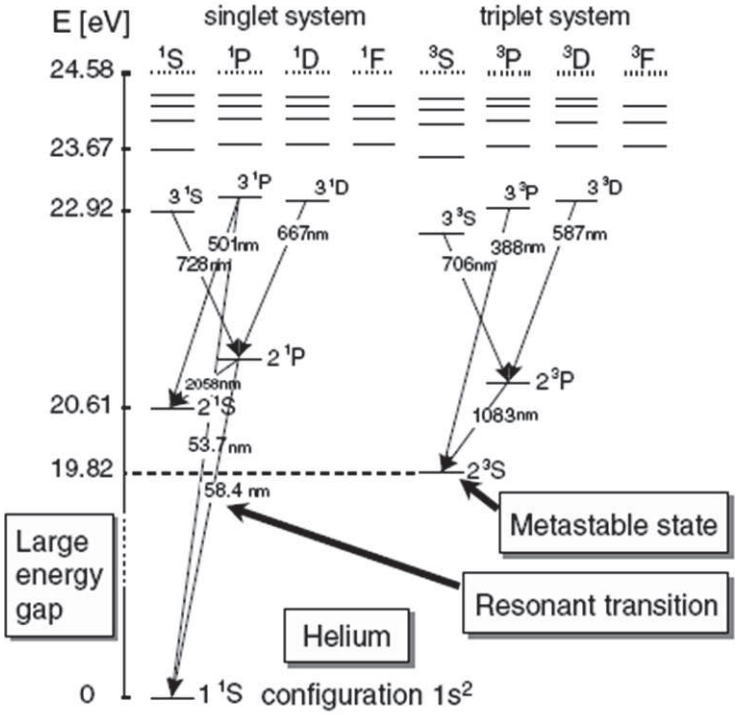

Figure 3.8: Grotrian energy level diagram for Helium. [ref: Fan-06]

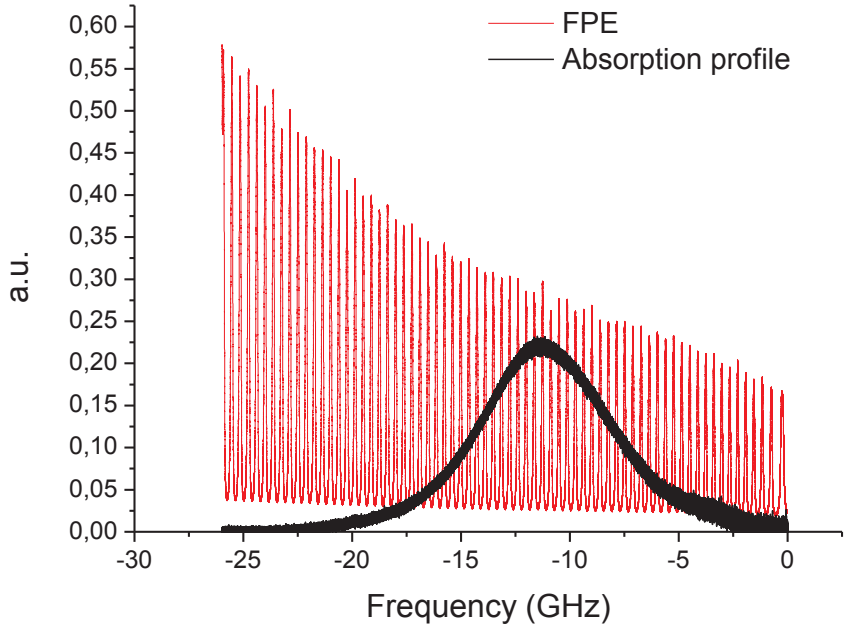

Figure 3.9: Typical absorption profile obtained from TDLAS experiment under stable plasma operation at 500 Torr He and 15 mA of discharge current.

A typical absorption profile is given in figure 3.9 (black curve). In the plot, we also added the signal coming from the Fabry-Perot etalon (red curve), which indicates the Free Spectral Range (FSR) for calibration. Here the FSR is equal to 0.375 GHz.

Using the plots obtained from TDLAS experiments, the He metastable density can be calculated for a discharge current at a particular pressure. First, the surface area S under the absorption line is calculated. This area (S) is proportional to the metastable density and can be given by following the relation (3.1) ***[Sad-04]:***

$$S = \int_0^\infty ln\left(\frac{I(0,\nu)}{I((l,\ \nu)}\right) d\nu = h\nu_0 f_{ik} l \langle N_i \rangle \qquad (3.1)$$

where $\frac{I(0,\nu)}{I((l,\ \nu)}$ is the absorption rate for a frequency ν, and h is the Planck's constant. The mean absolute density of absorbing atoms is then given by equation (3.2):

$$\langle N_i \rangle = \frac{1}{h\nu_0 f_{ik} l} S = \frac{4\varepsilon_0 m_e c}{e^2 f_{ik} l} S = \frac{1}{l f_{ik}} 3.8 \times 10^{14} S \qquad (3.2)$$

where S is given in GHz, $<N_i>$ is the mean metastable density in m^{-3}, l is the absorption length in m and f_{ik} is the oscillator strength of the lines as discussed above (figure 3.8) and have the following values ***[Nis-12]***:

f_{ik} = 0,060 for the 1082.909 nm $^3S_1 - {}^3P_0$ line

f_{ik} = 0.18 for the 1083.025 nm $^3S_1 - {}^3P_1$ line

f_{ik} = 0.30 for the 1083.034 nm $^3S_1 - {}^3P_2$ line

But in current case, the two later lines are not resolved (figure 3.8), so f values must be added and the relation (3.2) becomes ***[Sad-04]***:

$$\textit{For 1083.03} \quad \langle N_i \rangle = 7.92\ 10^{14} * S / l_{eq} \qquad (3.3)$$

To be more accurate, the equivalent absorption length (l_{eq}) can be the addition of the MHCD cavity length and the length corresponding to the plasma spread of the cavity. But, in this evaluation, we considered only the cavity length of our MHCD reactor (~ 270 µm) because we did not measure the length of the plasma spread.

Using the relation (3.3), we can calculate the metastable density of species under the MHCD plasma operation. The calculated metastable density versus the discharge current is presented in figure 3.10 for 3 different pressures.

A factor, which can affect the calculations, is the gas flow during the experiment ***[Pen-02]***. The discharge operation in MHCD, without a gas flow can cause the depopulation of the excited levels due to volume processes like two and three body collisions and due to quenching by impurities. This can result in a significant decrease of the density of excited species with time ***[Pen-02]***. This is why a small gas flow of about 15 to 20 sccm was maintained during our experiments.

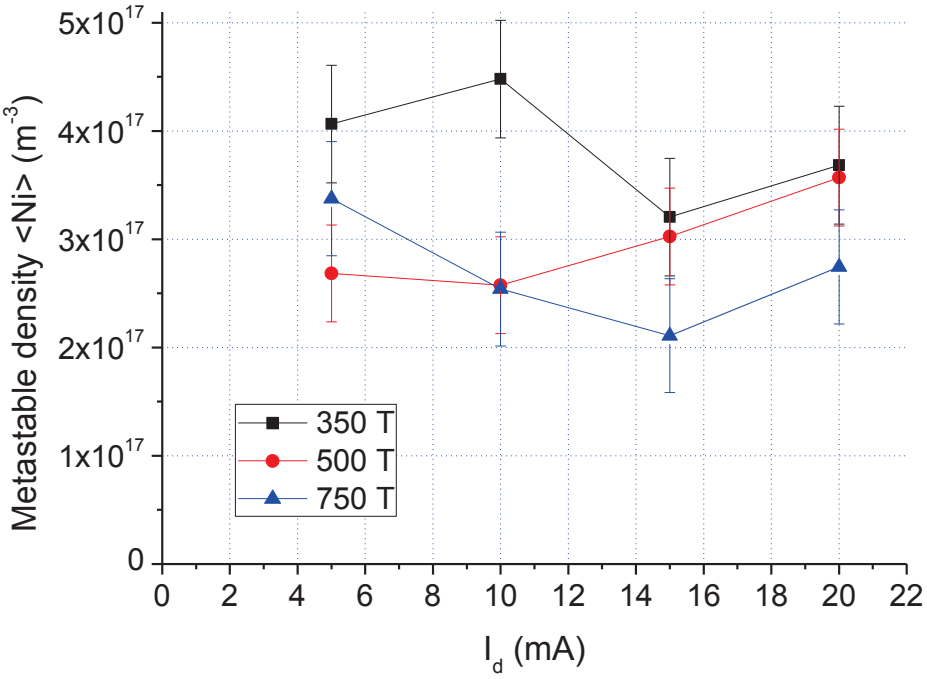

Figure 3.10: Calculated metastable density for alumina based MHCD using TDLAS method.

3.4.2 Gas temperature measurements

The gas temperature inside a single hole MHCD during the plasma operation can also be evaluated by TDLAS experiments. The variations of pressure and current in a MHCD modify the gas temperature inside the microreactor cavity.

In plasma operation, various mechanisms contribute to the broadening of the atomic transition lines. We consider three main broadening factors of the absorption lines: Stark, Doppler and pressure broadening.

The Stark broadening is the result of the coulomb interaction of the absorbing atom with the charged particles present in the plasma and related to Lorentzian distribution.

Due to the high electron density in DC excited atmospheric microplasma, Stark broadening could be important in the present case.

The Doppler broadening is directly related to the gas temperature. It follows a Gauss distribution. The line width $\Delta\nu_{Doppler}$ (FWHM) is linked to the gas temperature through the relation (3.4) ***[Sad-04]:***

$$\Delta\nu_{Doppler}\ [GHz] = 7.16 \times 10^{-7}\ (c/\lambda)\ (T/M)^{1/2} \qquad (3.4)$$

For instance, for an individual Helium 1083 nm line at 300 K, we obtain $\Delta\nu_{Doppler}$ = 1.718 GHz.

Pressure broadening arises from perturbation of the energy levels of the emitting atoms due to the presence of surrounding neutral species. This broadening leads to a Lorentzian

distribution profile. Here, as the experimental number ratio of metastable to normal helium atoms is very small, only the pressure broadening and shift of levels resulting from collisions between the ground He ($1\ ^1S_0$) atoms with He ($2\ ^3S_1$) and He ($2\ ^3P_j$) metastable atoms need to be considered ***[Vri-04]***.

Thus, to calculate the gas temperature inside the MHCD cavity, the absorption line shape can be described by a Voigt function, i.e., a convolution of Lorentzian and Gaussian functions. The main idea is to compare the experimental Voigt profiles of absorption obtained from the TDLAS measurements with the simulated Voigt profiles obtained from the simulations for a considered gas temperature. The Voigt profiles are simulated by taking in account different parameters viz. Doppler broadening, Stark broadening, cavity length, and the evaluated electron density. The electron density used in these simulations was evaluated by Thierry Dufour during his PhD work on alumina based MHCDs ***[Duf-09].*** In figure 3.11 the results obtained by T. Dufour are given, taken from optical emission spectroscopy (OES) by analysing the Stark broadening of the Hβ line. The plot gives the electron density for different pressures and discharge currents.

The estimated gas temperature (T_g) for different He pressures and MHCD currents is given in figure 3.12. This graph presents the comparison of gas temperatures calculated using TDLAS and those obtained by OES. In TDLAS experiments, the gas temperatures are calculated for 350, 500 and 750 Torr and for 5, 10 and 15 mA. In OES experiments, the rovibrational band of the second positive system of N_2 was fitted to evaluate the gas temperature ***[Duf-09]***. He gas temperature was evaluated for 400, 750 and 1000 Torr at different discharge currents up to 15 mA. Note that the OES based gas temperature measurements are taken from T. Dufour PhD studies ***[Duf-09]***. From figure 3.12, it can be seen that the gas temperature increases more or less linearly with current. Gas temperature increases with pressure as also observed in ref. ***[Duf-09]***.

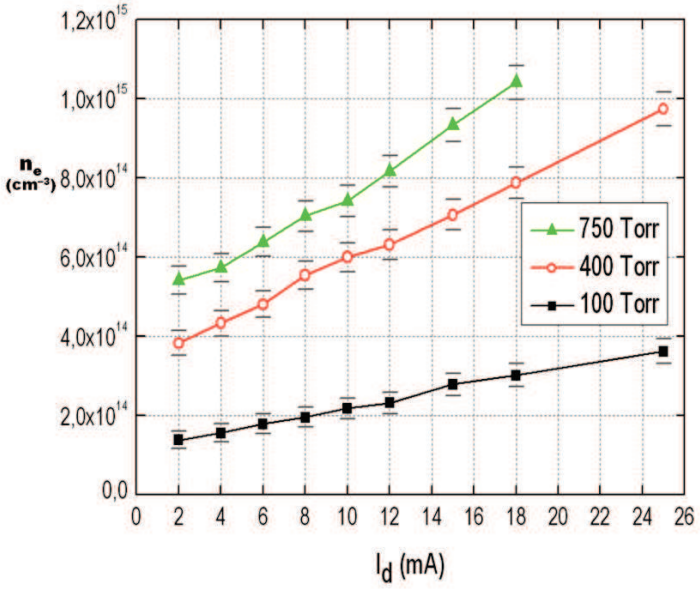

Figure 3.11: Electron number densities versus the operating current for a single hole microdischarge working at 100, 400 and 750 Torr in He. The MHCD cavity diameter is approximately 260 µm.

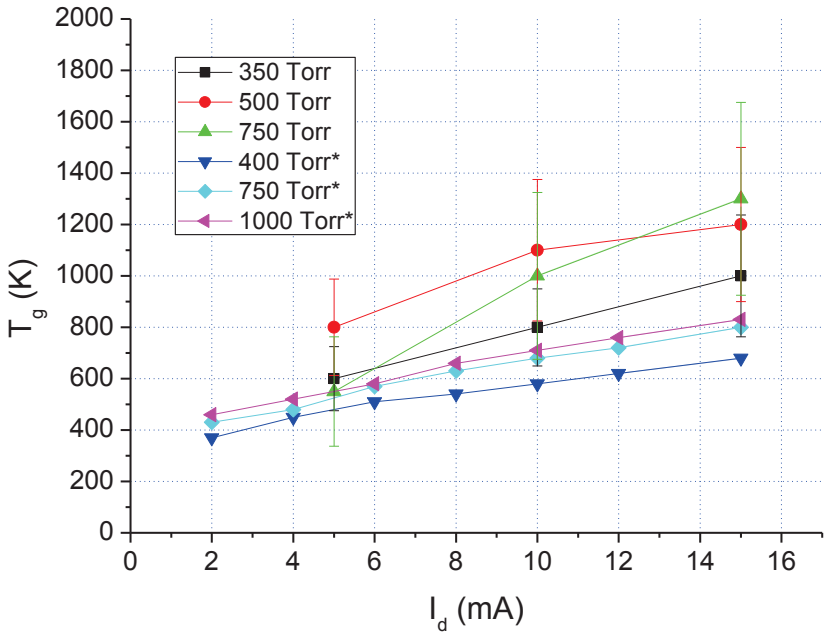

Figure 3.12: Estimated gas temperature of He using TDLAS and comparison with the gas temperature obtained from N_2 rovibrtional spectrum using OES (results are indicated with an asterisk in the legend of the graph) for MHCD.

3.4.3 TDLAS characterisation for ignition and extinction

In this subsection, the TDLAS based characterisations for the ignition and the extinction of the MHCD are presented.

To investigate the ignition and the extinction of MHCD, we first evaluated the width of the absorption profiles for different discharge currents and for two gas pressures 350 and 750 Torr. Then, to evaluate the absorption evolution during the ignition and the extinction, the laser was fixed to the center of the profile line. The MHCD was igniting using a triangular voltage ramp from the power supply.

Assuming a Lorentzian profile, with ν_L (FWHM) in unit of GHz; the density is related to the peak value of ln (I_0/I) when the laser is set at the center of the line profile, and can be given the by relation (3.5):

$$\langle N_i \rangle = \frac{\pi \Delta \nu_L}{2} \frac{1}{l f_{ik}} \, 3.8 \times 10^{14} \, ln\left(\frac{I_0}{I}\right) = \frac{\Delta \nu_L}{l f_{ik}} \, 5.97 \times 10^{14} \, ln\left(\frac{I_0}{I}\right) \qquad (3.5)$$

In this case, the oscillator strength to consider is f_{ik} = 0.48 and using this value in the above equation (3.5), the equation becomes:

$$\langle N_i \rangle = \frac{\Delta \nu_L}{l} \, 1.24 \times 10^{15} \, . l_n \left(\frac{I_0}{I}\right) \qquad (3.6)$$

Here, the mean metastable density is in m^{-3}, l is the absorption length in m**.** A cavity length (l) of 270 µm was used for the calculations. In experiments, a small gas flow of about 15 to 20 sccm was also maintained to renew the gas during operation.

Using the above equation (3.6), metastable densities were estimated for the starting and the ending of the plasma. For this estimation, the values of FWHM $\Delta\nu_L$ were taken from the regular absorption curves (figure 3.9) obtained in the last section with TDLAS experiments for different discharge currents. Table 3.1 shows the calculated FWHM of the absorption profiles obtained using TDLAS experiments for different pressures with their corresponding discharge currents.

Table 3.1: Approximated FWHM of absorption profiles obtained from TDLAS experiment, for different discharge currents at pressures 350 and 750 Torr

Pressure (Torr)	Current (mA)	FWHM (GHz) ± 0.01
350 Torr	5	7.07
	10	6.53
	15	5.76
	20	5.70
750 Torr	5	13.96
	10	9.12
	15	7.69
	20	8.70

Ignition

Figure 3.13 (a) shows the time evolution of the metastable density and the discharge current during the ignition of the microplasma at 750 Torr in He. After breakdown, we observe that the metastable density increases roughly monotonically with a time scale of 40 µs. However, a small peak of metastable density is obtained during the current pulse. Then the plasma switches to the normal regime and the metastable density remains constant at around 1.2 x 10^{18} m^{-3} with a discharge current of around 2.5 mA. A similar behaviour was observed for the 350 Torr pressure with a metastable density of 7 x 10^{17} m^{-3} for a discharge current of around 2 mA. The peak in metastable density could be linked with the current pulse at the starting of the plasma. After this peak, metastable density reached to a stable state within 40 µs. This metastable density stabilisation time could be linked with the thermal effect caused by the variations in gas temperature during the starting of the plasma.

Extinction

Figure 3.13 (b) shows the time evolution of the metastable density and the discharge current during the extinction of the microplasma at 750 Torr in He.

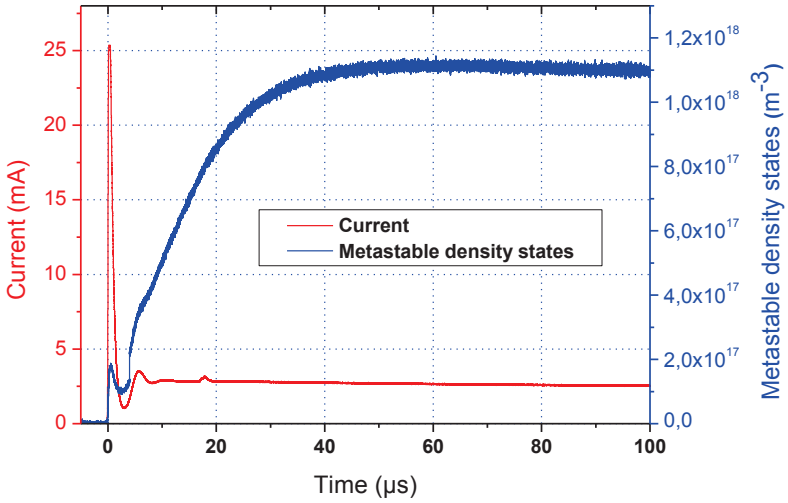

(a)

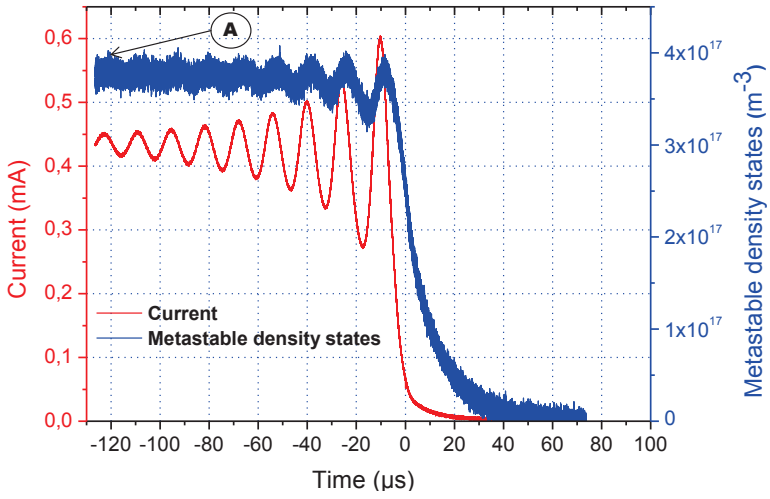

(b)

Figure 3.13: Metastable density states obtained from TDLAS and current vs. time at 750 Torr He for (a) Starting (b) ending of discharges for a MHCD reactor.

The metastable density changes according to the variation of discharge current with a slight delay of 2 µsec. At point A (figure 3.13 (b)), we see the presence of some very low amplitude oscillations in metastable density states with a value of around 4 x 10^{17} m^{-3}. For lower pressures (below 350 Torr), the current decreases to zero smoothly with the extinction of the plasma and hence the metastable density also smoothly decreases to zero from a value of 3 x 10^{17} m^{-3}. In fact the oscillations in the metastable density could be linked with the change in the electron density of the plasma, OR the variations in the metastable densities (and their stabilisation time) could lead to the change in electron density during the plasma operation

near its extinction. But in each case, it is clear that the oscillations seen in the current and voltage curves are caused by the plasma operation inside the micrometric scale cavity.

3.5 Conclusions

In this chapter, we presented and discussed the phenomena related to the ignition and the extinction of alumina based MHCD. For the ignition of the MHCD, a huge current peak of few 10's of mA was observed for each pressure, using electrical characterisations. For the ignition peaks, a typical pulse width of 2 µs was observed. For the extension of plasma, at high pressures, an oscillating behaviour was observed with a time period of few µs. Studies with photomultiplier tube, indicated that these oscillations were not occurring due to the power supplier. Then, the phenomenon of the ignition of the microdischarges was explained by using an equivalent electrical circuit. Then, by using TDLAS experiments, it was discovered that metastable densities change with the variation in currents for the ignition and extinction of the microdischarges. For the ignition, it was found that the discharge current can affect the metastable density. In this case a metastable stabilisation time of 40 µs was observed. Here, the metastable density was on the order of 10^{18} m^{-3}. For the extinction of the discharges, metastable density was found with the oscillating behaviour. By this experiment, it was concluded that the observed oscillations for the extinction of the plasma were the result of the plasma operation inside the microcavity. For the extinction part, a metastable density on the order of 10^{17} m^{-3} was calculated.

With TDLAS experiments metastable densities and gas temperatures were also calculated for different pressures of 350, 500 and 750 Torr in He at different discharge currents for steady state operation of the microdischarges. A typical metastable density on the order of 10^{17} m^{-3} was found. The calculated gas temperature was found varying from 500 K to 1300 K, depending on the gas pressure and the respective discharge current.

Chapter 4

Study of microdischarges on silicon in DC

4.1 Introduction

In this chapter, the results obtained with different arrangements of silicon based microdischarge reactors (MDRs) operating in DC are presented. V-I characteristics for single hole devices, multiple hole arrays and some exotic configurations are presented. Subsequently, other physical characteristics of the arrays (ignition trends, proximity effects etc) are discussed by comparing them for different arrangements. Then a detailed study for failure mechanism of the devices is given.

4.2 Single hole micro discharge

This section presents the results for single hole microdischarge reactors (MDRs). As described in second chapter of fabrication, these MDRs can have cavity diameter varying from 25 µm to 150 µm. By using different etching techniques, one can have isotropic, anisotropic or through hole cavities. For single hole MDRs, deep cavities were preferred for the experiments as shallowly etched cavities with few microns of depth can have a very short life time of typically few seconds. For them, it was very difficult to perform any kind of characterisation.

4.2.1 V-I characteristics for Standard Polarity (SP) and Reverse Polarity (RP)

4.2.1.1 Anisotropic cavity

First, the results of experiments performed on single hole microdischarge reactors consisting of an anisotropic cavity are presented. The single hole microdischarge reactor had a diameter of 150 µm and a depth of approximately 200 µm.

Figure 4.1 shows, the V-I curves obtained in (a) argon and (b) helium for two different configurations: in standard (black line) and reverse (red line) polarity. The gas pressure was 370 Torr in both cases. In inset, pictures of the microdischarges are also shown for each case (SP & RP case for Ar and He) with the corresponding graphs.

In SP case (Figure 4.1), after the breakdown, both discharge current (I_d) and voltage increase with increasing power supply voltage ramp ("abnormal glow" regime behaviour). The discharge current is limited to approximately 0.5 mA while the voltage reaches 320 V for the case of Ar. In this case, current density (J) and power densities (P_d) can be easily evaluated by considering the MDR cavity as a cylinder. The values were found 0.38 $A.cm^{-2}$ and 45 $kW.cm^{-3}$ respectively for J and P_d. In the case of He, after breakdown, the discharge current is limited to 0.7 mA approximately, while the voltage increases to around 320 V. For He, the approximated J and P_d were 0.54 $A.cm^{-2}$ and 63 $kW.cm^{-3}$ respectively. In addition, the discharge remains inside the cavity in SP case, as shown in inset pictures of the corresponding graphs.

In contrast, during the operation in RP, the V-I curves show that the discharge voltage increases much less in reverse polarity and the curves follow an almost "normal glow" regime behaviour. The inset pictures show that the plasma is spreading out over the cathode (nickel) electrode. In the case of Ar, we can clearly see the diameter of the hole which appears brighter. J and P_d for maximum discharge current (~ 2.4 mA) were found 1.80 $A.cm^{-2}$ and 189 $kW.cm^{-3}$ respectively. In the case of He, I_d reaches 2.6 mA (maximum value) with a voltage of 230 V approximately. For He, the approximated value of J and P_d were 2.00 $A.cm^{-2}$ and 169 $kW.cm^{-3}$ respectively.

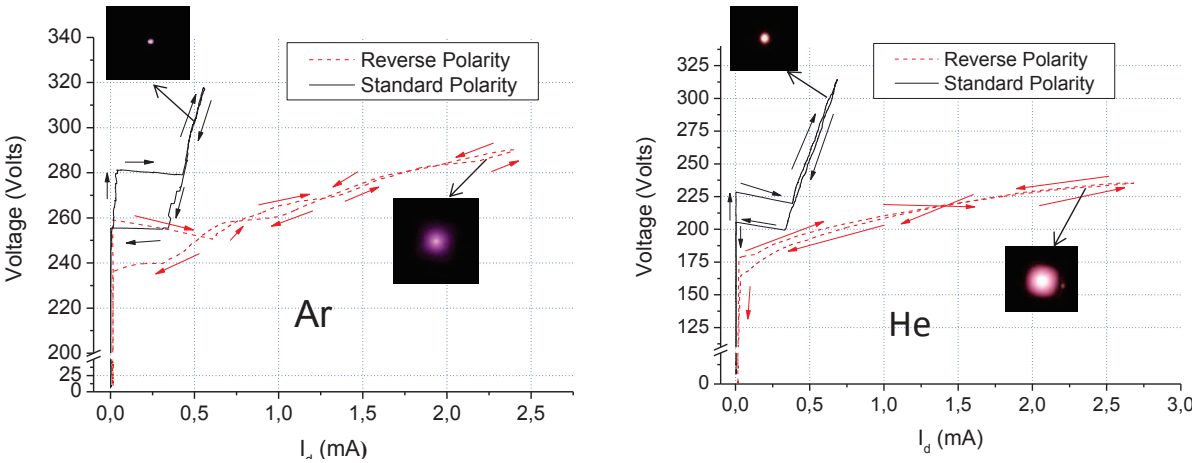

Figure 4.1: VI-characteristics for single hole microreactor of 150 µm hole diameter (~ 180 µm deep anisotropic cavity) (a) in argon (Ar) and (b) in helium (He), at 370 Torr in both standard and reverse polarities.

During the experiments, current and voltage spikes were systematically observed in the SP configuration. Those spikes were not obtained in reverse polarity. These spikes are discussed later in this chapter. In figure 4.1, the curves are presented after having indirectly removed these spikes by applying an adjacent averaging smoothing technique to improve the readability of the graph, (and this is the case for most of the V-I characteristics presented in this chapter). More precisely, the adjacent averaging smoothing was first performed individually on the current and voltage waveforms, and then the averaged data were used to plot the V-I curves. This method of averaging was chosen, because the current and voltage spikes were found in both directions of the Y-axis. Thus, this type of adjacent averaging improved the readability of the graphs.

4.2.1.2 Isotropic cavity

Figure 4.2 shows the V-I characteristics of SP and RP cases for a single isotropic hole micro-reactor (50 µm diameter, 150 µm deep). The experiment was performed in He at 750 Torr.

In SP case (shown in figure 4.2 black line), similar to anisotropic case, after breakdown, the V-I curve follows a slight abnormal regime. Both current and voltage increase with increasing power supply voltage. Similar to the anisotropic cavity case, the discharge remains inside the

cavity in SP. To study the ignition behaviour of single hole microdischarges in SP case, continuous images using an ICCD camera were taken during the plasma operation. Figure 4.3 shows a plot of the microdischarge intensity versus discharge current in a 50 µm diameter single hole MDR. The intensity was calculated by considering the MDR hole and plasma spread region as a square. Then intensity of this square area was integrated to get a total normalised intensity of the area. Inset pictures with this plot show the ICCD images for single hole MDR at the plasma ignition, at the peak point of plasma ignition, and at the ending of the plasma for 4.84, 6.04, and 3.40 mA discharge currents respectively. In figure 4.3, it can be clearly seen that the discharge remains almost inside the cavity during the glow regime. For the calculations of J and P_d, the isotropic cavity was considered as a hemisphere with a radius of 75 µm. For the peak value of discharge current (6.5 mA, 300 V), the approximated J and P_d values were 18.41 A.cm^{-2} and 2208 kW.cm^{-3} respectively.

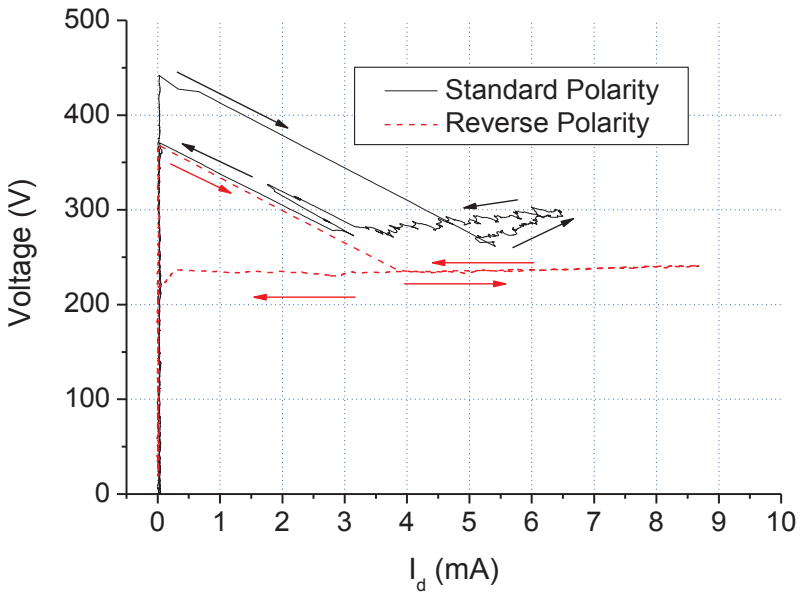

Figure 4.2: V-I characteristics for a single hole micro-reactor of 50 µm hole diameter (~150 µm deep isotropic cavity), in helium at 750 Torr.

In RP case, similar to the anisotropic case, the current increases after the breakdown at constant voltage and follows a "normal glow" regime behaviour. The discharge current and the total plasma intensity including the emission from its spread area were plotted in figure 4.4. The experiment was carried out in He at 750 Torr in a 50 µm diameter microdischarge reactor. A 150 µm deep isotropically etched cavity was used. A series of ICCD images are also shown in inset of the figure, for some values of discharge current. At around 3.80 mA the spread area is about 6 x10^{-3} cm^2. In this image, it can be clearly seen that the surrounding glow emits weakly around the cavity. In this case, at I_d = 8.52 mA, J and P_d were found to be equal to 24.13 A.cm^{-2} and 2219 kW.cm^{-3} respectively. At this value, the plasma spread area is 8 x 10^{-3} cm² high. In figure 4.4, it can be clearly seen that the glow spreads outside the microdischarge cavity. At minimum value of discharge current (1.08 mA) and just before the plasma extinction, we see very low plasma intensity, concentrated inside the MDR hole.

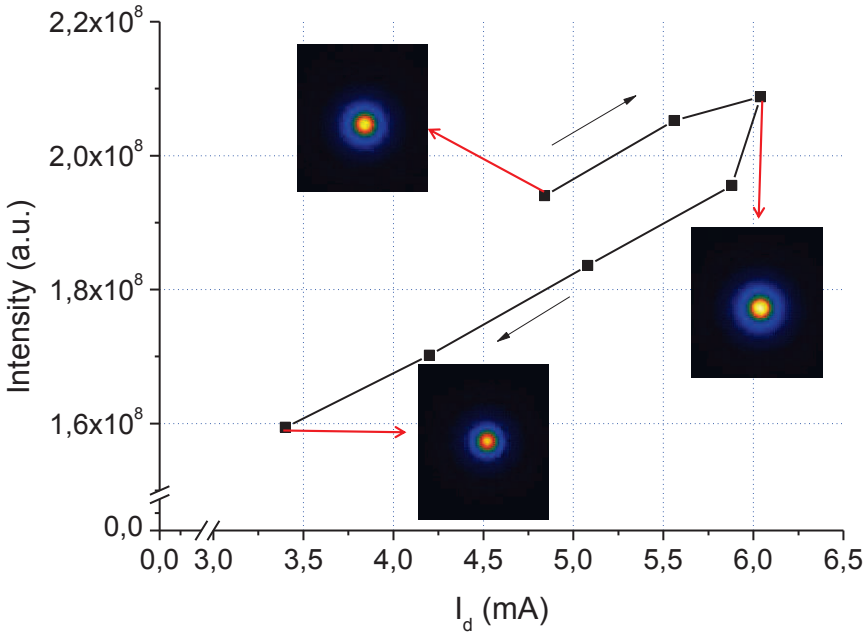

Figure 4.3: Intensity vs. discharge current (I_d) plot of microdischarge for a single hole MDR in SP case (50 µm diameter and ~150 µm deep isotropic cavity) at 750 Torr in He. Inset ICCD images show discharge operation of MDRs near the ignition, peak and ending points. (Note: the images have false colour).

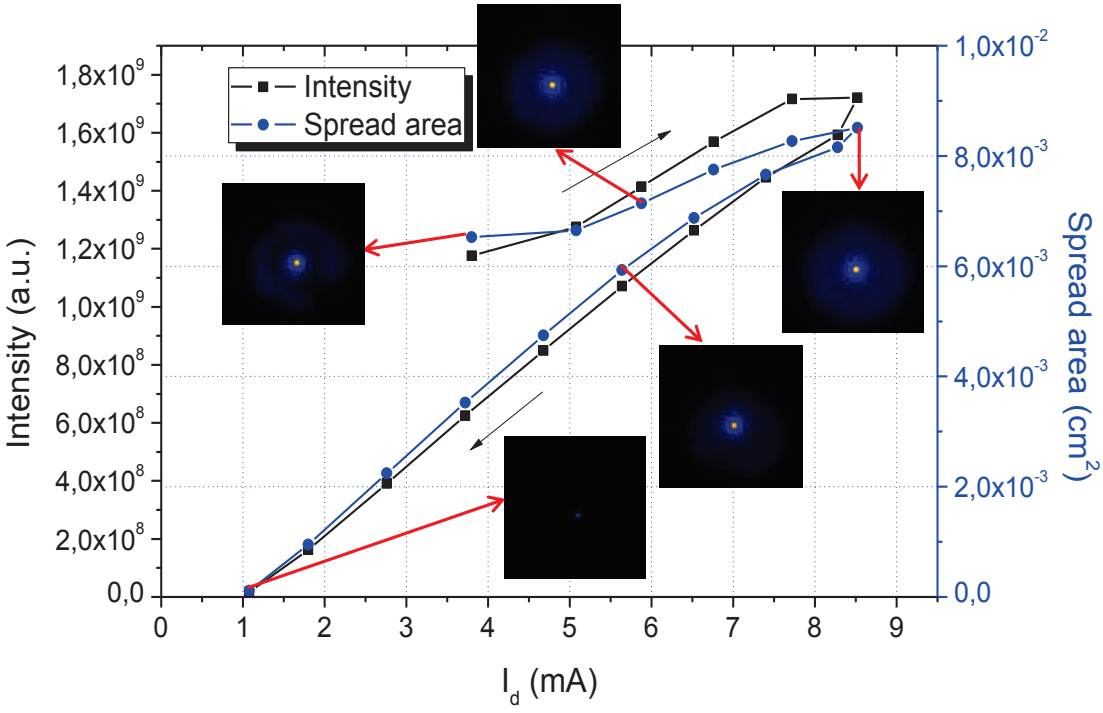

Figure 4.4: Intensity and respective plasma spread area vs. discharge current for a single hole microdischarge reactor (50 µm diameter and ~150 µm depth isotropic cavity) in He at 750 Torr operating in RP. Inset: ICCD images in RP taken at different values of current (Note: the images have false colour).

As observed in figure 4.4, the total plasma intensity curve follows the discharge current. Figure 4.5 (a) shows the relationship between the plasma intensity and the calculated plasma spread area. It can be seen that the plasma intensity varies linearly with the spread area for both increasing and descending current ramp. Also, current densities related to the plasma spread area were calculated as shown in the figure 4.5 (b). From this graph, it is clear that current density remains constant with the plasma spread area. Note that, in this graph, the data points near to the plasma ignition and extinction are not shown.

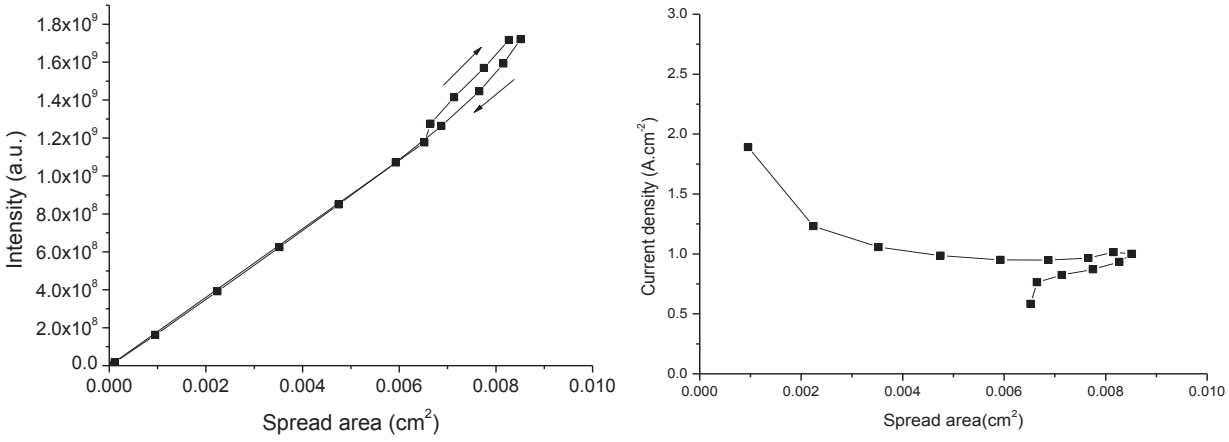

Figure 4.5: (a) Plasma spread area vs. normalised intensity of the area and (b) current density of the microdischarge vs. plasma spread area.

To summarise, the analysis of V-I curves and the ICCD images show the increase of current with the plasma spread on the cathode surface. If we divide the discharge current by the plasma spread area, we obtain a quite constant current density, which is consistent with the normal glow regime.

4.2.1.3 Through hole cavity

This subsection presents the V-I characteristics of a single hole microdischarge reactor having a through hole cavity from anode to cathode. In this case, anisotropic etching was performed using the so-called STiGer process by drilling a straight through hole in the 500 µm thick Si surface. Deep reactive ion etching (DRIE) technique was used at -110 ºC, as explained in the second chapter. The etching was performed for 120 minutes to obtain silicon through hole in the substrate. The diameter of the cavity was 150 µm. Figure 4.6 presents V-I characteristics of the through hole microdischarge in He at 200 Torr in SP and RP. In SP case, the current follows a normal glow regime behaviour. Again, the current rises at a constant discharge voltage. This curve is similar to the one obtained with the isotropic cavity microdischarge operating in RP (figure 4.2). The discharge can spread over the cathodic surface (i.e. silicon surface). Here, the discharge current I_d rises up to the approximate value of 6.5 mA with a voltage of 225 V. Thus, by considering this cavity as a cylinder, the current density and the power density were calculated and were equal to 2.4 $A.cm^{-2}$ and 165 $kW.cm^{-3}$ respectively. In RP case, the V-I curve also follows an almost “normal glow” regime as in the previous case.

In both SP and RP cases for this through hole sample, a current was flowing through the device before breakdown and no plasma could be seen. This leakage of the current was caused due to the microscopic holes present in the SiO_2 layer. These holes were the result of treating the SiO_2 layer with strong HF solution, as explained in the chapter 2.

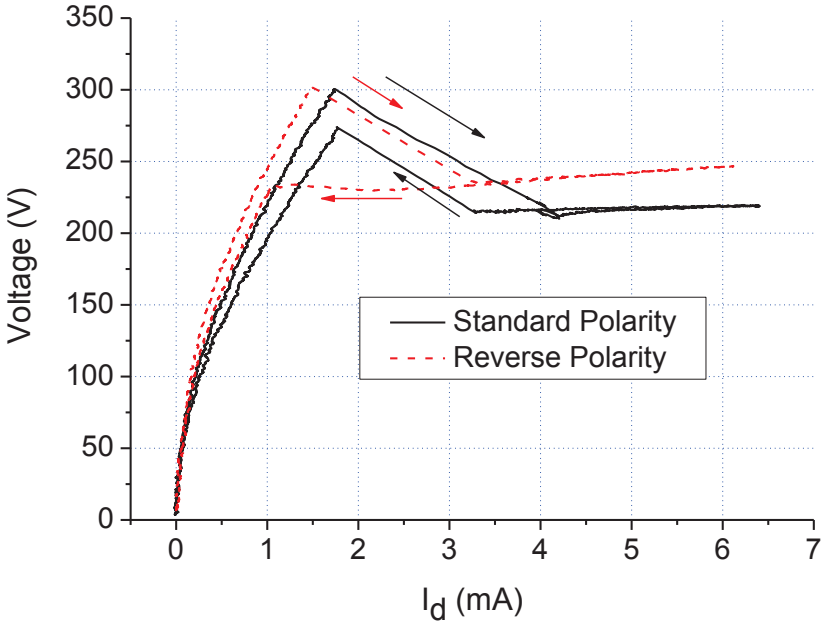

Figure 4.6: VI-characteristics for a 150 µm diameter single through hole micro discharge operating in helium gas at 200 Torr.

4.2.1.4 Discussion for single hole devices

In fact, the behaviour of the V-I curves obtained with our devices can be explained with the help of figure 4.7. In SP case (figure 4.7 (a)), the cathode area is limited since the silicon cavity which corresponds to the cathode is closed. In this case, discharges cannot expand on the cathodic area with the increase of current. Hence, "abnormal glow" regime is obtained for SP case as explained in ref ***[Duf-08]***. In the isotropic case (figure 4.2), the same phenomenon appears. The only difference that can be noticed is the surface area, which is greater for the isotropic case so that a slightly higher current can be reached. The interelectrode distance is also larger in the isotropic case.

The case of through hole cavity is different (figure 4.6). In this case, the discharge is no more limited by the closed cathodic cavity. Thus the discharge can expand on the cathode surface outside the cylindrical cavity and provide a behaviour similar to the case of RP as explained in next paragraph.

Figure 4.7 (b) shows the behaviour of plasma for RP case. In RP, the cathode area is not limited. The microdischarge can spread over it, while the current increases without requiring an increase of the current density at the cathode side. As a result, a normal glow regime is obtained ***[Iza-08, Duf-08]***.

Sometimes, the plasma spread on the nickel cathode was also limited by the photoresist boundary in the RP case and was providing a limited cathode area as well. One example of

this case can be seen in figure 4.1 (a) and (b) in the RP case. In this case, a slight increase of the discharge voltage was obtained.

In isotropic case (figure 4.2), the photoresist layer had been removed by using acetone before operating the MHCD. Thus, in this case, the plasma could expand out of the cavity without any surface limitation, this is why we could observe a perfect normal regime, where current increases at constant discharge voltage (shown in figure 4.2 for RP case).

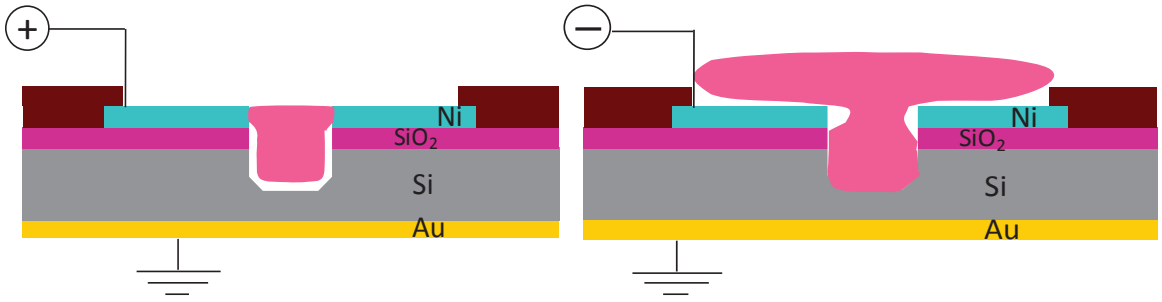

(a) (b)

Figure 4.7: Behaviour of microdischarges in (a) Standard Polarity (SP) and (b) in Reverse polarity (RP).

4.2.2 Breakdown (V_{br})

The study of breakdown voltage (V_{br}) for different single hole configurations has been performed by considering the V-I characteristics as discussed in previous paragraphs. The influence of different parameters viz. pressure, cavity shape, and cavity depth and polarity configuration has been studied.

4.2.2.1 Effect of polarity and gas type

From figure 4.1 and figure 4.2, it can be noticed that the breakdown voltage is higher in the SP case (225 and 440 V for He) than in the RP case (175 and 360 V for He). However, in figure 4.3, the breakdown voltage in both cases seems to be the same. In general, it is found that the breakdown voltage is higher for the SP configuration as compared to the RP one. Nevertheless, sometimes, an opposite behaviour could also be observed, in which the breakdown voltage in RP was higher than in the SP case. Figure 4.8 shows such an example. It corresponds to a 100 µm diameter and 150 µm depth single anisotropic cavity. Microdischarges in this case are operating in He at 500 Torr. From the V-I characteristics shown in figure 4.1, it can be seen that the breakdown voltage is higher in argon than in helium ***[Kul-12]***.

The polarity inversion not only changes the geometric configuration of the discharge, but also changes the cathode material. The main factor responsible for the change in the breakdown voltage seems to be the cathode surface material. It is well known that the cathode material and the electrode topography both affect the breakdown voltage ***[Sch-12]***. Also, sometimes non-uniform cavity etching or cavity defects can lead to a change in the breakdown voltage in the MDR devices ***[Sch-12]***.

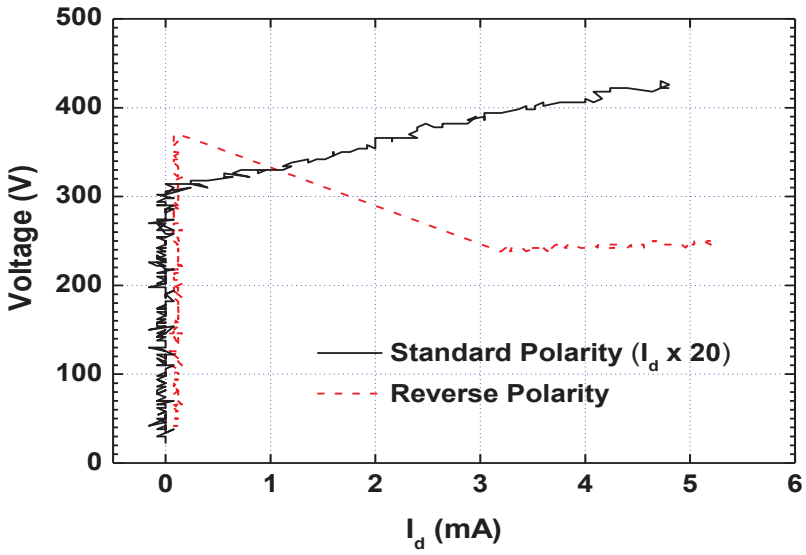

Figure 4.8: V-I characteristics for a single hole microdischarge reactor operating in He at 500 Torr (100 µm diameter and 150 µm deep anisotropic cavity) for both reverse (red dashed line) and standard (black solid line) polarities.

In fact, the secondary emission coefficient γ of the material has a significant impact on the breakdown voltage ***[Nad-96]***. The surface roughness of the nickel layer and silicon cavity also influence the electron emission and consequently the breakdown voltage. Indeed, the cathode surface topography evolves with operation time and can give results different from the very first experiments. A rough surface of a used micro reactor can enhance the emission of electrons from the cathode surface through field emission, thus reducing the breakdown voltage.

To summarise, V_{br} is usually higher when the cathode corresponds to the silicon side and it is also higher in Argon than in Helium for a same pressure.

4.2.2.2 Effect of pressure

In this part, the effect of gas pressure on the breakdown voltage is shown. The V-I characteristics have been obtained for pressures ranging from 100 to 1000 Torr.

Cavity diameter

First, results showing the effect of the pressure on the breakdown voltage for two single holes having different cavity diameters (100 and 150 µm) are given. The experiment was carried out with 150 µm deep anisotropically etched cavities. Figure 4.9 shows breakdown voltages versus pressure for two different cavity diameters (100 and 150 µm) in the Standard Polarity.

As observed in this graph, a higher breakdown voltage is necessary for the 100 µm diameter MDR compared to the 150 µm diameter MDR. This was the case for both SP and RP configurations. The graph for each cavity follows a Paschen like curve. Note that in our case, it is difficult to determine the interelectrode distance (d) since we do not use parallel plate electrodes. So, the graphs show breakdown voltage with respect to the pressure.

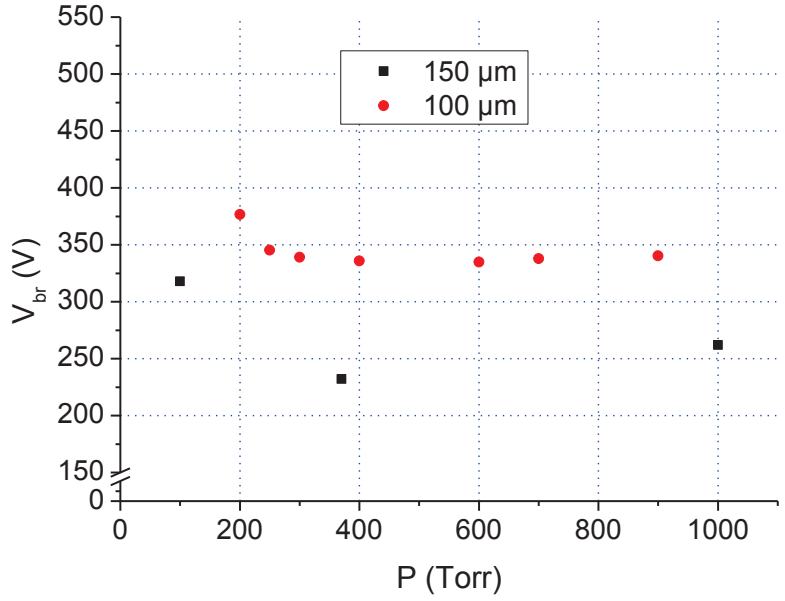

Figure 4.9: Breakdown voltage (V_{br}) vs. pressure for different diameters: 100 µm and 150 µm for a single hole microdischarge reactor in SP case.

Cavity depth

In this part, the effect of the cavity depth on the breakdown voltage is discussed. Figure 4.10 shows the graph of the breakdown voltage versus pressure for two different cavity depths. 150 µm diameter single hole MDRs were used. The cavities were anisotropically etched. For one MDR, the cavity was closed and etched down to ~ 180 µm. For the other MDR, the sample was etched through the silicon (~ 500 µm). From figure 4.10, it can be seen that there is no big difference between the breakdown voltages of the through hole cavity and of the 180 µm deep limited cathode cavity.

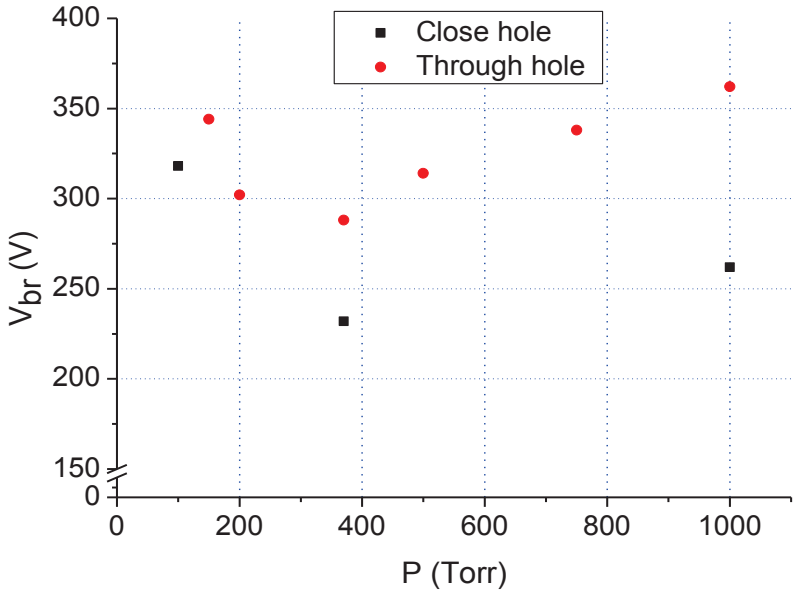

Figure 4.10: Breakdown voltage vs. pressure for different cavity depths (L) of 180 µm and 500 µm (through hole), for single hole devices with 150 µm diameter in SP case.

4.2.3 Hysteresis

In this section, the effect of hysteresis is presented for single hole MDRs. In our experiments, we can observe two different types of hysteresis effects. The first one is obtained between the Townsend regime and the normal glow. It is observed at low pressure in DC discharge experiments: when decreasing the current, the discharge maintains itself in glow regime to a point at considerably lower value and only then makes a transition back to the Townsend regime ***[Rot -95]***.The second one was observed by Thierry Dufour in limited cathode area experiments. In abnormal glow regime, when decreasing the current, the discharge voltage was found higher than the one obtained by increasing the current ***[Duf-08]***.

Figure 4.11 shows V-I characteristics for single hole MDR of 50 µm hole diameter (~ 150 µm deep isotropic cavity) in helium, at 300 Torr in both standard and reverse polarities. This graph shows the two types of hysteresis effects. In the RP case, the curve shows a behaviour similar to the first type of hysteresis. In this case, breakdown voltage is higher with a value of around 325 V as compared to the voltage near to the plasma extinction point (~225 V). In SP case, the second type of hysteresis effect can be seen. In this case, after breakdown, the discharge voltage increases with current and the hysteresis curve follows an anticlockwise direction. Similar kind of hysteresis effect was observed in other types of single hole MDRs (e.g.: anisotropic cavity, through hole cavity…).

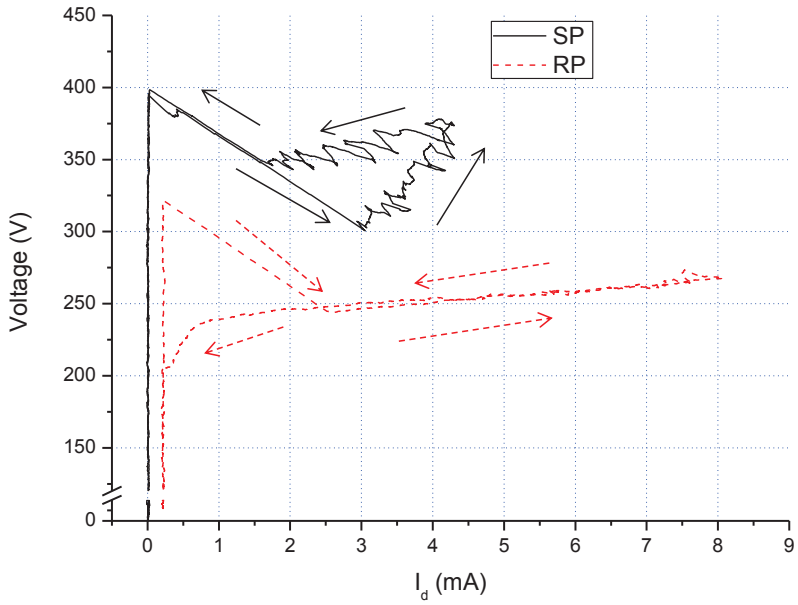

Figure 4.11: VI-characteristics for a 50 µm diameter single hole microreactor of (~ 150 µm deep isotropic cavity) in helium at 300 Torr in both standard and reverse polarities.

As explained in ref. ***[Duf-08],*** the V-I slope between the breakdown voltage and the operating discharge voltage depends on the ballast resistor. Thus the first hysteresis effect observed in our curves depends on the ballast resistor. The second type of hysteresis could be due to the gas heating, enhanced by the limited cathode area. According to T. Dufour ref. ***[Duf-08]***, by reducing the operation time to 1 s, the hysteresis becomes much weaker during the first cycles. Hysteresis might also be attributed to a thermal relaxation time or other slow

processes. A thermal relaxation time will depend on the thermal conductivity of the gas and of the microdevice material ***[Duf-10]***.

4.2.4 Simulations

Simulations for a single hole MDR were performed in collaboration with the team of L. Pitchford, in the Laplace laboratory at Toulouse. These simulations were carried out by Laurent Schwaederlé, a former post-doctorate researcher of our team. Similar types of simulation studies were performed by our group for the Alumina based samples within the PhD work carried out by Thierry Dufour ***[Duf-09]***.

The modelling of micro-plasmas can follow two approaches, which differ in how to calculate the source terms of electrons and ions. The first one is a hybrid approach (fluid and Monte Carlo) that uses first three equations of Boltzmann (conservation of particles, conservation of momentum and conservation of energy) and a Monte Carlo simulation to determine the source term. The second approach consists of using a fluid model. This approach was selected for these simulations. This fluid model approach was used because it is fast and it allows understanding the main trends involved in microdischarges. The simulations were performed with the software GDSim (Glow Discharge Simulation), developed by J.P. Boeuf and L. Pitchford ***[Boe-95]***.

4.2.4.1 Description

The model used in this study was a 2 dimensional (axisymmetric) self-consistent multi-fluid model in the drift-diffusion approximation. Moreover, due to high power densities (100's $kW \cdot cm^{-3}$), gas heating effects are expected to be important in microdischarge. For the model, different equations were used.

- The equation of continuity for ion and electron densities of all the species

$$\begin{cases} \dfrac{\partial n_e}{\partial t} + \vec{\nabla}\left(\vec{\Gamma}_e\right) = S_e \\ \dfrac{\partial n_i}{\partial t} + \vec{\nabla}\left(\vec{\Gamma}_i\right) = S_i \end{cases} \qquad (4.1)$$

where, n_e and n_i are the electron and the ion density respectively, $\overrightarrow{\Gamma_p}$ is the drift-diffusive flux density of species p and S_p is the gas-phase species generation rate.

- The equation of conservation of momentum in the drift-diffusion coefficient approximation

$$\begin{cases} \vec{\Gamma}_e = -n_e \mu_e \vec{E} - D_e \vec{\nabla} n_e \\ \vec{\Gamma}_i = +n_i \mu_i \vec{E} - D_i \vec{\nabla} n_i \end{cases} \qquad (4.2)$$

where, μ_p and D_p are the mobility and diffusion coefficient (transport coefficients) of the species p.

- The equation of conservation of energy for electron mean energy

$$\frac{\partial}{\partial t}(n_e.\varepsilon_e)+\vec{\nabla}.\Gamma_{\varepsilon,e}+\frac{2}{3}n_e\varepsilon_e\vec{\nabla}.\vec{v}+\vec{\nabla}\vec{q}=S_{\varepsilon,e} \qquad (4.3)$$

With heat flux $\overrightarrow{q_e} = -\frac{2}{3}k\,\vec{\nabla}\epsilon_e$, where $k = \frac{5}{2}n_eD_e$

- The Poisson's equation for self-consistent electrical potential in the discharge

$$\nabla.V = -\frac{e}{\epsilon_0}(n_i - n_e) \qquad (4.4)$$

- The heat equation for the calculation of gas temperature.

$$\frac{\partial(\rho c_v T_g)}{\partial t}-\vec{\nabla}\kappa\vec{\nabla}T_g = H \qquad (4.5)$$

where, H is the power deposited in the gas by electrons and ions.

More details about the model can be found in the references ***[Boe-95, Duf-10, Duf-09]***.

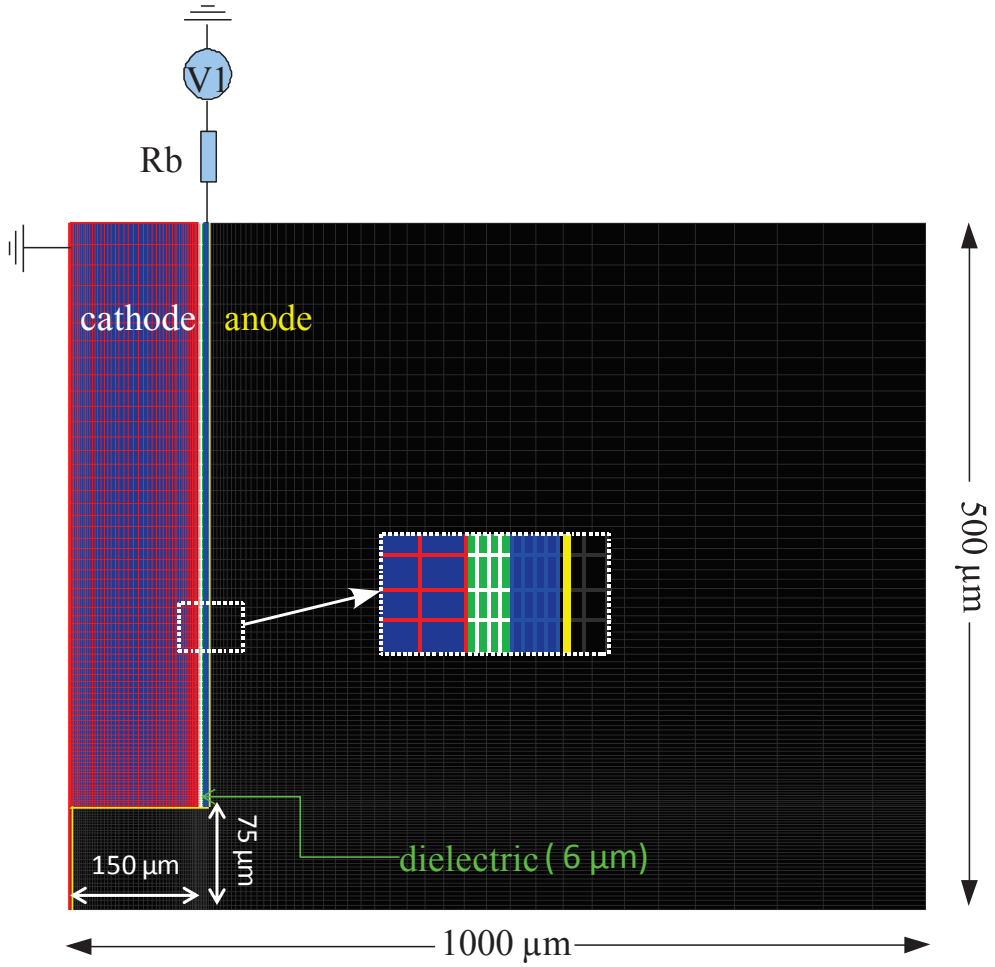

Figure 4.12: Scheme of the simulated microdischarge reactor cavity geometry and the computational grid.

The computational domain is shown in figure 4.12 for the simulated microdischarge reactor cavity geometry. It is 500 µm wide in the radial direction and has 1000 µm length along the axial direction. The model equations were solved in an axisymmetric cylindrical cavity with a non-uniform rectangular numerical mesh. As shown in figure 4.12, the resolution was adapted to the regions of the computational domain with a fine mesh in the regions of interest: i.e. the cavity. The differential equations were spatially solved using a finite volume technique. Few assumptions were made for these simulations as given below:

(1) The continuum assumption required for the fluid approach is supposed to be valid, which is reasonable taking into account the operating pressure range (100's Torr) and the dimensions (~100 µm). At 500 Torr and 300 K, the electron mean free path in helium is on the order of few micrometers, which is smaller than the gradient length scales of the discharge. The simulations were performed for a microdischarge diameter of 150 µm.

(2) The electron transport coefficients and the rate coefficients of electron impact reactions are assumed to be function of the local electron average energy, which requires the solving of the electron mean energy balance equation.

(3) In normal polarity, the silicon cathode is considered as a perfect conductor in the simulations.

(4) In the heat transport model, the source term is due to the heat deposited locally by ions in the sheath. The fraction of the deposited power is assumed to be 25 %. The gas heating source term includes both ion and electron currents, but the ion contribution is by far dominant. Computing the gas heating caused by ion current in the sheath would require a Monte Carlo simulation of the ions and of the fast neutral species in the sheath. This estimation of 25% is given by Revel et al. ***[Rev-00]***, who showed that, in the case of a glow discharge in argon over a range of conditions, 75% of the total ion energy in the cathode sheath is deposited directly at the cathode and 25% is converted to gas heating in the sheath. In addition, the cathode and dielectric surfaces were assumed to be at a constant temperature of 300 K. A thermal boundary layer is included as a boundary condition in the calculation ***[Ser-97]***.

The transport coefficients and rate coefficients for helium were determined by using the solver BOLSIG+, which solves the Boltzmann equation from collision cross-section data ***[Hag-05]***. Afterwards, the source terms S_e, S_i and $S_{\varepsilon,e}$ were solved with the solver GDSim using the data obtained from the solver BOLSIG+. For electron transport, the secondary electron emission from the surface by ion and metastable impact was taken into account. The secondary electron emission coefficient was set to $\gamma+ = 0.25$ for ions and $\gamma^* = 0.15$ for metastables. For electric potential, an electric circuit was implemented in the model which incorporated the series ballast resistor (R_b = 39 kΩ) between the supply voltage and the cathode. A constant DC voltage was applied. The voltage at the electrode surfaces was determined by the current flow through the discharge and the Ohms law. Different current levels can be established in the discharge by changing either the ballast resistance or the supply voltage.

4.2.4.2 Plasma chemistry

For simulations, pure helium plasma was considered. Six different species are considered for this model: electrons (e), helium ions (He+), metastable helium atoms (He*), dimer ions (He_2^+), dimer metastable atoms (He_2*) and the background helium atoms (He). As shown in Table 4.1, pure helium high-pressure reaction mechanisms were used ***[Kot-05]***. Included reactions were direct electron impact ionisation (1), stepwise ionisation (2 and 3), direct electron-impact excitation (4), metastable quenching (5), dissociative recombination (6), Penning ionisation (7), three-body conversion of metastables (8) and ions (9) to corresponding dimers. More details about the reactions can be found in the reference ***[Kot-05]***.

Table 4.1: Pure helium plasma chemistry in the present study.

S.No.	reaction
	electron impact ionisation
(1)	$e + He \rightarrow He^+ + e + e$
(2)	$e + He^* \rightarrow He^+ + e + e$
(3)	$e + He_2^* \rightarrow He_2^* + e + e$
	electron impact excitation
(4)	$e + He \rightarrow He^* + e$
	metastable quenching
(5)	$e + He^* \rightarrow He + e$
	dissociative recombination
(6)	$e + He_2^+ \rightarrow He^* + He$
	Penning ionisation
(7)	$He^* + He^* \rightarrow He^+ + He + e$
	three-body collisions
(8)	$He^* + He + He \rightarrow He_2^* + He$
(9)	$He^+ + He + He \rightarrow He_2^+ + He$

4.2.4.3 Results and discussions

The simulations were performed by considering 500 Torr He pressure in a 150 µm diameter MDR . The dielectric layer and the top electrode were both 6 µm thick. Microdischarges in 70

and 150 µm deep cavities were simulated. Here, only the results for 150 µm deep cavity are presented. In the simulation, the cathode was kept at 0 V and the anode voltage was varied from 200 to 500 V. The initial electron density was 10^{-4} cm^{-3}, which is the minimum necessary value to start the ionisation of the gas. With a 39 kΩ ballast resistor in standard polarity and for I_d = 1.2 mA, the discharge voltage was 150 V; and for I_d = 5.3 mA, the discharge voltage was 188 V.

I_d = 1.2 mA

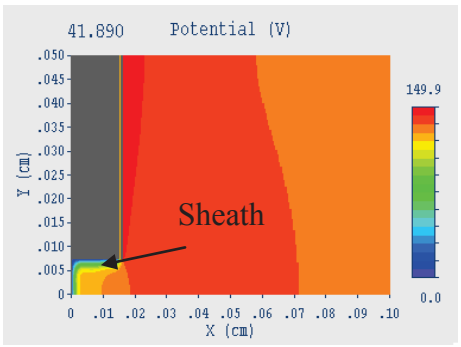

(a)

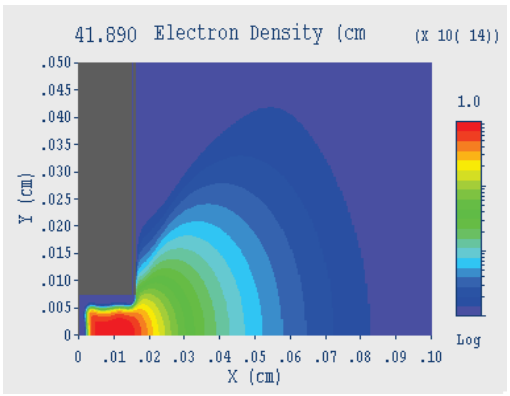

(b)

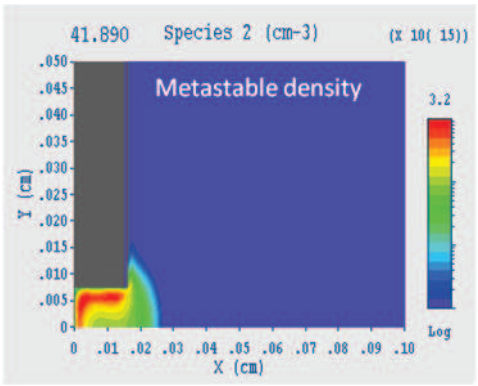

(c)

I_d = 5.3 mA

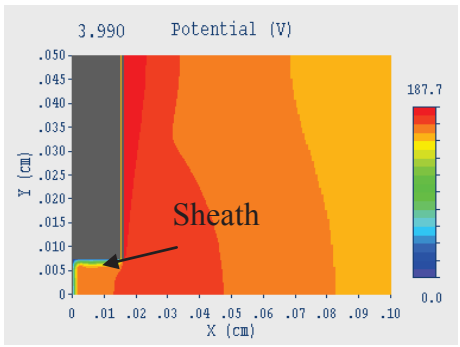

(a1)

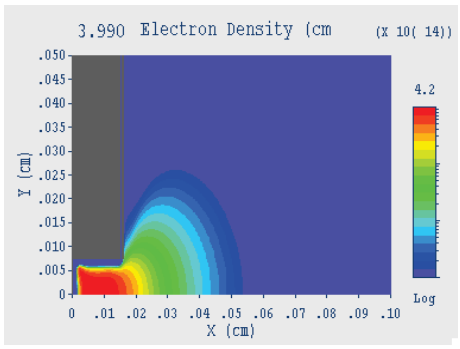

(b1)

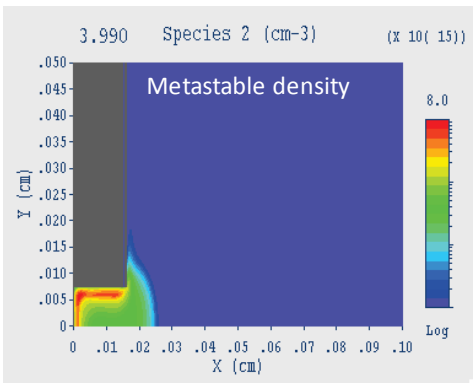

(c1)

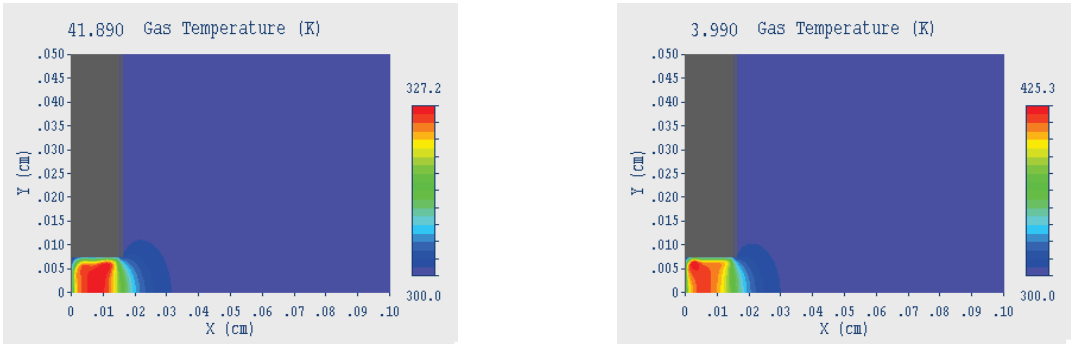

(d) (d1)

Figure 4.13: Simulation results for 150 µm deep cavity with 150 µm cavity diameter at 500 Torr He; (a) and (a1) Potential distribution, (b) and (b1) Electron density distribution, (c) and (c1) Metastable density distribution, (d) and (d1) Gas temperature distribution for I_d of 1.2 and 5.3 mA respectively.

Figure 4.13 shows the comparison of GDSim simulation results for two currents. From figure 4.13 (a) and (a1), the formation of discharge sheath can be seen as indicated. It can be seen that the sheath area is wider for I_d = 1.2 mA than for I_d = 5.3 mA. The maximum of the electron density (figure 4.13 (b) and (b1)) is on the order of 10^{14} cm^{-3}. For I_d = 1.2 and I_d = 5.3 mA, the maximum electron density reaches to 1.0 x 10^{14} and ~ 4.2 x 10^{14} cm^{-3}. The metastable density (species 2 in figure 4.13 (c) and (c1)) is on the order of 10^{15} cm^{-3} in both cases. Gas temperature has a maximum value of 325 K for I_d = 1.2 mA and 425 K for I_d = 5.3 mA (figure 4.13 (d) and (d1)).

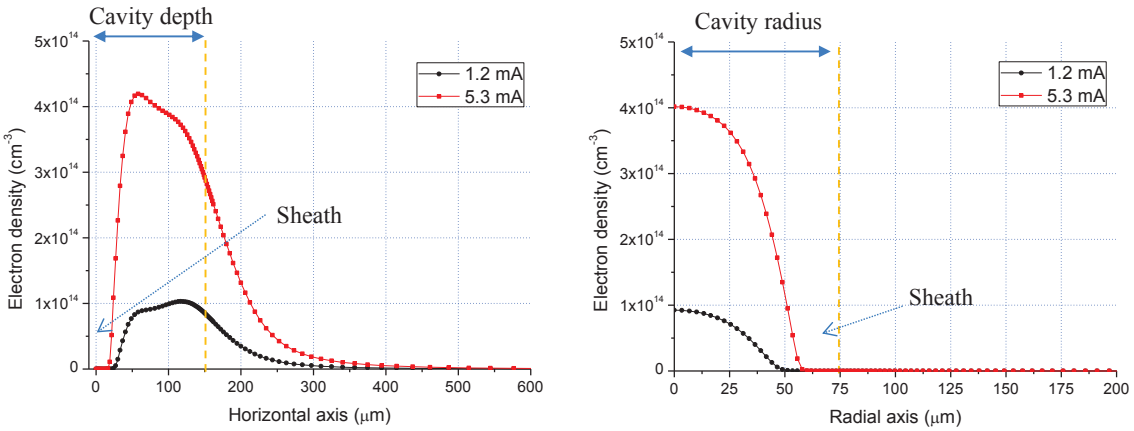

(a) (b)

Figure 4.14: Electron density for 1.2 and 5.3 mA discharge currents, (a) along the longitudinal axis and (b) along the radius of the cavity at the middle of its depth.

The electron density profiles along the longitudinal axis and along the radius of the cavity are shown in figure 4.14 (a) and (b) respectively. As observed in figure 4.14 (a), for I_d = 5.3 mA, the electron density starts to increase sharply at x = 18 µm, which gives an idea of the sheath thickness. The maximum of the electron density is reached at x = 60 µm. Along the radius,

(figure 4.14 (b)), the electron density reaches its maximum value near the center of the cavity. In this case, the sheath thickness is also equal to 18 µm along the radius at the middle of the cavity. A similar trend is observed for I_d = 1.2 mA, with an approximate sheath thickness of 27 µm.

In fact, the reduction in the sheath thickness at higher current can be explained on the basis of matrix collisional sheath ***[Lie-05, Rot-95]***. The thickness of matrix collisional sheath can be expressed as:

$$S = \sqrt{\frac{2.\varepsilon_0.V_s}{e.n_i}} \qquad \textbf{(4.6)}$$

where ε_0 is the dielectric permittivity of vacuum, Vs is the voltage drop at the sheath, e is the electron charge, and n_i is the ion density. For a particular gas pressure, the thickness of collisional sheath as a function of reduced ion mobility can be expressed as:

$$S = \frac{2\mu_i}{v_i}.V_s \qquad \textbf{(4.7)}$$

where μ_i is the reduced ion mobility and V_i is the velocity of the ions at a given pressure. If A is the area of the cylindrical cavity and γ_{se} is the coefficient of secondary ions emission then the discharge current can be written by using equations (4.6) and (4.7):

$$I_d = A.\left(\frac{2\varepsilon_0 V_s}{S^2}\right).\left(\mu_i \frac{2V_s}{S}\right).(1+\gamma_{se}) \qquad \textbf{(4.8)}$$

Using this equation (4.8) sheath voltage as a function of sheath thickness can be given by the equation (4.4):

$$V_s = \sqrt{\frac{I_d.S^3}{(4.\varepsilon_0.\mu_i.A).(1+\gamma_{se})}} \qquad \textbf{(4.9)}$$

From this relation sheath thickness (S) can be expressed as a relation of sheath voltage (V_s) and discharge current (I_d):

$$S = \left[\frac{V_S^2}{I_d}.(4.\varepsilon_0.\mu_i.A).(1+\gamma_{se})\right]^{1/3} \qquad \textbf{(4.10)}$$

Thus, from equation (4.10), at a given pressure, the sheath thickness for a particular sheath voltage and discharge current can be calculated. In table 4.2, the calculated sheath thicknesses using equation (4.10) for the discharge currents 1.2 and 5.3 mA are compared with the results of the simulations. For the calculations, γ_{se} is considered as 0.25 and the area of the cylindrical cavity is taken as 7.06 x 10^{-8} m^2. The reduced ion mobility (µi) is deduced for a pressure of 500 Torr He from the data provided by H. W. Ellis in ref. ***[Ell-76]***.

Table 4.2: Comparison of simulated and calculated sheath thickness for different Id :

I_d (mA)	V_s (V)	Simulated sheath thickness (µm)	Calculated sheath electric field (V/cm)	μ_i (cm^2/V/s)	Calculated sheath thickness (µm)
1.2	125	27	3.68E+04	9.6	37
5.3	165	18	7.38E+04	7.0	27

The simulated sheath thickness and the calculated one have the same order of magnitude. The metastable density for I_d = 5.3 mA is higher (~ 8.0 x 10^{15} cm^{-3}) as compared to the one for I_d = 1.2 mA (~ 3.2 x 10^{15} cm^{-3}). At low I_d, metastables are distributed in a larger cavity area. At higher current, metastables are more concentrated near the sheath inside the cavity. This could be the effect of the higher electron density obtained at higher current.

4.2.5 Neutral temperature measurements

The temperature of the gas can be determined by measuring the rotational temperature (Trot) of the nitrogen. For the measurements, the small fraction of nitrogen present in the gas chamber is used. But sometimes, to facilitate the measurements, a very small amount of nitrogen gas can be also added with the working gas. According to ref. ***[Lau-03]***, T_{rot} is close to the gas temperature because the rotational relaxation is fast at high pressures (about atmospheric pressure). Specifically, the rotational temperature of nitrogen can be determined by analysing the spatial structure of two rovibrational bands of the second positive system (transition $C\,^3\Pi_u \rightarrow B\,^3\Pi_g$). These two bands are the following:

- The band at 3755.4 Å, between the vibrational levels v = 1 and v '= 3.

- The band at 3804.9 Å, between the vibrational levels v = 0 and v '= 2.

So, to deduce the gas temperature inside the Si MDR cavity, optical emission spectroscopy (OES) was performed using a TRIAX 550 spectrometer. With OES, it is possible to trace the profile of the two bands, i.e. the emitted light intensity as a function of wavelength. For these measurements, the through single hole MDR was used. The diameter of the cavity was 150 µm. Plasma was ignited in He at 370 Torr. The discharge light coming from the anode side (Ni electrode side) of the MDR was focused on the entrance slit of the spectrometer as explained in chapter 2. Rovibrational emission spectra were recorded for different discharge currents, for the second band of 3804.9 Å (Figure 4.15).

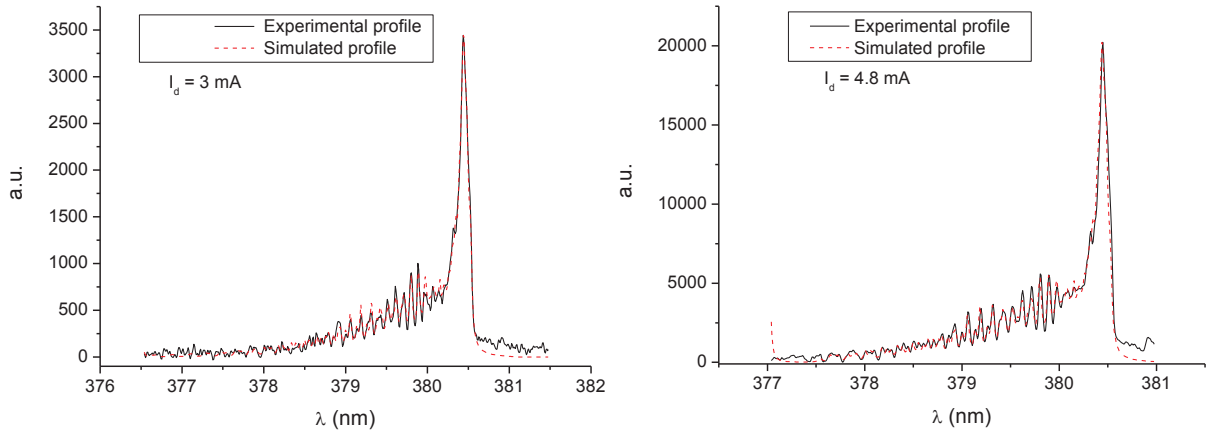

(a) (b)

Figure 4.15: Rovibrational emission spectra obtained with OES (black solid line) and simulated spectra (red dashed line) for discharge currents (I_{ds}) of (a) 3 mA and (b) 4.8 mA for a through hole MDR with diameter 150 µm at 370 Torr He.

Then, the obtained rovibrational experimental spectra were simulated using the home-made software to determine the gas temperature of the MDR cavities. Note that this software was made by V. Schulz-von der Gathen at RUB, Bochum, Germany. Figure 4.15 (a) and (b) show the experimental (black solid line) and the simulated (red dashed line) spectra for the I_{ds} of 3 and 4.8 mA respectively. By fitting the simulated spectra with the experimental spectra, the gas temperatures for their respective discharge currents were approximated. For the I_d of 3 mA and 5 mA, the deduced gas temperatures were 410 ± 30 K and 450 ± 30 K respectively. It can be seen that the gas temperature is higher for the higher discharge current.

By comparison with the simulated results given in the above section, it can be seen that the 425 K simulated gas temperature for I_d of 5.3 mA is close to the experimental gas temperature 450 ± 30 K for I_d of 4.8 mA.

To summarise the studies of single hole microdischarge, we have shown electrical characterisations for different types of single hole cavities viz. anisotropic, isotropic and through hole cavity. From electrical characterisation, it was observed that if the Si cavity cathodic region is limited in the SP case then V-I curves can show abnormal glow type regime behaviour. But if the device is running in RP case or in the case, where cathode is not limited, the V-I curves can show normal glow regime behaviour. Breakdown voltage in general, in the case of SP was found higher as compared to the RP case. For the bigger diameters 100 and 150 µm the breakdown voltage for anisotropically etched cavity was found almost same. Two types of hysteresis effects were also shown for single hole microdischarge. Simulations were performed for a single hole cavity with a diameter of 150 µm. Electron density, metastable states, sheath thickness and gas temperature for two discharge currents of 1.2 and 5.3 mA were calculated. The gas temperature results were then compared with the experimentally obtained results using OES.

4.3 Array of micro discharges

After the study of a single hole micro discharge, the investigations on different multiple hole arrays are presented in this section.

4.3.1 Array of 16 holes

In this section, the results obtained with 16 hole arrays are presented. For the first array, the interhole distance from side to side was 200 µm. For the second one, the interhole distance from side to side was 2800 µm. The hole diameter was 150 µm.

4.3.1.1 4 x 4 hole array with short interhole distance

The results of a 4 x 4 microdischarge array with an interhole distance of 200 µm are given in this part. The 130 µm deep cavities were isotropically etched. Figure 4.16 shows V-I characteristics of the 16 microdischarge array in He at 200 Torr in standard and reverse polarity. Again, the adjacent averaging of the data points for the current and voltage curves individually with respect to time were performed, to make the curve more readable.

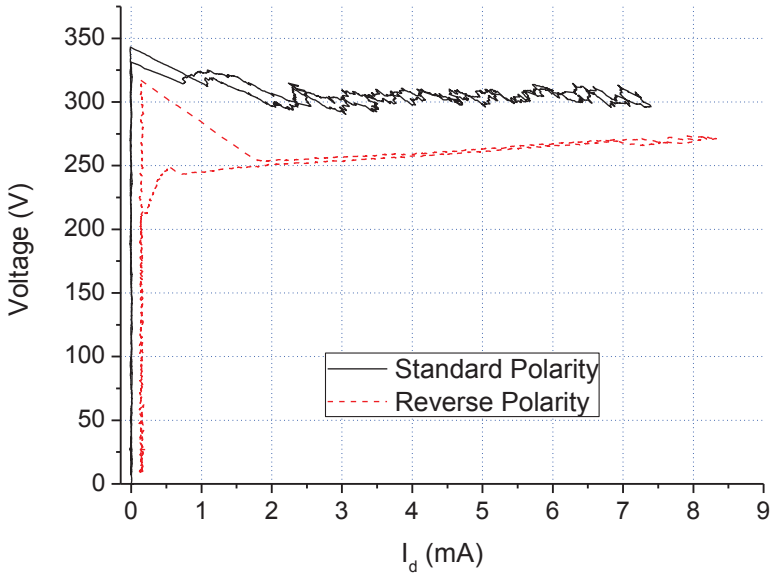

Figure 4.16: V-I characteristics for 16 hole (4 x 4) array (interhole distance 200 µm) with cavity diameter of 150 µm and isotropic cavity of 130 µm depth at 200 Torr He.

After breakdown, the discharge current increases with the applied voltage ramp (Figure 4.16). A series of images was recorded using an ICCD camera during the microdischarge operation, as shown in the figure 4.17. In SP case, at 1.72 mA, a single microdischarge is lit as shown in the first image of figure 4.17. By further increasing the current, some other discharges start to ignite. At 7.16 mA, all the cavities are ignited (third picture of figure 4.17). By decreasing the discharge current, MDR cavities start extinguishing one by one. At 2.20 mA, only 5 cavities are still ignited and seem to have very low light intensity.

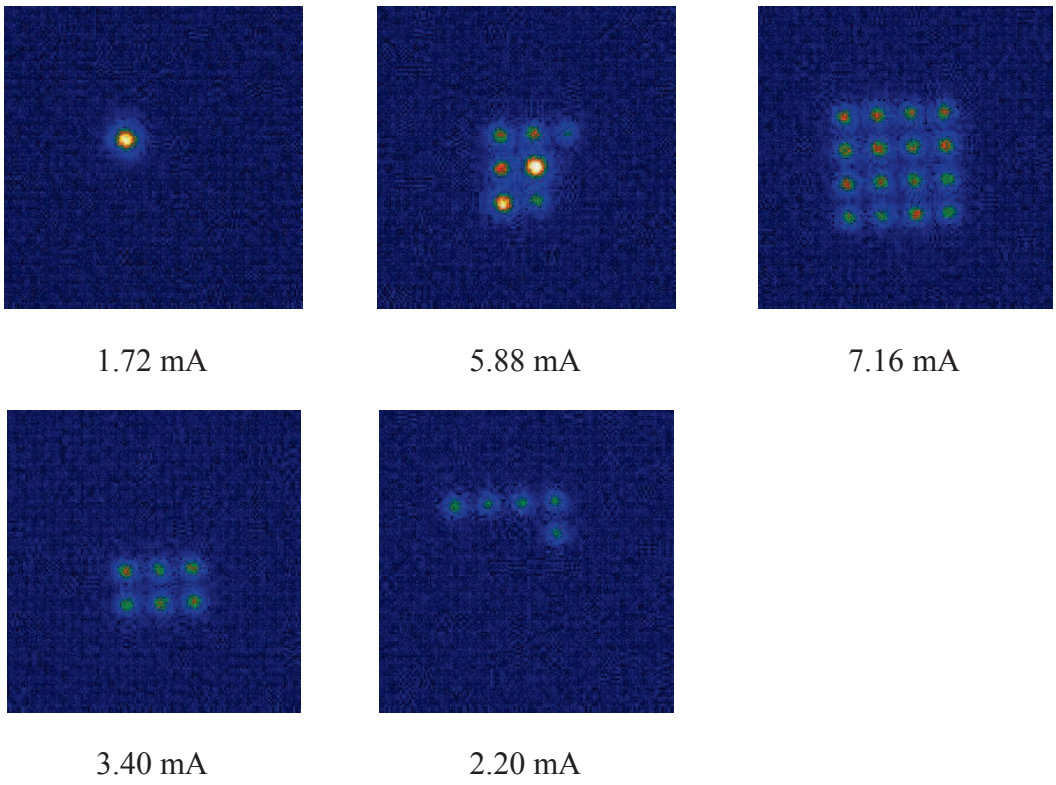

Figure 4.17: Series of ICCD images for a 16 hole array (interhole distance 200 µm) with cavity diameter of 150 µm and isotropic cavity of 130 µm depth. SP case in He at 200 Torr. (Note: the images have false colours).

In this case, due to the reason that cavities are near to each other, the effect of proximity can be seen. The initially ignited holes with discharge help the neighbouring holes to ignite easily by lowering the breakdown voltage due to electron seeding. Thus, in this case, one can see a smooth V-I curve ***[Kul-12]***.

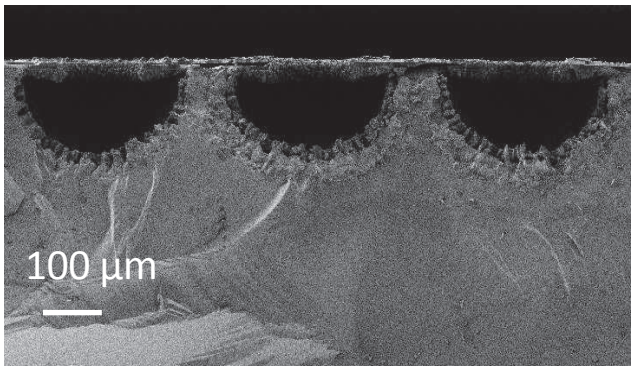

Figure 4.18: SEM image of the 16 hole (4 x 4) array (interhole distance 200 µm) with cavity diameter of 150 µm and isotropic cavity of 130 µm depth.

As observed in figure 4.18, deep isotropic etching induces a quite large undercut below the SiO_2 dielectric. As a consequence, nearby cavities in Si can join or the sidewalls between two holes become very narrow. By analysing the sample with SEM for the current case (Figure 4.18), it was found that, the width of sidewalls between two holes was on the order of 60 - 80

µm. In fact, the plasma ignition inside a cavity can modify the electric field distribution of the nearby cavities. This modification could affect the breakdown voltage of the neighbour cavities and helps them igniting more easily. In RP case (dashed red line in figure 4.16), the curve also follows a normal glow regime as discussed previously for other cases.

4.3.1.2 4 x 4 hole array with long inter-hole distance

The experiments were performed in He at 500 Torr. The cavities in this case are far from each other (2.8 mm) and cavities are shallow (20 µm). Figure 4.19 shows the V-I characteristics of the 16 microdischarges in both SP and RP cases. After breakdown, only one microdischarge ignites. Then, the discharge voltage increases with current following an abnormal regime. Each discharge ignites one by one. Each ignition is followed by a discharge voltage decrease (inset of figure 4.19). Then the voltage increases again, which allows the ignition of the next microdischarge. At the maximum of I_d (~ 7.5 mA), all the 16 microdischarges are lit.

The expansion of plasma on the cathodic surface (Si cavities) is restricted to a very small area. Hence, due to this cathodic limitation, a steep abnormal regime in this case can be seen ***[Duf – 08]***. As the cavities are far from each other, there is no significant proximity effects ***[Kul – 12]***.

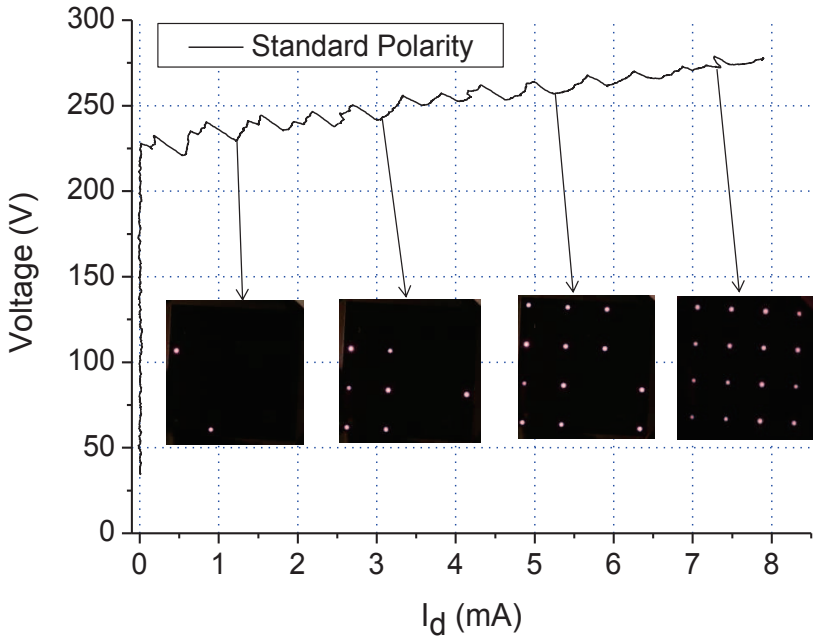

Figure 4.19 : V-I characteristics for 16 hole (4 x 4) array (inter hole distance 2800 µm) (150 µm diameter, isotropic cavity, 20 µm depth) in He at 500 Torr under SP (solid black line). Inset: camera images.

4.3.1.3 Discussion

By comparing both cases of the 16 hole (4 x 4) arrays, with short and large inter hole distances, we clearly see the proximity effect on the microdischarge array operation. In the case of short interhole distance, the complete array ignites in standard polarity and any clear abnormal regime between the ignitions of each microdischarge is not observed. In this case,

initiatory electrons can pass more easily to the nearby holes and facilitate the ignition process. In the other case, the ignition of new holes requires a clear discharge voltage increase to reach again the breakdown voltage and strike another microdischarge. In this case, initiatory electrons cannot be obtained from the nearby holes. UV radiation can also play an important role in the ignition of nearby microdischarges as observed in DBDs ***[Boe-10]***.

4.3.2 Self pulsing mode in array of 16 x 16 holes

In this subsection, studies related to the self pulsing mode in Si based arrays are presented. The experiments were carried out on a 256 (16 x 16) hole array in He and Ar. The cavities were etched isotropically for ~ 60 µm depth. The average discharge current was limited to ~1.5 mA. Figure 4.20 (a) shows current and voltage versus time plots in He. The self pulsing regime can be clearly observed from the image. A zoomed part of one pulse is shown in the figure 4.20 (b). The typical current pulse width is on the order of 2 µs. The rise time of the current pulse is 400 ns. Similarly, the voltage drop has a fall time of 800 ns. Then it rises exponentially with a characteristic time of 50 µs. Figure 4.21 (a) shows the self pulsing regime in SP configurations for Ar gas. Figure 4.21 (b) is the zoomed part of one pulse as indicated by the black dashed lines. From this figure, it can be seen that in the case of Ar, the current and voltage pulses have a slightly different amplitude at each time they appear. In SP case, the amplitude of current peaks varies from 55 mA to 85 mA approximately. In this case, the pulse trend is similar to the self pulsing regime of He.

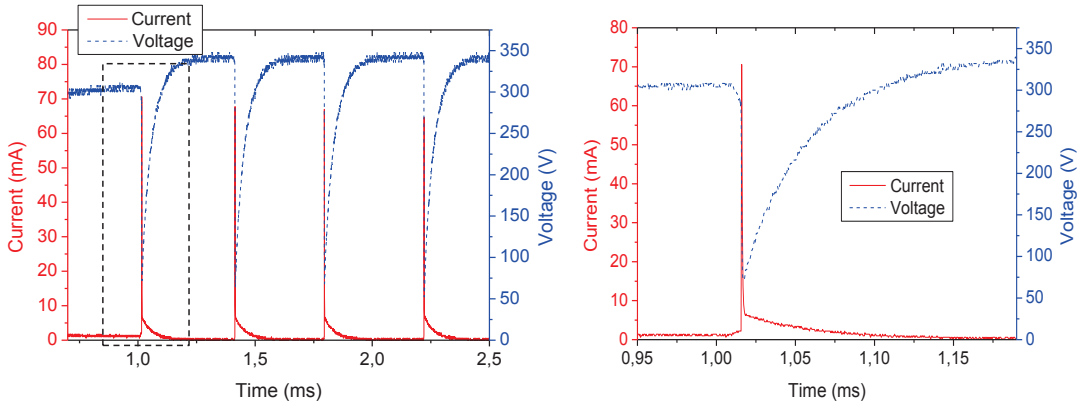

Figure 4.20: (a) Self pulsing regime of 256 hole array with cavity diameter of 150 µm and an isotropic cavity depth of around 60 µm in SP at 200 Torr He and (b) zoomed part of the graph as indicated by the black dashed lines.

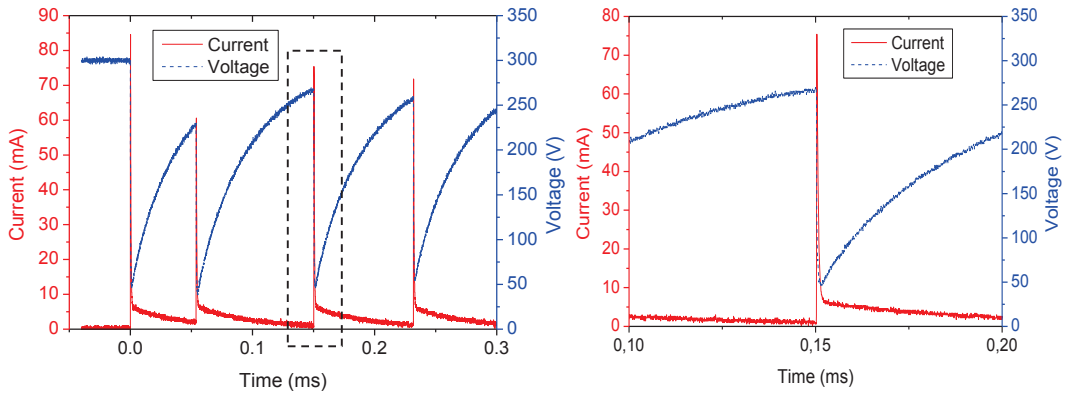

(a) (b)

Figure 4.21: (a) Self pulsing regime of 256 hole array having cavity diameter of 150 µm and an isotropic cavity depth of around 60 µm in SP at 200 Torr Ar and (b) zoomed part of the graph as indicated by the black dashed lines.

Discussion

As observed in figure 4.21, a self pulsing regime can be obtained in silicon devices, but the difference with alumina samples is that this self pulsing regime appears also for quite high average current (> 1 mA). In alumina samples, this self pulsing regime was appearing because the power supply was limited in current and was not able to supply the necessary electrons for secondary emission from the cathode. In current case of Si, the average current is higher, but current peaks are also higher than those obtained with alumina samples. This phenomena can be explained, by analysing the equavelent capacity of the devices.

The MDR chip area is 1.4 cm^2, the dielectric constant of SiO_2 is 3.9 and the distance between the two electrodes is 6 µm. So, we can deduce the equivalent capacitance of our silicon device which is on the order of 1 nF. This value is much higher than the value for alumina samples (typically 50 pF). With 39 kΩ ballast resistance, the RC time constant τ is around 40 µs. This is the typical value for the charging time as shown in figure 4.21 (a) and (b). For comparison, this value is reduced to 200 ns in the case of an alumina sample with the same ballast resistor. The discharge time of the Si based device is typically 2 µs, which is similar to the alumina sample as shown in chapter 3. Thus in this discussion, it is worthy to comment that self pulsing can be observed if the charging time becomes greater than the discharging time.

In silicon devices, the shape of the current pulse is different. The 2 µs high current peak is followed by a slower decrease of the current during the charging time. We don't see this part in alumina. This part corresponds to displacement current. After calculations, the value of displacement current is typically 4 mA, which corresponds to what we obtain in figure 4.21. In alumina, this value can be around 0.4 x 10^{-4} mA, which is much less than what we obtain for silicon. Also, the high capacitance of the Si devices can lead to the current peaks with a high value of current and it may be the cause for the presense of the micro arcs inside the cavity. These micro arcs could empty the MDR capacitor in a short duration similar to the pulse duration of the alumina based devices.

4.3.2.1 4 sub-arrays of 256 holes on a chip

In this subsection, the results of the array with the second arrangement described in chapter 2 are presented. The array chip has 4 sub-arrays of 256 holes, each with different hole diameters (D) of 25, 50, 100, and 150 µm (see chapter 2). The experiments were performed in He. These arrays were etched isotropically and were 70 µm deep.

V-I characteristics

Figure 4.22 presents a V-I characterisctic of a 256 mixed hole array operating in standard polarity at 100 Torr. In both cases, after breakdown, the discharge currrent starts increasing with the increase of the power supply voltage ramp. The voltage is more or less constant versus the discharge current. The breakdown is ~ 270 V. Figure 4.23 shows images of the array for plasma operation in (a) SP and (b) RP cases.

In SP case, after the breakdown at 270 V, due to the ballast resistor, the current I_d reaches a value of 2 mA and the discharge voltage drops to around 220 V. A single microdischarge ignites in a 150 µm diameter cavity. At the highest discharge current (~ 9 mA), the complete array of 256 holes with 150 µm diameter is ignited, and a single hole in the array of 100 µm diameter is ignited. At 3 mA, while the current decreases, half of the 150 µm diameter hole array is lit with a very feeble light intensity. Then, discharges extinguish at a lower current value.

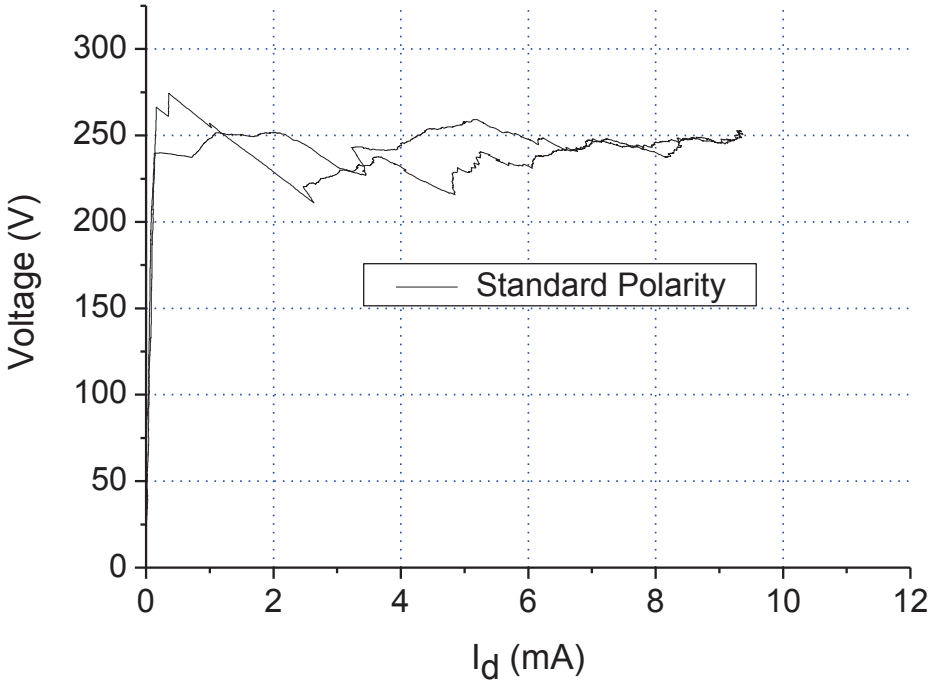

Figure 4.22: V-I characteristics of 256 mixed holes arrays at 100 Torr He in SP case.

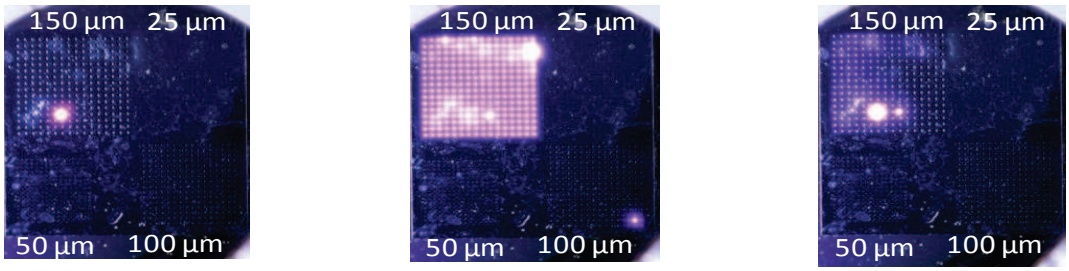

~ 2 mA ~ 9 mA ~ 3mA

(a)

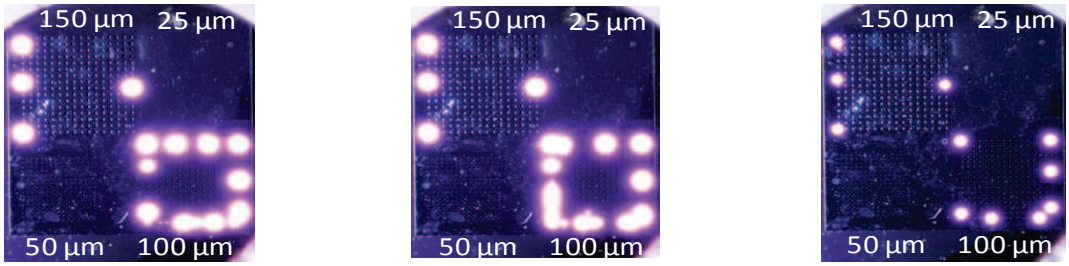

~ 8.5 mA ~ 10 mA ~ 4 mA

(b)

Figure 4.23: Images of 256 mixed holes sub-arrays at 100 Torr in He, during plasma operation in (a) standard polarity and (b) in reverse polarity.

In RP case, the first image is obtained for a discharge current of 8.5 mA. This image shows 12 ignited cavities in the 100 µm diameter sub-array and 4 ignited cavities in the 150 µm diameter sub-array. The microplasma emission diameter is bigger than the one obtained in standard polarity. As explained previously, in reverse polarity, the plasma spreads on the nickel area (figure 4.23 (b)). The image at I_d ~10 mA shows a total of 19 ignited cavities : 4 microplasmas in the 150 µm diameter cavity sub-array and 15 microplasmas in the 100 µm diameter hole sub-array. For the decreasing voltage ramp, an image is taken at 4 mA. We still have 4 microplasmas lit in the 150 µm hole subarary and 7 microdischarges are still lit in the 100 µm diameter sub-array.

In both SP and RP cases, a normal glow regime has been observed. In RP configuration, this is due to the fact that a the plasma can spread easily on the cathodic surface and provides a normal glow regime ***[Duf-08]***. In RP case, a edge ignition phenomenon can be clearly seen. As explained in the next sections, the cavities prefentially ignite from the edges of the array. Also, in standard polarity, at 100 torr, only the 100 µm diameter sub-array ignites.

Breakdown (V_{br})

We report the results for the breakdown studies performed with different cavity diameter arrays. The influence of cavity diameter on the electrical discharge characteristics was studied using a mixed hole array consisting of anisotropic cavities with a depth l of 150 µm. For the determination of the breakdown voltage, the acquisition of discharge voltage and current

during eight periods was made in order to obtain an average value for each pressure. The signal frequency (f) used for V–I characteristic acquisition was 200 mHz. This corresponded to a voltage rate of about $200Vs^{-1}$. The error bars, shown on all the graphs, were considered as random errors and obtained by considering a Gaussian distribution of the experimental values.

To study the breakdown effect, only two sub-arrays of 100 and 150 µm were kept open and other two sub-arrays were covered with a kapton tape. The geometrical characteristics of both cavities are indicated in table 4.3. For surface and volume calculations, the cavity was considered to be cylindrical. Figure 4.24 (a) and (b), show the corresponding breakdown curves with respect to pressure and the V-I curves at 500 Torr in He respectively.

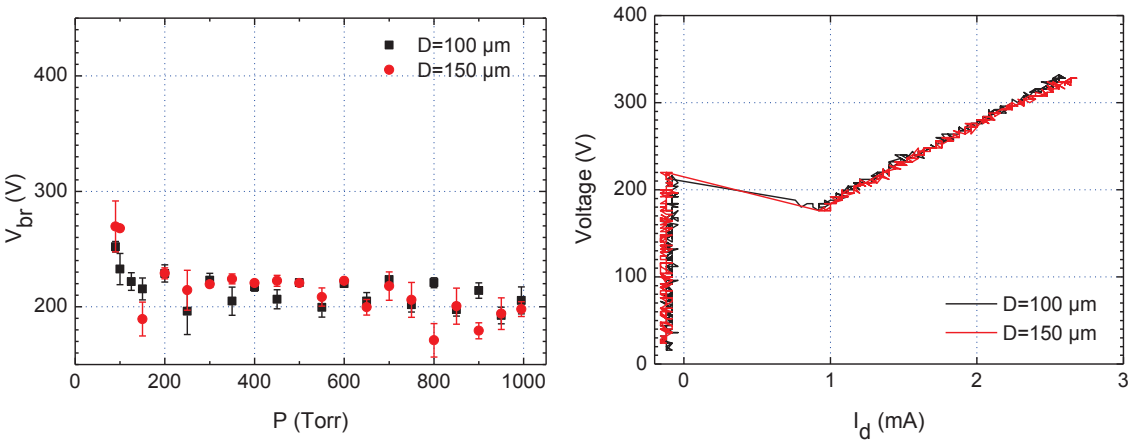

(a) (b)

Figure 4.24: Electrical characteristics of two 256 cavity sub-arrays having the same cavity shape and depth (anisotropic, l = 150 µm), but different diameters (D = 100 and 150µm), (a) breakdown voltage versus pressure and (b) V-I curves at 500 Torr He, for f = 200 mHz.

The breakdown voltage curves match quite well over the full pressure range. For this type of cavity (anisotropic l = 150 µm deep), experiments show that the cavity opening diameter does not influence the breakdown voltage. The calculations are shown in the in table 4.3. This table shows that the opening diameter does not influence the geometrical electric field strength distributions significantly, if the two diameters are closer to each other (e.g. 100 and 150 µm).

Table 4.3: Geometrical features of the cavities of the two micro-reactors (16 × 16 = 256) used for cavity opening diameter study; D: opening diameter, d_n: distance to nearest neighbour cavity, l: depth, Scath: wall surface area (cathode surface), V: volume.

D(µm)	d_n (µm)	l (µm)	S_{cath} (mm^2)	V (mm^3)
100	150	150	0.055	1.8×10^{-3}
150	150	150	0.088	2.65×10^{-3}

The V-I curves of figure 4.24(b) show that a single microdischarge ignites in both cases and follows an abnormal regime in a same manner. This type of ignition indicates that, in the current case, the breakdown does not depend on diameter. However, it was also observed in other experiments, considering diameter ranging from 25 to 150 µm that opening diameter does have an influence on the ignition. The smaller diameter cavities tend to ignite first at higher pressures, while bigger diameter cavities ignite preferentially at lower pressures ***[Kul-12]***. Details will be provided in next coming sections.

4.3.3 Array of 1024 holes

In this section, results with 1024 microdischarge arrays are presented. First, V-I characteristics are shown, and then the difference between isotropic and anisotropic cavities is discussed. Afterwards, the working behaviour for deeply etched and shallowly etched cavities is presented. The ignition mechanism and the current density measurements for 1024 holes are discussed further.

4.3.3.1 V-I characteristics

In this section, we present the measurements for 75 µm deep cavity reactors. Figure 4.25, shows the V-I characteristics in standard polarity for a 1024 cavity array (diameter ~150 µm, anisotropically etched). Experiments were performed in Ar (Figure 4.25 (a)) and in He (Figure 4.25 (b)). The V-I curves show that the device follows a series of abnormal regimes. Here, a significant positive slope in the V-I characteristics is followed by a dip. When the breakdown voltage is reached, one or more discharges ignite and we see a voltage dip. Each dip in the V-I curve indicates that other microdischarges ignite in new cavities.

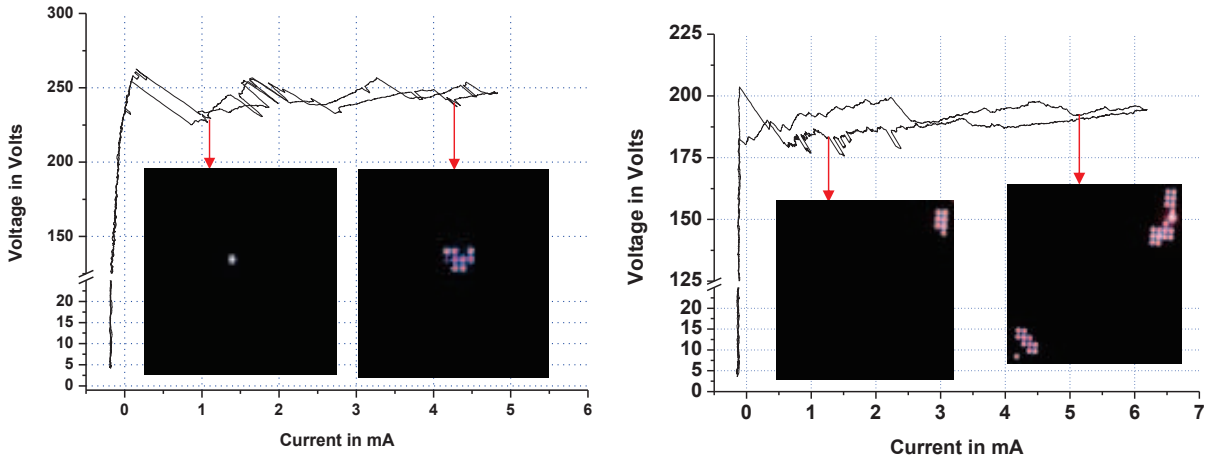

(a) (b)

Figure 4.25: V-I characteristics for arrays of 150 µm diameter holes with cavity depth of 75 µm at 350 torr (a) in Ar and (b) in He.

Thus, by increasing the total voltage further, the current increases until the breakdown voltage is reached again to ignite microdischarges in other cavities. The ignition of these new cavities provides a voltage dip as discussed earlier. The number of 75 µm deep ignited cavities remained small. In addition, the plotted V-I curves were smoothed to allow one to see their

behaviour. From these curves, it can be seen that the number of ignited cavities in Ar is smaller than in He at the same current and pressure (see inset images). This is also due to the larger first Townsend coefficient in He ***[Lie-05, Kul-12]***. As a consequence, we can expect a higher plasma current density in Ar and so, a higher electron density for the same pressure and total current.

4.3.3.2 Breakdown

Effect of cavity shape

To find the effect of the cavity shape on the operation of microreactors, two different geometries of 1024 microreactor array with an opening diameter D of 100 µm are tested. The cavities of each array are etched differently. One is etched anisotropically and the other one is etched isotropically as shown in figure 4.26 (after operation). Note that the complete microreactor structure is not visible in the pictures because the nickel electrode (top electrode) had been removed during the cleavage of the MDR chip. In the figure, the upper layer corresponds to the dielectric (SiO_2) and the lower one with the cavity is the Si electrode. The geometrical cavity features for both arrays are given in table 4.4. For calculations, the cavities were considered either as cylindrical (anisotropic cavity) with diameter D_{cav} = 100 µm and depth L = 150 µm, or as hemispheric (isotropic cavity) with diameter D_{cav} = 130 µm (due to a symmetrical undercut of about 15µm) and depth L = 75 µm. The cathodic surface and volume of the isotropic cavity is both half of the anisotropic ones.

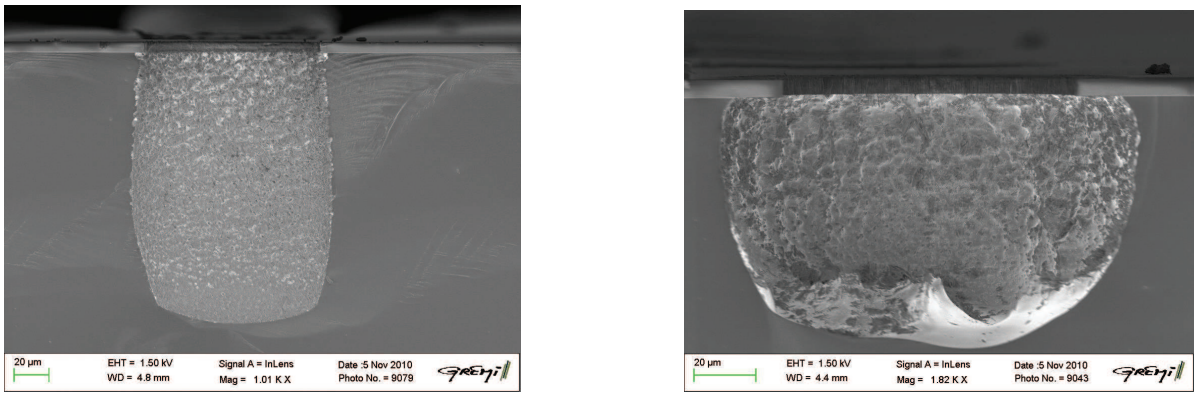

(a) (b)

Figure 4.26: SEM cross-section views of (a) anisotropic and (b) isotropic cavities with D = 100 µm opening diameter (after operation) for 1024 hole arrays.

Breakdown voltage measurements were performed in He at a pressure ranging from 50 to 1000 Torr. The electrode separation (dielectric thickness) was about 6 µm for the microreactors with anisotropic cavity. This corresponds to a range of pd product of 0.03–0.6 Torr.cm for the anisotropic cavities. Note that these values are given as an indication, but they are not well defined because of the non-uniformity of the electric field. For this reason, the breakdown voltage curves are presented with respect to pressure. In the isotropic case, due to an undercut of about 15 µm and if we consider the electrode gap as the shortest distance between electrodes, i.e. d ~ 20 µm, then the corresponding pd range is 0.2–2 Torr.cm. On comparison with Paschen's curve for breakdown voltage of parallel plane electrodes in

helium gas, it is found that both present cases are situated in the region of the left branch (pd ~5 Torr cm).

Table 4.4: Geometrical features of the cavities (shown in figure 4.26) of the 1024 microreactor array (D = 100 µm); D is the opening diameter, d_n is the side to side distance between two neighbour cavities, D_{cav} is the inner cavity diameter, L is their depth, S_{cath} is the cathode area and V is the cavity volume.

D (µm)	dn (µm)	Cavity	Dcav (µm)	L (µm)	Scath (mm^2)	V (mm^3)
100	150	Isotropic	130	75	0.027	0.58×10^{-3}
100	150	Anisotropic	100	150	0.055	1.8×10^{-3}

Figure 4.27 shows the averaged breakdown voltages V_{br} versus pressure P for both types of microreactors. One can immediately note that, although the cavity shape is very different, the corresponding breakdown curves versus pressure are very similar and match quite well, with a small tendency for higher values for the isotropic case. Generally speaking, during each voltage period, a few microdischarges ignite one after the other and operate together at the highest driven current, which ranges between a few mA to about 20 mA maximum. Their number varies from one to five and remains very small with respect to the total number in the arrays (1024). For determination of breakdown voltage curves, only the first breakdown voltage values of each ramp have been used.

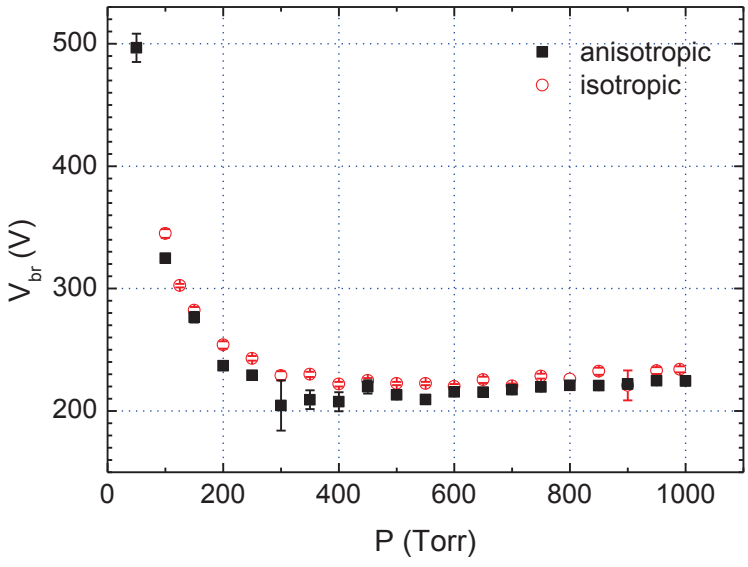

Figure 4.27: Breakdown voltage V_{br} versus pressure P for two arrays of 1024 cavities with D = 100 µm having different cavity shapes: anisotropic and isotropic.

Figure 4.28 shows V-I curves for array with 1024 holes, D = 100 µm in (a) anisotropic and (b) isotropic cases, during a period (f = 200 mHz, T = 5 s), in He at P = 500 Torr. Some

similarities in the characteristics of both cases can be seen from these plots. First, after the breakdown has occurred, the microdischarges enter in an abnormal glow regime, with a linear increase in discharge current with voltage. The immediate entrance in abnormal regime is due to the intrinsic limited cathode surface inside the micro cavity. The extension of the cathode sheath area being limited by the cavity surface, the discharge current I_d can only increase if the externally applied voltage increases. Second, the abnormal regime allows successive ignition of a few microdischarges in both cases. We can notice that, even if the number of ignited cavities remains small in both cases, the isotropic case tends to ignite more microdischarges (generally, two times more: 4 compared with 2).

The voltage drop after the successive ignitions is, in general, lower in the isotropic case. This is characterised by an abnormal regime whose differential resistance is slightly higher (r ~ 25 kΩ) than in anisotropic cavities (r ~ 17 kΩ). This difference in differential resistance might be due to the smaller cathode surface, in the case of the isotropic cavities. This could explain the slightly higher number of microdischarges ignited in the isotropic case because it is faster in this case to reach again the breakdown voltage.

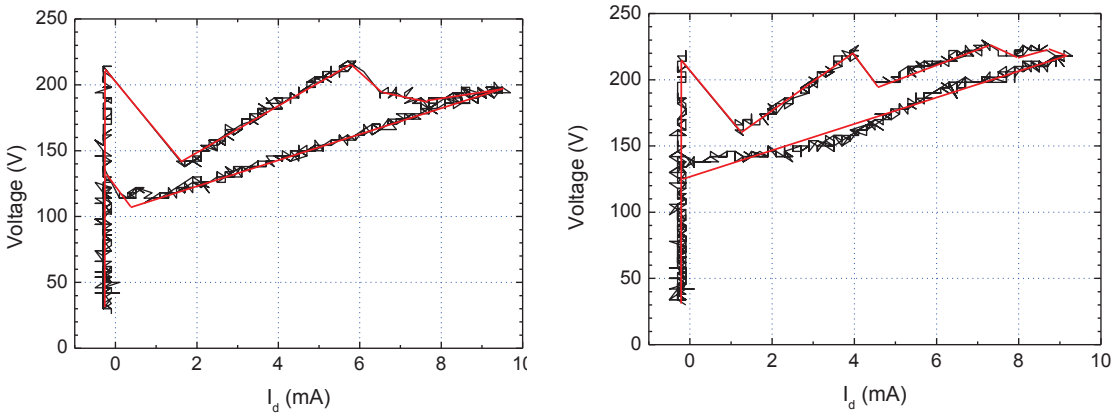

(a) (b)

Figure 4.28: V-I curves for a 1024 hole array , D = 100 µm in (a) anisotropic and (b) isotropic cases, during a period (f = 200 mHz, T = 5 s), in He at P = 500 Torr.

Indeed, as indicated in table 4.4, the cathode surface in the isotropic case is half of that in the anisotropic case. Dufour et al. ***[Duf-08]*** have shown that the smaller the cathodic surface, the more emphasised the abnormal glow regime.

Effect of rate of voltage ramp

In general, to obtain the V-I characteristics, we use triangular voltage ramp as discussed in chapter 2. Usually a constant rate of voltage ramp was used for our measurements. But this rate of voltage ramp may also affect the breakdown voltage of MDRs. In this subsection, we present the studies related to the influence of voltage ramp on the V-I characteristics. The period (frequency) of the signal was changed while keeping the amplitude constant. Measurements were carried out using 1024 array of 100 μm diameter isotropic cavities as

shown in figure 4.26. Figure 4.29 shows V-I plots, obtained for two different frequencies, f = 50 and 200 mHz in He at 500 Torr. Those waveform frequencies correspond to waveform periods of T = 20 s and 5 s respectively. The voltage rise rates are $60Vs^{-1}$ and $240Vs^{-1}$ for f = 50 and 200 mHz respectively. From this plot, it can be seen that the ignition of multiple microdischarges in an array depends on the rate of voltage ramp. From the figure 4.29, we see that at higher frequency (f = 200 mHz), only three cavities are ignited as compared to the eight ignited cavities for the lower frequency (f = 50 mHz). So, with the longer period ramp a higher number of cavities ignite. This could be explained through the statistical generation time t_s discussed in the next subsection. The probability of the appearance of initiating electron from natural sources is higher in the case of slow voltage ramp, for a same array configuration ***[Sch-12]***. In conclusion, it is worthwhile to say that the number of ignited microdischarges can be controlled with the variations of the slope and amplitude of the voltage ramp.

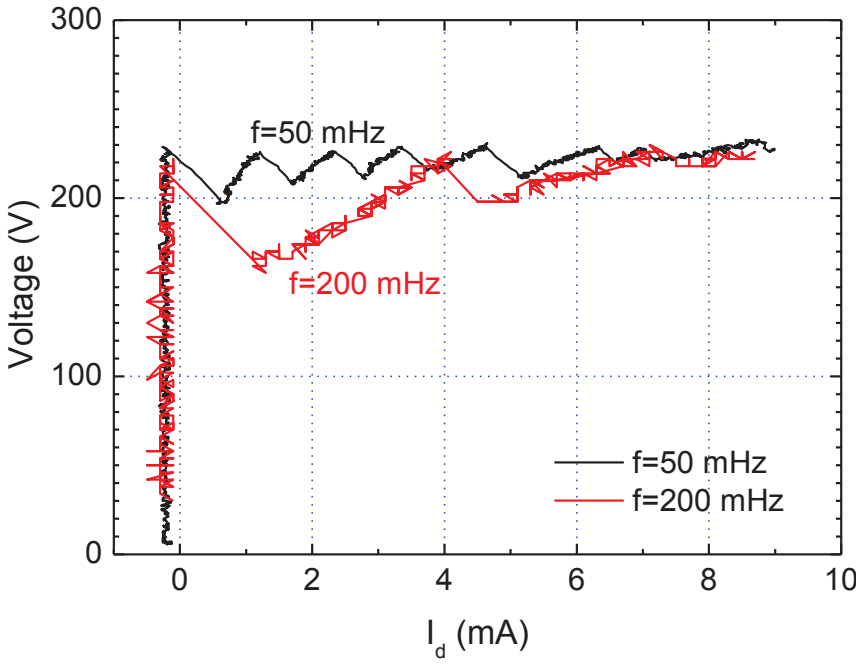

Figure 4.29: V-I characteristics of 1024 holes array with isotropically etched cavity with diameter D = 100 µm, depth 75 µm, in He at 500 Torr for two different voltage ramp signal frequencies f = 200 mHz (T = 5 s) and f = 50 mHz (T = 20 s).

Effect of cavity depth

The effect of cavity depth was studied using the 1024 microdischarge array (hole diameter of 150 μm). Two similar arrays were used; one was anisotropically etched down to a depth of 70 µm and the other one was not etched. The breakdown voltage was recorded for different pressures from 100 to 1000 Torr in He. The results are shown in the figure 4.30 (a). The corresponding V-I characteristics were also recorded at 500 Torr in He as shown in figure 4.30 (b). For the non-etched cavity array, a much lower (160 V) voltage is required to strike the microdischarges over the pressure range 200 – 1000 Torr. Some effect must compensate the higher statistical time expected in the non-etched case due to a lower electron generation

probability (because of the smaller cavity volume) which should have increased the breakdown voltage ***[Sch-12]***.

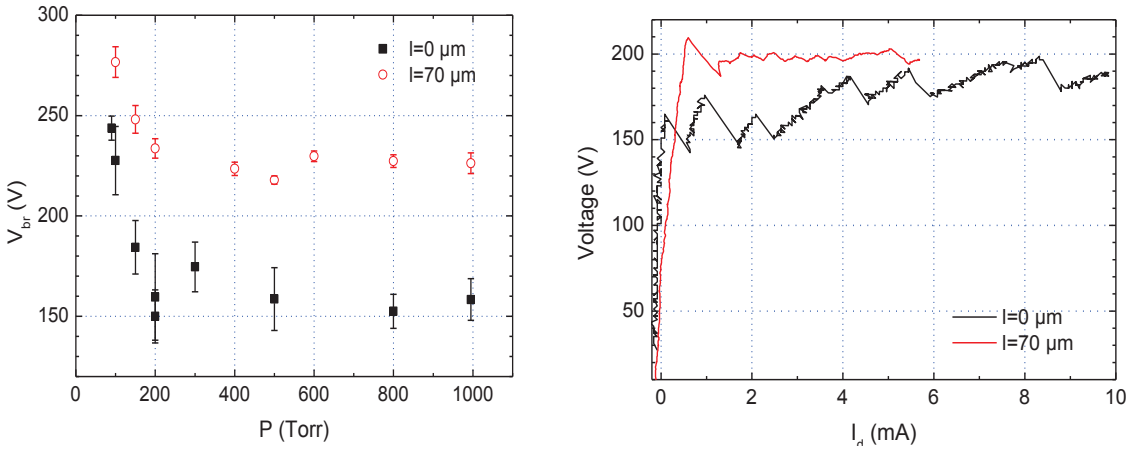

(a) (b)

Figure 4.30: Characteristics of two 1024 cavities arrays with same cavity shape and diameter (anisotropic, D = 150 µm) but different depths L = 70 and 0 µm: (a) breakdown voltage versus pressure and (b) V –I curves at P = 500 Torr, in He for f = 200 mHz.

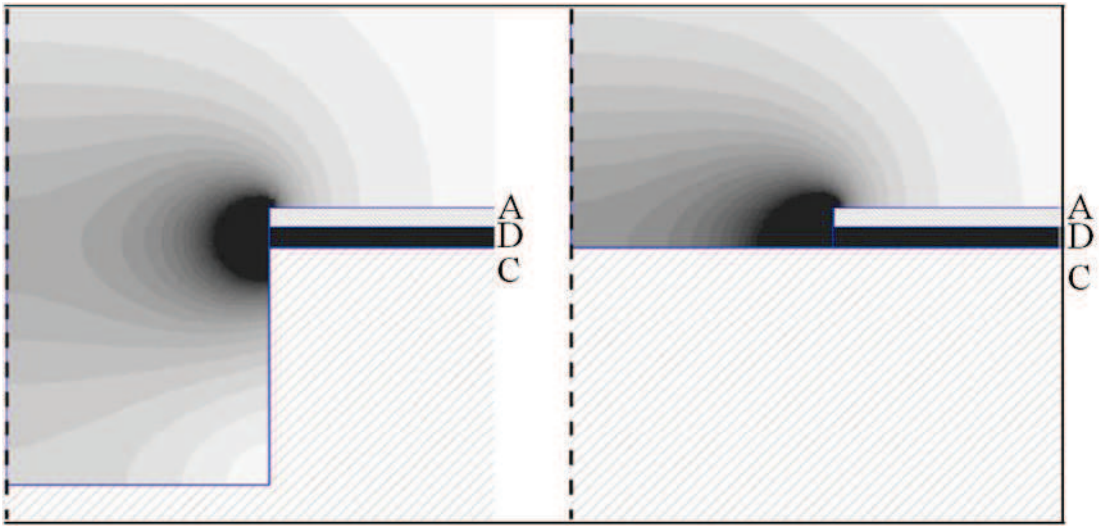

(a) L = 70 µm Vd = 225 V (b) L = 0 µm, Vd = 160 V

Figure 4.31: Simulated electric field in a 150 µm diameter single cavity; A (nickel), D (SiO_2) and C (silicon) stand for anode, dielectric and cathode respectively; the dotted line represents the cylindrical symmetry axis; the darker zone in the electric field strength distribution corresponds to values higher than 5 x 106 Vm^{-1}.

The most straight forward explanation could come from the difference between electric field strength distributions in the etched and non-etched cases. Using the finite element method software FEMM ***[MEE]***, the geometrical electric field distribution before the breakdown, was simulated. Figure 4.31 shows the 2D axi-symmetric electric field distribution. The darker zone of figure 4.31 corresponds to the highest values of the electric field (up to 5 x 10^6 Vm^{-1}).

In these simulations, the electric field distribution looks quite similar, but for a same voltage difference between the electrodes, the electric field is higher in the non-etched cavity case. Here, another 65 V in voltage drop between the electrodes would be necessary for the etched cavity to obtain similar electric field distribution.

From the above discussion, it can be concluded that shallower microdischarges have lower breakdown voltage as compared to the deeper or through hole cavities.

Effect of pressure

The effect of pressure on the operation of microreactors was studied by using the 1024 hole arrays shown in figure 4.26. This array was composed of 100 µm diameter isotropic cavities and the cavity depth was 75 µm. The V-I characteristics were obtained in He for pressure ranging from 100 to 1000 Torr. The V-I curves for two pressures 500 and 750 Torr are plotted in figure 4.32 (*a*). Here, the waveform frequency is f = 50 mHz.

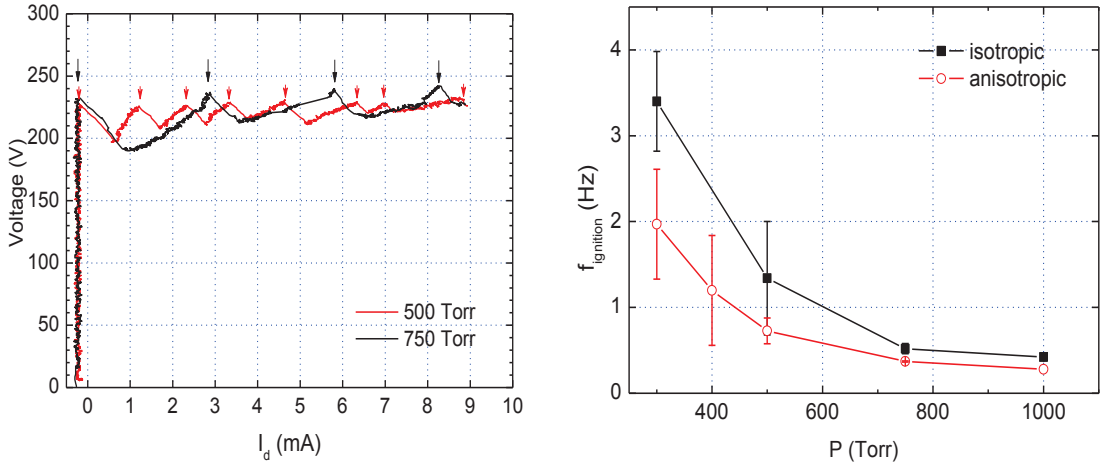

(a) (b)

Figure 4.32: Effect of pressure on the ignition of the 1024 isotropically etched cavity array (diameter D = 100 µm and depth L = 75 µm), (a) V–I characteristics (the arrows indicate microcavity discharge ignition: the small arrows for 500 Torr and long arrows for 750 Torr), (b) microcavity discharge ignition frequency, for the same voltage ramp with f = 50 mHz.

Only the increasing phase of the voltage waveform is shown in the figure (that is half the period: $T/2$ = 10 s), in order to emphasise the effect on microdischarge ignition. The number of microdischarges which are ignited (indicated by arrows) during this time interval varies with pressure. Higher numbers of MDRs ignite at lower pressure and vice-versa. The time interval between successive ignitions is quite constant at a given pressure, if we speak in terms of ignition frequency. In other words, the ignition frequency decreases as the pressure increases as shown in figure 4.32 (*b*). This tendency is also observed for anisotropic cavities. The efficiency of the ionisation process depends on the reduced electric field E/n, which decreases with increasing pressure as explained in ***[Lie-05] and [Sch-12]***.

Effect of number of cavities

In this sub-section, studies related to the effect of the number of cavities per array on the breakdown voltage are presented. The influence of the number of cavities on both breakdown and operation was studied using three different arrays composed of identical cavities, but with a different number on a chip: 1024, 256 and single cavity.

The cavities were identical in shape (anisotropic) with a diameter of D = 100 μm, and a depth of L = 150 μm. The breakdown voltage curves versus pressure were obtained in He between 100 and 1000 Torr, as shown in figure 4.33 (a). Qualitatively, the three curves have the same trend. However, the value of breakdown voltage for the single cavity configuration is about 100 V higher than the one of the two array configurations over the full pressure range. Two hypotheses could be given to explain this phenomenon.

The first hypothesis originates from the fact that gaseous electrical breakdown is a stochastic process, i.e. its actual occurrence depends on the probability that an initiatory/seed electron will be available and then it will lead to an avalanche of sufficient size for the development of a conductive breakdown channel in the gas ***[Sch-12]***. That initiatory electron must be available in a suitable location (preferably close to the cathode) for maximum electron amplification. As already stated, the measurements for the breakdown voltage were carried out by powering the microreactor using an increasing voltage ramp. The ramp rise time was 2.5 s. During this period, the discharge could only be ignited if the electron density reaches a critical value. The real time needed to reach that critical value after the voltage has reached the minimum static breakdown voltage (V_s) (that is the lowest breakdown voltage which would ignite the discharge after a sufficiently long application time) is known as the breakdown delay time ***[Kuf-00, Sch-12]***.

This delay time is statistically distributed and consists of two parts $t = t_s + t_f$. The statistical time (t_s) is the time that elapses from the moment when V_s is reached until an initiatory electron appears in the high-field region to initiate the discharge. The formative time (t_f) is the time required for the breakdown to develop after the discharge initiation. The statistical time (t_s) depends on the amount of pre-ionisation in the gap which in turn depends upon the size of the gap and the sources producing the seed electrons. The over voltage is the difference ($V_p - V_s$) between the peak voltage V_p, at which breakdown is measured, and the minimum static breakdown voltage V_s. In our case, no external source exists, and the initiatory electrons originate only by natural external ionizing radiation, i.e. cosmic rays and natural radioactivity of materials. The rate of initiatory electron generation by such external radiation is about 4 x 10^{-5} electrons.s^{-1}.cm^{-3}.Pa^{-1} in most gases ***[Chr-90, Sch-12]***.

At atmospheric pressure, the electron generation rate in each cavity with a volume of about $\sim 10^{-3}$ mm^3, is about 4 x $10^{-6}s^{-1}$. This corresponds to a prohibitively long statistical time. In the case of the 1024 cavities, the electron generation rate in the volume corresponding to the sum of the 1024 cavity volumes and is about 10^3 times higher as compared to the single cavity. Hence, the probability for initiatory electron generation in the case of an array is 10^3 times higher and the statistical time (t_s) in this case could be reduced as compared to the

single-cavity MDR. This could induce a lower over voltage and explain the difference of breakdown voltages between different MDR configurations ***[Kuf-00, Sch-12]***.

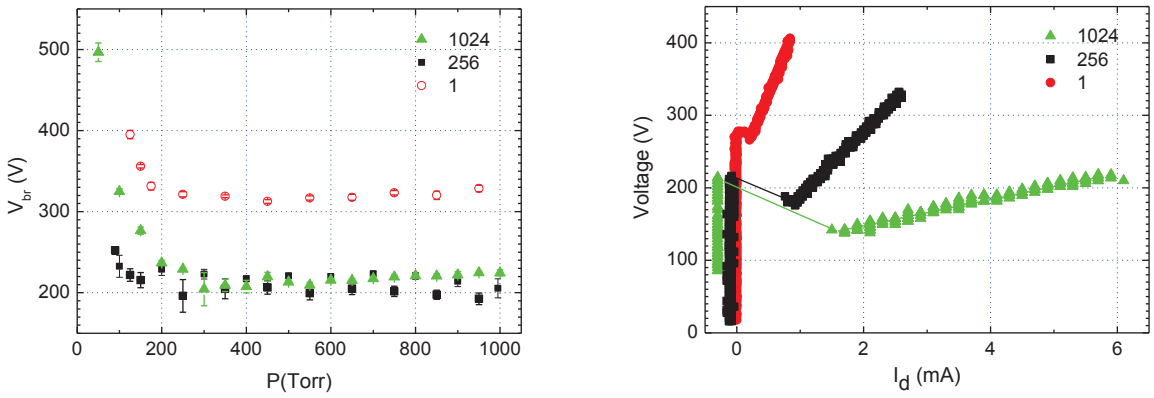

(a) (b)

Figure 4.33: Electrical characteristics for three different microreactor configurations consisting of same type of cavities (anisotropic, D = 100 µm, L = 150 µm) and having different number of cavities 1024, 256, and 1; (a) breakdown voltage versus pressure and (b) V–I curves at P = 500 Torr, in He, for f = 200 mHz.

The second hypothesis could be provided by considering the possible presence of electron field emission. The voltage, just before breakdown is about 220 V, for both 1024 and 256 arrays. Here, this applied voltage through a 6 µm thick dielectric corresponds to an electric field of about 5 x 10^7 Vm^{-1}. The possible presence of cathode surface deformities (e.g.: scalloping and non-uniform etching) of a few tens of microns, would enhance locally the electric field and could induce electron field emission ***[Sch-12]***. The probability of encountering such surface irregularities might be higher in the array case compared with the single-cavity case.

Figure 4.33 (b) shows the V-I curves corresponding to the three micro-reactors having 1024, 256 and 1 cavities. As discussed earlier, the breakdown voltage of the multiple hole arrays is about 220 V and is much less than that of the single cavity MDR. As expected from the limitation of the cathode area, the discharge enters in an abnormal regime in all three cases. But this abnormal regime also depends on the array configuration although only single microplasma is lit for all three configurations. For exactly the same cavity features, depending on the micro reactor configuration, the maximum current apparently driven by a single cavity is quite different. It is 1, 2.5 and 6 mA for the 1, 256 and 1024 cavity micro-reactors respectively. In fact, a lit microplasma seems to lead to an additional current leak in the neighbouring cavities of multiple hole arrays.

Electrons from the lit microplasma could be the source of seed electrons for neighbouring microdischarges. The seed electrons could lead to the Townsend regime for these microdischarges. This can be the source of the additional current, but has no intensity because microdischarges are not self-sustained. It could be possible that the secondary electrons are not produced in sufficiently high number to make the microdischarges self-sustained.

This could explain why a higher value of the discharge current is obtained inside a multiple hole array whereas a single microplasma is ignited. This explanation is not yet confirmed.

4.3.3.3 Ignition dynamics

In this section, the results related to different ignition phenomena are presented. This study covers the evolution of the discharges on a multiple hole array and the analysis of array ignition trends.

Ignition trend

From breakdown studies, discussed in the above sections, it was concluded that shallowly etched cavity array allowed many more cavities to ignite in parallel. To show this, the results obtained from a 32 x 32 array of microdischarge reactors having an opening diameter of 100 µm are presented. The cavities were formed by isotropic etching with a cavity depth of approximately 28 µm. The experiment was performed in standard polarity with He at 350 Torr. The current of the microdischarge reactor array was gradually increased. A series of photographs is shown in figure 4.34. It corresponds to the very first ignition of the holes in the array at different current levels.

The experiment was performed by igniting and switching off the array and again reigniting the array a few times. It was observed that the very first ignition of a given cavity was obtained for a higher voltage than in the following ignitions. It seems that during the first ignition, the cathode is treated by the discharge, which changes the secondary electron yield. Thus it becomes easier to ignite plasma after first ignition inside the microcavities. As observed from the series of pictures in figure 4.34, some (seemingly random) microdischarges in the array ignite at 0.2 mA. Then at 2 mA, more MHCDs are ignited surrounding those first microdischarges. At a total current of 5 mA, some additional discharges - located on the other side of the array - start to ignite. Then the microdischarge ignition propagates from the two ignition regions and preferentially at the edge (10 mA to 15.5 mA). After the MHCDs at the array edges are ignited, the ignition propagates towards the centre (15.5 mA to 21.2 mA). Finally, the whole array can be ignited and the emission becomes quite homogeneous. The last fully ignited array image at 21.2 mA is shown separately in the figure 4.35. It clearly shows the homogeneous optical emission intensity from the MHCDs.

This ignition phenomenon, which occurs preferentially at the edge, can be explained on the basis of the resistance of the nickel layer. Once some microdischarges are ignited at the edge, a voltage drop can be obtained between the edge and the centre of the microdischarge array due to the resistance of the nickel layer ***[Kul-12]***. Indeed, holes are very close to each other (150 µm edge to edge separations) and the nickel layer is only 6-8 µm thick. This close separation could be the origin of an additional resistance for currents, which would flow towards the middle of the array. This could explain why the cavities located at the edge ignite first and the cavities in close proximity to those first ignited MHCDs also ignite preferentially. Due to the proximity of the ignited holes, the plasma is more easily initiated in the adjacent holes ***[Duf-08, Kul-12]***. But on calculating, the ratio between the resistances for a structured Ni surface and a plane Ni surface was 1.3. Also the sheet resistance of the Ni was found on the order of 0.01 Ω. This sheet resistance is very small and it can not provide a large

difference of voltage drop between the edges and at the center of the MDR chip. Thus, another hypothesis for the edge ignition phenomenon could be linked to the processing steps. It could be possible that there exist some processing defects on the chip caused during the fabrication of the device. These processing defects could also lead to the edge ignition phenomenon.

The current and the current density driven by each microcavity can be evaluated. For the calculations, the last image from figure 4.34 with a current of 21.2 mA is taken. At this stage, every hole of the array is ignited and the array is quite uniform in intensity. In this case, each individual hole drives around 20 µA current in average. To calculate the current density (J) of the isotropically etched cavities, we took the area of a sphere cap by considering the cap radius of 55 µm and depth 20 µm. The estimated total surface area of a cavity is around 0.110 cm^2.

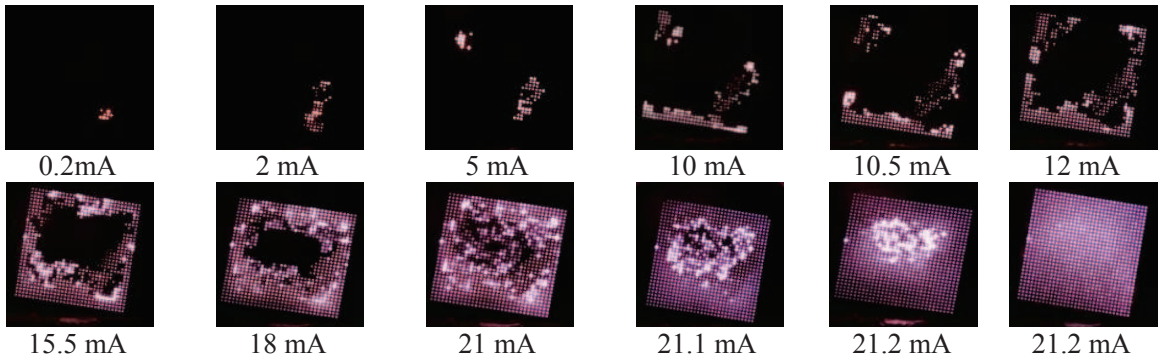

Figure 4.34: Ignition of 1024 cavities array with 100 µm diameter and 28 µm deep isotropic cavities operating in He at 350 torr for different discharge currents.

The average calculated current density (J) for 1024 holes is on the order of 0.192 $A.cm^{-2}$. The calculated power density (P_d) for 1024 holes is 261 $kW.cm^{-3}$. These calculations were performed by taking into account a discharge current of 21.2 mA and voltage of 1250 V. The value of J is on the order of the value estimated from the thermally affected zone reported in ref. ***[Dus-10]*** and by some other authors (ref. ***[Whi-59, Che-02]***).

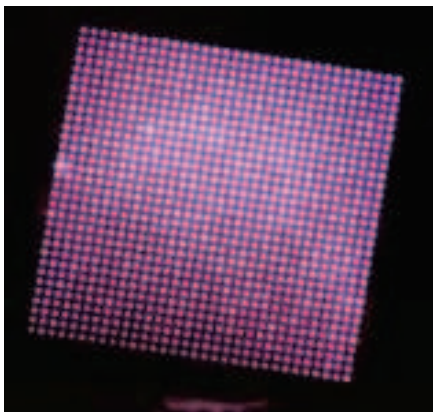

Figure 4.35: Fully ignited array with 1024 cavities having D = 100 µm and L = 28 µm isotropic cavity operating in He at 350 torr for 21.2 mA discharge current.

The same kinds of plasma characteristics were observed in p-type MDRs, reported in ref. ***[Dus-10]***. In addition, there was not any significant difference found in the V-I characteristics of n-type Si MDRs with 5 Ω.cm and 5000 Ω.cm resistivities. In addition, the microdischarge characteristics depend on many other factors (cavity shape, dimensions and surface) which can vary a little from a device to another. As a consequence, it remains difficult to distinguish the effect of doping density.

Cavity dimensions and effect of pressure on ignition

To see the gas pressure effects on the ignition of the microdischarges depending upon the cavity dimensions, a study was carried out using a sample having sub-arrays with different hole diameters. Figure 4.36 shows the three arrays of holes having 50 (bottom – "ANR"), 100 (top – "CNRS") and 150 µm diameters (center – "GREMI"). All cavities were 20 µm deep and isotropically etched. In the experiment, the He pressure was initially set to 900 Torr and the total current was held at 15 mA. The gas pressure was decreased to 350 Torr while a movie recorded the ignition of the microdischarges. The sequence of images is shown in figure 4.36 from 900 Torr to 400 Torr.

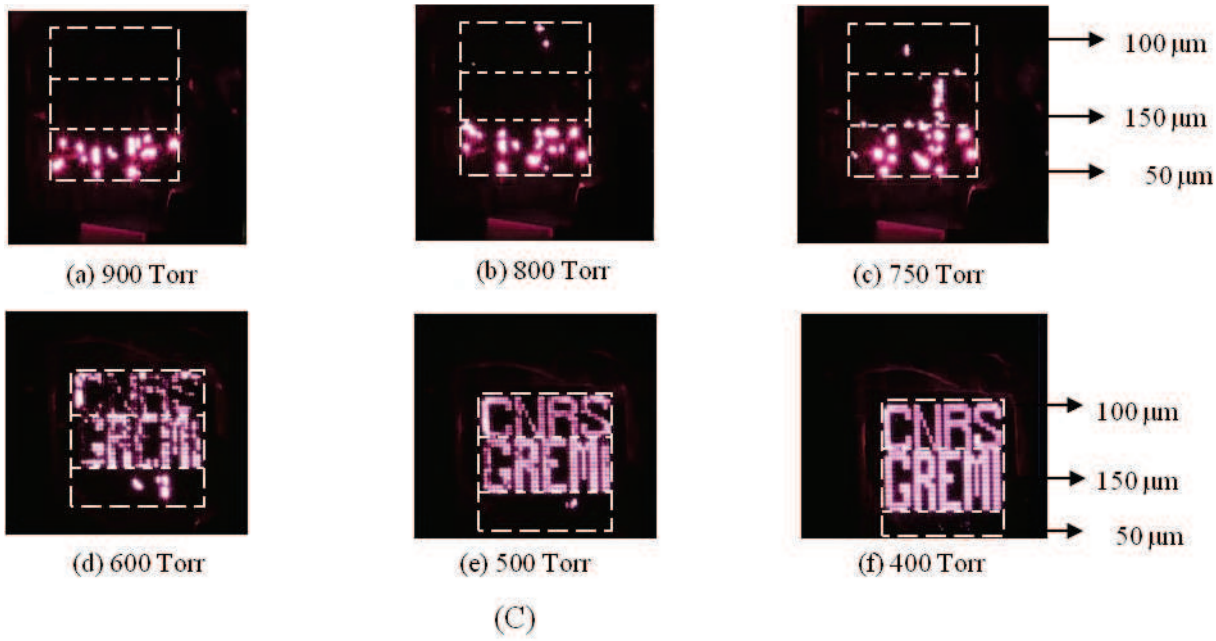

Figure 4.36: Effect of pressure variation in He gas environment on the arrays having different hole diameters 100, 150 and 50 µm on the same chip. (Dotted windows on the images indicate the border lines for different arrays)

Focusing on the images in figure 4.36, one can note that only the smallest diameter cavities ignite at the largest pressure (900 Torr). As the pressure decreases down to 800 Torr (Figure 4.36 (b)) a couple of 100 µm diameter cavities at the top ignite, but, before the whole array of 100 µm holes ignite, the 150 µm diameter cavities start to ignite as well (750 Torr Figure 4.36 (c)). From this analysis, it is clear that the ignition propagates from the 50 µm diameter discharges to the 150 µm hole region because of their proximity. With further pressure decrease, more 100 and 150 µm holes ignite and fewer 50 µm holes remain ignited. At 400 Torr, no 50 µm holes remain ignited and all the 100 and 150 µm discharges are operating. As shown in the breakdown studies of above sections, there are no such differences between 100

and 150 µm diameter holes for the breakdown voltage. But here, we clearly show that 50 µm diameter holes are preferentially ignited at high pressure ***[Kul-12]***. While all the cavities have the same interelectrode distance, the smallest diameter cavities ignite first at high pressure. In this configuration, the cavity diameter matters in the breakdown mechanism as reported in literature ***[Duf-10, Che-02, Whi-59, Ree-95]***. Note that in some other geometrical configurations, the interelectrode distance is more important than the diameter ***[Duf-10]***.

It is found that, when operating, 50 µm discharges are much brighter than 100 and 150 µm discharges. To study the difference in plasma intensities of different holes, we have calculated the current densities of the 50 µm holes ignited at 900 torr, and 150 and 100 µm holes ignited at 400 torr. The calculated current densities were found to be approximately 1.00 Acm^{-2} for the 50 µm holes, 0.30 Acm^{-2} for the 100 and 0.14 Acm^{-2} for 150 µm holes respectively. This difference in the current densities appears consistent with the difference in brightness. It was noticed with another characterisation of our MHCD arrays that plasma operation is more stable in shallowly etched isotropic cavities than in anisotropic cavities having the same depth. This might be due to a different electric field distribution. In the isotropically etched configuration, we can expect that the electric field should be more homogeneous inside the cavity, which can explain the stable plasma operation.

4.4 Exotic geometries

In this section, the studies of some special types of arrays are presented. Ar and He gases were used for the experiments.

4.4.1 TRENCH shape microdischarges

In this section, the experiments performed on the arrays with trench shape cavities (figure 4.37), are presented. The MDR chip contains four different sub-arrays of trenches with different dimensions. For each sub-array, the length of the trenches was fixed to 500 µm and the height was varied from 25 µm to 150 µm. Each of the four arrays contains trench structures in a matrix of 16 x 5 (see chapter 2).

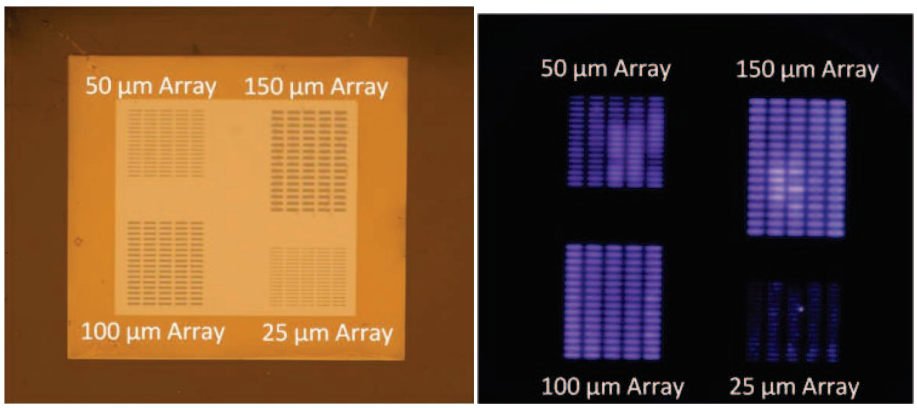

Figure 4.37: Silicon chip containing 4 sub-arrays made with 16 x 5 trenches (320 trenches) with 500 µm length and 25, 50, 100, and 150 µm height.

This kind of MDR device could be useful to study the ignition effect if only one dimension (in current case width) is varied. The experiments were performed in two different gases He and Ar, by varying the pressure from 10 Torr to 1000 Torr in DC regime in SP. These trenches were etched isotropically in silicon and having a cavity depth of around 30 µm. Figure 4.38 shows the trenches ignited at four different pressures of 50, 100, 300 and 1000 Torr at around 20 to 21 mA of current, (a) in Ar and (b) in He. From this figure, it can be seen that at low pressure, almost all trenches seem to be ignited or covered by plasma.

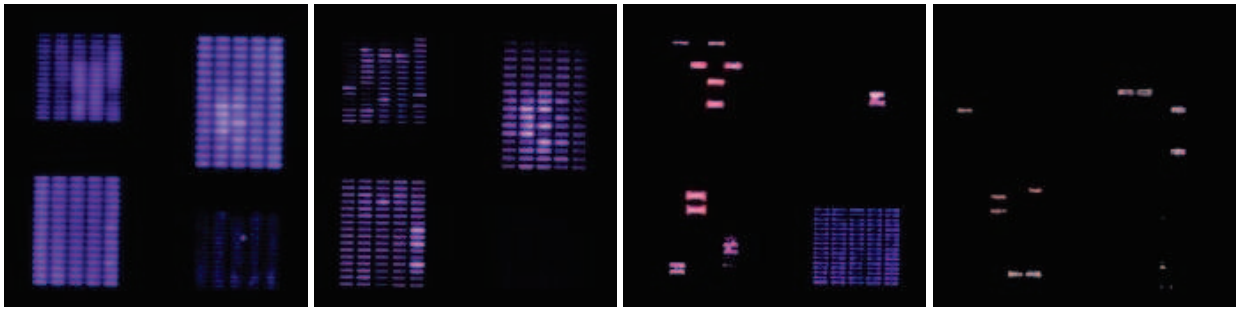

50 Torr 100 Torr 300 Torr 1000 Torr

(a)

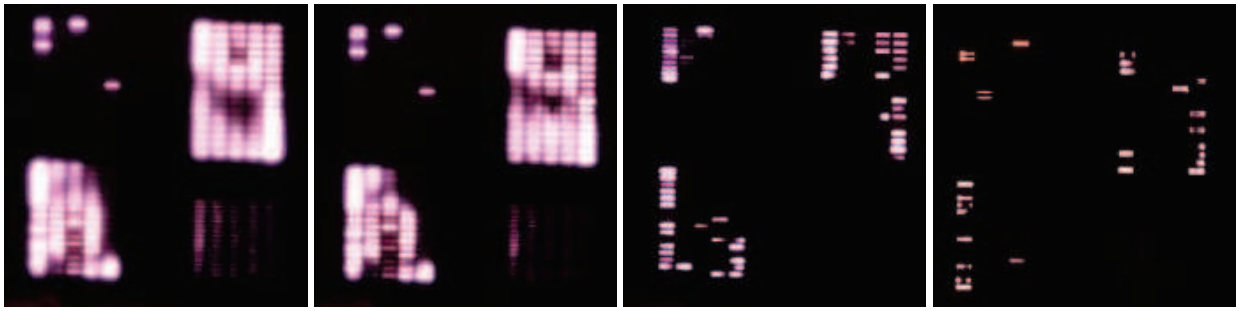

80 Torr 100 Torr 300 Torr 1000 Torr

(b)

Figure 4.38: Images of the Trench array ignited at different pressures at around 20 to 21 mA of current, (a) in Ar and (b) in (He).

At high pressure (around 1000 Torr), the plasma remains inside the cavity and only few cavities are ignited. At higher pressure, a phenomenon of edge ignition can also be seen, as shown in figure 4.39. In figure 4.39 (a) only the two cases at 50 Torr and 1000 Torr in Ar are shown. Further, from the image of 1000 Torr, different sizes of cavity are shown separately in figure 4.39 (b), to present the edge ignition phenomenon.

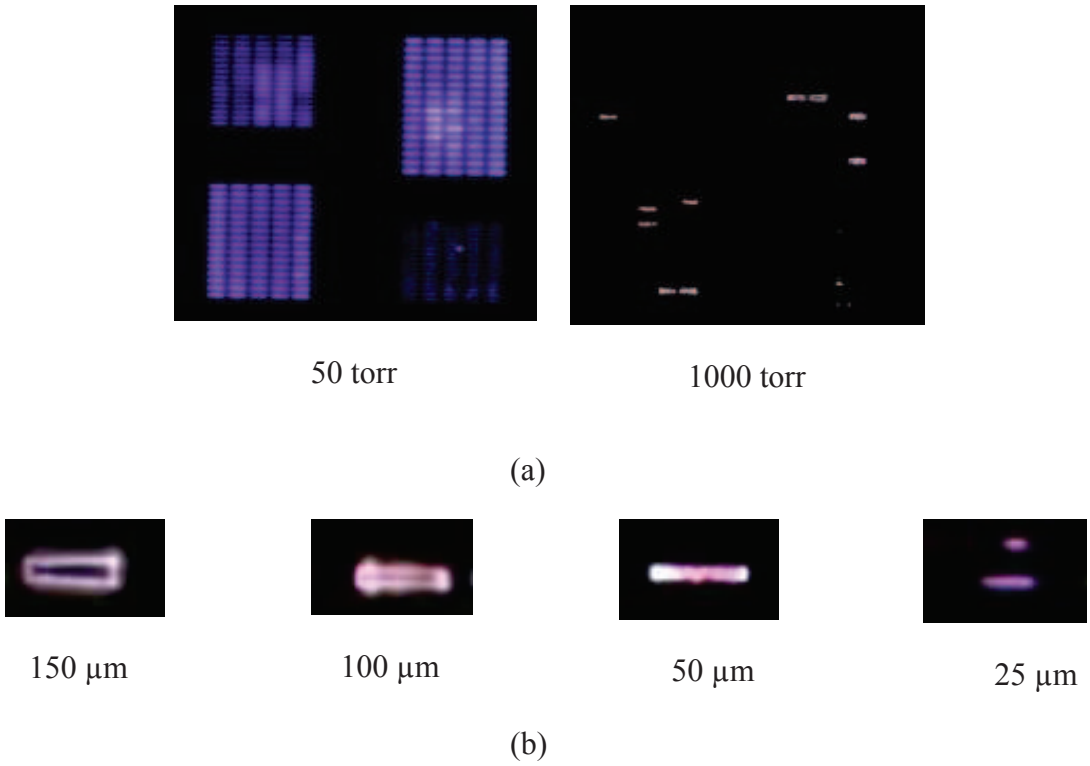

Figure 4.39: Trench array in Ar, (a) ignited at different pressures of 50 and 1000 Torr at around 20 mA of I_d, and (b) edge ignition phenomenon at high pressure (1000 Torr) in different trenches with 150 µm to 25 µm heights and 500 µm width.

In this case, microdischarges appear only at the edge or just at the boundary of the anode. In bigger trenches of 150 µm width, a dark region at the centre can be clearly seen and we observe an annular emission of the discharges. But for narrow trenches (50 and 25 µm), this dark region is not obtained. In fact, at high pressure due to shorter mean free path of the electrons, the discharge is more concentrated at the shorter interelectrode distance, that is at the edges of the trenches. In 25 and 50 µm trenches, this feature overlaps from the sides and this is why, we do not see any annular emission feature in the cavities having narrow dimensions.

4.4.2 Mixed Concentric Rings (MCR) arrays

In this section, the study of the arrays designed with an idea to ignite discharges in a wider range of pressures is presented. Figure 4.40 shows mixed Concentricrings (MCR) array of 196 (14 x 14) holes as discussed in chapter 2. The idea behind this design was to achieve all the igniting holes of the array at each pressure ranging from 100 Torr to 1000 Torr. Current experiment was performed in He. In the figure 4.40 (a), an image of the ignited array at 150 Torr in SP case can be seen. Each hole of the array can be seen with a discharge, at $I_d \sim 8$ mA. In the figure 4.40 (b), an image of the ignited array at 450 Torr in SP case, at $I_d \sim 12$ mA can be seen. Also in this case, an almost complete ignited array can be seen.

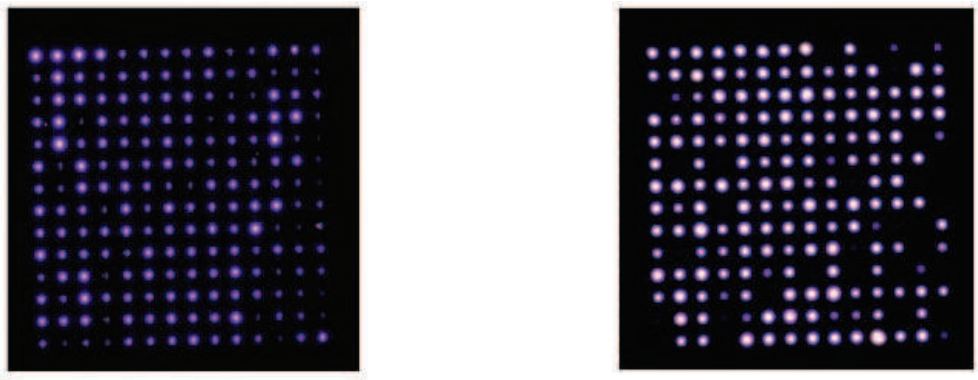

(a) (b)

Figure 4.40 : Camera images for MCR array of 196 (14 x 14) holes in He (a) at 150 Torr, ~8 mA (SP), and (b) at 450 Torr, ~ 12 mA (SP).

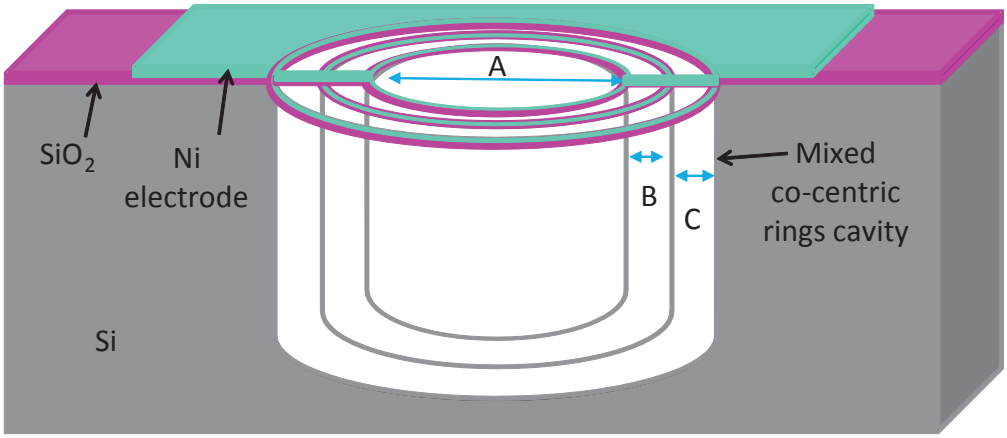

Figure 4.41: Design of concentric rings cavity with different opening dimensions (A, B, and C).

From these experiments, it is quite clear that the proposed design worked well in the case of SP for a pressure range from 150 Torr to 500 Torr. Here, it seems to fulfil the condition of having microdischarges at multiple pressure range.

This experiment was performed with an idea that, if the etching of the cavities in Si is performed in such a way that the cavities remain anisotropic up to few 10's of µm, then this configuration is supposed to provide a multi-wall cavity structure with different dimensions, as shown in figure 4.41. In this figure, the different Concentriccavities are shown with different cavity dimensions A, B and C. Each cavity opening is supposed to work at different pressure, i.e. the cavity with larger dimension is supposed to ignite at lower pressure and cavity with smaller dimension is supposed to ignite at higher pressure. Thus a multiple hole array with such a configuration could work at all pressures (e.g.: from 50 to 1000 Torr).

4.5 Failure and life time of the silicon Micro-Discharge Reactors

In this section, the effects of plasma operation on the cavities are presented. Then, the study of the life time for different configurations and the factors affecting it are given. These investigations were carried out using SEM and EDX analysing tools.

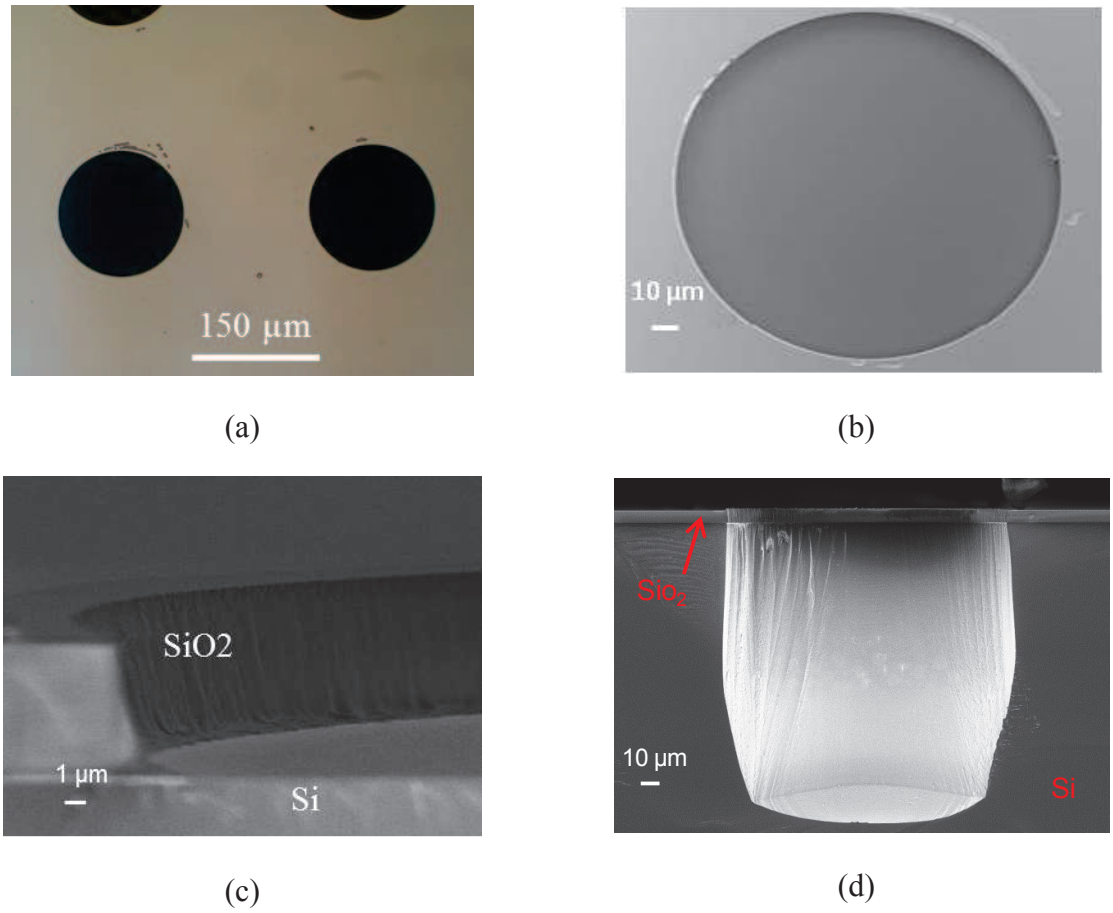

Figure 4.42: Microdischarge cavities before operation, (a) cavities with Ni layer on the top, (b) SiO_2 etched single cavity without top Ni layer (SEM image), (c) cross-sectional view of the cavity after cleaving (SEM image,) and (d) cross-sectional view of an anisotropically etched cavity (SEM image).

Figure 4.42 shows the microdischarge reactors before operation. Figure 4.42 (a) is an image of the cavities with the electrodeposited top Ni layer around them. Figure 4.42 (b) is a SEM image of a single cavity without any Ni layer and after the SiO_2 etching step. Figure 4.42 (c) is a SEM image showing the cross-sectional view of the cavity taken after cleavage of the sample. The 6 µm thick SiO_2 layer was etched. The nickel was removed during the cleavage. Figure 4.42 (d) is a SEM image of an anisotropically etched cavity. We can notice that the silicon surface is quite smooth before operation.

Plasma operation can affect the MDR cavity surfaces. Figure 4.43 shows the aspect of the cavities after plasma operation. Figure 4.43 (a) is an optical microscope image, showing the effect of plasma operation on the top Ni layer. Figure 4.43 (b) is an optical microscope image, showing the effect of the plasma operation at the bottom of the cavity. Figure 4.43 (c)

is a SEM image taken from the top of the cavity, showing the plasma effect on the SiO_2 layer and on the silicon at the bottom of the cavity.

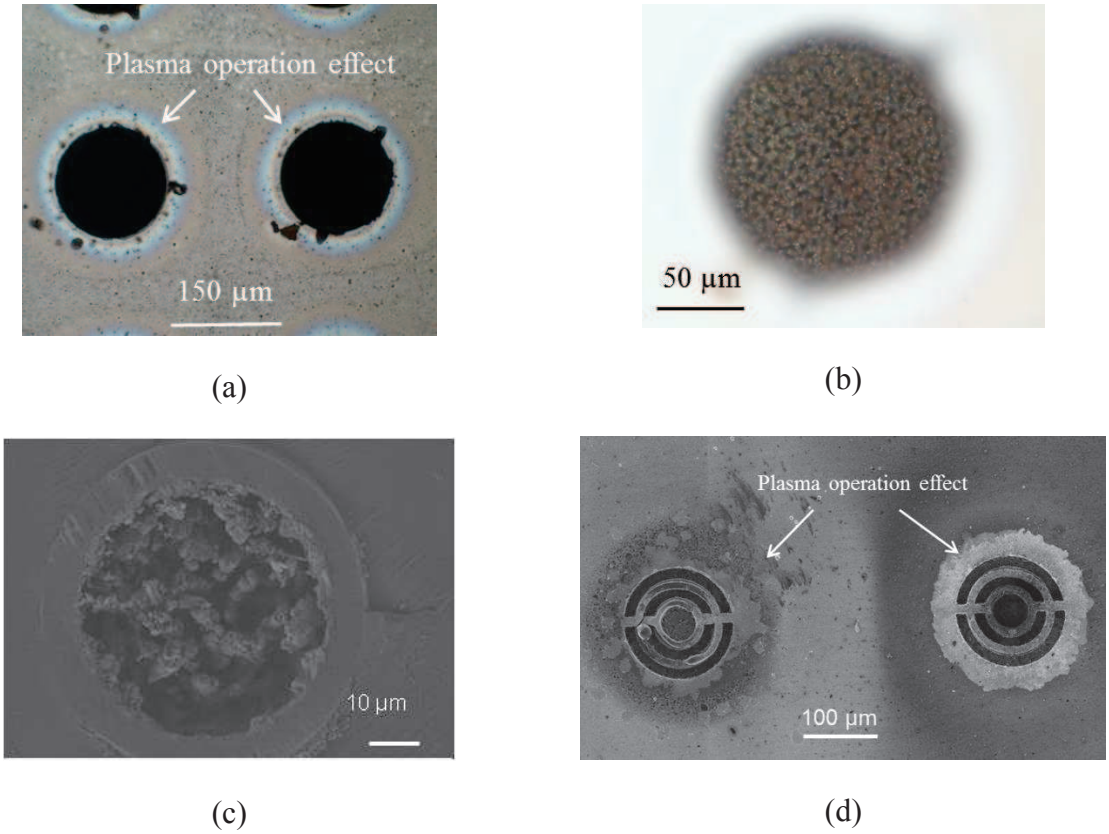

Figure 4.43: Thermally effected zones after plasma operation (a) top view of the cavities with Ni layer with a microscope, (b) view inside the cavity with Ni layer using a microscope, (c) SEM top view of a cavity without Ni layer, surrounded with a circular thermally effected zone on SiO_2, and (d) SEM top view of a cavity with Ni layer.

Figure 4.43 (d) is a SEM image, showing the effect of plasma operation on the Ni layer of the cavity. A few 10s of microns wide ring appeared around the cavity on the top Ni layer after plasma operation (Figure 4.43 (a) and (d)). This side corresponds to the anode, which means that the electron current was flowing on that area. As a consequence, a thermally affected zone appeared around this area. The surface of the Ni layer became colorized and rougher as observed at the microscopic scale. After removing the top Ni layer, it was found that the similar type of ring with the same dimension as on the Ni layer appeared on the SiO_2 layer (Figure 4.43 (c)). From these images, it is clear that the plasma affects significantly the different surfaces of the microdischarge reactors.

To know more about the effect of plasma operation, the values of J and P_d were estimated. For example, in the case of a single isotropic cavity with a hole diameter of 50 µm and a depth of 150 µm (section 4.2), the calculated values (from section 4.2) of J and P_d were 18.41 $A.cm^{-2}$ and 2208 $kW.cm^{-3}$ with the MDR operating in standard polarity. The values of J and P_d are quite high. Therefore, it is probable that a fraction of the electron current to the anode is injected on the top surface and should be the origin of the observed 10s of µm wide ring

[Dus-10]. A part of the current was driven through a larger ring around the cavity opening. This ring could be heated and as a result, eroded and roughened. It may also be that the metal evaporates at this location *[Dus-10, Kul-12]*.

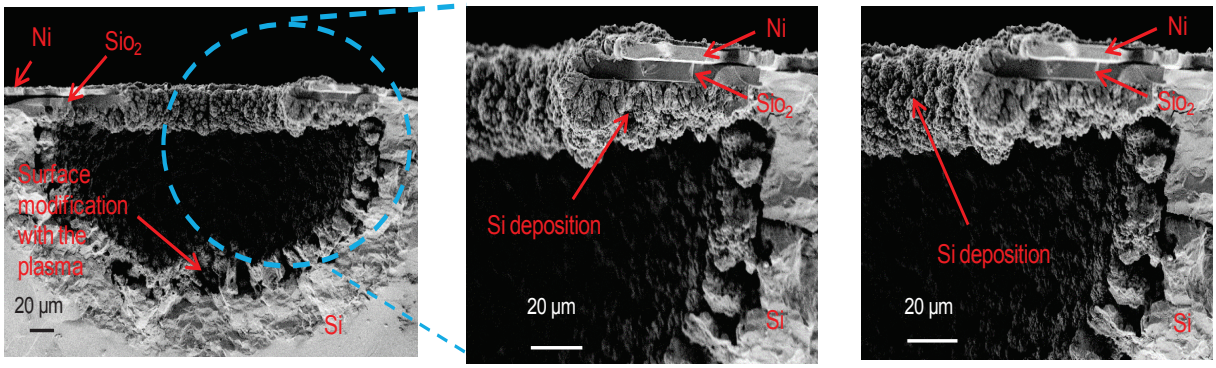

(a)

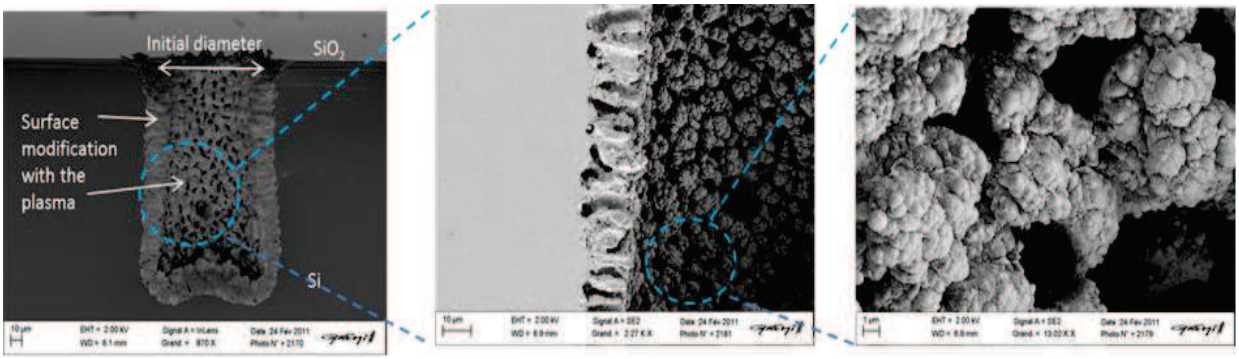

(b)

Figure 4.44: SEM images of micro-cavities after plasma operation, (a) isotropically etched cavity with 120 µm cavity depth in Si of 150 µm diameter and (b) single 160 µm deep anisotropic cavity with a diameter of 100 µm after plasma operation

Figure 4.44 shows the effect of the plasma operation on the microdischarge cavities. As observed, the Si surface is severely damaged. Figure 4.44 (a) shows an isotropically etched MDR after operation with a 150 µm diameter and a cavity depth of 120 µm. It appears that some silicon has been removed from the cavity and redeposited on the silicon sidewalls and over the SiO_2 insulator. We can even observe some deposition on the nickel layer as well. An Energy-dispersive X-ray spectroscopy (EDX) analysis on these cavities confirmed that the deposited material was Si (Figure 4.45).

Figure 4.44 (b), shows the effect of plasma operation on an anisotropically etched cavity having a depth of 160 µm and a hole diameter of 100 µm. The top Ni layer was removed before the SEM diagnostic. The images in figure 4.44 (b) clearly indicate that some kind of Si ablation and redeposition has occurred on the sidewalls. Due to this effect, the cavity diameter was modified. The original diameter is shown in figure 4.44 (b). A 20 µm thick layer of macro-porous silicon is then obtained on the cavity sidewall. Conventional cathodic sputtering cannot produce such anisotropic structures. Other mechanisms are probably

responsible for this silicon ablation. In fact, this effect might be due to a mechanism of transient micro-arcs inside the cavities during plasma operation ***[Mit-08]***.

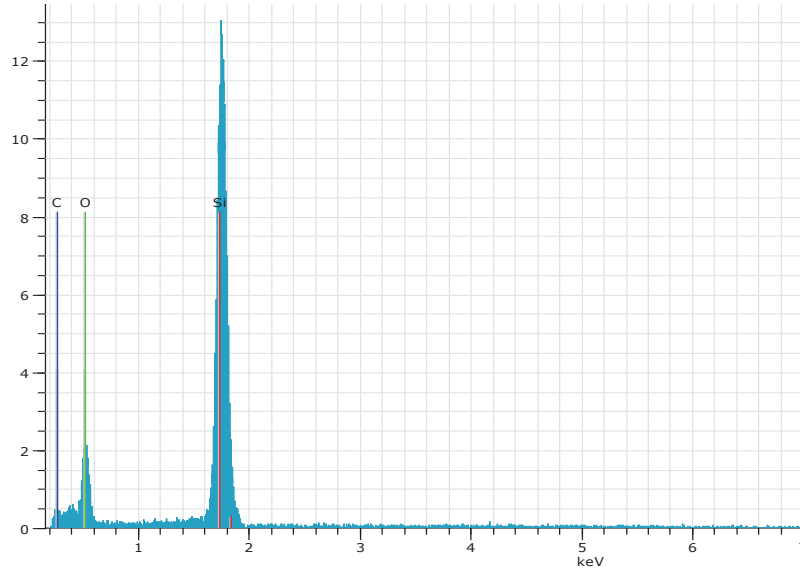

Figure 4.45: EDX analysis shows the sputtered Si deposition on the side walls of the cavities.

By electrically characterising the plasma of an array on different time scales, as already mentioned, many large current spikes were found. The microdischarge current and voltage waveforms (raw data plots) are shown in figure 4.46. The spikes in the current and drops in the voltage can be clearly seen in the three plots. The smallest time scale plot (µs) in figure 4.46 (c) shows the current spike in detail. Note that the observed spikes on the voltage and current waveforms of figure 4.46 (b) have the shape of a noise since they occur in both directions along the Y axis.

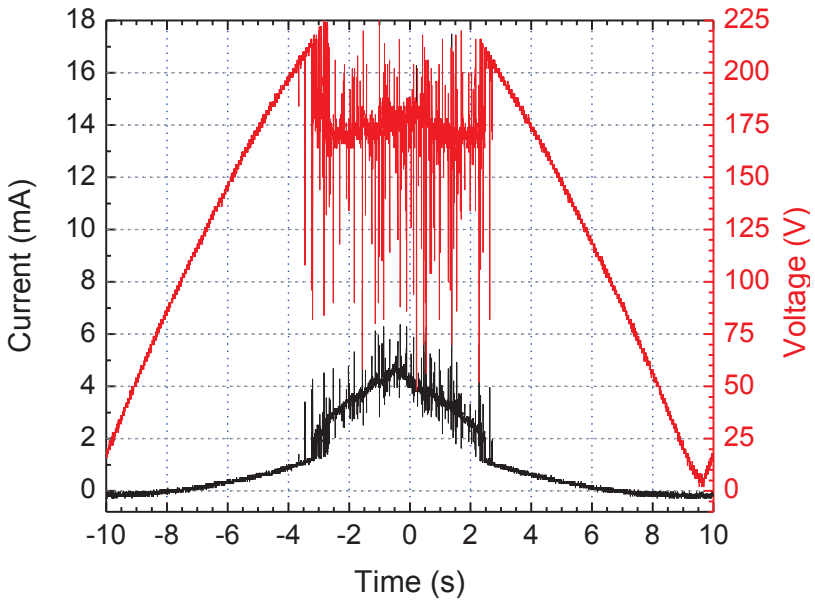

(a)

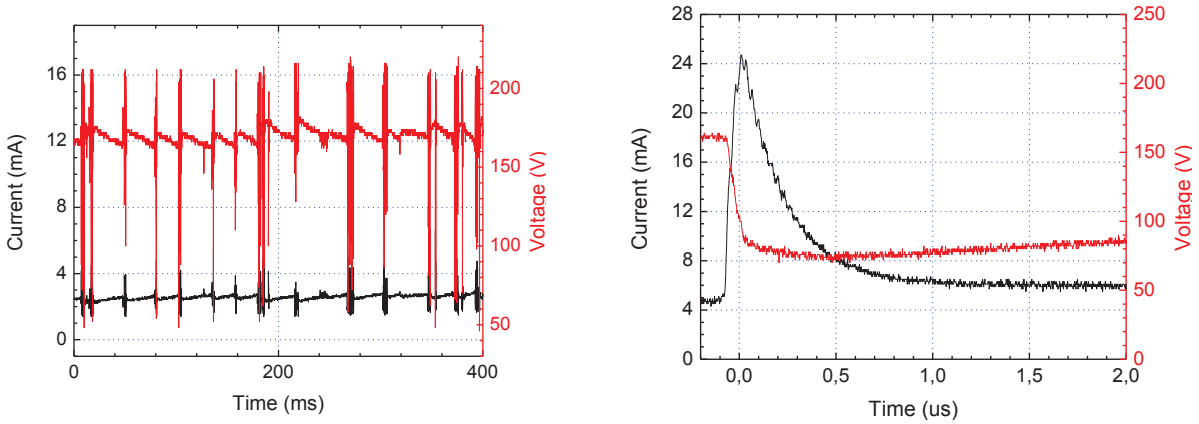

Figure 4.46: Electrical characterisation of the MDR arrays with mixed Concentricholes in He at 450 Torr pressure in SP (a) normal time window, (b) in ms time window, and (c) in µs time window.

From figure 4.46 (c), one can clearly see the large current peaks with less than 0.5 µs width that are produced during the plasma operation. Here, the current peak has a typical amplitude of few tens of mA (here 24 mA) and the voltage drop is 75 V. As already noted above, one can speculate that the cathode heats and melts during those current spikes by the formation of a micro-arc and then the cathodic material re-deposits on the cavity sidewalls.

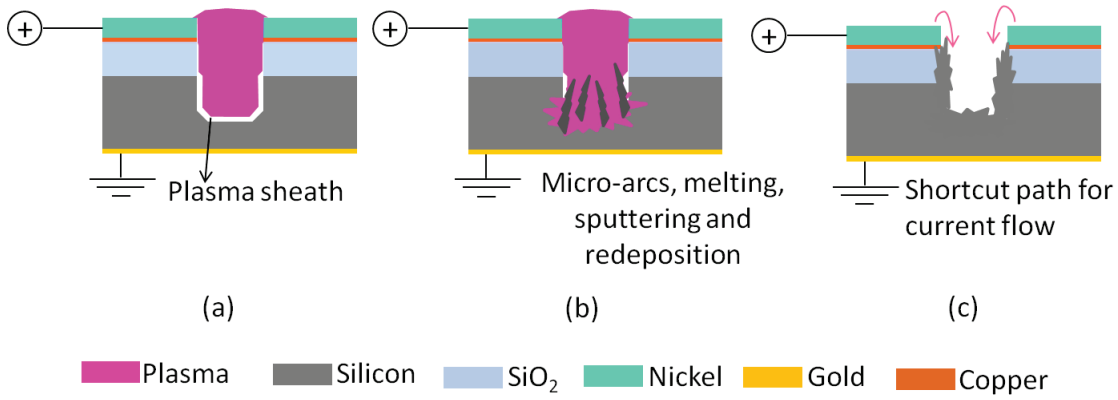

Figure 4.47: Phenomenon explaining the life time of a micro-discharge reactor (a) normal plasma ignition, (b) micro-arc erosion effect with material redeposited on the side walls of the cavities, and (c) short-cut path due to the cathodic material deposition on the side walls which induces the microdischarge switch off.

Figure 4.47 is an illustration of the mechanism: figure 4.47 (a) shows the normal plasma operation inside the microdischarge reactors. Figure 4.47 (b) illustrates the envisioned transient micro-arcs causing ablation of the silicon on the sidewalls as well as redeposition. Figure 4.47 (c) shows the short-circuit caused by the redeposition on the SiO_2 ring between the two electrodes. Figure 4.44 (a) (right) clearly shows the silicon redeposition on the SiO_2 layer. Some of the microdischarge reactor chips were resurrected by performing a second SF_6 etching process to remove the redeposited Silicon from the SiO_2. This clearly shows that the life time is limited by Si redeposition across the dielectric.

From the SEM analysis of different MDR cavities used in different experiments, it was found that the duration of the plasma operation also affects the Si projection from the side walls of the cavities. SEM images of such type of three microreactors with single hole were compared after the cleaving. From the images, it is clear that, if the plasma runs for longer duration inside the cavity, then it etches more and more silicon from the sidewalls of the MDR. Figure 4.48 shows three single hole cavity MDRs anisotropically etched, after plasma operation used for different experimental purposes with different durations of (a) 10 - 12 minutes with D = 150 µm and L ~ 160 µm, (b) few tens of minutes (25 - 30 minutes) with D = 100 µm and L = 200 µm, and (c) few hours (1.5 - 2 hours) with D = 150 µm and L ~ 500 µm respectively. From these images, it can be seen that the etching of Si in different cavity walls have different depths. The etched Si micro-cavity depths were found on the order of ~ 5 µm, ~ 14 µm, and ~ 25 µm in the figure 4.48 (a), (b), and (c) respectively.

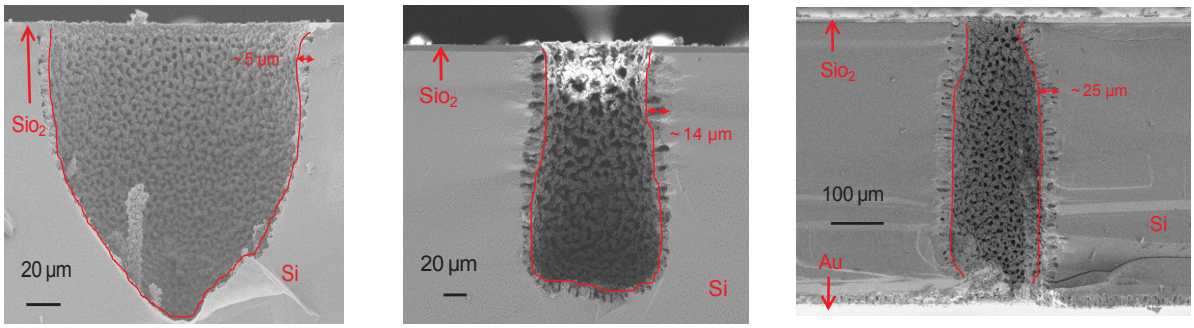

(a) (b) (c)

Figure 4.48: Anisotropically etched single hole cavity MDR, after plasma operation of (a) few minutes (10-12 mins) D = 150 µm, (b) few tens of minutes (25-30 minutes) D = 100 µm and (c) few hours (1-2 hours) D = 150 µm.

The typical microdischarge reactor life time ranges from a few minutes to a few hours depending upon the injected current, the dimensions and the structure of the cavities. From the results shown in this section, it can be concluded that the MDR cavities that are deeply etched can survive for a longer time. It also depends on the cavity configuration: for example, a multiple hole array has a longer life time than a single hole MDR. Similarly, the array with etched cavities can last longer (few 10s minutes to a few hours) as compared to the array with non-etched cavities (a few seconds to a few minutes).

4.5.1 Suggestions for the longer life time of MDRs

In this sub-section, the possible ideas to have a longer working life time for the Si based microdischarge reactors in DC regime are given. Two suggestions are proposed and described in the following paragraph.

1. Deep etching: With the deep etching of Si cavities (isotropic or anisotropic), the MDR can work for a longer duration. As discussed in the last section (figure 4.48 (c)), through hole MDR is more suited for a MDR operation of few hours.

2. Metal deposition inside the cavities: Longer life time of the MDRs is obtained if the cathodic surface (e.g. Si) is not affected by the micro-arcs or high temperature. To avoid sputtering of Si, a thin layer coating of a suitable material inside the cavity should be helpful. It is suggested to deposit a metal layer coating inside the cavities, on the top of Si cathodic surface. To deposit metal on the top of the Si, two methods are suggested.

The first suggested method consists of depositing a metal layer by electrochemical deposition. By following this idea, the deposition of nickel (Ni) metal was tested on the top of Si surface inside the cavities. Figure 4.49 shows the SEM images for the deposited Ni in (a) an isotropically etched cavity. Figure 4.49 (b) shows a part of the cavity selected to perform EDX experiment. Figure 4.49 (c) and (d) are the EDX results confirming the Ni metal deposition on the top of the Si surface inside the cavity. These results confirmed the presence of Ni on the selected area (inside the cavity).

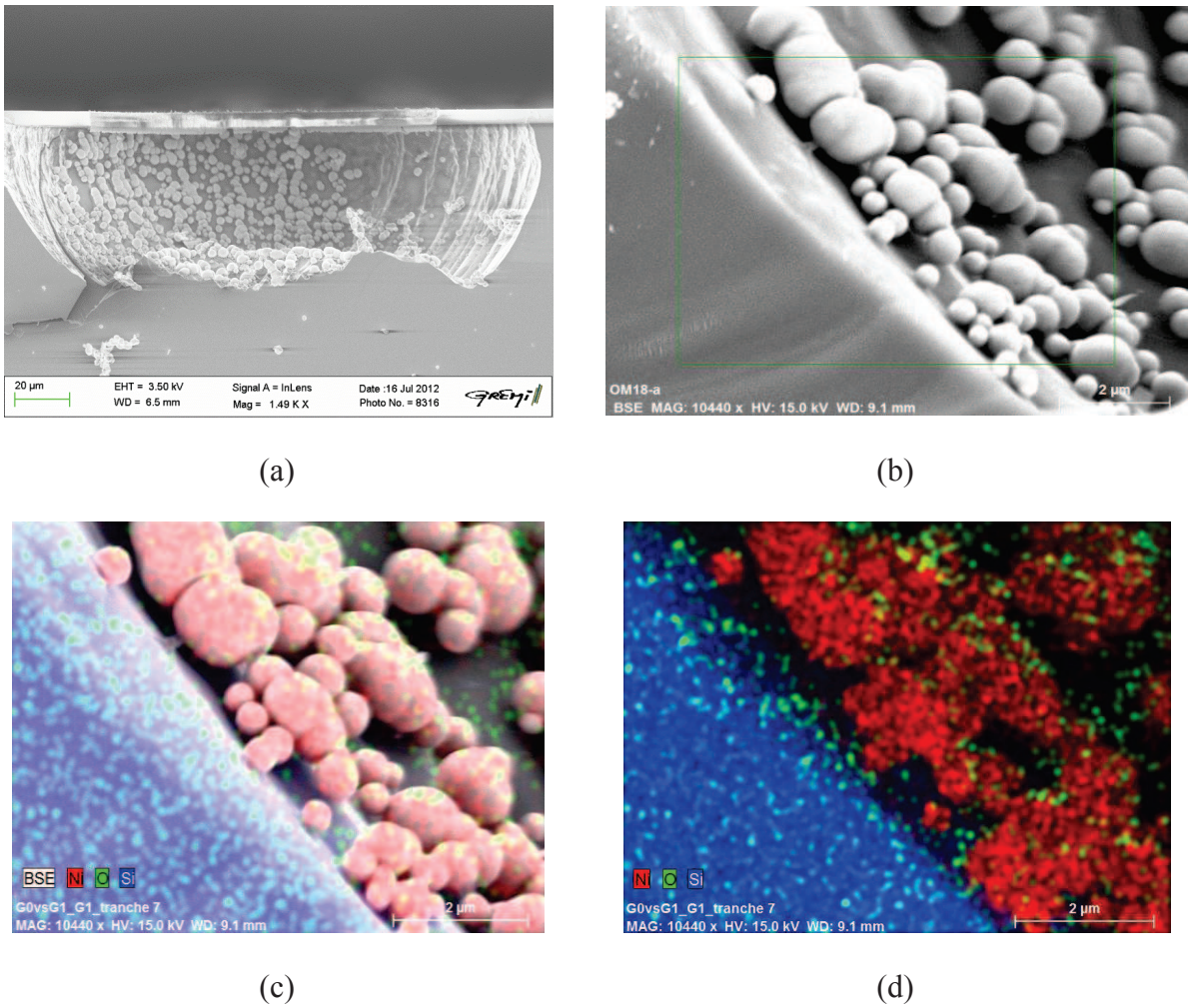

Figure 4.49: SEM images for electrochemically deposited Ni on the Si surface inside the MDR cavity (a) a complete isotropic cavity, (b) part of the cavity that is used for EDX analysis, (c) and (d) showing EDX results with the material composition inside the cavity.

In this technique, the most important limitation is the hydrophobic nature of the Si. To implement electrochemical deposition technique, first, the Si surface needs to become hydrophilic using oxygen plasma. But with oxygen plasma, a SiO_2 layer can form inside the

cavity, which can act as an insulating coating. This could again lead to some problems for the metal deposition. Thus, the metal deposition was not uniform inside the cavities (Figure 4.49).

The second suggested method is to deposit the metal inside the cavities by using metal sputtering deposition technique. Results showed that metal can be deposited quite uniformly on the top of the Si surface inside the cavity. Figure 4.50 (a) shows an isotropically etched cavity of the 4 x 4 array with a cavity diameter of 150 µm (L = 160 µm) and cavities interhole distance of 200 µm. Tungsten (W) metal with a thickness of ~1 µm was sputter deposited inside the cavities of this array. Figure 4.50 (b) shows a zoomed image of the side wall of the cavity with W. A metal layer with a thickness of ~ 700 nm can be seen from the image. Thus, using this method, the deposited metal layer seems more uniform on the top of the Si surface inside the cavity, as compared to the electrochemical deposition technique.

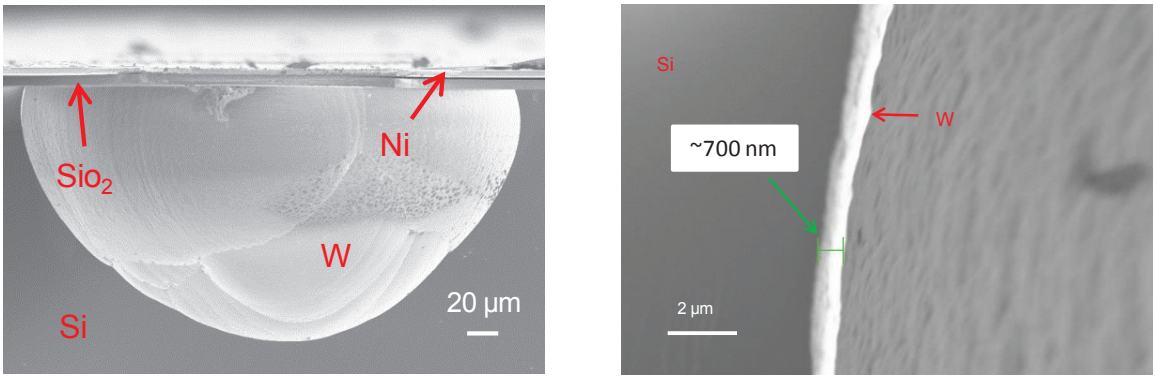

Figure 4.50: SEM image of a Si isotropic cavity (D = 150 µm and L = 160 µm)from the array of 4 x 4 holes (200 µm interhole distance) with deposited Tungsten (W) metal, (a) full cavity and (b) a zoomed part of the side wall of the cavity.

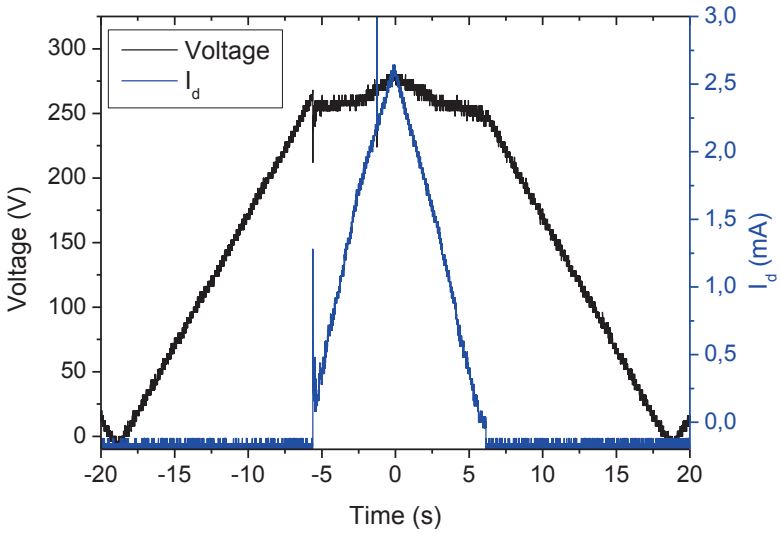

Figure 4.51: Voltage and current plots vs. time for 4 x 4 array with a cavity diameter of 150 µm (L = 160 µm isotropically etched) and interhole distance of 200 µm in 150 Torr He, with a deposited thin layer of Tungsten (W) metal inside the cavities. The thickness of the deposited metal layer is ~ 1 µm.

Electrical characterisations were made with this array. Figure 4.51 shows voltage and current plots vs. time in 150 Torr He. From this figure, it can be seen that the plots are smooth and they have a minimum level of noise as compared to the figure 4.46.The minimum level of noise in the plots indicates the absence of micro-arcs inside the cavity. Hence, it can be assumed that in the absence of the micro-arcs, the MDR arrays could be able to survive for a long duration. Note that these voltage and current waveforms were recorded within the very first experiments performed with this microdevice. We did not want to use it for a long time in order to analyse it by SEM, when no high current pulses were obtained.

But the main drawback of this technique is the deposition of sputtered metal on the other layers, i.e. on the top electrode layer and on the SiO_2 dielectric layer. This makes difficult to use the MDR after the metal deposition. As MDR becomes a conductor due to the metal contact between the two electrodes with the sputtered metal.

From the results presented in this section, it can be concluded that, plasma operation could cause damages on the inner Si surface of the cavities. This damage mainly seems to be the result from the locally generated micro-arcs inside the cavities during the plasma operation. These micro-arcs were able to etch the Si from the cavities and the etched Si then could deposit on the side walls of the microdischarge reactor. This Si deposition leads to a short circuit between the electrodes and cause the failure of the MDR.

From the experiments, it is concluded that deeply etched cavities can have longer life time as compared to the non-etched cavities. Also multiple hole array can have longer life time as compared to the single hole MDR. To extend the life time of the microdischarge device, the idea of protecting the inner Si cavity surface with a more or less thin metal layer was suggested. Electrochemical metal deposition and metal sputtering deposition techniques can be used for this purpose. Results from the metal sputtering deposition technique showed a smooth uniform deposition of the W metal inside the cavity. The V-I characteristics of the MDR array with W deposition, showed the absence of micro-arcs during the plasma operation. Hence, the idea of protecting the inner cavity Si surface with a thin metal layer is quite promising to provide a longer life time to the Si based microdischarge devices.

4.6 Conclusions

In this chapter, Si based MDRs were presented. Single hole MDRs with anisotropic, isotropic, and through hole cavities were studied with electrical and optical characterisations. Each of these configurations was compared for the SP and RP cases. In SP case, plasma remained concentrated inside the cavity of MDR. In the case of closed Si cathodic cavity, an abnormal glow regime was obtained due to the limited cathodic surface of the cavity. In RP case, a plasma spread over the Ni cathodic surface and a normal glow regime were obtained due to a larger cathodic surface. Breakdown studies for the single hole MDR were performed and breakdown voltage was found higher generally in SP case as compared to the RP case. The breakdown voltage for Ar microplasma was found higher as compared to the He case for a same pressure. Non-etched or shallowly etched single hole MDRs have lower breakdown voltage than the deeply etched single hole MDRs. Two types of hysteresis effects for single hole MDR were observed. Simulations based on the software GDSim (Glow Discharge

Simulation) for single hole anisotropic MDR with a cavity depth of 150 μm and with a cavity diameter of 150 μm were presented for two different discharge currents: 1.2 and 5.3 mA. From these simulations, an electron density of the order of 10^{14} cm^{-3} was calculated. The deduced sheath thicknesses for 1.2 and 5.3 mA were 37 and 27 μm respectively. The simulated gas temperature was having a maximum value of 325 K for I_d 1.2 mA and 425 K for I_d 5.3 mA. These simulated gas temperatures were found in agreement with the experimentally deduced gas temperature using OES method. For the I_d of 3 mA and 5 mA the deduced gas temperatures were 410 ± 30 K and 450 ± 30 K respectively.

Studies of multiple hole arrays, having different electrode configurations were presented. Different array characteristics were compared and discussed. It was found that the arrays with isotropic cavities can provide a more stable discharge as compared to the anisotropic cavity arrays. The ignition of discharges in an array was found to start from the side cavities and then move towards the center of the array. For an array, if the cavities are deeply etched, then a valley type dip can be observed in the V-I curves, indicating the ignition of single or multiple holes with the increasing ramp of the applied voltage. Statistical ignition time was found less for the multiple hole array as compared to the single hole MDR. In the same study, it was seen that multiple hole array can have a higher discharge current as compared to the single hole MDR for an ignited cavity. The characteristics for some exotic multiple hole arrays were shown in this chapter. In case of the array with trenches, edge ignition phenomenon was observed for the bigger trenches at higher pressures. The characterisation of a Concentricring array showed the possibility to ignite the complete array at multiple pressures. The phenomenon responsible for the failure of the devices was studied and explained, using SEM and EDX analysis. Some suggestions to increase the life-time of the Si based microdischarges were also presented.

Chapter 5

Characterisation of Si based microplasma reactors in AC

5.1 Introduction

In this chapter, experimental results related to microdischarges operating in AC regime are presented. Results obtained for single hole devices and multiple hole arrays having different arrangements are discussed. First, V-I characteristics including some general characteristics of the devices are shown. Subsequently, dynamics of the devices and other related behaviours are explored using Phase Resolved Optical Emission Spectroscopy (PROES). In particular, wave like behaviour, effect of change of pressure and effect of change of frequency are presented.

5.2 Discharge characteristics

In this section, we present some general characteristics including voltage and current characteristics for single hole and multiple hole arrays. For these experiments, mainly Ar and He gases were used. The voltage and current characteristics were recorded using oscilloscope (DSO) controlled via computer as explained in the chapter 2. A photomultiplier tube (PMT) was used to measure the intensity of the devices. PMT signals were recorded via the same oscilloscope. MDRs were having anisotropic cavities with cavity a depth of 2 μm or 8 μm. These experiments were performed in collaboration with the microplasma group of J. Winter and V. Schulz-von der Gathen at Ruhr University Bochum (RUB), Bochum, Germany.

5.2.1 Electrical and optical time resolved characterisation of an array

5.2.1.1 Current, voltage and emission time evolution

Figure 5.1 (a) shows the voltage and current characteristics for a 100 μm diameter single hole MDR in He at a pressure of 500 mbar. A 590 V peak to peak triangular voltage waveform was applied to the sample at 10 kHz. Figure 5.1 (b) shows the voltage and current characteristics for a hole array composed of 1024 cavities having a diameter of 50 μm in Ar at a pressure of 980 mbar. A 580 V peak to peak voltage was applied in this case.

Both graphs show similar types of behaviour. In the plots, a voltage signal (black solid line), a current signal (blue dot-dash line) and a PMT signal (red dashed line) are shown. With remote triangular signal ramp, voltage starts rising. At some breakdown point in the first positive half period, microdischarges ignite and PMT signal shows the emission peak. After few microseconds, discharges collapse and PMT signal drops to zero. With the increase in voltage along the rising ramp, the discharge reignites and again PMT signal shows the emission peak. Such a pulse in the PMT signal can be observed in Figure 5.1 (b). This leads to a kind of multi peak PMT or current signals in both positive and negative half periods. This effect could be

related to the asymmetric electrode designs and is discussed in details in the next coming sections.

Near the maximum voltage of positive half cycle, the discharge extinct until the discharge reaches the breakdown voltage in the next negative half cycle. The same phenomenon of ignition is repeated in the negative cycle. In general, current signal has very low amplitude. For a single hole MDR, the amplitude of the current signal is lower than the one from an array.

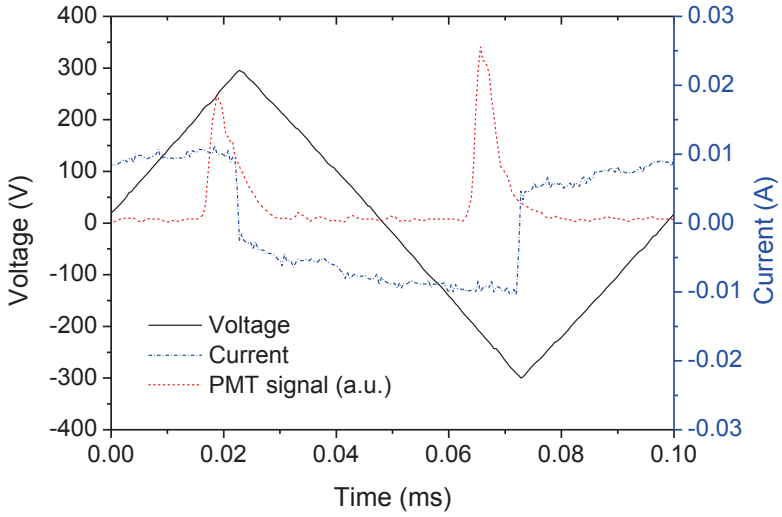

(a)

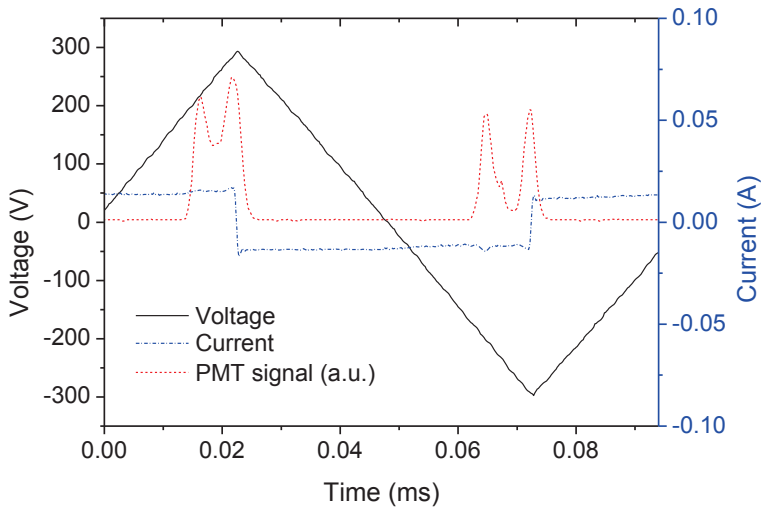

(b)

Figure 5.1: Voltage and current characteristics for 10 kHz frequency (a) single hole device with D = 100 µm in 500 mbar He at 590 V and (b) 1024 hole array with D = 50 µm in 980 mbar Ar at 580 V.

The fabricated devices are capacitive in nature due to their electrode designs, the displacement current can be given by the derivative of the applied voltage signal. For the experiments, we measured and analysed the discharge current and the emissivity. In general,

the voltage and current waveforms were found to be comparable for all MDRs running in AC. Note that the voltage and current waveforms that are shown in the above figures are not averaged and give the instantaneous values during a particular cycle.

These measurements are not sufficient to analyse the ignition dynamics of an array. We made some Phase Resolved Optical Emission Spectroscopy (PROES) measurements to obtain a space resolved characterisation of the MDR ignition during one cycle.

As mentioned in the first chapter, it was previously observed that the ignition of individual microplasmas do not occur at the same time, but rather successively just like an ignition wave as reported by Waskoenig J. and Böttner H. in refs. ***[Was-08, Boe-10].*** These experiments had been carried out using samples prepared in G. Eden's lab. We have proposed some new geometries to further investigate the ignition behaviour of original reactors.

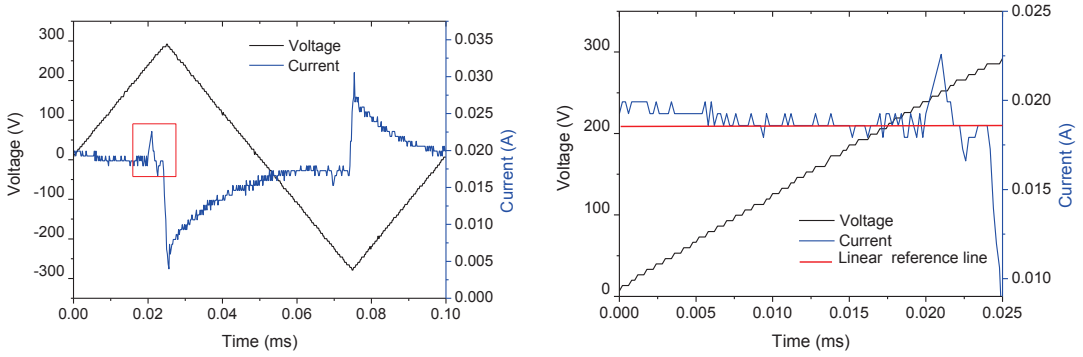

(a) (b)

Figure 5.2: (a) Voltage and current waveforms of 1024 hole array with D = 100 µm at 10 kHz in 500 mbar Ar at 570 V and (b) zoomed in part (marked by red square in the plot (a)) showing current peak with linear reference line (red solid line) for the current amplitude measurements.

Figure 5.2 (a) shows the voltage and current waveforms for a 1024 hole array with hole diameter (D) 100 µm in AC with 10 kHz frequency. The Ar gas pressure was 500 mbar and the peak to peak voltage was 570 V. We measured the full width at half maximum (FWHM) of current peaks, for both positive and negative cycles. Figure 5.2 (b) shows the zoomed part of the current peak during positive half cycle (indicated by a red square in Figure 5.2 (a)). For the measurement of the current peak, a linear reference line is marked along the displacement current plateau level and serves as base line. Typically, a current peak amplitude of 4 mA was obtained with a FWHM of 1.2 µs. The value of the discharge current corresponds to the sum of currents, distributed in the cavities of the array. For the measurements, a frequency range between 5 and 30 kHz was used. At lower frequencies (<5 kHz), the current signal to noise ratio was too small, current peaks were not clearly identified and current pulses could not be detected fully, although PMT pulses were observed. For this array, the current density was calculated by considering the cavities as cylinders having a depth of 4 µm and a radius of 50 µm. The calculated maximum current density per cavity was found around 43 $mA.cm^{-2}$. Note that all cavities are not necessarily ignited at the maximum of the current pulse. Again, during this current pulse, a wave of ignition is propagating through the array. The maximum of the

current pulse corresponds to a maximum of ignited discharges, but may be not all of them. So this value is a minimum value of the current. In this case the current density is much lower than in DC. Indeed, in DC, we found a current density of 0.8 A.cm^{-2}, which is about 18 times higher than in AC.

5.2.1.2 Optical space resolved characterisation of the array

Examples of time integrated emission for multiple hole arrays are shown in figure 5.3. Figure 5.3 (a) shows a time integrated camera image of a 1024 hole array operating at 10 kHz in 500 mbar of Ar. The diameter of each cavity was 150 µm. Figure 5.3 (b) shows an image of mixed trench (4 x 5 x 16) array with rectangular cavities running at 10 kHz with 570 V voltage peak to peak in 500 mbar Ar.

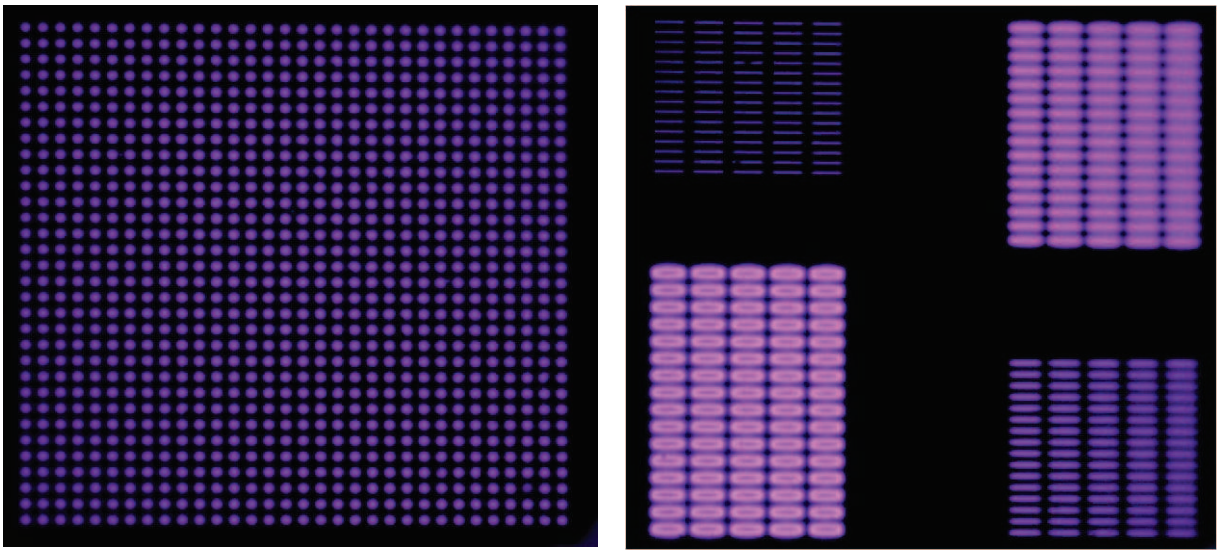

(a) (b)

Figure 5.3: Time integrated images taken by a photo camera, showing the discharge mode of the AC operated MDRs with 10 kHz frequency in 500 mbar Ar (a) 1024 hole (32 x 32) array with D = 150 µm and (b) mixed trench (4 x 5 x 16) array.

This MDR chip has four different sub-arrays having cavities width 25, 50, 100 and 150 µm and length 500 µm.

In figure 5.3 (a), we see that all microdischarges emitting within this exposure time. The emission seems quite homogeneous on the array. Note that the intensity of the array is much lower than what we obtained in DC. This is why the exposure time was around 1/30 seconds to record the emission of the array. In figure 5.3 (b), we also see that each sub-array emission is quite homogeneous. The intensity and appearance are different from a sub-array to another. For 25, 50 and 100 µm trench sub-arrays, the emission seems homogeneous in each cavity. But in 150 µm trench sub-array, the emission within the trench is not homogeneous: a ring shape of emission is obtained.

These images are interesting to have a rough idea of the emission, but since the images are time integrated over a thousand of cycles, we cannot infer the dynamics of ignition of these arrays. This is why PROES and time resolved optical measurement using the PMT are

necessary to better understand the mechanisms. In the next part, we present the results for a single hole device, before showing the results for arrays.

5.2.2 Single hole MDR

Most of the published studies for MDRs operating in AC were carried out on multiple hole arrays ***[Was-08, Boe-10]***. But to better understand the mechanisms involved in a multiple hole array, we first studied the ignition dynamic of a single hole device. In that way, we can deduce if an effect is due to the individual cavity itself or if it is rather due to nearby cavities and proximity effects. For this study, we designed several diameters of single hole MDR to carry out this study and investigate the effect of the diameter on the ignition.

5.2.2.1 Effect of frequency

Operating AC frequency can affect the behaviour of the microdischarges. In this section, we present the results related to the operating frequency variations. PMT signal was considered instead of discharge current (I_d) to study the different characteristics of the MDRs. In fact, the I_d amplitude is quite low and it was sometimes hard to distinguish I_d from the noise present in the V-I characteristic plot. PMT signal follows the I_d signal. An example of I_d and PMT signals is shown in figure 5.4 for a 50 µm diameter single hole during a positive half cycle at 5 kHz and for 750 mbar of Ar. We can clearly check that the PMT signal follows the I_d peaks.

Figure 5.5 shows PMT and voltage signals for a 100 µm diameter single hole in 760 mbar of He. The peak to peak applied voltage was 600 V and the frequency was 10 kHz. On the same graph, MDR evolution images are also shown with the PMT signal. During the positive half cycle, we see that the breakdown voltage is at around 250 V on the voltage ramp, which corresponds to the sudden increase of the PMT signal. During this positive half cycle, a single pulse is obtained indicating the ignition of the discharge. The ignition of the discharges can also be seen by the related inset images. It lasts for approximately 23 µs in pulse width. After this pulse, the voltage between the two electrodes is too low to maintain the microplasma. The microplasma could ignite again if the applied voltage was rising further to reach again the breakdown voltage. But before reaching this value, the applied voltage reaches its maximum and the voltage ramp is inversed. During the negative half cycle, we observe that the breakdown is reached for a voltage of -150 V on the voltage ramp, which is lower in absolute value than the one obtained during the first half cycle. A first pulse of the PMT signal appears. Its duration and intensity are slightly smaller than the one obtained in the positive half cycle. The applied voltage keeps rising in absolute value, and a second pulse is obtained when the applied voltage reaches -280 V with the voltage ramp. This time, the PMT pulse is quite similar to the one obtained in the first half cycle. This third pulse is followed by a broader semi-developed PMT pulse.

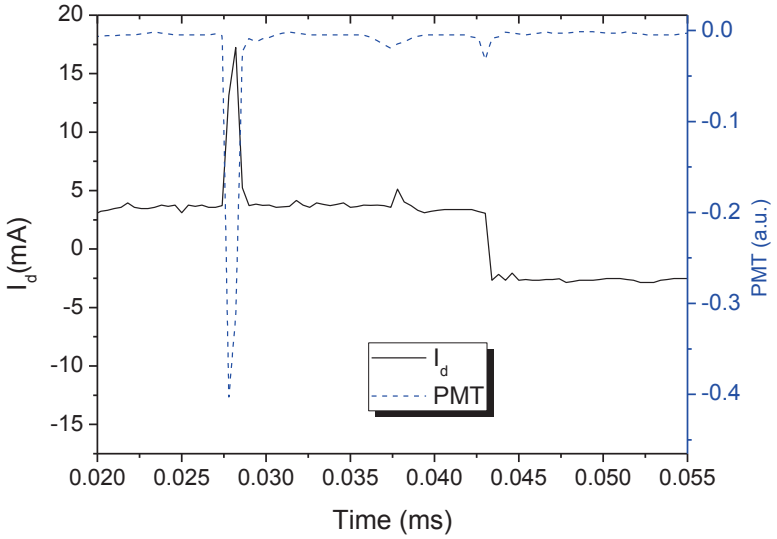

Figure 5.4: Discharge current (I_d) and PMT behaviour w.r.t. time for a single hole MDR with a cavity diameter of 50 µm during the positive half cycle at 750 mbar Ar.

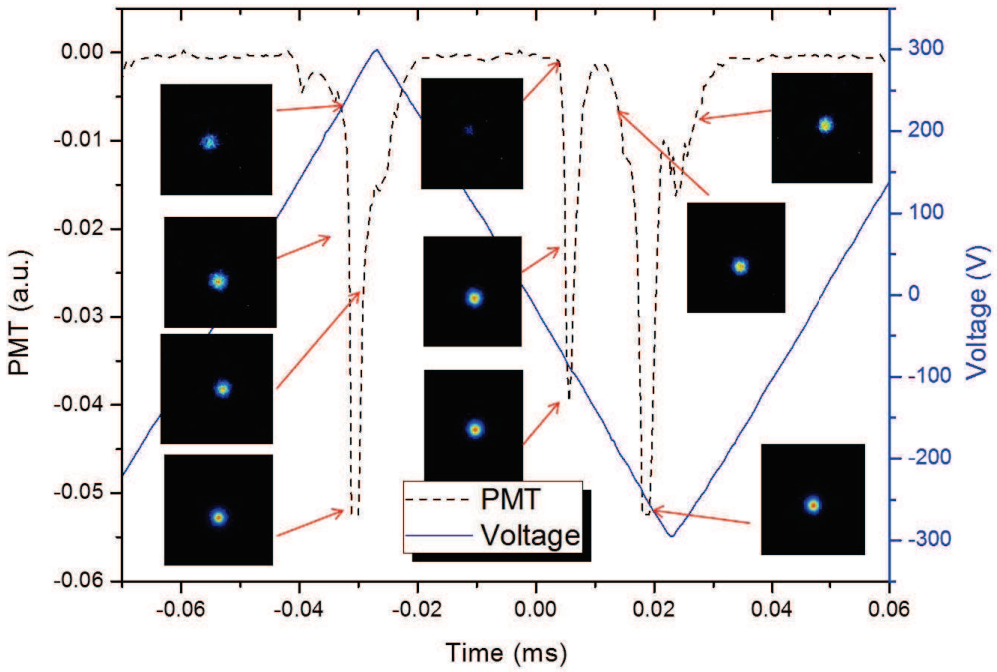

Figure 5.5: PMT and Voltage signals w.r.t. time for a single hole MDR with a cavity diameter of 100 µm in 760 mbar He at 600 Vpp. Inset images show ICCD pictures of the microplasma at different instants.(Images have false colours)

This phenomenon of having some shorter pulses in the half cycle could be related to the memory effects. For example, after the end of the positive half cycle, the next coming negative half cycle occurs within few 10s of microseconds. Thus due the preceding memory effect (as explained in the last section) the discharge tends to ignite earlier, at a lower value of voltage. But on the meanwhile, the voltage is slightly low to ignite the discharges completely with a high intensity and we see a dip in the PMT signal. Then, due to the increasing voltage ramp, discharge ignites again with a high intensity and we get a strong PMT signal. At the

same time, the voltage reaches its peak value and then it starts decreasing again. Thus for this moment, we could get a very small half PMT pulse.

5.2.2.2 Ignition dynamics

As already mentioned, to study the ignition dynamics of MDRs, we used phase resolved optical emission spectroscopy (PROES) as described in chapter 2. In this section, we present the results obtained for a single hole. An ICCD camera was mounted in front of the single hole. For each phase, a series of images was recorded and accumulated. The time delay between two images in a series was 200 nanoseconds. Then using the software of the ICCD camera "La Vision", a phase resolved movie could be generated.

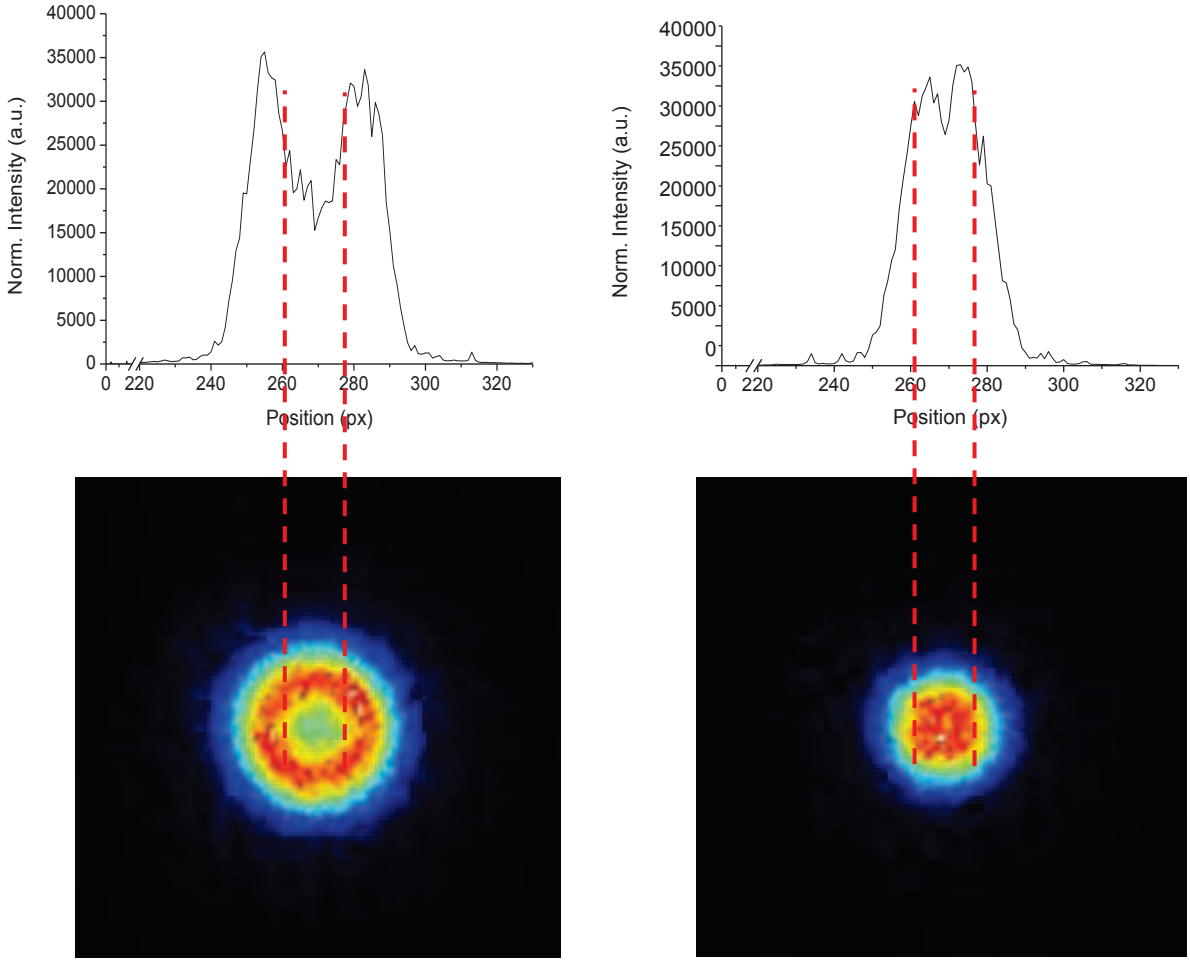

(a) (b)

Figure 5.6: ICCD images taken for a 50 µm diameter single cavity during (a) positive half cycle and (b) negative half cycle at 750 mbar Ar, 720 Vpp, 10 kHz frequency. The red dashed line shows the approximated cavity diameter. The plot for each corresponding image shows the intensity profile of the discharge in positive and negative half cycles. (Images have false colours)

ICCD images taken for a 50 µm single hole MDR are shown in figure 5.6 (a) during positive and (b) negative half cycles. The experiment was performed in 750 mbar Ar with a 720 Vpp applied voltage at 10 kHz. In figure 5.6, the approximated cavity diameter is marked by red dashed vertical lines on the ICCD images. These red dashed lines are then extended to the

corresponding image profiles to show the approximate limit of the cavity diameter on the plots. The images were taken for a single pulse, from a series of the burst pulses.

In figure 5.6 (a), an intense ring shape maximum emission of the micro discharge can be seen near to the cavity edge. Thus the intensity is very low in the center of the cavity. For bigger cavity diameters (e.g. 150 µm), the intensity at the center was even lower. The emission profile made on a diameter also confirms this lower amplitude at the center of the cavity whereas a maximum of emission is obtained at the edge.

In the negative half cycle (Figure 5.6 (b)), a maximum emission of the discharge can be seen at the center of the MDR cavity. The corresponding plot confirms this by the plateau like structure which appears at the center and thus shows a bell like shape for the emission plot.

In fact, different excitation processes are involved in the asymmetrical emission of the pulses during positive and negative half cycles. Brighter emission from the single hole MDR was observed during the positive half cycle as compared to the negative one. This phenomenon was observed in all cases, whatever the applied voltage amplitude, the frequency and the nature of the gas were. But this effect is less prominent in small cavity diameters around 25 µm. This phenomenon is related to the emission which follows the electron impact excitation.

In the positive half cycle, the electron density is maximum near the cavity edge of the discharge. ***[Boe-10]*** In the positive half cycle, Ni is acting as anode. Electrons are accelerated out of the MDR cavity towards the Ni surface. Thus, due to their direction on the top Ni electrode layer, the emission from the cavity looks broader and has a maximum intensity at the edge as shown in the plot of figure 5.6 (a). But in the negative half period, electrons are accelerated from the Ni electrode into the MDR cavities, reaching the excitation threshold deeper inside the cavities. In this direction more electrons can get lost due to surface neutralization so that fewer electrons can reach the threshold. Thus, fewer species are excited in a smaller volume and a more confined and sometimes less bright emission feature is observed.

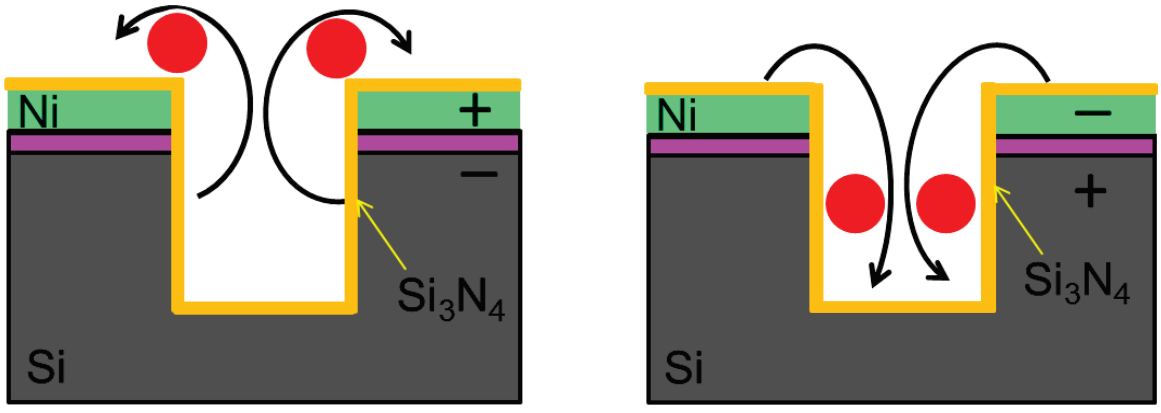

(a) (b)

Figure 5.7: Scheme of the cross-section of the cylindrical cavity for a single hole, showing the concept of asymmetrical emission dynamics in (a) positive half cycle and (b) in negative half cycle.

This concept can be explained by the sketch of the cross-sectional view of the single hole MDR as shown in figure 5.7. In this figure, the cavity arrangements of single hole reactor are shown for (a) positive and (b) negative half cycles. As shown in this section, in positive half cycle, excitation is more effective near the cavity edge and thus MDR is brighter near the edge and above the nickel surface. This can be represented by the motion of electrons (black arrows in sketch) as shown in the figure 5.7 (a), where electrons are directed towards the top Ni electrode. A higher electron density should be obtained in the area represented by the red circles. On the contrary, for the negative half cycle, electron's direction and trajectories are reversed. Thus, the electrons excitation is more pronounced inside the cavity leading to a smaller emission region concentrated in the center of the cavity. This phenomenon is shown in figure 5.7 (b), where the red filled circular area shows the area of higher electron density in this cycle.

5.2.2.3 Effect of pressure

For single hole MDRs, we studied the effect of pressure change on the ignition dynamics. Figure 5.8 shows the normalised intensity plots for (a) positive and (b) negative half cycles for different pressures in Ar. Here, a single hole MDR with a cavity diameter of 150 µm was used for the characterisation. The applied voltage was kept around 620 Vpp at 10 kHz frequency. For different gas pressures, ICCD images were recorded using PROES techniques with a time resolution of 200 ns for both positive and negative half cycles. Normalised intensity plot for each half cycle for corresponding pressures were plotted using the software.

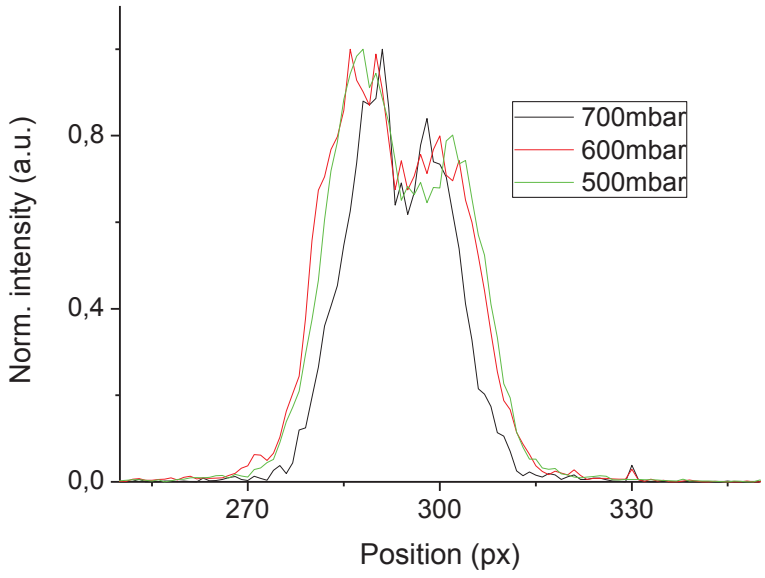

(a)

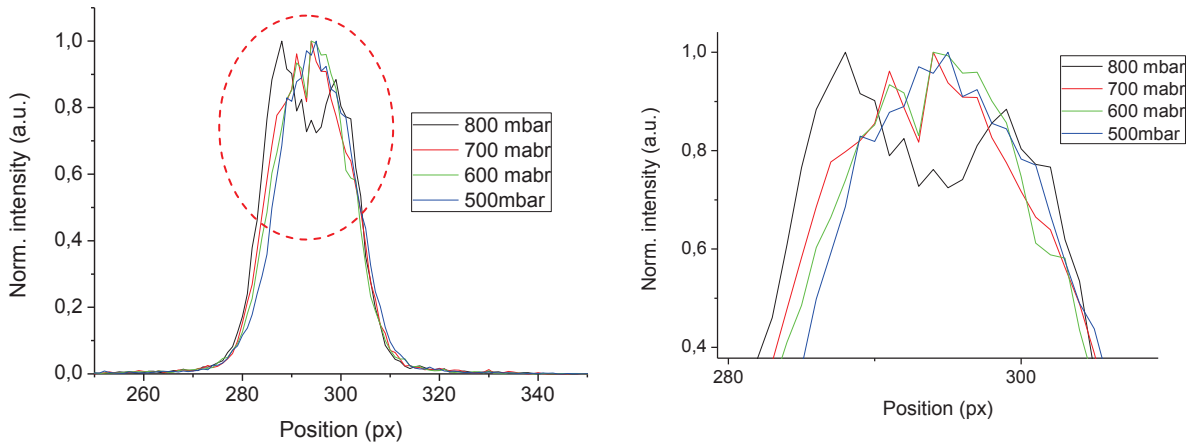

(b)

Figure 5.8: Normalized emission intensity for single hole MDR with 150 µm cavity hole diameter in (a) positive and (b) in negative half cycles for 650 Vpp applied voltage at 10 kHz in argon gas at different pressures (figure on the right side is a zoom of the figure figure b).

For positive half cycles, figure 5.8 (a) shows the normalised intensity plots for three different pressure 500, 600 and 700 mbar. All the plots have the same characteristics for positive half cycle as discussed in the last sub-section. Here, we observe the decrease of the pulse width, with the increase of pressure.

For the negative half cycle, figure 5.8 (b) shows the normalised intensity plots for 500, 600, 700, and 800 mbar gas pressures. They have bell shape curves as discussed in the last sub-section. From these plots, it can be seen that the pulse width increases with pressure.

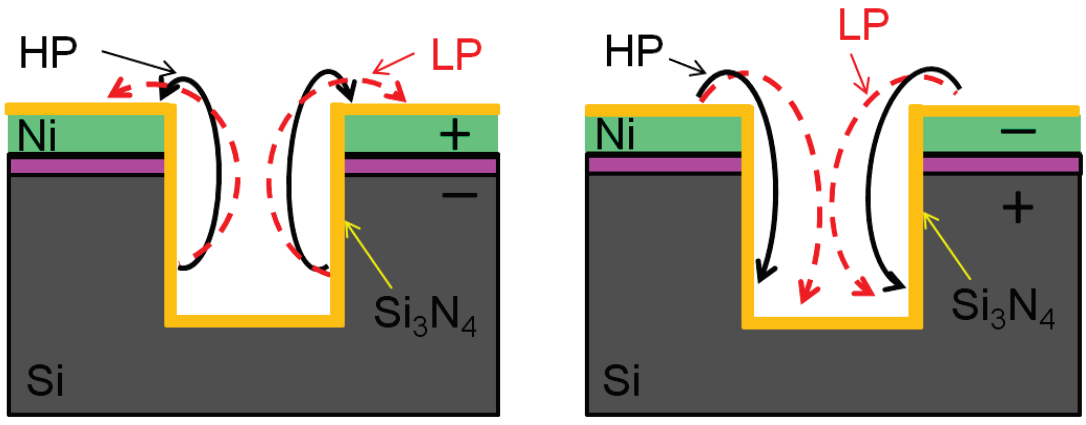

(a) (b)

Figure 5.9: Sketch of single hole MDR showing effect of pressure (higher pressure [HP], lower pressure [LP]) for (a) positive and (b) negative half cycle.

This characteristic of the variation of the curve width (FWHM) could be connected to the motion of the electrons and their trajectories during positive and negative half cycles of the applied voltage. At higher pressures, electrons have smaller mean free path. In positive half cycle, at lower pressure, electrons follow a path far from the cavity edge and have a longer

trajectory. But, at higher pressure, they just fall near the cavity boundary, as shown in figure 5.9 (a). Thus for lower pressures, we can have intensity plots with larger pulse width and vice-versa.

In the negative half cycle, at lower pressure, electrons cover a longer distance towards the center of the cavity from the top Ni layer, making the intensity curve width shorter. Whereas, at higher pressure, they just fall inside the cavity near the cavity boundary and produce a wider intensity curve as shown in the figure 5.9 (b).

5.2.2.4 Self-pulsing

As discussed earlier in this chapter, our device behaves like a DBD. The ignition of microdischarges is not continuous. To study the self-pulsing phenomenon for single hole MDRs more deeply with the variation of different parameters, we used PROES measurements. The discharge behaviour under the frequency variation was first investigated. Figure 5.10 shows the effect of change in operation frequency for an applied voltage of 720 Vpp for a single hole MDR with a cavity diameter of 50 μm at 750 mbar Ar. These plots of the normalised intensity w.r.t. time were obtained from the PROES experiments by using the software developed at Bochum. Here, the normalised intensity for the selected area of the single pixel was calculated. In this measurement, different frequencies (a) 5 kHz, (b) 10 kHz, (c) 20 kHz and (d) 30 kHz were used. From the figure 5.10, it can be seen that at low frequency, the intensity profiles are not separated completely as compared to the higher frequencies: a kind of continuous emission is superposed to the emission pulses. For example, at 5 kHz, it is difficult to distinguish the total number of emission bursts per half cycle, but for higher frequency (e.g. 30 kHz), three well evolved peaks can be seen in both positive and negative half cycles.

In fact, at lower frequencies, some species can form (e.g. metastables) due to the longer time duration of the half cycles. From chapter 3 (section 3.4.3), the typical time to reach the steady state of the metastables density was found to be around 30 μs. This time is reached at low frequency (figure 5.10 (a)). Thus, at low frequency, these species accumulate during the half cycle and when the discharge starts to ignite, they can contribute in the formation of the continuous emission. This accumulation of metastable is not obtained at higher frequencies. This is why we see multiple peak ignition behaviour.

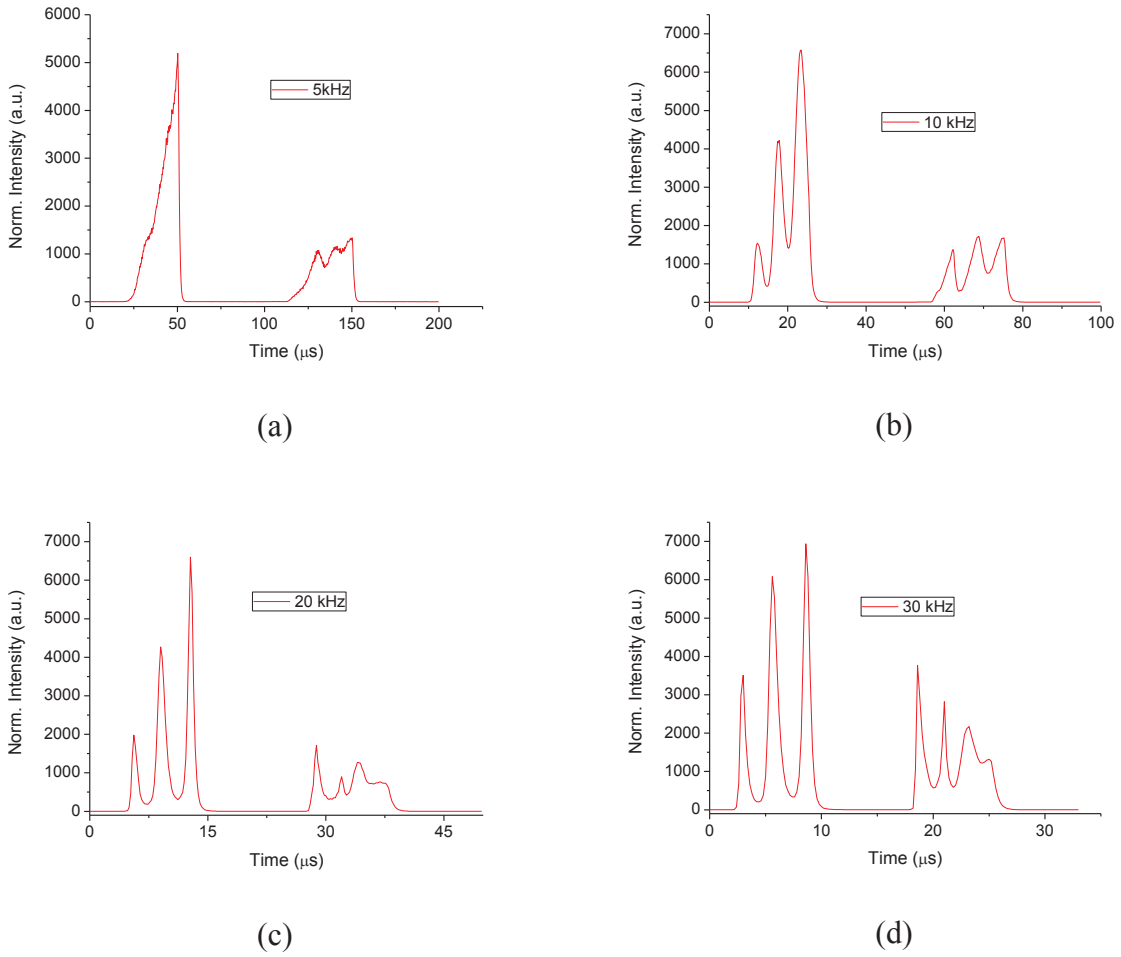

Figure 5.10: Intensity evolution versus time within one period for two different frequencies for a single hole MDR having a cavity diameter of 50 µm, excited by a 720 Vpp AC voltage in 750 mbar of Ar.

5.2.3 MDR array

In this section, we present the results for the array devices having 1024 holes with diameters of 25, 50, 100 and 150 µm. For these arrays, different parameters were varied to study them thoroughly.

5.2.3.1 Effect of variation in frequency and voltage

For this study, gas pressure was kept at 500 mbar in Ar. MDR array having 1024 cavities with 100 µm cavity diameter was studied by varying the operating frequency and the applied voltage, from 2 to 20 kHz and from 530 to 600 Vpp respectively. PMT signals for corresponding positive and negative half cycles were recorded and analysed. The figure 5.11 shows plots for the calculated width (in ms) of the PMT signals, obtained by the oscilloscope for (a) positive and (b) negative half cycle of the applied voltage.

From this figure, we clearly see that, the width of the PMT signal decreases as the frequency increases. More exponential type of decay can be seen in the case of negative half cycle. As observed in these graphs, at a particular frequency, the width of the PMT signal increases with the increasing voltage in both positive and negative half cycles. With the increasing

pulse width, the numbers of pulse trains are increased in both cases of increasing frequency and increasing voltage. Correlating with the respective peak amplitudes of the PMT signals, it is concluded that with the increasing width of the PMT signals, the corresponding peak amplitudes decreases.

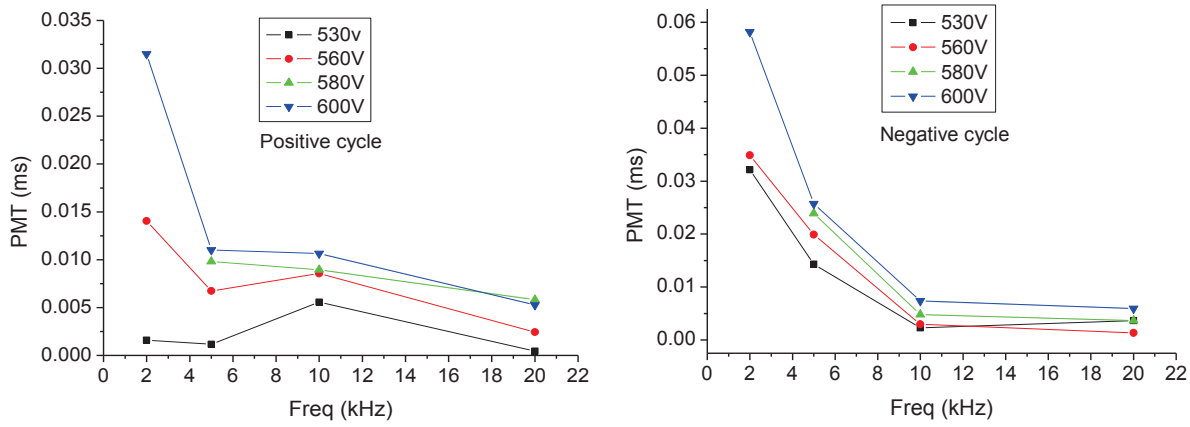

(a) (b)

Figure 5.11: Width of PMT signal for varying frequencies for (a) positive half cycle and (b) negative half cycle.

The phenomenon of increasing the number of peaks with the increasing frequency is similar to the one obtained for the single hole MDR. Thus, metastables and excimers accumulation with successive discharge current pulses could lead to this effect. On the other hand, increasing in number of peaks, with the increasing peak to peak voltage at a particular frequency, could be related to the life time of the excited species and the corresponding voltage ramp for positive and negative half cycles. An increase of the applied peak to peak voltage at a particular frequency leads to an increase of the slope of applied voltage dU/dt. Thus after the first ignition in one half cycle, the increasing voltage ramp may provide sufficient energies to the device to produce next pulse in the same phase before the polarity change. This will lead to an increasing number of emission bursts per half cycle, as well as higher surface charge densities at the dielectric surfaces ***[Amb-10]***. So, increasing peak to peak voltage and hence the higher surface charge densities, may lead to a slight decrease of the necessary voltage to generate the next bursts. This could lead to multiple peaks with in one half cycle.

5.2.3.2 Dynamics of the array

The dynamics of MDR arrays was studied as well with PROES method. For this study, MDR device having sub-arrays of 50, 150 and 100 µm diameters (bottom to top) on a single chip was used, as shown in the figure 5.12.

PROES measurements were performed at 1000 mbar of Ar with 10 kHz frequency at around 540 V peak to peak voltage. An area containing 150 µm hole array was focused on ICCD

camera. For positive and negative half cycles, images were captured. The corresponding normalised intensity profiles are shown in figure 5.13.

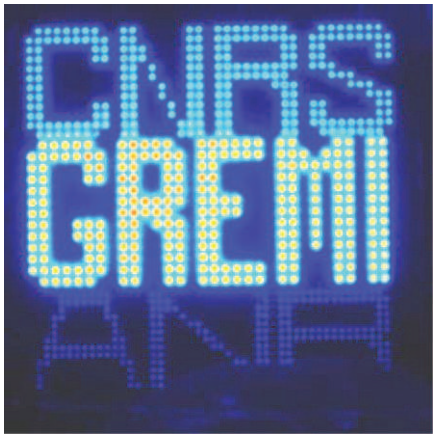

Figure 5.12: ICCD image with static mode of the array with mixed holes discharge reactors with 50, 150 and 100 µm diameters sub-hole arrays (bottom to top). (Image has false colours)

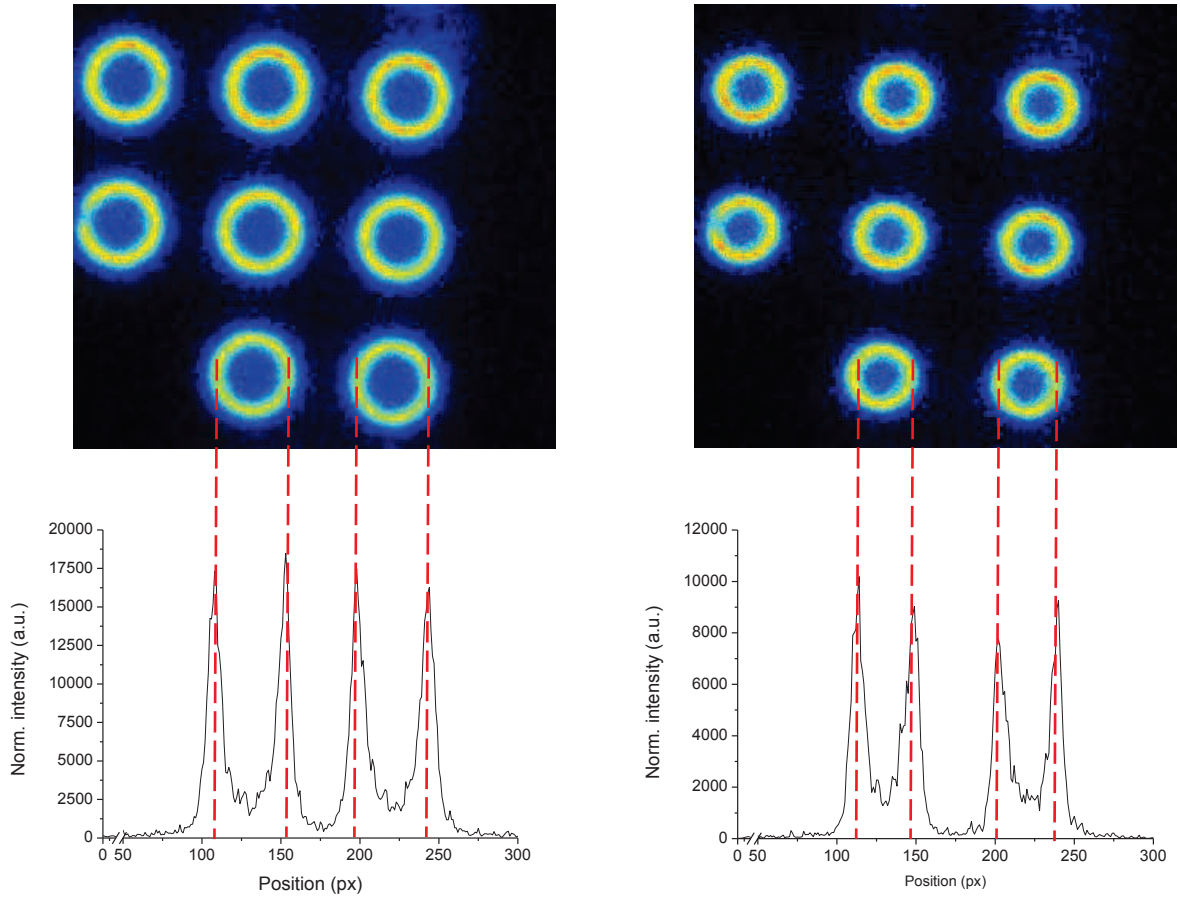

(a) (b)

Figure 5.13: Normalised intensity profiles with corresponding ICCD camera images (with false colours) taken at the maximum of the PMT signal for 150 µm sub array of the mixed holes array, (a) in positive and (b) negative half cycle.

Red dashed lines indicate peak-intensity areas on the plots and as well as on the corresponding ICCD images. Similar to the single hole MDRs (as discussed in the above section), for positive half cycle, the ignited cavities have wider areas as compared to the negative half cycle. The ignition phenomenon is similar to the one for a single hole. But in this case, cavities are larger, with a 150 µm cavity diameter as compared to the 50 µm single hole MDR (shown in figure 5.6). Here, the effect of wider area can be compared easily with smaller cavity area for edge ignition phenomena.

Due to a larger area, the center of the cavity seems to have a very low intensity. This could be linked to the assumed trajectory of electrons during the positive and the negative half cycles as explained above ***[Boe-10]***. In negative half cycle, even if the direction of the electrons is toward the center of the cavity, an area with very weak light intensity is obtained at the center due to very large cavity diameter. This is completely opposite for smaller cavities, where we see a much brighter area near the center of the cavity. This conclusion strengthens the idea about the relationship of the direction of electrons per half cycle and the edge ignition effect.

5.2.3.3 Ionisation wave

Two-dimensional space and phase resolved optical emission spectroscopy show the existence of an ignition wave for each emission burst of the array ***[Was-08, Boe-10]***. Figure 5.14 shows the existence of such an ignition wave on an array of 1024 cavities (100 µm diameter) at 500 mbar Ar, 570 Vpp at 10 kHz frequency for the negative half cycle. The images were taken using PROES setup and at the start of the array ignition in the negative cycle at 19400 ns. On each image, the time corresponds to the delay time between images. Ignition waves occurring from the corners and going toward the center of the array can be seen from this series of images. In this case, the ignition waves are converging to the center of the MDR chip. This can be clearly seen from the figure 5.14, in terms of the increasing intensity towards the center of the chip.

Generally, the ignition wave starts from a corner of the array and then propagates through the surface of the array. But, no privileged direction of the wave propagation was observed. They can start from any corner or form at the center of the array. Due to the not perfect reproducibility of the reactor fabrication, some different behaviour can be observed from an array to the other. Sometimes, waves were originating from the cavities having some defects as shown in the figure 5.14.

The origin of this ignition wave is not yet very well understood. According to ref. ***[Was-08, Boe-10]***, the ignition wave phenomenon could be indirectly due to the ions, which drift toward the cathode and generate secondary electron emission. Thus, the transition from Townsend to glow discharge occurs during the evolution of an emission burst for the initial cavities. The consecutively emission passes to the adjacent cavities and could lead to an ignition wave like behaviour. This observed collective behaviour of the cavities with an ionisation wave has a significant influence on the device performance. This can help to ignite all the MDR cavities present in an array by the charge transfer to the neighbouring cavities. This type of behaviour including energy exchange between the cavities may have some of the potential applications; e.g.: a type of lab-on-a-chip device is possible to make, which can

provide analysis of different biological species with the time evolution by using ignition wave phenomenon.

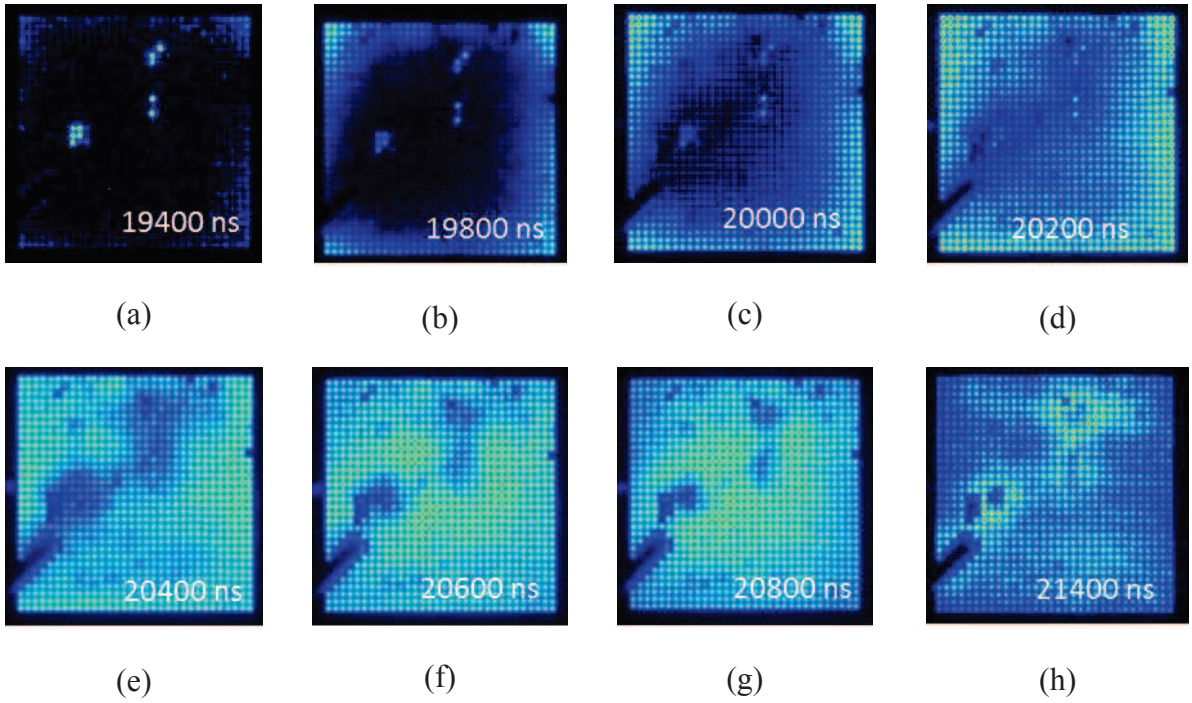

Figure 5.14: Ignition waves on an array having 1024 holes with cavity diameter 100 µm at 500 mbar Ar for negative half cycle. (Images have false colours)

5.2.4 Mixed trench Array

Arrays containing four sub-arrays of different trench dimensions were studied under AC regime. As explained in chapter 2, the four arrays were having 80 (5 x 16) trenches with length of 500 µm and a width of 25, 50, 100 and 150 µm respectively. This special type of arrangement allowed comparing the behaviour of the different subarrays under the same parametric conditions. Having the four sub-arrays on the same Si chip makes certain that the fabrication and physical parameters are the same for each sub-array. In this section, we present the results of the PROES experiments performed for these arrays.

5.2.4.1 Edge ignition phenomena

Figure 5.15 shows one example of a 150 µm x 500 µm trench sub-array in 1000 mbar of Ar with 800 V peak to peak voltage and an operating frequency of 10 kHz. From these images, the difference between positive (figure 5.15 (a)) and negative half cycles (Figure 5.15 (b)) can be clearly seen. We see a wider ignited trench area for the positive half cycle as compare to the negative half cycle. The explanation of this phenomenon can be given on the basis of the motion of the electrons with the positive and the negative half cycles, as explained in the section of single hole MDRs. Thus, due to the direction of the electron towards the Ni electrodes during the positive half cycle, we see a wider ignited trench area. For negative half cycle, this direction is reversed and electrons moves towards the Si electrode side and this provides the smaller trench ignited area.

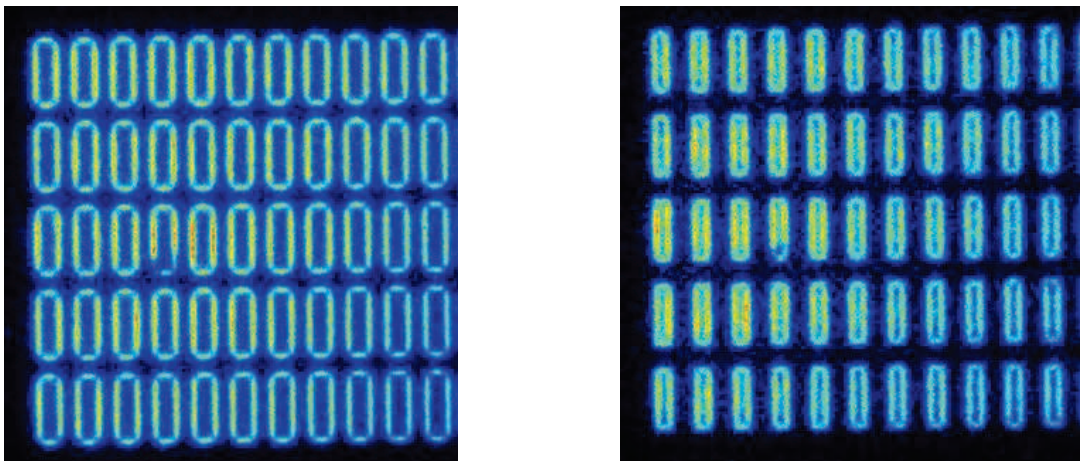

(a) (b)

Figure 5.15: Edge ignition phenomena of 150 µm x 500 µm trench arrays in (a) positive half cycle and (b) negative half cycle. (Images have false colours)

5.2.4.2 Ignition wave

Figure 5.16 shows ignition waves for the 50 µm trench sub-array. PROES experiments were performed at 750 mbar Ar with 530 Vpp applied voltage at 10 kHz frequency. This figure shows the results obtained during the positive half cycle. In this figure, images with their corresponding normalised intensity plots with respect to the position are shown.

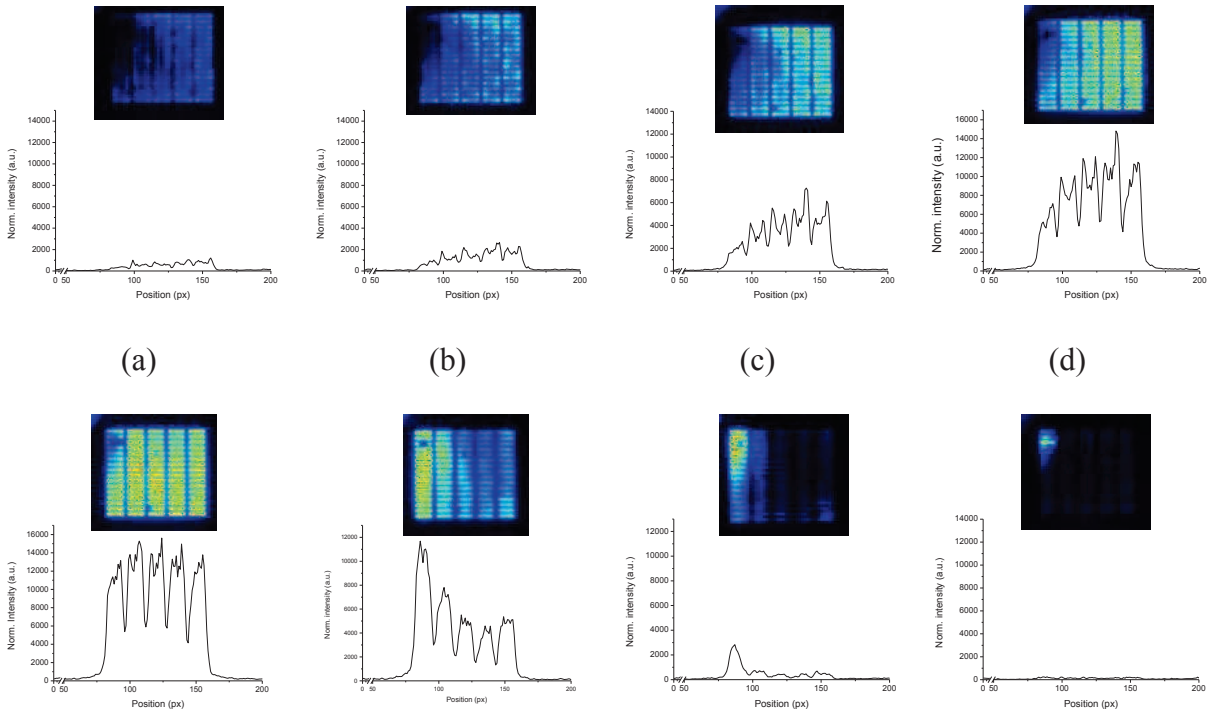

(a) (b) (c) (d)

(e) (f) (g) (h)

Figure 5.16: Ignition waves on 50 µm trench sub-array at 750 mbar Ar with 530 Vpp applied voltage with 10 kHz frequency. (Images have false colours)

From this figure, an ionisation wave travelling from right to left can be clearly seen. The wave starts from the right corner of the array as shown in the image/profile of the figure 5.16 (a). Then by passing through the entire array, this wave ends at the left corner as shown in the figure 5.16 (h).

The corresponding normalised intensity profiles indicate that the occurrence of these ionisation waves is a continuous phenomenon: a train of continuous pulses can be seen from the profiles. This phenomenon is the same as the one explained in the above sub-section.

5.2.4.3 Trends of ignition

In this sub-section, we present the trends of ignition related to each sub-array present on the chip. The ignition behaviour for each sub-array was studied by relating them with the applied voltage. The applied voltage was varied by two different ways. In the first case, the voltage was manually increased and images from static ICCD camera mode were registered for each increase in the applied voltage. In the second case, an applied peak to peak voltage was maintained, which was sufficient to ignite all the four sub-arrays together. Then PROES experiments were performed with a triangular voltage ramp.

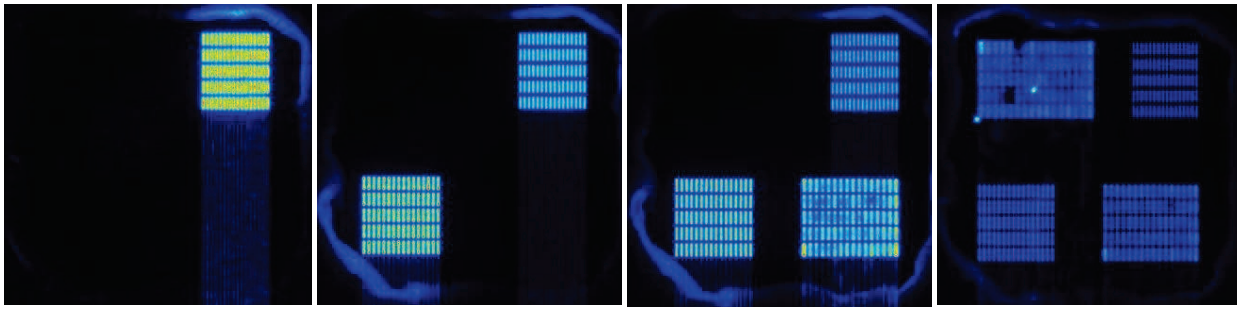

(a) (b) (c) (d)

Figure 5.17: ICCD static mode images with ignition trend during the manual increase of applied peak to peak voltage at (a) 517 V, (b) 531 V, (c) 544 V and (d) 550 V for a mixed trench array at 700 mbar Ar. (Images have false colours)

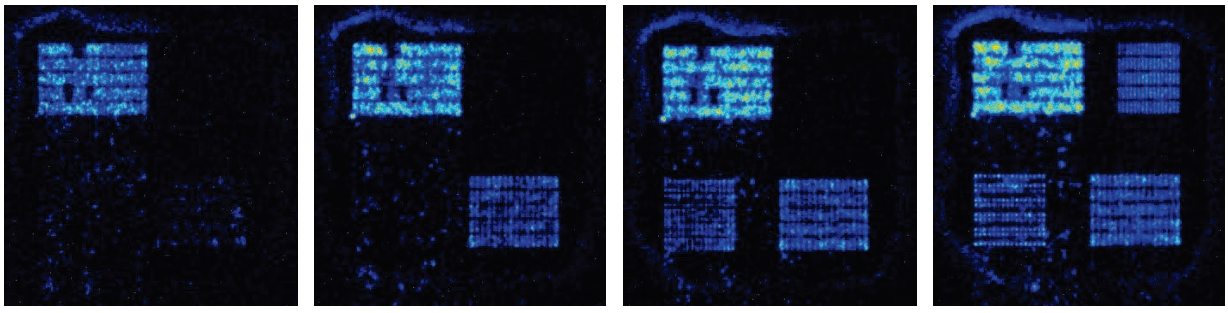

(a) (b) (c) (d)

Figure 5.18: Ignition trend registered with PROES experiment for an applied peak to peak voltage of ~ 545 V with triangular ramp of 10 kHz frequency at 700 mbar Ar. (Images have false colours)

Figure 5.17 shows the ignition trend recorded by manually increasing the peak to peak voltage. The pressure was maintained at 700 mbar of Ar. From this image series, we can see that the 25 wide trenches start igniting first when the peak to peak voltage reaches 517 V. On further increasing the peak to peak voltage to 531 V, wider trench sub-array (50 µm wide trenches) ignites with a higher intensity. When the peak to peak applied voltage is set to 550 V, all four sub-arrays with 25, 50, 100 and 150 µm ignite.

Now, by keeping the peak to peak voltage constant at ~ 545 V, PROES experiments were performed with a triangular ramp having 10 kHz frequency with 200 ns time resolution. As observed in figure 5.18, we find that bigger trenches (100 and 150 µm wide) ignite first. Then, at higher voltage, 50 µm trenches start igniting. Finally, all the four sub-arrays ignite (image d).

To summarise, when the peak to peak applied voltage is high enough to ignite all sub-arrays, the wider trench sub-arrays ignite first. But, when the peak to peak applied voltage is not sufficient to ignite all trenches, then, only narrow trench sub-arrays ignite. The ignition trend for both cases could be related to the excitation of the metastables with the supply of sufficient energy.

For the first case, where peak to peak voltage was increased manually, it could be possible that smaller cavities got sufficient energy density for the threshold and they ignite first. On the other hand, with the increasing ramp for the 545 V peak to peak voltage, it could be possible that bigger cavities reached first the threshold and they get ignited first. As explained in the ref ***[Sch-12]***, the statistical time for the initiatory electrons to start the discharge is higher in the bigger cavities, thus on applying a same voltage, the probability to ignite bigger cavities is higher.

5.3 Conclusions

In this chapter, we have shown the voltage and current characteristics for a single hole and multi hole arrays running in AC. Studies of ignition dynamics for the single hole and for the arrays of MDRs were presented using PROES. For the single hole devices phenomena of edge ignition with the effect of positive and negative half cycles was studied. It was found that in positive half cycle, the hole appeared wider with a bright light intensity at the edges due to the motion of the electrons from cathode towards the Ni anode. But in negative half cycle the same hole appeared with a bright intensity towards the center of the cavity due to the motion of the electrons from top Ni cathode towards the Si anode. The same phenomenon was observed for the multiple hole arrays. Effect of pressure and frequencies on discharge ignition using the normalised intensity profiles of single hole MDRs was studied. It was found that for positive half cycle, these profiles have large profile width for small pressure and the normalised intensity profile width decreases with the increase of pressure. But in negative half cycle, an opposite phenomenon as compared to the positive half cycle was observed. This phenomenon was also connected with the direction of the electrons during the positive and the negative half cycles. For single hole devices it was found that the numbers of pulse trains per cycles increases with the increase of the frequency and this effect could be related to the stabilisation time of the metastable states. For the multi hole arrays, the existence of ionisation

waves was presented using PROES. It was shown that the each cavity in a multiple hole array cannot ignite at a same time, but instead they ignite with a series of burst pulses i.e. ionisation wave. But any particular trend related to the direction of these ionisation waves was not observed. For multiple trench arrays the phenomenon related to the ignition trend for an applied peak to peak voltage and for varying peak to peak voltage was also studied.

In next chapter, we summarise the main results obtained from the study of microdischarges. An outlook for future work and potential applications is also presented.

Conclusions

The aim of this PhD work was to investigate several physical mechanisms and specific operating conditions of silicon microdischarge reactors (MDRs) operating in DC and AC regimes.

We have shown the successful fabrication of the Si based devices using standard CMOS and MEMS based technology, in a standard cleanroom environment. The devices were fabricated to operate in both DC and AC regimes. MDRs were designed with several different configurations to study the microdischarge characteristics. The microdischarge reactor designs include single hole devices with hole diameters varying from 25 µm up to 150 µm, multiple hole devices with different numbers of cavities, with cavity diameter varying from 25 µm up to 150 µm. Some special arrays like mixed hole arrays and mixed trench arrays were also designed to study some specific mechanisms of the microdischarges in different conditions.

In DC operating regime, ignition and extinction of the discharges for alumina based MHCD devices were studied in He. In this study, during the ignition of the MHCD, the existence of huge current pulses with an amplitude on the order of few 10's mA was evidenced. During the ignition, a typical metastable stabilisation time of 40 µs was observed. At higher pressures (> 400 Torr), for the extinction of the discharges some oscillations having exponential sinusoidal behaviour with time period of few microseconds were found. The ignition behaviour was explained with a simple equivalent electrical circuit. Using TDLAS, we also showed that metastable density was following the amplified sinusoidal waveform as observed during the extinction for gas pressures higher than 400 Torr. Using the TDLAS method, metastable densities for the normal operation of the MHCD were calculated for He, at different discharge currents and gas pressures. The metastable densities were varying from 2.0 x 10^{17} to 4.5 x 10^{17} m^{-3}, depending on the particular gas pressure (from 350 to 750 Torr) and discharge current (from 5 to 20 mA). Gas temperature inside the MHCD cavity was also evaluated using TDLAS for different discharge currents and pressures. The approximated gas temperature was varying from 500 to 1300 K ± 25%, depending on the discharge current (5 to 15 mA) and the corresponding gas pressures (350 to 750 Torr).

Si based single hole MDRs were characterised electrically and optically for DC regime for He and Ar gases. For close anisotropic cavities in Si, in SP case, an abnormal glow regime was observed due to the limited cathode: the discharge voltage was increasing with the discharge current. Here, plasma remained confined inside the cavities. In this case, for a 180 µm deep and 150 µm diameter cavity the current density (J) and the power density (P_d) were calculated. For Ar, they were found to be 0.38 $A.cm^{-2}$ and 45 $kW.cm^{-3}$ respectively. For He, the approximated J and P_d were 0.54 $A.cm^{-2}$ and 63 $kW.cm^{-3}$ respectively. For the RP case a slight abnormal regime was observed with the same anisotropic cavity. This slight abnormal glow regime was occurred due to the presence of protective PR coating on the top Ni cathode. In RP case, J and P_d for Ar were equal to 1.80 $A.cm^{-2}$ and 189 $kW.cm^{-3}$ respectively. In case of He, the approximated values of J and P_d were 2.00 $A.cm^{-2}$ and 169 $kW.cm^{-3}$ respectively.

The same type of study was performed for single hole MDRs with isotropic and through hole cavity configurations. For these configurations, a normal glow type of behaviour was observed for both SP and RP cases. This was due to the fact that Si cavities were having larger cathodic area and plasma was able to expand over the surface.

Effects of cavity diameter and pressure on the breakdown voltage were also studied using single hole devices. In the study, it was demonstrated that smaller hole diameter cavities need higher applied voltage for the breakdown. Effect of hysteresis for anisotropic, isotropic and through hole cavities was studied for single hole MDRs. Two types of hysteresis effects were evidenced.

To discover the plasma behaviour, simulations were performed with GDSim (Glow Discharge Simulation tool, for single hole anisotropic MDR. Simulations were performed for two discharge currents 1.2 mA and 5.3 mA. From simulations, electron density was found on the order of 10^{14} cm^{-3}. In these simulations, it was shown that at higher $I_{d,}$ electrons were more concentrated towards the cavity and had higher electron density as compared to the lower I_d. Metastable densities were on the order of 10^{15} cm^{-3} near the cathode boundary. The gas temperature was found to be higher inside the cavity, in particular near the cathode. Gas temperature had a maximum value of 325 K for 1.2 mA and 425 K for 5.3 mA. The sheath thickness was also calculated. It was on the order of 20 µm for higher discharge current 5.3 mA and 40 µm for lower value of discharge current 1.2 mA, at same gas pressure. Optical emission spectroscopy (OES) was performed to calculate the gas temperature inside the single hole MDR cavity. For 3 mA discharge current, the approximated gas temperature was 410 ± 30 K and for 4.8 mA discharge current, the approximated gas temperature was 450 ± 30 K. The experimental gas temperatures were found in agreement with the GDSim simulation results.

Multiple hole arrays with different configurations were studied in DC regime. Study of 4 x 4 hole arrays, having two different side to side interhole spacings was performed in He gas. For the array having larger interhole distance (few mm), an abnormal glow regime was obtained in SP case due to the limited surface of the cathode.

Breakdown studies of the deeply etched arrays, showed dips in their V-I plots. This indicated the need of higher voltage for the ignition of new MDR cavities. Breakdown studies for different pressures revealed that at higher pressure (~1000 Torr), smaller cavities with a diameter of 50 µm or less ignite preferentially, but at lower pressure cavities with bigger diameters (100 and 150 µm) ignite preferentially. However, there was no any ignition preference observed between the cavity diameters of 100 and 150 µm. Effect of voltage ramp was found affecting the ignition of the arrays. It was discovered that, if the voltage ramp is slow then more MDR cavities in an array can ignite as compared to the faster voltage ramp. It was also shown that the number of holes in an array can affect the breakdown voltage. So, the arrays having many holes (256 or 1024 holes) have lower breakdown voltage as compared to the single hole MDRs. This was due to fact that, the statistical probability to find an initial seed electron in an multiple hole array is higher as compared to the single hole MDR. Also in general, a higher breakdown voltage was observed for Ar gas as compared to the He gas at

same pressure. A higher discharge current was obtained for 1024 hole array as compared to the single hole device, when only a single cavity was igniting in both cases.

On further characterising these arrays, it was found that the arrays having isotropic and shallowly etched cavities can be ignited completely and easily as compared to the deeply etched anisotropic cavities. For fully ignited shallowly etched 1024 hole array with a cavity diameter of 100 μm and a cavity depth of 28 μm, the average calculated current density (J) was on the order of 0.8 $A.cm^{-2}$ and power density (P_d) was 1.5 $kW.cm^{-3}$. In the study, it was found that the discharge started to ignite from the corner of the array. This was the effect of microstructured electrodes and the resistivity of the top surfaces. This was attributed to the fact that, at the corner, the resistance was less as compared to the center of the array, and thus discharge preferentially ignites from the edge cavities present on an array.

Some exotic geometries were also investigated. With the multiple trench arrays, edge ignition phenomenon was observed for the higher pressures (~1000 Torr). At lower pressure ~100 Torr, we were able to show a complete array ignition with Ar. We also demonstrated the concentric hole arrays with the possibility of their working at any pressure ranging from 100 to 1000 Torr.

Life time studies were performed for single hole and the multiple hole arrays having isotropic and anisotropic cavities. It was found that the MDRs with deeply etched cavities and isotropically etched cavities can have longer life time. Life time for a single hole device was from few 10's of seconds to few 10's of minutes. Life time for multiple hole arrays was from few minutes to few hours. In this study, the existence of micro-arcs during the plasma operation was shown and found to be the cause of the failure of the microdischarge devices. Here, it could be possible that the high capacity of the Si devices (~ 1 nF) may able to deliver a high energy to the current pulses. And these high energy current pulses could lead to the transient micro-arcs. These micro-arcs can generate locally inside the cavity of the MDR and were able to erode and project cathodic material, which was then redeposited on the side walls of the cavities. This redeposition made contact between anode and cathode. This caused the death of the MDRs. SEM and EDX analysis results confirmed the deposition of Si on the side walls and on the top Ni electrode.

Studies of single hole and multi hole arrays MDRs were also performed in AC regime. Optical characterisation was performed by using PROES method. For single hole devices, edge ignition phenomenon was shown for positive half cycle using PROES. In fact, it was shown that this phenomenon was related to the motion of the electrons. In positive half cycle, the direction of the electrons was towards the Ni electrode, which could lead to the higher light intensities at the cavity edges. But in the negative half cycle, the direction of the electrons was toward the cavity and the central part of the cavity brighter area. Similarly, the effect of pressure on the ignition was studied and it was found that the light intensity profile became wider at lower pressure for positive half cycle and the opposite effect was seen for the negative half cycle. Effect of frequency on the ignition dynamics was studied using PROES. It was found that at lower frequencies, discharge could ignite continuously in a single hole MDR. But at higher frequencies, a self-pulsing type of ignition behaviour was observed. This phenomenon was related to the stabilisation time of the metastable density states.

Electrical characterisations for 1024 arrays allowed calculating the current density of the order of few 10's of mA cm^{-2} (for 1024 hole array), which was 18 times smaller than the current densities in DC regime. Static images of the arrays showed the homogeneous emission of the arrays. But the PROES experiment revealed that the ignition of the microdischarges is not a continuous phenomenon, but instead it corresponds to a successive ignition phenomenon. Two-dimensional space and phase resolved optical emission spectroscopy showed the existence of an ignition wave for each emission burst of the array. Generally, the ignition wave starts from a corner of the array and then propagates through the surface of the array. But, no particularity, for the propagation directions of these waves was observed. They can start from any corner or form at the center of the array. Due to a not perfect reproducibility of the reactor fabrication, some different behaviour could be observed from an array to the other. Also edge ignition phenomenon similar to the single hole MDRs was observed for the arrays.

Mixed trench arrays with 256 trenches were also studied in AC regime. Edge ignition phenomenon for the bigger trenches of 150 and 100 μm trenches was clearly observed. In this case, the presence of ignition wave was noted. Ignition trends, for the different applied voltage conditions were studied. It was found that, when the peak to peak applied voltage was high enough to ignite all sub-arrays, the wider trench sub-arrays ignited first. But, when the peak to peak applied voltage was not sufficient to ignite all trenches, then, only narrow trench sub-arrays ignite. The ignition trend for both cases could be related to the excitation of the metastables with the supply of sufficient energy.

In this PhD thesis, we have evidenced and explained several physical phenomena related to the microdischarge in DC and AC regime. The results of this study will be useful for the next fabrication of microdischarge reactors in silicon.

Based on the PhD thesis results, some suggestions for the future studies can be given. Fabrication of new generation devices with a long life time could be an interesting point for future studies. On chip integration of the devices for many applications like lab-on-a chip, can also be a potential motive for future studies. The present Si and alumina based devices can be used in three electrodes configurations. This configuration could be useful for gas treatment and surface treatment applications. Controlling the ignition of the individual microdischarges in a multiple hole array could be an another interesting aspect for the future studies. This type of controlled devices then may have applications in the display technologies.

List of Figures

Figure 1.1: Effect of pressure on gas (heavy particle) temperature (T_h) and electron temperature (T_e), in mercury (Hg) plasma. [Bou-94] 11

Figure 1.2 : Paschen curves for different gases. [Pap-63] 13

Figure 1.3: Standard V-I characteristics of a low pressure discharge tube in DC. [Rot-95] 13

Figure 1.4: Images of glow discharge in atmospheric pressure air at different electrode spacing. [Sta-05] 17

Figure 1.5: Examples of Atmospheric Pressure Plasma Jets (APPJs (a) A photo of four Ar plasma microjets operating in parallel [San-02], (b) a module consisting of six APPJs, and [Wel-08] (c) Digital camera pictures of neon PAPS propagation in a 45 cm long borosilicate capillary for the three voltage waveforms. [Rob-12] 18

Figure 1.6: Examples of generally used DBD configurations. 19

Figure 1.7: Positive or cathode-directed streamer, (a) Streamer at two consecutive moments of time, with secondary avalanches moving towards the positive head of the streamer, wavy arrows are photons that generate seed electrons for avalanches, (b) Lines of force of the field near the streamer head. Taken from ref. [Rai-91] 20

Figure 1.8: Negative or anode-directed streamer, (a) Photons and secondary avalanches in front of the streamer head at two consecutive moments of time, (b) Field in the vicinity of the head. Taken from ref. [Rai-91] 21

Figure 1.9: Structure of cathode boundary (CBL) layer discharges. 21

Figure 1.10: CBL discharges images for Xe gas as a function of pressure and current for 200 and 400 torr pressure, with decreasing current for various pressures. The diameter of the anode opening is 0.75 mm. [Sch-04] 22

Figure 1.11: Examples of Si based microdischarge reactors fabricated by G. Eden's team, (a) Cross-sectional diagram of an inverted pyramid microcavity and a dielectric structure designed for ac or bipolar operation; (b) SEM top view image of a single micro discharge device. [Bec-06]The silicon nitride covering the whole structure is not present when operating in DC. 24

Figure 1.12: Pyramidal Cavity MDR array fabricated by G. Eden's group (a) SEM image of a 10 x 10 device array of 50 µm cavities with 50 µm spacing and (b) image of the same 10x10 array running in DC at 244 V, 20 mA, 1200 Torr Ne. [Che-01] 25

Figure 1.13: Images showing example of Si based arrays produced by the team of G. Eden running in AC at 700 Torr Ne, (a) single pixel and (b) a part of the array of pyramidal microplasma devices [Bec-06] 25

Figure 1.14: Edge ignition phenomena reported by the German research group of RUB using PROES, image is registered with the ICCD camera (false colours) for a gate interval of 200 ns (p = 1000 mbar, f = 10 kHz, Vpp = 780 V). [Boe-10] 26

Figure 1.15: MCSD system with the appearance of the discharge plasma, end-on and side-on. [Sta-99b] 27

Figure 2.1: Alumina based MHCD reactor with a varying cavity diameter from the top to bottom. 32

Figure 2.2 : General and simplified MDR structure for Si platform based devices. 32

Figure 2.3: (a) Mask with square type top electrode design used in the first step of optical lithography (b) mask used for second step of optical lithography to facilitate MDR cavities etching by covering the unwanted wafer area by PR. 33

Figure 2.4: Mask layout having oval type top electrode design with 16 MDRs chips. 33

Figure 2.5 : Single hole MDR having (a) rectangular and (b) square chips. 34

Figure 2.6: MDR arrays with different arrangements (a) 1024 (32 x 32) hole array (D between 50 and 150 µm), (b) 256 (16 x 16) hole array (for D = 25 and 150 µm), (c) 16 (4 x 4) hole large distance array for D = 150 µm, (d) 16 (4 x 4) hole short distance array for D = 150 µm and, (e) 1600 (40 x 40) hole array (for D = 50 and 100 µm). 36

Figure 2.7 : Electrode structure arrangements for (a) mixed holes and (b) mixed trenches arrays. 37

Figure 2.8: Electrode structure arrangements for mixed hole arrays having acronym for GREMI, CNRS and ANR. 38

Figure 2.9: (a) Design for the 196 (14x14) concentric ring array, (b) zoomed in part of the mixed holes MDRs and concentric arrays (marked in red circle). 39

Figure 2.10: Structure configuration of Long trench MDR 39

Figure 2.11: Cross-sectional view of silicon substrate with 6 µm thick SiO_2 layer. 42

Figure 2.12: MDR fabrication steps for (a) Ti and Cu deposition, (b) PR spin coat, (c) optical lithography and (d) PR development. 43

Figure 2.13: Fabrication step with electrochemical deposition of top Ni electrodes. 44

Figure 2.14: Fabrication steps for microdischarge reactors for (a) wet etching of Cu and Ti layer, (b) second mask optical lithography, (c) PR development, and (d) back side ohmic contact with Ti and Au layers. 45

Figure 2.15: Pictures of the wafer after back side Ti and Au layer deposition. 45

Figure 2.16: Etching step of SiO_2 layer. 46

Figure 2.17 : MDR cavity after SiO_2 etching. 46

Figure 2.18: Si cavity etching (a) isotropically and (b) anisotropically. 47

Figure 2.19: (a) Isotropically and (b) anisotropically etched cavities. The nickel anode film unstuck when the sample was cleaved for anisotropic case. 47

Figure 2.20: (a) Cavity configuration arrangement of the MDRs for AC regime and (b) SEM image showing different layers of a MDR after cleaving without Ni electrode. 49

Figure 2.21: Ni electrode adhesion issues. 49

Figure 2.22: Example of the non-uniform etching of Si cavities due to residual micromasking effect. 50

Figure 2.23: Problem of backside gold layer detachment. 51

Figure 2.24: Examples of problems in the deposition of Si_3N_4 layer; (a) images of two MDR arrays of 32 x 32 holes, having holes' diameters 150 μm (left) and 50 μm (right); and (b) image of Mixed holes sub-arrays chip with holes' diameters of 150, 100 and 50 μm 52

Figure 2.25: Experiment setup for DC operation of MDR. 53

Figure 2.26: Configuration of TRIAX 550 spectrometer used in OES. 55

Figure 2.27: TDLAS experimental setup used for MHCD characterisation. 56

Figure 2.28: Experimental setup used for AC operation of MDRs. 57

Figure 2.29: PROES gating mechanism. 59

Figure 3.1: Standard voltage and current plots with respect to (w.r.t.) time for a single hole MHCD reactor at 400 Torr He. 61

Figure 3.2: MHCD current and voltage waveforms at the ignition of Helium micro discharges (a) at 350 Torr and (b) at 750 Torr. 62

Figure 3.3: Current and voltage plots w.r.t. time for the MHCD operating in self-pulsing regime in 200 Torr helium. 63

Figure 3.4: Current and voltage curves w. r. t. time for the ending of the microdischarges at (a) 350 and (b) 750 Torr He. 64

Figure 3.5: PMT signal recorded for the extinction of the microdischarge. 65

Figure 3.6: Equivalent electrical circuit used in the simulations, to show the ignition of microdischarges inside MHCD reactors. Red dashed lines indicate the equivalent circuit for MHCD 65

Figure 3.7: (a) Output of the simulated equivalent electrical circuit for the ignition of microdischarge in terms of voltage and current curves vs. time using PSPICE, and (b) is the zoomed part of the graph as indicated by red dashed lines in the part (a). 66

Figure 3.8: Grotrian energy level diagram for Helium. [ref: Fan-06] 68

Figure 3.9: Typical absorption profile obtained from TDLAS experiment under stable plasma operation at 500 Torr He and 15 mA of discharge current. 68

Figure 3.10: Calculated metastable density for alumina based MHCD using TDLAS method. 70

Figure 3.11: Electron number densities versus the operating current for a single hole microdischarge working at 100, 400 and 750 Torr in He. The MHCD cavity diameter is approximately 260 µm. 71

Figure 3.12: Estimated gas temperature of He using TDLAS and comparison with the gas temperature obtained from N_2 rovibrtional spectrum using OES (results are indicated with an asterisk in the legend of the graph) for MHCD. 72

Figure 3.13: Metastable density states obtained from TDLAS and current vs. time at 750 Torr He for (a) Starting (b) ending of discharges for a MHCD reactor. 74

Figure 4.1: VI-characteristics for single hole microreactor of 150 µm hole diameter (~ 180 µm deep anisotropic cavity) (a) in argon (Ar) and (b) in helium (He), at 370 Torr in both standard and reverse polarities. 78

Figure 4.2: V-I characteristics for a single hole micro-reactor of 50 µm hole diameter (~150 µm deep isotropic cavity), in helium at 750 Torr. 79

Figure 4.3: Intensity vs. discharge current (I_d) plot of microdischarge for a single hole MDR in SP case (50 µm diameter and ~150 µm deep isotropic cavity) at 750 Torr in He. Inset ICCD images show discharge operation of MDRs near the ignition, peak and ending points. (Note: the images have false colour). 80

Figure 4.4: Intensity and respective plasma spread area vs. discharge current for a single hole microdischarge reactor (50 µm diameter and ~150 µm depth isotropic cavity) in He at 750 Torr operating in RP. Inset: ICCD images in RP taken at different values of current (Note: the images have false colour). 80

Figure 4.5: (a) Plasma spread area vs. normalised intensity of the area and (b) current density of the microdischarge vs. plasma spread area. 81

Figure 4.6: VI-characteristics for a 150 µm diameter single through hole micro discharge operating in helium gas at 200 Torr. 82

Figure 4.7: Behaviour of microdischarges in (a) Standard Polarity (SP) and (b) in Reverse polarity (RP). 83

Figure 4.8: V-I characteristics for a single hole microdischarge reactor operating in He at 500 Torr (100 µm diameter and 150 µm deep anisotropic cavity) for both reverse (red dashed line) and standard (black solid line) polarities. 84

Figure 4.9: Breakdown voltage (V_{br}) vs. pressure for different diameters: 100 µm and 150 µm for a single hole microdischarge reactor in SP case. 85

Figure 4.10: Breakdown voltage vs. pressure for different cavity depths (L) of 180 µm and 500 µm (through hole), for single hole devices with 150 µm diameter in SP case. 85

Figure 4.11: VI-characteristics for a 50 µm diameter single hole microreactor of (~ 150 µm deep isotropic cavity) in helium at 300 Torr in both standard and reverse polarities. 86

Figure 4.12: Scheme of the simulated microdischarge reactor cavity geometry and the computational grid. 88

Figure 4.13: Simulation results for 150 µm deep cavity with 150 µm cavity diameter at 500 Torr He; (a) and (a1) Potential distribution, (b) and (b1) Electron density distribution, (c) and (c1) Metastable density distribution, (d) and (d1) Gas temperature distribution for I_d of 1.2 and 5.3 mA respectively. 92

Figure 4.14: Electron density for 1.2 and 5.3 mA discharge currents, (a) along the longitudinal axis and (b) along the radius of the cavity at the middle of its depth. 92

Figure 4.15: Rovibrational emission spectra obtained with OES (black solid line) and simulated spectra (red dashed line) for discharge currents (I_{ds}) of (a) 3 mA and (b) 4.8 mA for a through hole MDR with diameter 150 µm at 370 Torr He. 95

Figure 4.16: V-I characteristics for 16 hole (4 x 4) array (interhole distance 200 µm) with cavity diameter of 150 µm and isotropic cavity of 130 µm depth at 200 Torr He. 96

Figure 4.17: Series of ICCD images for a 16 hole array (interhole distance 200 µm) with cavity diameter of 150 µm and isotropic cavity of 130 µm depth. SP case in He at 200 Torr. (Note: the images have false colours). 97

Figure 4.18: SEM image of the 16 hole (4 x 4) array (interhole distance 200 µm) with cavity diameter of 150 µm and isotropic cavity of 130 µm depth. 97

Figure 4.19 : V-I characteristics for 16 hole (4 x 4) array (inter hole distance 2800 μm) (150 μm diameter, isotropic cavity, 20 μm depth) in He at 500 Torr under SP (solid black line). Inset: camera images. 98

Figure 4.20: (a) Self pulsing regime of 256 hole array with cavity diameter of 150 μm and an isotropic cavity depth of around 60 μm in SP at 200 Torr He and (b) zoomed part of the graph as indicated by the black dashed lines. 99

Figure 4.21: (a) Self pulsing regime of 256 hole array having cavity diameter of 150 μm and an isotropic cavity depth of around 60 μm in SP at 200 Torr Ar and (b) zoomed part of the graph as indicated by the black dashed lines. 100

Figure 4.22: V-I characteristics of 256 mixed holes arrays at 100 Torr He in SP case. 101

Figure 4.23: Images of 256 mixed holes sub-arrays at 100 Torr in He, during plasma operation in (a) standard polarity and (b) in reverse polarity. 102

Figure 4.24: Electrical characteristics of two 256 cavity sub-arrays having the same cavity shape and depth (anisotropic, l = 150 μm), but different diameters (D = 100 and 150μm), (a) breakdown voltage versus pressure and (b) V-I curves at 500 Torr He, for f = 200 mHz. 103

Figure 4.25: V-I characteristics for arrays of 150 μm diameter holes with cavity depth of 75 μm at 350 torr (a) in Ar and (b) in He. 104

Figure 4.26: SEM cross-section views of (a) anisotropic and (b) isotropic cavities with D = 100 μm opening diameter (after operation) for 1024 hole arrays. 105

Figure 4.27: Breakdown voltage V_{br} versus pressure P for two arrays of 1024 cavities with D = 100 μm having different cavity shapes: anisotropic and isotropic. 106

Figure 4.28: V-I curves for a 1024 hole array , D = 100 μm in (a) anisotropic and (b) isotropic cases, during a period (f = 200 mHz, T = 5 s), in He at P = 500 Torr. 107

Figure 4.29: V-I characteristics of 1024 holes array with isotropically etched cavity with diameter D = 100 μm, depth 75 μm, in He at 500 Torr for two different voltage ramp signal frequencies f = 200 mHz (T = 5 s) and f = 50 mHz (T = 20 s). 108

Figure 4.30: Characteristics of two 1024 cavities arrays with same cavity shape and diameter (anisotropic, D = 150 μm) but different depths L = 70 and 0 μm: (a) breakdown voltage versus pressure and (b) V –I curves at P = 500 Torr, in He for f = 200 mHz. 109

Figure 4.31: Simulated electric field in a 150 μm diameter single cavity; A (nickel), D (SiO_2) and C (silicon) stand for anode, dielectric and cathode respectively; the dotted line represents the cylindrical symmetry axis; the darker zone in the electric field strength distribution corresponds to values higher than 5 x 106 Vm^{-1}. 109

Figure 4.32: Effect of pressure on the ignition of the 1024 isotropically etched cavity array (diameter D = 100 μm and depth L = 75 μm), (a) V–I characteristics (the arrows indicate

microcavity discharge ignition: the small arrows for 500 Torr and long arrows for 750 Torr), (b) microcavity discharge ignition frequency, for the same voltage ramp with f = 50 mHz. 110

Figure 4.33: Electrical characteristics for three different microreactor configurations consisting of same type of cavities (anisotropic, D = 100 μm, L = 150 μm) and having different number of cavities 1024, 256, and 1; (a) breakdown voltage versus pressure and (b) V–I curves at P = 500 Torr, in He, for f = 200 mHz. 112

Figure 4.34: Ignition of 1024 cavities array with 100 μm diameter and 28 μm deep isotropic cavities operating in He at 350 torr for different discharge currents. 114

Figure 4.35: Fully ignited array with 1024 cavities having D = 100 μm and L = 28 μm isotropic cavity operating in He at 350 torr for 21.2 mA discharge current. 114

Figure 4.36: Effect of pressure variation in He gas environment on the arrays having different hole diameters 100, 150 and 50 μm on the same chip. (Dotted windows on the images indicate the border lines for different arrays) 115

Figure 4.37: Silicon chip containing 4 sub-arrays made with 16 x 5 trenches (320 trenches) with 500 μm length and 25, 50, 100, and 150 μm height. 116

Figure 4.38: Images of the Trench array ignited at different pressures at around 20 to 21 mA of current, (a) in Ar and (b) in (He)..... 117

Figure 4.39: Trench array in Ar, (a) ignited at different pressures of 50 and 1000 Torr at around 20 mA of I_d, and (b) edge ignition phenomenon at high pressure (1000 Torr) in different trenches with 150 μm to 25 μm heights and 500 μm width. 118

Figure 4.40 : Camera images for MCR array of 196 (14 x 14) holes in He (a) at 150 Torr, ~8 mA (SP), and (b) at 450 Torr, ~ 12 mA (SP). 119

Figure 4.41: Design of concentric rings cavity with different opening dimensions (A, B, and C). 119

Figure 4.42: Microdischarge cavities before operation, (a) cavities with Ni layer on the top, (b) SiO_2 etched single cavity without top Ni layer (SEM image), (c) cross-sectional view of the cavity after cleaving (SEM image,) and (d) cross-sectional view of an anisotropically etched cavity (SEM image). 120

Figure 4.43: Thermally effected zones after plasma operation (a) top view of the cavities with Ni layer with a microscope, (b) view inside the cavity with Ni layer using a microscope, (c) SEM top view of a cavity without Ni layer, surrounded with a circular thermally effected zone on SiO_2, and (d) SEM top view of a cavity with Ni layer. 121

Figure 4.44: SEM images of micro-cavities after plasma operation, (a) isotropically etched cavity with 120 μm cavity depth in Si of 150 μm diameter and (b) single 160 μm deep anisotropic cavity with a diameter of 100 μm after plasma operation 122

Figure 4.45: EDX analysis shows the sputtered Si deposition on the side walls of the cavities. 123

Figure 4.46: Electrical characterisation of the MDR arrays with mixed Concentricholes in He at 450 Torr pressure in SP (a) normal time window, (b) in ms time window, and (c) in µs time window. 124

Figure 4.47: Phenomenon explaining the life time of a micro-discharge reactor (a) normal plasma ignition, (b) micro-arc erosion effect with material redeposited on the side walls of the cavities, and (c) short-cut path due to the cathodic material deposition on the side walls which induces the microdischarge switch off. 124

Figure 4.48: Anisotropically etched single hole cavity MDR, after plasma operation of (a) few minutes (10-12 mins) D = 150 µm, (b) few tens of minutes (25-30 minutes) D = 100 µm and (c) few hours (1-2 hours) D = 150 µm. 125

Figure 4.49: SEM images for electrochemically deposited Ni on the Si surface inside the MDR cavity (a) a complete isotropic cavity, (b) part of the cavity that is used for EDX analysis, (c) and (d) showing EDX results with the material composition inside the cavity. 126

Figure 4.50: SEM image of a Si isotropic cavity (D = 150 µm and L = 160 µm)from the array of 4 x 4 holes (200 µm interhole distance) with deposited Tungsten (W) metal, (a) full cavity and (b) a zoomed part of the side wall of the cavity. 127

Figure 4.51: Voltage and current plots vs. time for 4 x 4 array with a cavity diameter of 150 µm (L = 160 µm isotropically etched) and interhole distance of 200 µm in 150 Torr He, with a deposited thin layer of Tungsten (W) metal inside the cavities. The thickness of the deposited metal layer is ~ 1 µm. 127

Figure 5.1: Voltage and current characteristics for 10 kHz frequency (a) single hole device with D = 100 µm in 500 mbar He at 590 V and (b) 1024 hole array with D = 50 µm in 980 mbar Ar at 580 V. 132

Figure 5.2: (a) Voltage and current waveforms of 1024 hole array with D = 100 µm at 10 kHz in 500 mbar Ar at 570 V and (b) zoomed in part (marked by red square in the plot (a)) showing current peak with linear reference line (red solid line) for the current amplitude measurements. 133

Figure 5.3: Time integrated images taken by a photo camera, showing the discharge mode of the AC operated MDRs with 10 kHz frequency in 500 mbar Ar (a) 1024 hole (32 x 32) array with D = 150 µm and (b) mixed trench (4 x 5 x 16) array. 134

Figure 5.4: Discharge current (I_d) and PMT behaviour w.r.t. time for a single hole MDR with a cavity diameter of 50 µm during the positive half cycle at 750 mbar Ar. 136

Figure 5.5: PMT and Voltage signals w.r.t. time for a single hole MDR with a cavity diameter of 100 µm in 760 mbar He at 600 Vpp. Inset images show ICCD pictures of the microplasma at different instants.(Images have false colours) 136

Figure 5.6: ICCD images taken for a 50 µm diameter single cavity during (a) positive half cycle and (b) negative half cycle at 750 mbar Ar, 720 Vpp, 10 kHz frequency. The red dashed line shows the approximated cavity diameter. The plot for each corresponding image shows the intensity profile of the discharge in positive and negative half cycles. (Images have false colours) 137

Figure 5.7: Scheme of the cross-section of the cylindrical cavity for a single hole, showing the concept of asymmetrical emission dynamics in (a) positive half cycle and (b) in negative half cycle. 138

Figure 5.8: Normalized emission intensity for single hole MDR with 150 µm cavity hole diameter in (a) positive and (b) in negative half cycles for 650 Vpp applied voltage at 10 kHz in argon gas at different pressures (figure on the right side is a zoom of the figure figure b). 140

Figure 5.9: Sketch of single hole MDR showing effect of pressure (higher pressure [HP], lower pressure [LP]) for (a) positive and (b) negative half cycle. 140

Figure 5.10: Intensity evolution versus time within one period for two different frequencies for a single hole MDR having a cavity diameter of 50 µm, excited by a 720 Vpp AC voltage in 750 mbar of Ar. 142

Figure 5.11: Width of PMT signal for varying frequencies for (a) positive half cycle and (b) negative half cycle. 143

Figure 5.12: ICCD image with static mode of the array with mixed holes discharge reactors with 50, 150 and 100 µm diameters sub-hole arrays (bottom to top). (Image has false colours) 144

Figure 5.13: Normalised intensity profiles with corresponding ICCD camera images (with false colours) taken at the maximum of the PMT signal for 150 µm sub array of the mixed holes array, (a) in positive and (b) negative half cycle. 144

Figure 5.14: Ignition waves on an array having 1024 holes with cavity diameter 100 µm at 500 mbar Ar for negative half cycle. (Images have false colours) 146

Figure 5.15: Edge ignition phenomena of 150 µm x 500 µm trench arrays in (a) positive half cycle and (b) negative half cycle. (Images have false colours) 147

Figure 5.16: Ignition waves on 50 µm trench sub-array at 750 mbar Ar with 530 Vpp applied voltage with 10 kHz frequency. (Images have false colours) 147

Figure 5.17: ICCD static mode images with ignition trend during the manual increase of applied peak to peak voltage at (a) 517 V, (b) 531 V, (c) 544 V and (d) 550 V for a mixed trench array at 700 mbar Ar. (Images have false colours) 148

Figure 5.18: Ignition trend registered with PROES experiment for an applied peak to peak voltage of ~ 545 V with triangular ramp of 10 kHz frequency at 700 mbar Ar. (Images have false colours) 148

List of Tables

Table 3.1: Approximated FWHM of absorption profiles obtained from TDLAS experiment, for different discharge currents at pressures 350 and 750 Torr..... 73

Table 4.1: Pure helium plasma chemistry in the present study. 90

Table 4.2: Comparison of simulated and calculated sheath thickness for different Id : 94

Table 4.3: Geometrical features of the cavities of the two micro-reactors (16 × 16 = 256) used for cavity opening diameter study; D: opening diameter, d_n: distance to nearest neighbour cavity, l: depth, Scath: wall surface area (cathode surface), V: volume. 103

Table 4.4: Geometrical features of the cavities (shown in figure 4.26) of the 1024 microreactor array (D = 100 μm); D is the opening diameter, d_n is the side to side distance between two neighbour cavities, D_{cav} is the inner cavity diameter, L is their depth, S_{cath} is the cathode area and V is the cavity volume. 106

Bibliography

[Amb-10] Ambrico P.F., Ambrico M., Colaianni A., Schiavulli L., Dilecce G and Benedictis S. De, 2010, J. Phys. D: Appl. Phys. 43 (32), 325201.

[Aub-07] Aubert X., Bauville G., Guillon J., Lacour B., Puech V., Rousseau A., 2007, Plasma Sources Sci. Technol., 16, 23-32.

[Baa-03] Baars-Hibbe L., Sichler P., Schrader C., Geßner C., Gericke K-H., Büttgenbach S., 2003, Surface Coat. Technology 519, 174-175.

[Baa-04] Baars-Hibbe L., Schrader C., Sichler P., Cordes T., Gericke K-H., Büttgenbach S., Draeger S., 2004, Vacuum 73, 327.

[Bec-04] Becker K. H., Kogelschatz U., Schoenbach K. H., Barker R. J., Eds., Non-Equilibrium Air Plasmas at Atmospheric Pressure, 2004, IOP Publishing Ltd, Bristol, UK, (now: Taylor & Francis, CRC Press).

[Bec-05] Becker K. H., Koutsospyros A., Yin S-M., Christodoulatos C., Abramzon N., Joaquin J. C. and Brelles-Marino G., 2005, Plasma Phys. Control. Fusion 47, B513.

[Bec-06] Becker K. H., Schoenbach K. H. and Eden J. G., 2006, J. Phys. D: Appl. Phys. 39, R55–70.

[Boe-10] Boettner H., Waskoenig J, O'Connell D, Kim T. L., Tchertchian P A, Winter J. and Schulz-von der Gathen V., 2010, J. Phys. D: Appl. Phys. 43 (12), 124010.

[Boe-95] Boeuf J.P., Pitchford L.C., 1995, Phys. Rev. E 51, 1376.

[Bou-94] Boulos M. I., Fauchais P., Pfender E., 1994, Thermal Plasmas: Fundamental and applications I, Plenum Press, New York, ISBN: 0-306- 44607-3, 452 pp.

[Cha-10] Chabert P., Lazzaroni C. and Rousseau A., 2010, JAP 108.

[Che-01] Chen J., Park S-J., Eden J. G., Liu C., 2001, Proceedings of Transducers '01 Eurosensors XV: The 11th International Conference on Solid-State Sensors and Actuators, Munich 2001, edited by E. Obermeier (Springer 2001), Paper 2C1.05P.

[Che-02] Chen J., Park S.-J., Eden J. G., and Liu C., 2002, Journal of microelectromechanical systems, 11 (5), 536-543.

[Cho-99] Choi K. C. and Tae H-S., 1999, IEEE Trans. Electron Devices 46, 2344.

[Chr-90] Christophorou L. G. and Pinnaduwage L. A., 1990, *IEEE Trans. Electr. Insul.* 25, 55–74.

[Dei-08] Deilmann M., Halfmann H., Bibinov N., Wunderlich J. and Awakowicz P., 2008, J. Food Prot. 71, 2119–23.

[Den-07] Deng S., Ruan .R, Mok C. K., Huang G., Lin X. and Chen P., 2007, J. Food Sci. 72, M62-66.

[Don-05] Dong L., Liu F., Liu S., He Y., Fan W., 2005, Phys. Rev. E 72, 046215.

[Duf-08] Dufour .T, Dussart R., Lefaucheux P., Ranson P., Overzet L. .J, Mandra M., Lee J-B., Goeckner M., 2008, Appl. Phys. Lett. 93, 0715081.

[Duf-09] Dufour T., 2009, PhD thesis "Etude expérimentale et simulation des micro-plasmas générés dans des micro-cathodes creuses", GREMI, Univ. d'Orleans, France.

[Duf-10] Dufour T., Overzet L. J., Dussart R., Pitchford L. C., Sadeghi N., Lefaucheux P., and Kulsreshath M., and Ranson P., 2010, The European Physical Journal D, Volume 60, Number 3, 565-574.

[Dus-04] Dussart R., Boufnichel M., Marcos G., Lefaucheux P., Basillais A., Benoit R., Tillocher T., Mellhaoui X., Estrade-Szwarckopf H. and Ranson P., 2004, J. Micromech. Microeng. 14, 190–196.

[Dus-10] Dussart R, Overzet L.J., Lefaucheux P., Dufour T., Kulsreshath M., Mandra M.A., Tillocher T., Aubry O., Dozias S., Ranson P., Lee J.B., and Goeckner M. 2010, Eur. Phys. J. D 60, 601-608.

[Ede-03] Eden J. G., Park S-J., Ostrom N. P., McCain S. T., Wagner C. J., Vojak B. A., Chen J., Liu C., Allmen P. von, Zenhausern F., Sadler D. J., Jensen C., Wilcox D. L. and Ewing J. J., 2003, J. Phys. D: Appl. Phys. 36, 2869-2877.

[Ede-05] Eden J G and Park S-J, 2005, Plasma Phys. Control. Fusion 47 (12B), B83-B92.

[Ede-05a] Eden J. G., Park S-J., Ostrom N. P. and Chen K-F., 2005 J. Phys. D: Appl. Phys. 38, 1644–1648.

[Eij-00] Eijkel J. C. T., Stoeri H., Manz A., 2000, J. Anal. At. Spectrom. 15, 297.

[Ell-76] Ellis H. W., Pai R. Y., and Mcdaniel E. W., 1976, Atomic data and nuclear dta tables 17, 177-210.

[Evj-04] Evju J. K., Howell P. B., Locascio L .E, Tarlov M. J., Hickham J. J., 2004, Appl. Phys. Lett. 84, 1668.

[Fan-06] Fantz U., 2006, Plasma Sources Sci. Technol. 15, S137–S147.

[Far-94] Farin G. and Grund K. E. 1994, Endosc. Surg. Allied Technol. 2. 71–77.

[Foe-05] Foest R., Kindel E., Ohl A., Stieber M. and Weltmann K. D., 2005, Plasma Phys. Control. Fusion 47, B525–36.

[Foe-06] Foest R., Schmidt M. and Becker K. H., 2006, Mass Spectrom. 248, 87–102.

[Fra- 98] Frame J. W. and Eden J. G., 1998, Electron. Lett. 34, 1529.

[Fra-97] Frame J. W., Wheeler D. J., De Temple T. A. and Eden J. G., 1997, Appl. Phys. Lett. 71, 1165-1167.

[Fra-98a] Frame J. W., John P. C., DeTemple T. A., and J. G. Eden, 1998, Appl. Phys. Lett., vol. 72, pp. 2634–2636.

[Gol-05] Golubovskii Y. B., Maiorov V. A., Behnke J., Behnke J. F., 2005, Plasma Process. Polym., 2, 188.

[Gui-00] Guikema J., Miller N., Niehof J., Klein M., Walhout M., 2000, Phys. Rev. Lett., 85, 3817.

[Hab-98] El-Habachi A. and Schoenbach K. H., 1998, Appl. Phys. Lett. 72, 22.

[Hab-98a] El-Habachi A. and Schoenbach K. H., 1998b, Appl. Phys. Lett. 73, 885.

[Hag-05] Hagelaar G.J.M., Pitchford L.C., Plasma Source. Sci. Technol. 14, 722 (2005)

[Hip-07] Hippler R., Kersten H., Schmidt M., Schoenbach K. H., 2007, 2nd edition, Wiley-VCH, Weinheim.

[Hsu-03] Hsu D. D. and Graves D. B., 2003, J. Phys. D: Appl Phys. 30.

[Hsu-05] Hsu D. D. and Graves D. B., 2005, Plasma Chemistry and Plasma Processing, 25, 1-17.

[Iza-08] Iza F., Kim G. J., Lee S. M., Lee J. K., Walsh J. L., Zhang Y. T. and Kong M. G., 2008, Plasma Processes Polym. 5, 322–44.

[Kem-93] Kern W., Ed., Handbook of Semiconductor Cleaning Technology, 1993, Noyes Publishing: Park Ridge, NJ, Ch 1.

[Kle-01] Klein M., Miller N., Walhout M., 2001, Phys. Rev. E 64, 026402.

[Kog-03] Kogelschatz U., 2003, Plasma Chem. Plasma Process. 23, 1.

[Kog-99] Kogelschatz U., Eliasson B., Egli W., 1999, Pure Appl. Chem. 71, 1819.

[Kon-09] Kong M. G., Kroesen G., Morfill G., Nosenko T., Shimizu T., Dijk J. van and Zimmermann J. L., 2009, New Journal of Physics 11, 115012.

[Kor-98] Korolev Yu. D. and Mesyats G. A., 1998, Physics of pulsed breakdown in gases, URO-Press.

[Kot-05] Kothnur P.S. and Raja L.L., 2005, Journal of Applied Physics, 97, 043305.

[Kuf-00] Kuffel E., Zaengl W. S. and Kuffel J., 2000, High Voltage Engineering Fundamentals, London: Butterworth-Heinemann.

[Kul-12] Kulsreshath M. K., Schwaederlé L., Overzet L.J., Lefaucheux P., Ladroue J., Tillocher T., Aubry O., Woytasik M., Schelcher G., and Dussart R., 2012, J. Phys. D: Appl. Phys. 45, 285202.

[Kun-00] Kunhardt E. E., 2000, IEEE Trans. Plasma Sci. 28, 189.

[Kur-01] Kurunczi P., Lopez J., Shah H. and Becker K., 2001, Int. J. Mass Spectrom. 205, 277.

[Kus-05] Kushner M.J., 2005, J. Phys. D: Appl. Phys. 38, 1633.

[Laz-11] Lazzaroni C. and Chabert P., 2011, Plasma Sources Sci. Technol. 20.

[Led-09] Leduc M. et al., 2009, New J. Phys. 11, 115021.

[Lee-09] Lee M. H. et al, 2009, New J. Phys. 11, 115022.

[Lie-05] Lieberman M. A., Lichtenberg A. J., 2005, Principles of plasma discharges and materials processing, New York: Wiley, Hoboken, NJ.

[Mar-11] Martin V., Bauville G., Sadeghi N. and Puech V., 2011, J. Phys. D: Appl. Phys. 44, 435203.

[Mee] Meeker D. C., Finite element method magnetics, version 4.0.1 http://www.femm.info/wiki/HomePage

[Mic-02] Miclea M. et al., 2002, Proc. Hakone VIII (Puehajaerve, Estonia) vol 1, p 206.

[Mit-08] Mitra B, Levey B and Gianchandani Y B 2008 *IEEE Trans. Plasma Sci.* 36 1913

[Mit-12] Mitea S., Zeleznik M., Bowden M. D., May P. W., Fox N. A., Hart J. N., Fowler C., Stevens R. and Braithwaite N. St. J., 2012, Fast track communication, Plasma Sources Sci. Technol. 21, 022001.

[Moi-96] Moisan M., Calzada M.D., Gamero A., and Sola A., 1996, J. Appl. Phys. 80 (1), 46– 55.

[Mos-01] Moselhy M., Stark R. H., Schoenbach K.H. and Kogelschatz U., 2001, Appl. Phys. Lett. 78, 880.

[Mos-01a] Moselhy M., Shi W., Stark R. H. and Schoenbach K. H., 2001, Appl. Phys. Lett. 79, 1240.

[Mos-03] Moselhy M., Petzenhauser I., Frank K. and Schoenbach K. H., 2003, J. Phys. D: Appl. Phys. 36, 2922.

[Nad-96] Naidu M. S. and Kamaraju V., 1996, High Voltage Engineering ed. 2, New York: McGraw-Hill.

[Ner-04] Nersisyan G., Graham W. G., 2004, Plasma Sources Sci. Technol. 13, 582.

[Nis-12] Nist Data base: http://physics.nist.gov/PhysRefData/ASD/lines_form.html (seen on August 2012)

[Pap-63] Papoular R., 1963, "Phénomènes Electriques dans les Gaz", Dunod, Paris (Berlin Springer).

[Par-00] Park S-J., Wagner C.J., Herring C. M., and Eden J. G., 2000, Appl. Phys. Lett. 77, 199.

[Par-01] Park S-J., Chen J., Liu C., and Eden J. G., 2001, Appl. Phys. Lett. 78(4), 419-421.

[Par-02] Park S-J., Chen J., Wagner C. J., Ostrom N. P., Liu C., and Eden J. G., 2002, Journal on selected topics in quantum electronics 8 (2), 387.

[Par-05] Park S-J., Chen K-F., Ostrom N. P., and Eden J. G., 2005, Appl. Phys. Lett. 86, 111501.

[Pas-89] Paschen F., 1889, Ann. Phys., Lpz. 273, 69–96.

[Pen-02] Penache C., Miclea M., Bräuning-Demian A, Hohn O, Schössler S, Jahnke, Niemax K and Schmidt-Böcking H, 2002, Plasma source sci. Technology. 11, 476-483.

[Pen-93] Penetrante B. M. and Schultheiss S. E., 1993, Proc. NATO-ASI vol. 34A/B, New York: Plenum.

[Que] Questech Services Corporation, 2201 Executive Drive, Garland, Texas 75041, USA (http://www.questlaser.com).

[Rai-06] Raiser J. and Zenker M., 2006, J. Phys. D: Appl. Phys. 39 (16), 3520-3523.

[Rai-91] Raizer, Y. P., Gas discharge Physics, 1991, ISBN 3-540-19462-2 Springer-Verlag Berlin Heidelberg New York.

[Raj-09] Rajasekaran .P, Mertmann P., Bibinov N., Wandke D., Viöl W., and Awakowicz P., 2009, J. Phys. D: Appl. Phys. 42 (22), 1540-1543.

[Rev-00] Revel I., Pitchford L.C., Boeuf J.P., 2000, J. Appl. Phys. 88, 2234.

[Rob-12] Robert E., Sarron V., Ries D., Dozias S., Vandamme M. and Pouvesle J-M., 2012, Plasma Sources Sci. Technol. 21, 034017.

[Rot -95] Roth J. R., 1995 Industrial plasma Engineering vol-1, IOP Publishing Ltd.

[Rou-06] Rousseau A. and Aubert X., 2006, J. Phys. D: Appl Phys.. 39.

[Sad-04] Sadeghi N., 2004, Molecular Journal of Plasma and Fusion Research, 80, 767.

[San-02] Sankaran R.M., Giapis K.P., 2002, J. Appl. Phys. 92, 2406.

[Sch-00] Schoenbach K. H., El-Habachi A., Moselhy M., Shi W. and Stark R. H., 2000, Phys. Plasmas 7, 2186.

[Sch-00a] Schlesinger M. and Paunovic M., Modern electroplating, 2000, John Wiley & Sons, Inc.

[Sch-03] Schoenbach K. H., Moselhy M., Shi W. and Bentley R., 2003, J. Vac. Sci. Technol. A 21, 1260.

[Sch-12] Schwaederle L., Kulsreshath M. K., Overzet L. J., Lefaucheux P., Tillocher T. and Dussart R., 2012, J. Phys. D: Appl. Phys. 45, 065201.

[Sch-96] Schoenbach K.H., Verhappen R., Tessnow T., Peterkin F.E., Byszewski W.W., 1996, Appl. Phys. Lett. 68, 13.

[Sch-97] Schoenbach K. H., El-Habachi A., Shi,W. Ciocca M., 1997, Plasmas sources Sci. Technol., 6, 468-477.

[Ser-97] Serikov V.V., Nanbu K., 1997, J. Appl. Phys. 82, 5948.

[Sla-04] Sladek R. E. J., Stoffels E., Walraven R., Tielbeek P. J. A. and Koolhoven R. A., 2004, IEEE Trans. Plasma Sci. 32 (4), 1540-1543.

[Sta-05] Staack D., Farouk B., Gutsol A., Fridman A., 2005, Plasma Sources Sci. Technol. 14, 700.

[Sta-99a] Stark R. H. and Schoenbach K. H., 1999, J. Appl. Phys. 85 (4), 2075.

[Sta-99b] Stark R.H. and Schoenbach K.H., 1999, Applied Physics Letters, 74 (25), 3770.

[Sto-06] Stoffels E., Kieft .I E., Sladek R. E. J., Bedem L. J. M. van den, Laan E. P. van der and Steinbuch M., 2006, Plasma Sources Sci. Technol. 15(4), S169-S180.

[Van-12] Vandamme M., Robert E., Lerondel S., Sarron V., Ries D., Dozias S., Sobilo J., Gosset D., Kieda C., Legrain B., Pouvesle J-M. and Le Pape A., 2012, Int. J. Cancer: 130, 2185–2194.

[Wag-03] Wagner H-E., Brandenburg R., Kozlov K. V., Sonnenfeld A., Michel P., Behnke J. F., 2003, Vacuum 71, 417.

[Was-08] Waskoenig J., O'Connell D., Schulz-von der Gathen V., Winter J., Park S-J. and Eden J. G., 2008, Appl. Phys. Lett. 92 (10), 101503.

[Wel-08] Weltmann K-D., Brandenburg R., Woedtke .T von, Ehlbeck J., Foest R. , Stieber M. and Kindel E., 2008, J. Phys. D: Appl. Phys. 41,194008.

[Whi-59] White A. D., 1959, J. Appl. Phys. 30 (5), 711.

[Yin-03] Yin S-M., Christodoulatos C., Becker K. and Koutsospyros A., 2003, Proc. Int. Conf. on Environ. Syst. (ICES) SAE International, Paper No 2003-01-2501

Appendix — Publications

Parts of this work have already been published in different scientific journals. A list of the published articles is given as below:

- Mukesh Kulsreshath, Laurent Schwaederlé, , L.J. Overzet, P. Lefaucheux, J. Ladroue, T. Tillocher, O. Aubry, M. Woytasik, G. Schelcher, R. Dussart, "Study of DC micro-discharge arrays made in silicon using CMOS compatible technology", J. Phys. D: Appl. Phys. 45, 285202 (2012)

- Laurent Schwaederlé, Mukesh Kulsreshath, Lawrence Overzet, Philippe Lefaucheux, Thomas Tillocher, Remi Dussart, "Breakdown study of dc silicon micro-discharge devices", Journal of Physics D: Applied Physics, 45, 065201 (2012)

- T. Dufour, L.J. Overzet, R. Dussart, L.C. Pitchford, N. Sadeghi, P. Lefaucheux, M. Kulsreshath and P. Ranson, "Experimental study and simulation of a micro-discharge with limited cathode area", Eur. Phys. J. D 60, 565–574 (2010)

- R. Dussart, L.J. Overzet, P. Lefaucheux, T. Dufour, M. Kulsreshath, M.A. Mandra, T. Tillocher, O. Aubry,S. Dozias, P. Ranson, J.B. Lee, and M. Goeckner, "Integrated micro-plasmas in silicon operating in helium", Eur. Phys. J. D (2010)

Mukesh Kumar KULSRESHATH

Développement et étude de matrices microdécharge sur silicium

L'objectif de cette thèse est de fournir une meilleure compréhension des différents phénomènes physiques liés aux microplasmas/microdécharges. Pour cela, des matrices de microréacteurs sur silicium ont été étudiées. De nombreuses configurations ont été construites de manière à analyser l'influence de chaque paramètre physique sur le fonctionnement de ces dispositifs. Le présent travail porte sur l'élaboration et la caractérisation de dispositifs micro-décharge à base de silicium. Dans ce travail de thèse, les régimes de courant continu (DC) et de courant alternatif (AC) sont étudiés en utilisant des configurations de décharges différentes. Pour la fabrication de ces réacteurs, nous sommes partis de wafers de Silicium que nous avons structurés et traités en salle blanche. La technologie de fabrication utilisée est compatible avec les méthodes de fabrication de dispositifs CMOS. Les microréacteurs sont constitués d'électrodes de nickel et de silicium séparés par une couche diélectrique de SiO2 de 6 µm d'épaisseur. L'épaisseur du diélectrique est ici beaucoup plus faible que celle des microréacteurs étudiés jusqu'à présent. Les dispositifs sont constitués de cavités de 25 à 150 microns de diamètre. Les essais de microdécharge ont été effectués dans des gaz inertes à une pression comprise entre 100 et 1000 Torrs. Nous avons d'abord étudié les phénomènes d'allumage et d'extinction à partir de microdispositifs monocavité en alumine. Puis, nous avons étudié le fonctionnement en DC/AC de microréacteurs en silicium comportant un nombre de cavité compris entre 1 et 1024. Les caractéristiques des microdécharges ont été étudiées grâce à des mesures électriques, des mesures de spectroscopie d'émission optique (OES), de spectroscopie d'absorption à diode laser (DLAS) et de spectroscopie d'émission optique résolue en temps (PROES). Ces différents diagnostics nous ont permis de mettre en évidence les phénomènes d'allumage, d'extinction, d'instabilité et les mécanismes de défaillance de nos microdispositifs. Ce travail de thèse a permis de tester les performances et les limites technologiques des matrices de microdécharges sur silicium. Une attention particulière a été portée sur leur durée de vie.

Mots clés : microdécharge, microplasma, les matrices intégrés au silicium, MHCD, OES, PROES, TDLAS, DC, AC décharge décharge, plasma à pression atmosphérique, MDR.

Development and study of microdischarge arrays on silicon

The objective of this thesis is to provide a better understanding of various physical phenomena related to microplasmas/microdischarges. For this purpose, arrays of microreactors on silicon were studied. Different array configurations were fabricated to analyse the influence of each parameter on the physical operation of these devices. The present work focuses on the development and characterisation of micro-discharge devices based on silicon. In this thesis, direct current (DC) and alternating current (AC) regimes are studied using different discharge configurations. For the fabrication of these reactors, Silicon wafers are structured and processed in a cleanroom. Fabrication technology used is compatible with the CMOS technology. The microreactors are fabricated with nickel and silicon electrodes, separated by a dielectric layer of SiO_2 with a thickness of 6 µm. The thickness of the dielectric is much lower here than the microreactors studied so far. The devices consist of cavities with 25 to 150 µm in diameter. Experiments of the microdischarges are performed in inert gases at a pressure between 100 and 1000 Torr. We first studied the phenomena of ignition and extinction for the microdevices based on alumina. Then, we studied the microreactors based on silicon containing 1 to 1024 cavities under DC and AC regimes. Characteristics of microdischarges were studied by electrical measurements, measurements of optical emission spectroscopy (OES), laser diode absorption spectroscopy (DLAS) and phase resolved optical emission spectroscopy (PROES). These diagnostics allowed us to investigate the phenomena of ignition, extinction, instability and failure mechanisms of the microplasma devices. This thesis work allowed testing the performance and technological limitations of the silicon based microdischarge arrays. Particular attention was paid to their life time.

Keywords: microdischarge, microplasma, silicon integrated arrays, MHCD, OES, PROES, TDLAS, DC discharge, AC discharge, atmospheric pressure plasma, MDR.

Groupe de Recherches sur l'Energétique des Milieux Ionisés

14 rue d'Issoudun B.P. 6744 45067 ORLEANS Cedex 2